11

Final Focus

Contents

11.1 Introduction

The final-focus system comprises the region between the big bend and the main beam dump. Its function is to demagnify the transverse sizes of electron or positron beams by a factor 80 horizontally and 300 vertically, down to a value of about 250 nm $\times$ 4 nm at the interaction point (IP), where the beams collide. After the collision, an extraction line guides the beam remnants onto the beam dump.

The final-focus designs for 500 GeV and for 1 TeV which are described in this chapter, have a comfortable momentum bandwidth and can operate in the full ZDR parameter plane. A dedicated geometry-adjustment section at the entrance to the final focus facilitates the adiabatic upgrade from 350-GeV to 1.5-TeV-c.m. energy, with a constant IP position and only minor transverse displacements.

Important design issues of the final-focus system are linear and nonlinear optics; momentum bandwidth; effects of synchrotron radiation; tuning schemes; sensitivity to varying beam conditions, such as incoming orbit, emittance, and energy; tolerances on alignment, vibrations and field changes; response to ground motion; wakefield effects; stability of the final doublet; design and tolerances of the crab cavity; compensation of the solenoidal detector field; beam removal from the IP; maintenance, tuning and stabilization systems.

When compared to previous colliders, the NLC beam parameters and tolerances enter a distinctly new regime. The spot size at the IP is 125 times smaller than that at the SLC, which is already as small as 500 nm, and is 15 times smaller than the 70-nm spot size achieved at the FFTB. In addition to delineating the stringent tolerances which are a consequence of the small spot size, we will attempt to clarify how we propose to achieve these tolerances. The story is complex since there are several significant timescales, several distinct aberrations to consider at each timescale, many elements and element parameters which can influence each aberration, and many sources of change for the parameters of each element. Each timescale is associated with a tuning system and a maintenance system which stabilizes the final focus between tunings. We use the word tuning when the diagnostic involves determination of IP beam and collision conditions. Hence missteering at the IP is one of the aberrations which is tuned.

In the case of alignment, because everything is moving, it is often difficult to clearly convey what elements need to stay aligned, by how much, and with respect to what other elements or coordinate system. An important result of ground-motion studies, which are described in Appendix C, is that the ground (bedrock) can be used as a reference, in the sense that if all elements were moving as the bedrock below them, then the beams would remain in collision. Section 11.5.5 discusses these results as they apply to the final-focus system.

Aberrations are described in Section 11.5.3. A table in that Section (Table 11-9) lists all aberrations that will be tuned, how they will be tuned, frequency of tuning, what budget of luminosity is allotted to the final-focus system (since other upstream elements can contribute to these aberrations), and what systems maintain (stabilize) the system between tunings. Tuning and maintenance systems are described in more detail in Sections 11.3.1, 11.3.2, and 11.5.4. 11.5.4 and 11.5.8.

In Section 11.5.5, relevant timescales, each of which corresponds to a tuning frequency, are listed and named, and all tolerances described are specified relative to these timescales. Tolerances can be achieved if:

- The diagnostic systems used for tuning have the required resolution.
- Tuning and adjustment knobs have the required sensitivity.
- Maintenance systems stabilize the final focus between tunings.

The performance of the maintenance systems in turn depends on achieving the required resolution in their diagnostic systems. Diagnostic systems are described in Section 11.5.8.

In the SLC, only the IP steering and incoming beam launch conditions have been automated. Though a dither feedback has been considered for the other IP aberrations, it would be speculative at this point to believe such a system would work at the NLC, and we do not make this assumption. Automated tuning (steering) and automated maintenance systems are described in Section 11.5.6.

Tables 11-13 through 11-18 list the sensitivities of the parameters of each element. Using these sensitivities a tolerance is assigned to each element (Table 11-19) so that the system budget of each aberration is met. Elements with similar tolerances have been grouped together. Table 11-21 gives the luminosity loss that results from these tolerance assignments, to be compared with the final-focus system budget of Table 11-9. Corresponding to each tolerance in Table 11-19, there is a brief statement on how this tolerance can be met (Table 11-20). Finally, in Section 11.5.8, we present a table that lists every diagnostic element and the resolution required.

It is worth noting that both the optical design and proposed tuning algorithms draw heavily from SLC and FFTB experience. In the limited time available, every small aspect of the design could not be studied in minute detail. However, we feel that all potentially critical or problematic topics have been addressed in depth. Outstanding work includes, for instance, a more detailed study of certain tuning and alignment procedures, and a more exhaustive description of commissioning, operation and machine protection. These items are not expected to be difficult.

One of the reviewers of the August 95 ZDR workshop (K. Oide) has created an alternative final-focus design for NLC parameters at 500-GeV-c.m. energy, which is based on the odd-dispersion scheme [Oide 1992]. The bandwidth of this system, without any additional `Brinkmann'-sextupoles, is comparable to that of the present NLC design. An advantage of the odd-dispersion final focus is that it only uses about half the number of quadrupoles. A potential disadvantage is the nonexistence of an IP pre-image point, which may or may not be an operational aid. The tunability, upgradability, performance at higher energy, and background situation of the odd-dispersion design need to be evaluated, prior to a final decision on this alternative. In the present report, only the modular final-focus design by R. Helm is discussed, the performance of which appears to be entirely satisfactory.

11.2 Parameters and Specifications

11.2.1 Goals and System Boundaries

The purpose of the NLC final-focus system is to transport electron and positron beams of energy 180 GeV to 750 GeV from the end of the big bend to the IP, where the demagnified beams are collided, and to remove the beam remnants cleanly to facilitate crucial post-IP diagnostics. To accomplish its task, the final-focus system has to be stable and reliable, and it needs redundant diagnostics to detect and compensate all changes of beam parameters, magnet positions, or field strengths, which would otherwise reduce the luminosity.

For a c.m. energy of 500 GeV, the design spot size at the interaction point (IP) is about 4.2–6.5 nm vertically and 250–300 nm horizontally. The normalized emittances at the entrance of the final focus are assumed to be $\gamma\epsilon_x \approx 4\times10^{-6}$ m and $\gamma\epsilon_y \approx$ 7–10.5 $\times10^{-8}$ m. At a c.m. energy of 1 TeV, the design spot size is 3.4–5.2 nm vertically and 200–250 horizontally, for normalized emittances of $\gamma\epsilon_x \approx 4\times10^{-6}$ m, and $\gamma\epsilon_y \approx$ 9–13.5$\times10^{-8}$ m. The beam energy distribution in the final focus depends on bunch compressor and linac configurations. For most studies presented in this chapter, a Gaussian momentum distribution with a relative rms momentum spread of $\delta \approx 0.3\%$ is assumed. This distribution makes it easy to study the effect of a typical energy spread, but the real energy distribution will be non-Gaussian (compare Chapters 5 and 7).

The entrance of the final-focus system is formed by a skew correction section (SCS) and a diagnostics section (DS). These are followed by a geometry-adjustment section (GAS), beta- and phase-matching section (BMS), horizontal and vertical chromatic correction sections (CCX and CCY), which are separated by a beta-exchange module (BX), the final transformer (FT), the interaction region (IR), and the beam removal system (BRS). This chapter describes all these sections except for the IR which is discussed separately in Chapter 12.

The final-focus system is flexible enough to be operated in the entire c.m. energy range from 350 GeV to 1.5 TeV. Most of the data and figures in the following sections refer to the design for either 500-GeV or 1-TeV-c.m. energy.

11.2.2 Parameter List

Table 11-1 exemplifies beam parameters at the interaction point for c.m. energies of 500 GeV and 1 TeV. In this table, the values listed for luminosity and spot size do not include any dilutions, which may arise from high-order aberrations, synchrotron radiation residual uncorrected low-order aberrations, timing offsets or crab crossing errors. When dilutions are taken into account, the expected luminosity is reduced by about 20–30%, see Table 11-4 and the discussions in Section 11.5.

Most beam parameters are variable, as the NLC should function at any point inside a multi-dimensional operating plane [Burke 1995]. From the final-focus point of view, the largest IP divergences represent the worst case, since in this case the effect of nonlinear aberrations, the aperture requirements, and the Oide effect are most severe. The beam parameters listed in Table 11-1 refer to this case.

The minimum horizontal beta function at the IP is limited by nonlinear aberrations, by the maximum number of beamstrahlung photons that can be tolerated Chapter 12. and by the Oide effect (Sections 11.5.3 and 11.6.4). The value presently chosen was imposed by the beamstrahlung, whereas Oide effect and nonlinearities would allow for a 20% smaller beta function. It is, therefore, possible to compensate the increase of the horizontal spot size due to residual low-order aberrations by reducing β_x^*.

11.2.3 Energy Flexibility

The final focus should operate at least in the energy range from 350 GeV to 1.5 TeV. In the present design, this flexibility is accomplished with slightly different geometries for three overlapping energy ranges (Figures 11-9 and 11-10). The implication is that two minor reinstallations of magnets and supports are necessary during the energy upgrade, at around 500 GeV and 1.1 TeV. The IP position is held constant by means of a special bending section—the geometry-adjustment section—which is located at the entrance to the final focus.

At 500-GeV-c.m. energy, the final focus is operated with quadrupoles scaled down from the 1-TeV design. A complication arises in the final doublet, since the last quadrupole is a permanent magnet. Here, the energy scaling is accomplished by an adjacent superconducting quadrupole whose field changes sign during the energy raise from 500 GeV to 1 TeV. In order to keep the cost of a further upgrade low, the remaining final-focus magnets could be designed such that their strength can be increased to the 1.5-TeV values.

Comments	c.m. energy	500 GeV	1 TeV
Luminosity w/o dil.	L (10^{34} cm^{-2} s^{-1})	0.52	1.16
Luminosity w. pinch w/o dil.	L (10^{34} cm^{-2} s^{-1})	0.75	1.63
# particles per bunch	N_b (10^{10})	0.65	0.95
# bunches	n_b	90	90
# bunch trains per s	f	180	120
Enhancement factor w/o dil.	H_D	1.46	1.41
Hor. spot size w/o dil.	σ_x (nm)	253	200
Vert. spot size w/o dil.	σ_y (nm)	4.18	3.35
Hor. IP beta function	β_x^* (mm)	8	10
Vert. IP beta function	β_y^* (mm)	0.125	0.125
Norm. hor. emittance	$\gamma\epsilon_x$ (10^{-8} mr)	400	400
Norm. vert. emittance	$\gamma\epsilon_y$ (10^{-8} mr)	7	9
Hor. IP divergence	$\sigma_{x'}$ (μrad)	31.6	20.0
Vert. IP divergence	$\sigma_{y'}$ (μrad)	33.5	26.8
Bunch length	σ_z (μm)	100	125
Crossing angle	θ_c	20 mr	20 mr
Energy spread	δ_{rms}	$\geq 3 \times 10^{-3}$	$\geq 3 \times 10^{-3}$
Free length from IP	l^* (m)	2	2

Table 11-1. *Basic worst-case interaction-point beam parameters without dilutions (see also Table 11-4).*

11.2.4 Overview

On the next pages, the skew correction section (SCS) is discussed, along with two options for the adjacent diagnostics section (DS). Section 11.4 is devoted to the beta- and phase-matching section (BMS), which will be used to adapt the IP beta functions and the waist position to varying incoming beam conditions, and to adjust the betatron phase advance between the collimator section and the IP. The geometry-adjustment section (GAS) located upstream of the BMS, the horizontal chromatic correction section (CCX), the beta-exchange module (BX), the vertical chromatic correction section (CCY) and the final transformer (FT), as well as a tolerance analysis for this region are described in Section 11.5, which also contains lists of magnets and diagnostics for the entire region between the SCS and the IP. Section 11.6 discusses the final doublet; Section 11.7 discusses effects of the solenoidal detector field and the crab cavity. The beam removal system (BRS) and beam dump are described in Section 11.8. Section 11.9 concludes the chapter with a short perspective on the present design and on outstanding questions.

11.3 Skew Correction and Diagnostic Section

This beam line section follows the big bend and is used to measure and correct any anomalous cross-plane coupling and to precisely match the beam into the main body of the final focus. In order to minimize the projected emittance, especially for a flat beam, it is necessary to remove all cross-plane correlations. SLC experience has shown this to be a very difficult problem when provisions are not included in the design to reliably measure and/or correct all four betatron correlation phases. Rather than placing skew quadrupoles and wire scanners as post-design space allows, a dedicated coupling correction and diagnostic section is highly desirable, especially for large emittance aspect ratios as in the NLC ($\varepsilon_{x0}/\varepsilon_{y0} \sim 100$).

11.3.1 The Skew Correction Section

The ideal Skew Correction Section (SCS) contains four skew quadrupoles separated by appropriate betatron phase advance in each plane such that the skew correctors are orthonormal (orthogonal and equally scaled). A simple realization of such a section is possible if the skew quadrupoles each correct one of the four beam correlations $< xy >$, $< x'y >$, $< xy' >$, $< x'y' >$ and if, in addition, the values of the product of horizontal and vertical beta functions are equal at each of the skew quadrupoles. The relative emittance dilution for a thin skew quadrupole of focal length f is

$$\frac{\varepsilon_y}{\varepsilon_{y0}} = \sqrt{1 + \frac{\varepsilon_{x0}}{\varepsilon_{y0}} \cdot \frac{\beta_x \beta_y}{f^2}} \quad , \qquad \frac{\varepsilon_x}{\varepsilon_{x0}} = \sqrt{1 + \frac{\varepsilon_{y0}}{\varepsilon_{x0}} \cdot \frac{\beta_x \beta_y}{f^2}} \quad . \tag{11.1}$$

For a flat beam $(\varepsilon_{x0}/\varepsilon_{y0} \gg 1)$, and the vertical emittance is much more sensitive. Orthogonality of the skew quadrupoles is achieved by separating the first and second and also the third and fourth skew quadrupoles by FODO cells with betatron phase advances of $\Delta\psi_x = \Delta\psi_y = \pi/2$, and separating the second and third skew quadrupoles by $\Delta\psi_x = \pi, \Delta\psi_y = \pi/2$. Then if the first skew quadrupole controls the xy phase (by definition here) the second controls the $x'y'$ phase, the third is the $x'y$ phase and the fourth is at the xy' phase. This scheme allows total correction of any arbitrary linearly coupled beam with correction range limited only by available skew quadrupole strength. Initially (at zero strength) the skew quadrupoles are orthonormal. As correction strength is applied there is some deviation from this ideal situation due to the slight effect on the in-plane optics. For large corrections $(\varepsilon_y/\varepsilon_{y0} > 2)$. applied by repeated minimization of the projected emittance, some iteration may be necessary (Section 11.3.3). Figure 11-1 shows beta functions and quadrupole locations for the SCS. The full length of the correction section, $L_{\rm SCS}$, is limited by achievable skew quadrupole pole-tip field, $|B_0|_{\rm max}$, its length, l, and its pole-tip radius, r, as well as the maximum correctable vertical emittance dilution, $(\varepsilon_y/\varepsilon_{y0})_{\rm max}$, the nominal emittance aspect ratio, $(\varepsilon_{x0}/\varepsilon_{y0})_{\rm nom}$, and the beam energy, expressed here as magnetic rigidity, $(\beta\rho)$,

$$L_{\rm SCS} \geq \frac{15}{2} \cdot \frac{r(B\rho)}{l|B_0|_{\rm max}} \sqrt{\frac{\left(\varepsilon_y/\varepsilon_{y0}\right)^2_{\rm max} - 1}{\left(\varepsilon_{x0}/\varepsilon_{y0}\right)_{\rm nom}}} \quad . \tag{11.2}$$

Note, Eq. 11.2 is a thin-lens approximation for both the skew and the FODO cell quadrupoles. It does not hold for skew or FODO cell quadrupoles with focal lengths comparable to their magnetic lengths. For a 500-GeV/beam system intended to correct up to a factor of three in emittance dilution, and for an emittance aspect ratio of 100 with 30-cm-long, 6-mm-radius, $\pm$4-kGauss-skew quadrupoles, the system is $\sim$170 m in length. While it would be possible to reduce this length by $\sim$20%, the matching into the diagnostic section (Section 11.3.2) is simplified with the slightly longer design.

11.3.2 The Diagnostic Sections

In order to tune the skew quadrupoles and other matching elements an emittance measurement must be made downstream of the correction. In what follows, only emittance measurements made with multiple wire scanners [Ross 1991] are considered. The emittance measurement may be either a single plane (2D) measurement where the coupling is only inferred by the dilution, or it may be a fully coupled (4D) measurement where all four coupling parameters as well as the two intrinsic transverse emittances are measured. The following presents a design for each scheme with ideal wire-to-wire phase advances and also constant matched spot sizes and aspect ratios. In the present NLC design, a 2D section will be used immediately downstream of the post-linac collimation section, while a 4D section will be used in conjunction with a skew-correction section at the input to the final focus.

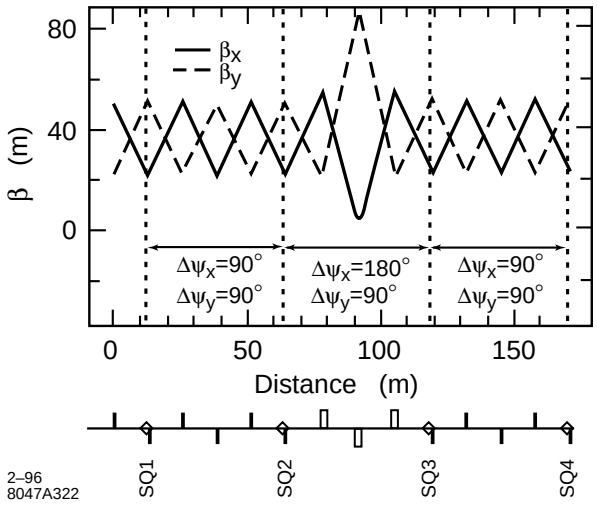

Figure 11-1. *Skew correction section (SCS) optics.*

The 2D Emittance Measurement Scheme

A space-saving, economical 2D emittance measurement system is probably adequate for regions in NLC where low levels of coupling are expected. In this case the optimal wire-to-wire phase advance per plane is π/N, where N is the number of wire scanners.[1] This conclusion is clear by viewing the normalized matched phase space as a circle with beam size measurements made at π/N phase intervals. With three single plane parameters to measure (ε, β, α) a four-scanner measurement provides some redundancy as well as better phase coverage for poorly matched beams. By separating each wire with a FODO cell of $\mu_{x,y} = 45°$, the phase coverage is optimum and, in addition, the matched beam will have a constant size per plane. Furthermore the aspect ratio, a, produced at (or near) a vertically focusing quadrupole is very reasonable and does not require precise wire-scanner roll alignment tolerances.

$$a \equiv \frac{\sigma_x}{\sigma_y} \cong \sqrt{\frac{\varepsilon_{x0}}{\varepsilon_{y0}} \cdot \frac{1-\sin\frac{\mu}{2}}{1+\sin\frac{\mu}{2}}} \approx \frac{2}{3}\sqrt{\varepsilon_{x0}/\varepsilon_{y0}} \tag{11.3}$$

In the case of the NLC $a \approx 6.7$ which requires an easily achieved roll tolerance[2] of $|\psi| \leq \sin^{-1}\left(\sqrt{2}/10\sqrt{3}a\right) \sim 1°$. Each wire scanner need only measure the x and y beam sizes (the correlation is not necessary in this 2D scheme). Figure 11-2 shows the lattice which includes the SCS followed by a matched 2D/four-scanner diagnostic section. The coupling is fully corrected by repeatedly minimizing the measured vertical emittance with each skew quadrupole in turn (some iteration may be necessary). Such a system should probably be preceded by four beta-matching quadrupoles to facilitate compensation of the slight in-plane focusing effect of energized skew quadrupoles. A clear advantage to this scheme is that the uncoupled, matched beam will be clearly evident as four precisely equal x and four precisely equal y beam sizes on the scanners. The lower limit on the length of the diagnostic section, $L_{2\mathrm{D}}$, is set by the minimum measurable beam size, σ_y, the normalized emittance, ε_{yN}, and the beam energy, γ.

$$L_{2D} \geq \frac{3}{2}\frac{\sigma_y^2\gamma}{\varepsilon_{yN}} \tag{11.4}$$

[1] The arguments presented here are the same whether these are actual carbon-filament-wire scanners or multibunch-capable laser-wire scanners.
[2] The following relation holds only for $a >\sim 3$ and achieves a systematic emittance measurement error of <2%.

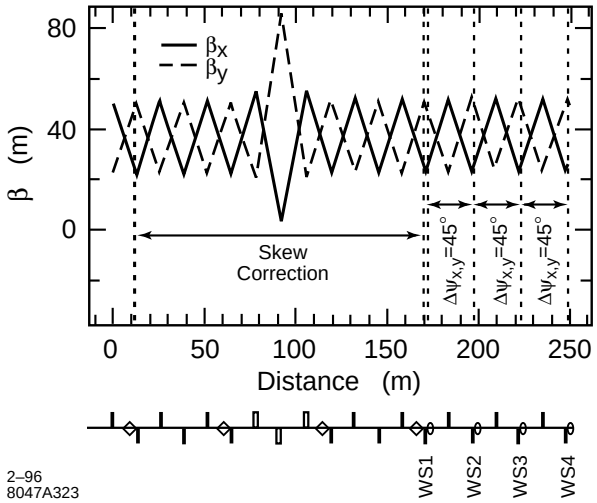

Figure 11-2. *SCS plus 2D emittance diagnostics section optics.*

For a 500-GeV beam with ∼1.5-μm vertical beam size and a normalized emittance of 5×10^{-8} m, the minimum length is ∼70 m.

The 4D Emittance Measurement Scheme

If it is expected that coupling may be a significant problem or the application of a faster, calculated correction is desirable, the 4D measurement scheme may be preferable. In this case a precise measurement of the four linear coupling coefficients is made with a set of σ_x, σ_y, and σ_{xy} measurements made for each of six wire scanners. Each wire scanner must have three independent angle filaments—in the simplest case, a horizontal, a vertical and a 45° filament typically used in the SLC [Ross 1991]. The wire-to-wire phase advances are chosen in a similar way to the skew quadrupole placement in the SCS (Section 11.3.1). With the first wire measuring the xy correlation, a second wire at $\Delta\psi_x = \Delta\psi_y = \pi/2$ measures $x'y'$ and a third wire advanced again by $\Delta\psi_x = \pi, \Delta\psi_y = \pi/2$ measures $x'y$ and finally a fourth at another $\Delta\psi_x = \Delta\psi_y = \pi/2$ sees xy'. The problem with this four-wire scheme is that the in-plane measurements are not determined. A fifth and sixth wire must be added to cover the missing single plane phases. Figure 11-3 shows the six-wire solution including the SCS, which is ideal for both the single plane and the coupling measurements. There are 10 parameters to measure ($\varepsilon_{x,y}$, $\beta_{x,y}$, $\alpha_{x,y}$, $< xy >$, $< x'y' >$, $< x'y >$ and $< xy' >$) and up to 18 profiles are scanned leaving 8° of freedom. It is also possible to use a subset of the 18 profiles in order to speed the measurement process. Note that this system can also be used as a 2D system by making single plane profile scans with wires WS3, WS4, WS5 and WS6 of Figure 11-3. The minimum length is approximately twice that of the 2D system.

$$L_{4\mathrm{D}} \geq \frac{\pi\sigma_y^2\gamma}{\varepsilon_{yN}} \tag{11.5}$$

11.3.3 Tuning Simulations

Tuning simulations were run using the Final Focus Flight Simulator [Woodley 1994] to test the convergence of the skew correction for a 500-GeV beam with an intrinsic emittance aspect ratio ($\varepsilon_{x0}/\varepsilon_{y0}$) of 100. Figure 11-4 shows the

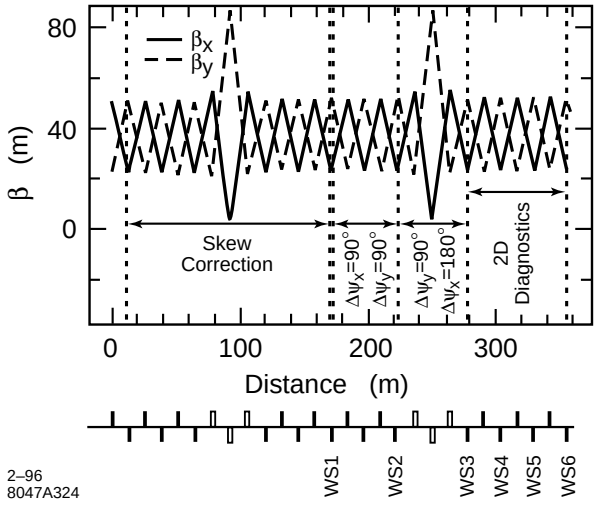

Figure 11-3. *SCS plus 4D emittance diagnostics section optics.*

relative vertical emittance achieved with each skew quadrupole scan. In this case, with the input coupling diluting the vertical emittance by more than a factor of two, a correction to less than 1% dilution is achieved after the first pass through all four skew quadrupoles. This beam line setup operation could probably be executed in less than an hour of real machine time. Of course, using the 4D system here could conceivably produce a reasonably well-calculated correction within a period of minutes. The final choice of appropriate systems depends on the expected phase space stability and magnitude of the errors.

11.4 Beta-Matching Section

The purpose of the NLC Beam Delivery Beta-Matching section is to provide a set of magnets upstream of the horizontal chromatic correction section which can be used to respond to variations in the incoming beam and/or the desired beam parameters at the IP, and also can be used to set the desired phase advance between the collimators in the Post-Linac Collimation region (Section 9.4) and the Final Doublet. Experiences at the SLC Final Focus and the Final Focus Test Beam have demonstrated that it is useful to be able to reduce the angular divergences at the IP (and hence the beam sizes inside all the other magnets in the Final Focus), while maintaining the chromatic correction and final telescope optics which are used in collision. Reducing the IP divergence is also useful during the early stages of a run cycle, when the emittances in the beam delivery region may be too large to permit collisions at the design betatron functions. Finally, the beta-matching quadrupoles can be used to correct various mismatches between the design incoming beam and the beam which is actually delivered from the linac.

In the design of the NLC Beta Match, it has been assumed that coupling correction and measurement of the incoming beam phase space has been accomplished in the preceding Decoupling and Diagnostics section (Section 11.3), leaving only the problem of the uncoupled beam matching. The design constraints on the beta-matching region can be summarized as follows:

- The region should contain at least six quadrupoles, in order that the six independent first-order transfer matrix values to the IP can be independently adjusted, and that for a given input beam and set of Twiss parameters there is a solution which provides the desired output conditions and phase advances.

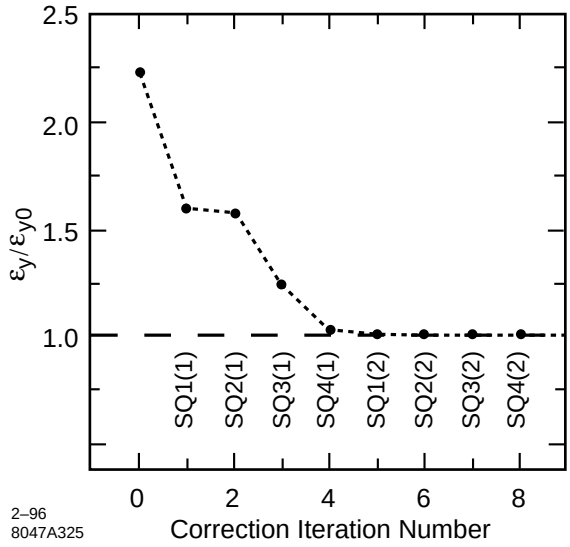

Figure 11-4. *Skew tuning simulation results.*

- The quadrupole specifications are consistent with warm-iron devices which can be easily manufactured and do not introduce emittance growth due to wakefields. Tolerances on field quality and mechanical stability should be no tighter than those upon quadrupoles in the chromatic correction sections. In general, the magnet specifications should be consistent with the technology and techniques of the rest of the beam delivery section.
- The contribution of the beta-matching region to overall chromaticity should be small enough to be easily cancelled out by reasonable increases in chromatic correction sextupole strengths.
- The range of accessible solutions for beam conditions at the IP should be as large as possible. Independent control of magnification and waist position control in x and y is essential.
- A dispersion-free pre-image point of the IP should be provided in each final focus, at which the magnification and waist position can be verified. This is necessary because the resolution of the incoming beam phase space is rarely adequate to match to collision conditions without such pre-IP verification. In addition, high-resolution (rf) BPMs that are placed close to the pre-image point will allow to correct the beam-beam deflection scans for pulse-to-pulse trajectory jitter in the IP betatron phase. Similar jitter-correction techniques have proven very successful at the SLC [Raimondi 1995] and are also being tested at the FFTB.
- The system should be as short, simple, and robust as possible.

11.4.1 Optical Design

At this time, there are two linear collider final-focus systems in existence, each of which has a unique beta-matching system. The SLC Final Focus uses a cluster of quadrupoles to focus on an image of the IP in the center of the first chromatic correction bend (Figure 11-5). A wire scanner in the center of the bend is used for match verification and tuning. In this case, the image is an existing symmetry of the design, and no additional quads are necessary to match from the image onto the CCS proper. The Final Focus Test Beam has no such naturally-occurring image point, and the five quadrupoles of its beta-matching section are used to focus the beam onto a pair of wire scanners in between

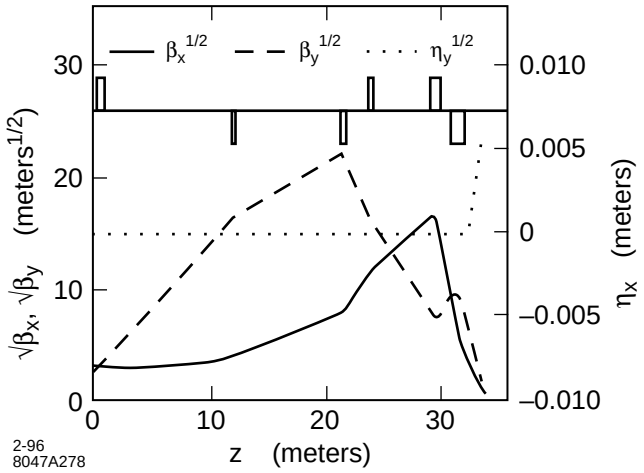

Figure 11-5. *Schematic representation of the SLC Final Focus Beta Matching region.*

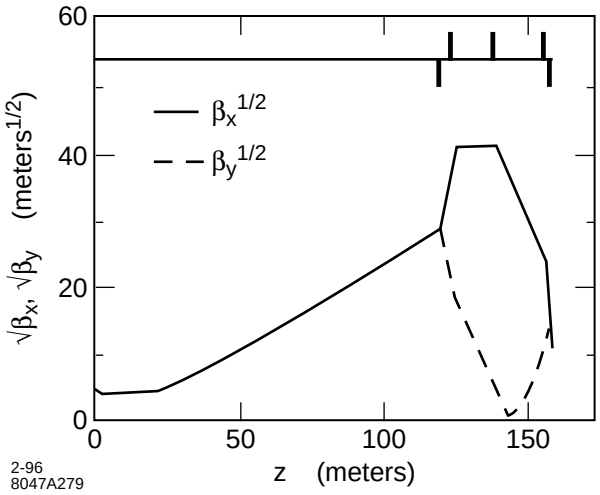

Figure 11-6. *Schematic representation of the Final Focus Test Beam Beta Matching region.*

the two chromatic correction sections (Figure 11-6). The SLC design is a more conventional mix of quadrupoles and modest drift regions, while the FFTB design precedes the first matching quadrupole with a 120-m drift space.

The current design of the NLC Final Focus includes several images of the IP, including a dispersion-free image in the beta exchange region (between the horizontal and vertical chromatic correction sections). The NLC Beta Matching section has been designed to resemble the FFTB system, including the use of the beta exchange image for tuning the match. This is for several reasons. First, the optics of the beta exchanger guarantees the presence of horizontal and vertical IP images which can be exploited for match verification, while use of an upstream image constrains the design of the dispersion matching section. In addition, the energy spread of the NLC is sufficient that chromatic correction of the beam at the IP image will be necessary during tuning. This can only be done downstream of the first chromatic correction section, by retuning the sextupoles in that section. As it is, only one plane can be corrected at a time at the

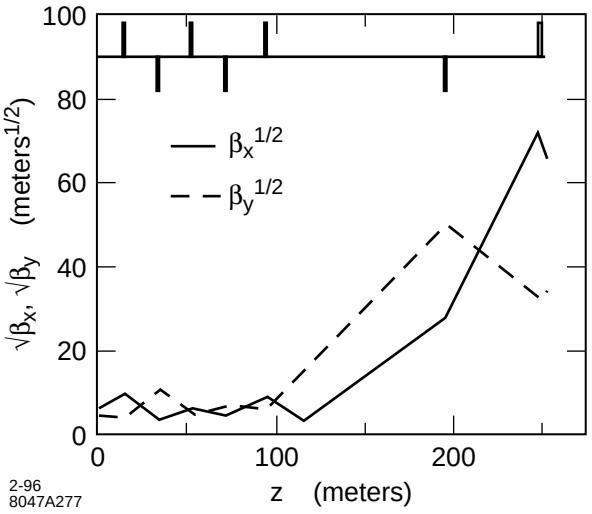

Figure 11-7. *Betatron functions of the beta-matching section.*

beta exchanger tune-up point; and the sextupole field required to correct the vertical chromaticity is opposite in sign to that used in normal running, necessitating a reversible power supply for the CCX sextupoles.

The optical functions of the NLC Beta Match are shown in Figure 11-7. The current design includes a total of seven quadrupoles, which satisfies the numerical requirement set forth above.

The total length of the system is 254 m. The maximal value of β_x within the section is 5,150 m, while the maximal value of β_y is 2,530 m. These values are far smaller than the typical values within the downstream region of the Final Focus, and the tolerances are expected to be correspondingly looser. Note that the beta-match region contains a drift of length 100-m upstream of the maximal betatron functions. Such a drift is an ideal location for a Single Beam Dumper (SBD), a kicker magnet capable of extracting individual bunch trains (*i.e.*, firing at 180 Hz). Extracting the beam after the Big Bend and Decoupling and Diagnostic sections would allow the beam to pass through the collimation section and the diagnostic wire scanner regions, while preventing it from entering the sensitive detector area. Thus, even beams which are not of sufficient quality to pass through the doublet into the detector can be maximally measured for diagnostic purposes if such an extraction magnet is placed at this location.

11.4.2 Tuning Elements

The tuning elements of the beta match include the seven normal quadrupoles in the region itself; the horizontal chromatic correction sextupoles (referred to as SX1 sextupoles); a beam size monitor at the IP image in the beta exchanger; and a divergence monitor just upstream of the vertical chromatic correction section.

Beta Matching Quadrupoles

Table 11-2 summarizes the design specifications of the seven quadrupole magnets in the beta-matching section. The magnets are physically identical with one another, with a length of 1 m and an aperture of 6 mm. The pole-tip fields for 1-TeV-c.m. go to a maximum of 6.5 kGauss for luminosity operations, and 7.3 kGauss for low-divergence operations

Quadrupole Name	Pole-tip Field (kGauss)	Length (m)	Aperture (mm)
QB1	5.9	1.0	6.0
QB2	-6.5	1.0	6.0
QB3	5.6	1.0	6.0
QB4	-3.2	1.0	6.0
QB5	6.4	1.0	6.0
QB6	-1.6	1.0	6.0
QB7	3.8	1.0	6.0

Table 11-2. *NLC beta-match quadrupole specifications.*

Conditions	$\sigma_{\rm x}$ at IP Image (μm)	$\sigma_{\rm y}$ at IP Image (μm)
Monochromatic Beam	1.85	0.20
Nominal Sexts, $\sigma_{\rm E}/{\rm E} = 0.003$	31.1	0.63
Sexts Off	14.8	0.41
SX1 = 33% design	2.00	0.48
SX1 = -130% design	74.1	0.20

Table 11-3. *Beam sizes at IP image location under varying conditions.*

$(\beta_x^* = 10\,\text{cm}, \beta_y^* = 1\,\text{cm})$; the same optics at the 1.5-TeV c.m. would require 10.9-kGauss pole-tip fields, and therefore these magnets are not usable at 1.5-TeV c.m. For all IP conditions in the operating plane, 6 mm is sufficient to maintain clearances in this region: worst-case rms beam sizes are 250 microns in the horizontal and 30 microns in the vertical.

The precise tunability of the beta-match design, in terms of range of IP betatron functions which can be delivered, range of waist knobs, and orthogonality of knobs, has not been studied for this design. A detailed study of the tunability should be carried out for final acceptance of this design.

The SX1 Sextupoles

Table 11-3 shows the beam size at the IP image location in the center of the beta exchanger with different sextupole configurations. In order to achieve the monochromatic beam size in the horizontal, the main CCX sextupoles (SX1) need to be set to a value roughly 33% of their design, while achieving the monochromatic vertical size requires a value 130% of design in the opposite polarity. This in turn indicates that the CCX sextupoles require reversible power supplies, with a capability to deliver significantly more current than is required for normal operations. The requirement of tuning the two planes with different sextupole strengths is also onerous in terms of time and difficulty level. While tuning the IP Image spot is the best tune-up procedure possible, next we will discuss a short-cut to this.

IP Image and Beam Size Monitor

The IP image at the center of the Beta Exchanger is a true image, with a pure demagnification in the horizontal and the vertical between it and the IP. The demagnifications are $(8.184)^{-1}$ in the horizontal, and $(57.65)^{-1}$ in the vertical.

The NLC operating plane indicates that beam sizes from 3.5 nm to 7.0 nm may be required at the IP, which in turn requires vertical beam sizes of 200 to 400 nm at the image. The horizontal beam sizes range from 226 nm to 320 nm at the IP, indicating sizes at the image from 1.85 microns to 2.6 microns. The horizontal beam sizes achievable at the image are within the expected range of laser wire technologies, while the vertical sizes are pushing the limits of these same technologies, and entering the range of Laser-Interferometer beam size monitors.

While the measurement of the horizontal corrected size in Table 11-3 presents relatively few problems, the vertical corrected size can only be achieved with a tremendous dilution of the horizontal spot, leading to an aspect ratio of 371:1. Measurements of the vertical beam size will therefore be tremendously sensitive to installation roll of the monitor: a roll of 1 mr will result in a contribution of 74 nm added in quadrature with the 200 nm of the focused vertical spot. For this reason as well as those outlined above, it may be impractical to use the IP image monitor to measure the size of the vertical beam; rather, the optimal use might be to use the monitor to constrain the vertical waist, and use the divergence monitor (see next Section) to verify the vertical betatron function at the IP image.

Angular Divergence Monitor

In addition to beam size measurements at an image of the IP, it is useful to be able to measure the horizontal and vertical angular divergences in this area. The divergences, along with the emittances measured upstream of the beta-match region, give the best estimate of the actual betatron function at the IP image monitor, as the divergence is insensitive to virtually all aberrations.

The ideal tactic for an angular divergence measurement is to measure the beam size at a point which is dominated by the divergence of the IP or IP image, and with a known transfer matrix to the IP or IP image. In this case, such a location is immediately upstream of the vertical chromatic correction section, at the end of the beta exchanger. The beam size at this location is 206 μm (x) by 140 μm (y) in the 1-TeV-c.m. design with 10 $\times$ 0.125-mm betatron functions at the IP and 50:1 emittance ratio; the beam size at this location is not drastically different for any optics in the operating plane, allowing a conventional metal-wire scanner such as the SLC linac scanners to be employed. However, the horizontal beam size listed here is significantly enlarged by dispersion present at this location. Therefore, an additional scanner with spectrum-measurement capability is needed to complete this measurement.

Because of the difficulties in measurement at each scanner, there are two conceivable schemes for tuning the incoming beam: one which "Caps the Ts and Dots the Is (CTDI)" and one which is "Close Enough for Government Work (CEGW)."

The CTDI tune-up is as follows:

- Measure incoming phase space with diagnostic wires (Section 11.3).
- Compute match optics for desired IP/IP Image conditions.
- Tune SX1 sextupoles to 33% design, tune x waist on image monitor.
- Measure beam on spectrum monitor and SY1 wire, compute monochromatic contribution at SY1 wire, compute x divergence.
- Use divergence computation to compute betatron function at IP image, correct with magnification knob, repeat waist for verification.
- Tune SX1 sextupoles to -130% design, tune waist on image monitor.
- Measure roll of IP image monitor spot (if possible), correct (if possible).

- Repeat waist scan on IP image monitor.
- Measure vertical divergence on SY1 monitor, compute IP image betatron function, correct if necessary with magnification knob.
- Repeat waist scan.
- Tune SX1 to colliding-beam strengths, go to IP.

The CEGW algorithm is the following:

- Measure incoming phase space with diagnostic wires (Section 11.3).
- Compute match optics for desired IP/IP Image conditions.
- Tune SX1 sextupoles to 33% design, tune x waist on image monitor; use waist scan to compute divergence.
- Use size of horizontal IP image spot and/or waist scan divergence value to tune magnification knob, iterate waist.
- Set SX1 to design strength.
- Tune y waist on IP image monitor to constrain waist location, ignore minimum spot size.
- Measure vertical beam size on SY1 monitor, compute vertical betatron function at IP Image monitor; tune magnification knob to correct SY1 size to predicted value.
- Iterate waist tuning if necessary, go to IP.

The CEGW algorithm makes maximal use of the diagnostic devices to bypass measurements which are difficult or time-consuming to make. A similar tuning algorithm in FFTB converges in a matter of hours; similar speed can be expected for tuning the beta match in NLC.

11.4.3 Tolerances

At this time, no detailed study of the beta-match section had been undertaken. However, based on the optics and some understanding of the functions of various magnets, it is possible to say a few things about operational tolerances of the system.

Field Strength Tolerances

The absolute accuracy tolerances on the beta-match quadrupole strengths are quite forgiving. The quadrupoles are set by matching the measured incoming beam to the desired IP conditions. Because the incoming phase space measurements are unlikely to have a greater precision than 1%, absolute quad strength accuracy of 0.1% will cause beam mismatch to be dominated by the errors in measurement, rather than errors in the magnets. The final settings of the magnets will be determined by tuning the IP image and/or the IP itself. This may require a granularity of the field strengths at the level of 0.01% of the maximum (assuming a maximum of 9.5-kGauss pole-tip fields). Stability of the fields with time will need to be approximately the same as the requisite granularity of the field.

Multipole Content Tolerances

Because the beam is much smaller in the beta-match quadrupoles than it is in other final-focus magnets, tolerances on higher multipole content will be correspondingly looser.

Vibration Tolerances

The beta-match quadrupoles are upstream of the first sextupole of the chromatic correction sections, and therefore these magnets are unable to induce steering between the sextupoles of a section. Tolerances for vibration will therefore be determined by dispersion and steering at the IP.

11.5 Chromatic Correction and Final Transformer

This beam line extends from the beta-matching section to the IP, and it comprises horizontal chromatic correction, beta-exchanger, vertical chromatic correction, and final transformer. Located at the end of the final transformer is the final doublet, which provides the last focusing before the beams collide (see Section 11.6 for a detailed discussion of the final doublet). The chromaticity of the final doublet is similar to that at the FFTB, and about five times as large as in the SLC. If the chromaticity were not corrected, the vertical IP spot size would increase by about a factor of 100 from the design value. The chromatic correction is accomplished in two separate beam-line sections, CCX and CCY, each of which accommodates a pair of sextupoles separated by an optical transform ($-I$) that cancels geometric aberrations and second-order dispersion. The chromatic correction is very similar to the FFTB, but it is different from the SLC in which the two sextupole pairs are interleaved. An interleaved placement of sextupoles is not acceptable for the NLC, because of the large higher-order aberrations this would generate. The bending section upstream of the beta-matching section is an innovation, unfamiliar from either SLC or FFTB. It allows the final focus to operate for any beam energy between 175 GeV and 750 GeV, without change of IP position, and hence it is known as "geometry-adjustment" section.

To obtain a proper estimate of the NLC luminosity, it is important to account for all possible sources of spot-size dilutions. To limit the total dilution, a budget was established for each effect contributing to the IP spot size, and, in particular, for each low-order aberration originating between the linac and the interaction point. Within this section, we present these dilution budgets, and discuss the implied tolerances on element strengths and positions, the frequency and accuracy of aberration tuning, and also the maintenance systems which stabilize the final focus between tunings. We believe that all the requirements can be met, and that there is even a potential for a further increase of the luminosity beyond that estimated here.

11.5.1 Introduction, Parameters and Dilutions

Final-focus and IP-beam parameters for different NLC scenarios are listed in Table 11-4. These parameters, in particular the cases Ia and IIa, form the platform on which the following discussion will be based. As indicated by the table, the final-focus designs for 500 GeV and 1 TeV deliver the desired horizontal and vertical spot sizes of about 250 nm and 4–8 nm, respectively. Both nominal luminosity and spot sizes quoted include various sources of dilution which are summarized in Table 11-5. The total and subtotals in Table 11-5 are calculated according to the formulae

$$1 - d_{subtot_j} \quad = \quad \Pi_i \, \mathrm{in}_j \, (1 - d_i) \tag{11.6}$$

$$1 - d_{tot} \quad = \quad \Pi_j \left(1 - d_{subtot_j}\right) \tag{11.7}$$

where d_i denotes the different relative luminosity dilutions.

To further understanding of Table 11-5: some supplementary comments on each table subsection are given below:

- **Emittance Growth.**
  The phase of the beam-line modules with respect to the IP must be very well-regulated and tuned for the beam line to function as designed. This can be easily monitored and arranged by studying betatron oscillations through the system. As a result of this phase regulation, elements within different beam-line modules affect the beam distribution in a way that is phase-related. What is of concern is the axis of the vertical (or horizontal) emittance in the IP phase. This we have denoted in Chapter 9 by the symbol $r_{y,IP}$. (If the beam distribution is looked at in a normalized phase space, where the beta functions are factored out, the distribution is normally assumed to be round, of radius $r_y = \sqrt{\epsilon_y}$. What we want to emphasize here is that the distribution will not remain round. The collimators in the FD phase, for example, give a kick in the IP phase, and enlarge the distribution along that axis only.) Emittance growth is not only generated by wakefields but also by synchrotron radiation, chromaticity, and higher-order optics. All of the entries in this subsection of the table refer to the enlargement of the IP axis of the emittance.

- **Collision.**
  The jitter is assigned according to the jitter budget proposed in Chapter 9 The calculation of the luminosity loss assumes that for the same luminosity loss the vertical missteering can be twice as large than for a rigid Gaussian bunch by virtue of the disruption. This is well-documented from simulations even for bunch charges that are a factor of 2 smaller than the design.

  Crab-cavity phase jitter (which is jitter of the positron beam cavity with respect to the electron-beam cavity) introduces an additional component to the horizontal jitter. So do field variations of the bending magnets, and quadrupole vibrations.

- **Tuned Low-order Aberrations.**
  In particular five aberrations—waist (x and y), dispersion (x and y) and skew coupling—must be scanned and corrected in regular intervals. (We do not assume a sublime dither technique.) Other aberrations will be more stable and can be scanned less frequently.

  Based on SLC experience, we expect to tune aberrations so that only a residual 0.5% luminosity loss per aberration remains. This number could conceivably be improved by developing a sensitive luminosity monitor for beam tuning purposes. In Table 11-5, the existence of such a monitor has been assumed neither for current nor for possible columns.

  We have assumed that the tuning of the five major aberrations is performed every 15 min, and that without tuning the design stability tolerances result in a 2% additional luminosity loss per aberration after 1 h. We expect that the aberrations increase from the minimum setting tolerance (0.5% per aberration) directly after tuning to the minimum plus the product of (time between tunings/1 h) and the budgeted spot-size increase for that aberration (as determined by system stability tolerances; typically 1–2%), added quadratically since they are independent.

  For the δ-dependent aberrations (chromaticity, dispersion, and chromatic skew), we presume that a smaller minimum (namely 0.25%) can be achieved by doubling the bunch energy spread for these scans.

  Dispersion has an effect on beam size due to energy spread within the bunch (an effect which is included under table subsection Tuned Aberrations) and also on beam jitter, since the individual bunches in a train and train-to-train will have different energies (an effect which is considered in the table subsection Collision). Insofar as the dispersion arises in the beam-delivery system, these two dispersions will be identical, and so the dispersion changes leading to increased beam size may be monitored by observing the correlation of position-jitter at the IP (which is being measured for each bunch train) with the energy of the bunch train (as can be measured

for each train by observing the orbit in the final-focus system). Thus the dispersion aberration can be tuned almost continuously and does not require allocation of a growth due to time between scannings. This potential improvement has not been included in Table 11-5.

It should be noted that dispersion can be present in the linac, and since inter-bunch energy spread and intra-bunch energy spread have different sources, and arise in different locations in the linac, it may occur that the beam size and the jitter due to dispersion cannot both be tuned together. In this case, one could try to tune by introducing orbit changes in the linac. However, this effect is considered an emittance dilution that originates in the linac, and not in the beam-delivery system, and thus we have not added it to our table.

Note that we equally have not added any aberration-induced dilutions originating in the collimation system. The reason is that such dilutions can be monitored non-invasively in the skew-correction section and can be corrected on a more frequent basis.

When an aberration affects both the vertical and the horizontal spot size, only the vertical effect needs to be considered, because, when the latter is tuned, the horizontal effect will be negligible as a result of the 100/1 spot-size ratio.

The crab-cavity adjustment refers to the voltage stability of the crab cavity. A 2% effect corresponds to a 6% voltage stability. We suppose that it can be tuned to 0.5% using a voltage scan, and then that it will be stable to 0.5% between tunings.

- **Other.**
  The entry for e^+e^- arrival time assumes an rms timing difference of the two beams equal to 170 fs (corresponding to 0.2° S-Band or 50 μm). This implies that the two bunches will be $0.2\beta_y^\star$ offset when colliding at the IP.

  Under table subsection Other, we have also listed the time devoted to beam-based alignment and tuning. Losses from tuning scans are calculated under the assumption that the five major aberrations are scanned every 15 min, the control system is designed to minimize the control-time overhead, the magnet settle time is 200 ms per field change, an aberration scan consists of seven steps with different magnet settings, and that at each step a beam-beam deflection scan over 50 pulses is performed.

  The time-out for beam-based alignment presumes the alignment to be completed in 24 h and to be executed every three months.

Table 11-5 lists two budgets of luminosity dilutions. The first refers to the Current Lattice and is based on tracking; the second is called Possible and assumes:

1. A reduced $\beta_x^\star$ which compensates the increase of the horizontal spot size due to design and tuning aberrations. This is consistent with the fact that the horizontal design spot size was chosen to limit the number of beamstrahlung-photons per electron radiated during collision. We do not suppose that the collision effect can be offset in this way, since it is not related to the beam size.
2. A redesign of the final-focus system which diminishes the effect of synchrotron radiation from bending magnets and final quadrupoles, We have learned during the design process, and we have reason to believe, that we can improve the performance of these modules. In many cases we have actually demonstrated this improvement.
3. Better control and adjustment of crab-cavity phase and voltage.
4. An improvement in the chromatic properties of big bend and IP switch.

The dilutions for the nominal lattice amount to a 46.6% overall loss in luminosity, which can possibly be reduced to a total of only 25.9% by the aforementioned means.

In Table 11-4, we have considered the nominal lattice, but have attributed a 13% spot-size increase to residual uncorrected vertical aberrations which is about twice the value listed in Table 11-5 and have assumed that the increase of the horizontal spot size due to residual tuned aberrations and horizontal steering (though not that due to horizontal emittance growth!) is compensated by a reduced $\beta_x^\star$. The expected increase of the spot-size product $\sigma_x \times \sigma_y$ then amounts to 50%, for 1-TeV-c.m. energy, and translates into a total luminosity loss of about 33%, which lies between the Current and the Possible value of Table 11-5.

The momentum bandwidth of the NLC final focus, defined by a 10% increase of either spot size for a mono-energetic beam, is at least $\pm 0.6\%$ for both c.m. energies (500 GeV and 1-TeV c.m.), even assuming the most difficult parameter set of the ZDR operating plane. The final focus is very forgiving in regard to increased emittances or to orbit variations: If β_y^* is held constant, the luminosity decreases roughly as the square root of the emittance, while the momentum bandwidth remains unaffected by the larger divergence. A 0.5-sigma variation of the incoming orbit causes an average spot-size increase by less than 1%.

The length of the final-focus system, from the geometry-adjustment section to the IP, is about 1800 m. This length is independent of energy, and is determined by the requirements for operation at 1.5-TeV-c.m. energy. Optimization of the final-focus system calls for a different dispersion and thus for a different bending angle at different c.m. energies. The different bending angle helps to balance nonlinear aberrations and synchrotron radiation effects at each energy. A dedicated geometry-adjustment section at the entrance to the final focus keeps the resulting geometry change at an acceptable level and the IP position constant. The horizontal magnet displacements required during an energy upgrade from 350 GeV to 1.5 TeV do not exceed 45 cm. The following discussion mainly refers to the two final-focus systems at 500 GeV and 1-TeV-c.m. energy with equal geometry, *i.e.,* Version II in Figure 11-10.

11.5.2 Layout and Optics

General Description

The basic layout of the proposed NLC final-focus system is very similar to that of the Final Focus Test Beam. In the region between the diagnostics section (DS) and the IP, the NLC final focus is constructed from six functional modules. These are, in the order of their location: geometry-adjustment section (GAS), beta- and phase-matching section (BMS), horizontal chromatic correction section (CCX), beta-exchanger (BX), vertical chromatic correction section (CCY), and final transformer (FT). Two conventional magnets, one superconducting and one permanent quadrupole at the end of the FT (the final doublet, or, perhaps more appropriately, the final quartet) provide the last focusing before the two beams collide.

The total distance from the entrance of the GAS to the IP is about 1820 m. A schematic of the magnet configuration is depicted in Figure 11-8, which also shows the beta functions corresponding to the 500-GeV parameter set listed in Table 11-1 (Case Ia in Table 11-4). In this case, the vertical beta function has a maximum value of 190 km at the main sextupoles in the CCY and peaks at about 75 km in the final doublet. The maximum value of the horizontal beta function is 75 km, at the CCX-sextupoles. A large beta function at the sextupoles is advantageous for chromatic correction, considering the effects of synchrotron radiation, chromo-geometric aberrations, and orbit-stability tolerances [Zimmermann 1995]. The length of the CCX is about two-thirds that of the CCY, which reflects the larger horizontal beta function at the IP. Note that, per a recent design modification, the beta-matching section has been augmented by two additional quadrupoles, to allow matching of the betatron phase advance between the collimator section and the IP. These two new quadrupoles and the accompanying minor optics change of the BMS are not included in the following discussion.

	c.m. energy	0.5 TeV			1 TeV		
		Ia	Ib	Ic	IIa	IIb	IIc
Luminosity w. dilution	L (10^{34} cm^{-2} s^{-1})	0.41	0.40	0.41	0.77	0.82	0.73
Lum. w. dil. & pinch	L (10^{34} cm^{-2} s^{-1})	0.58	0.55	0.60	1.02	1.10	1.06
Luminosity w/o dilution	L (10^{34} cm^{-2} s^{-1})	0.52	0.49	0.51	1.16	1.20	1.02
Lum. w. pinch w/o dil.	L (10^{34} cm^{-2} s^{-1})	0.75	0.71	0.78	1.63	1.72	1.56
# particles per bunch	N_b (10^{10})	0.65	0.75	0.85	0.95	1.1	1.25
# bunches	n_b		90			90	
# bunch trains per s	f		180			120	
Enhancement factor	H_D	1.41	1.40	1.48	1.33	1.35	1.46
Hor. spot size w. dil.	σ_x (nm)	264	<294	<294	231	<250	<284
Vert. spot size w. dil.	σ_y (nm)	5.07	<6.26	<7.76	4.35	<5.08	<6.52
Hor. spot size w/o dil.	σ_x (nm)	253	283	283	200	219	253
Vert. spot size w/o dil.	σ_y (nm)	4.18	5.20	6.48	3.35	3.97	5.20
Hor. IP beta function	β_x^* (mm)	8	10	10	10	12	16
Vert. IP beta function	β_y^* (mm)	0.125	0.15	0.2	0.125	0.15	0.2
Norm. hor. emittance	$\gamma\epsilon_x$ (10^{-8} mr)		400			400	
Norm. vert. emittance	$\gamma\epsilon_y$ (10^{-8} mr)	7	9	10.5	9	10.5	13.5
Hor. emittance growth	$\Delta(\gamma\epsilon_x)_{SR}$ (10^{-8} mr)		~ 23			~ 38	
Hor. IP divergence	$\sigma_{x'}$ (μrad)	31.6	28.3	28.3	20.0	18.3	15.8
Vert. IP divergence	$\sigma_{y'}$ (μrad)	33.5	34.6	32.4	26.8	26.5	26.0
Bunch length	σ_z (μm)	100	125	150	125	150	150
Crossing angle	θ_c (mr)			20			
Rms energy spread	$\delta_{\rm rms}$ (%)			≥ 0.3			
Total energy bandwidth	$\Delta E/E$ (%)		≥ 1.2			≥ 1.2	
Free length from IP	l^* (m)			2			

Table 11-4. *Interaction-point beam parameters for different NLC scenarios. Spot-size increases are scaled from NLC-Ia and NLC-IIa. Luminosity enhancement is estimated from P. Chen's scaling laws. Nominal luminosity and nominal spot sizes include dilutions due to synchrotron radiation (0–16%), high-order aberrations (7%), residual uncorrected low-order aberrations (here assumed as 13%), e^+e^- timing offset (2%), crab crossing error (2%) and vertical orbit jitter (3%); see also Tables 11-5 and 11-9. Effect of residual low-order aberrations and horizontal orbit jitter on the horizontal spot size is assumed to be compensated by a reduced β_x^*. The numbers quoted for luminosity and spot size "without dilution" (w/o) are calculated according to linear optics and do not include any of the additional effects.*

Category	Description	Current Lattice		Possible	
		Horizontal	Vertical	Horizontal	Vertical
Emittance Growth (*actually* r_{IP})		**20.6%**	**11.8%**	**—**	**8.1%**
	Collimation System	3.0%	2.0%	—	2.0%
	IP Switch, Big Bend, SCS	3.0%	1.6%	—	1.0%
	Final Focus	15.4%	7.3%	—	4.0%
	Uncorrected Aberrations	6.0%	1.5%	—	1.5%
	Synchrotron Radiation	10.0%	5.9%	—	2.5%
	In Dipoles	10.0%	2.1%	—	0.1%
	In Quadrupoles	0.0%	3.5%	—	2.0%
	In Solenoid	0.0%	0.4%	—	0.4%
	Wakes (res.-wall & geom.)	0.2%	1.34%	—	1.34%
	Protection Collimators	0.1%	0.5%	—	0.5%
	Main Collimators	0.1%	0.65%	—	0.65%
	Misalignment	0.0%	0.25%	—	0.25%
	Jitter Wake	0.1%	0.3%	—	0.3%
	Quadrupole Wake	0.0%	0.1%	—	0.1%
	IR Beampipe	0.0%	0.2%	—	0.2%
Collision		**5.1%**	**3.5%**	**4.1%**	**3.5%**
	Incoming (to BDS) Jitter	0.5%	0.8%	0.5%	0.8%
	Jitter Amplification of Coll.	0.6%	0.7%	0.6%	0.7%
	Quad Motion	0.8%	1.5%	0.8%	1.5%
	Bend Power Supply Ripple	0.7%	0.0%	0.7%	0.0%
	Crab Cavity Phase-diff. Jitter	2.0%	0.0%	1.0%	0.0%
	Dispersion (inter-bunch & centroid)	0.5%	0.5%	0.5%	0.5%
Tuned Aberrations		**3.0%**	**5.5%**	**—**	**5.5%**
	Linear	2.5%	4.0%	—	4.0%
	Waists	1.0%	1.0%	—	1.0%
	Skew Quad (2)	0.0%	1.5%	—	1.5%
	Dispersion (intra-bunch δ)	0.5%	0.5%	—	0.5%
	Crab-angle Adjustment	0.5%	0.0%	—	0.0%
	δ-dependent 'linear'	0.5%	1.0%	—	1.0%
	Chromaticity	0.5%	0.5%	—	0.5%
	Chromatic Skew	0.0%	0.5%	—	0.5%
	Higher Order	0.5%	1.5%	—	1.5%
	Normal & Skew Sextupole	0.5%	1.5%	—	1.5%
Subtotal:		**26.9%**	**19.6%**	**4.1%**	**16.2%**
Other (*down time not included!*)		**7.0%**		**6.0%**	
	e^+-e^- arrival-time diff.	2.0%		1.0%	
	Losses from tuning scans	4.0%		4.0%	
	Time-out for bm-based alignment	1.0%		1.0%	
Total:		**46.6%**		**25.9%**	

Table 11-5. *Expected luminosity losses from dilutions in the beam delivery systems for 1-TeV-c.m. energy. See also Table 11-9 for a detailed account of low-order aberrations, and Table 11-8 for the effect of synchrotron radiation and higher-order aberrations.*

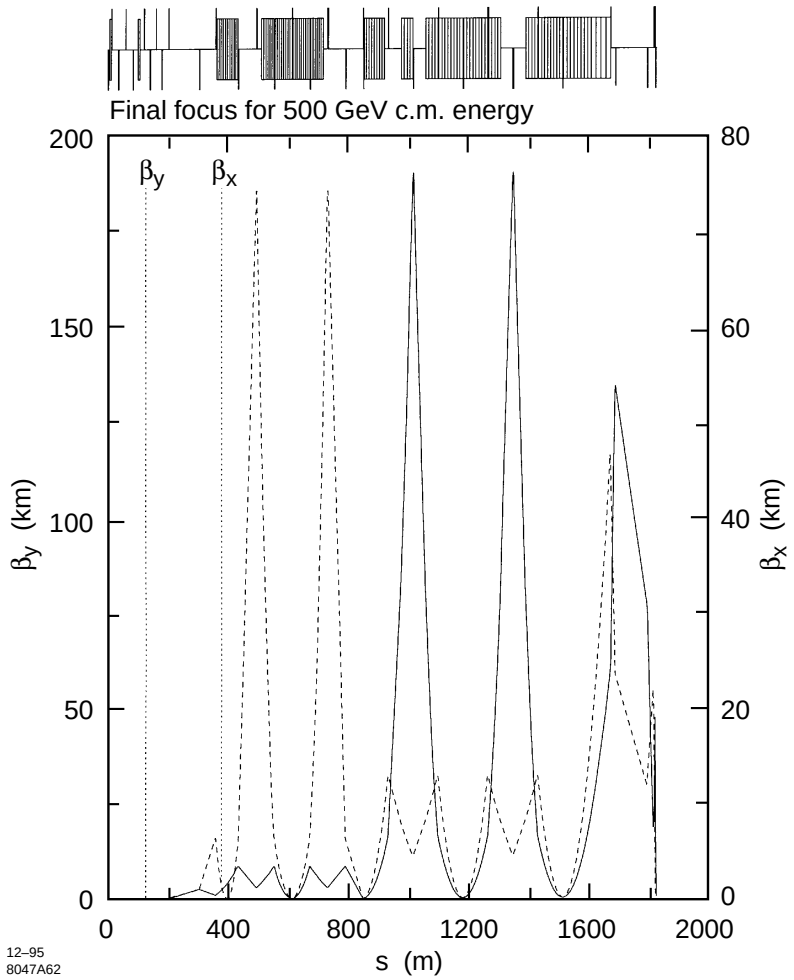

Figure 11-8. *Horizontal and vertical beta functions from BMS to IP, for the 500-GeV final focus.*

The optics at 1-TeV-c.m. energy is almost the same as that for 500 GeV. Again assuming the parameters of Table 11-4 (Case IIa), the peak values of horizontal and vertical beta functions at the CCX sextupoles are 60 km and 190 km, respectively.

The upper part of Figure 11-8 indicates that more than half of the final focus is occupied by about 100 bending magnets. These magnets generate the dispersion required for chromatic correction. Their maximum field at 1-TeV-c.m. energy is only 160 G, in order to restrict the emittance growth due to synchrotron radiation. The length of the entire system, the maximum beta functions, and the maximum dispersion (hence the bending angles) were optimized for the original design parameters, not only with regard to the effect of synchrotron radiation, but also with regard to nonlinear aberrations, magnet-vibration and field-ripple tolerances. The optimization procedure is discussed in the next section, and in [Zimmermann 1995].

The bending in CCX and CCY is in opposite directions, so that the final focus exhibits an “S”-shape geometry. For a c.m. energy of 1 TeV, the accumulated absolute bending angle, $\sum_i |\theta_i|$, is 6.3 mr, the bending angle inside the CCY alone is 0.9 mr, and, due to the `S' -geometry, the total net angle of the final focus is small: about 0.6 mr. At 350 GeV, due to shifted relative importance of aberrations and synchrotron radiation, the bending angles and the dispersion must

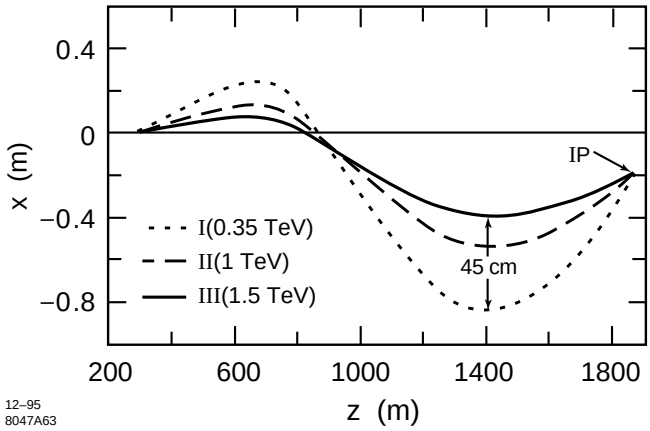

Figure 11-9. *Top view of the final-focus geometry. Magnet displacements by at most 45 cm are necessary during an upgrade from 500 (350) GeV to 1.5 TeV, while the IP-orbit angle changes by about 1.5 mr.*

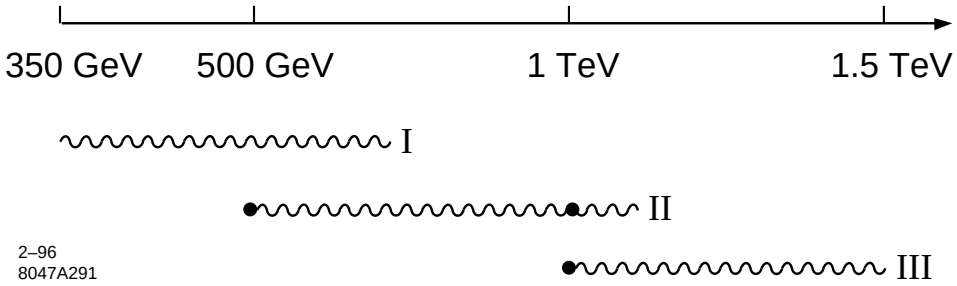

Figure 11-10. *Energy range of three different final-focus geometries. Dots show systems reported in the text.*

be increased by about 50%, with an accompanying change of geometry. The maximum horizontal displacement of magnets required for the upgrade from 350 GeV to 1.5 TeV is about 45 cm (Figure 11-9). The first geometry change occurs at about 500 GeV, the second around 1.1–1.2 TeV. The energy range covered by the three final-focus geometries is illustrated in Figure 11-10. The final-focus design for 1 TeV, including the final doublet, can operate in the entire energy range from 500 GeV to 1 TeV, and possibly beyond. Between 350 GeV and 1.5 TeV, the orbit angle at the IP varies by about 1.5 mr, while the IP position itself is independent of energy. A constant IP position is desirable, since the detector needs to be strongly coupled to the ground, to preserve the coherence of magnet motion caused by ground waves.

To protect the shielding masks in the final doublet region from hard synchrotron radiation, soft bending magnets of field strength 12 Gauss are placed over a distance of 64 m in front of the final transformer. The present soft-bend configuration was devised by S. Hertzbach and implemented by R. Helm. The soft bends deflect the beam orbit at the entrance to the final doublet (quartet) by about 8 mm horizontally, so that high-energetic photons generated in upstream bends and quadrupoles will not hit the inner bore of the last two final-doublet quadrupoles [Hertzbach 1995].

The 44 quadrupoles between the BMS and IP are typically 0.5-m long, and, for 1-TeV-c.m. energy, their pole-tip field is 3–5 kGauss. A few magnets, with larger apertures, require pole-tip fields of about 8 kGauss. The final focus also comprises between seven and 16 sextupoles which cancel chromatic aberrations. First, there are two conventional $-I$ sextupole pairs located in the chromatic correction sections. These are used to compensate the first-order chromaticity of the system. In addition, between three and 12 weaker sextupoles are interspersed in the GAS, CCX, BX, CCY, and

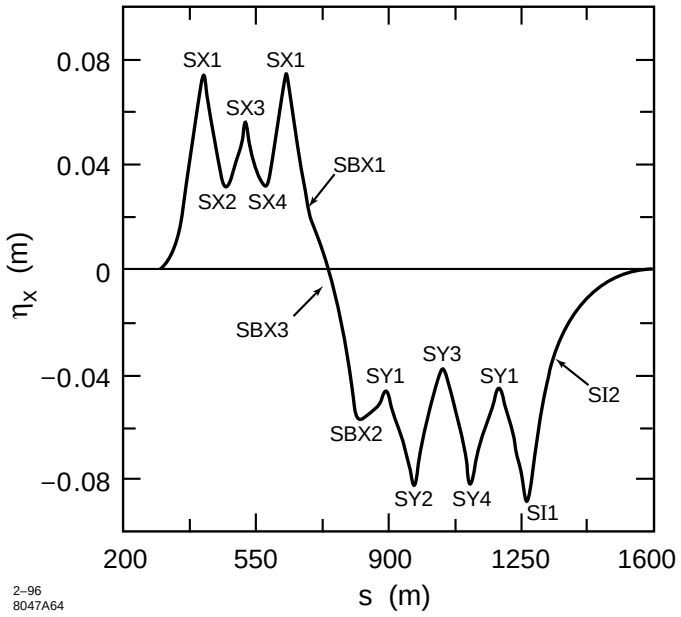

Figure 11-11. *Sextupole locations and dispersion for the 1-TeV design.*

FT; all at positions with nonzero dispersion. The sextupole locations and the dispersion function for the 1-TeV final focus are illustrated in Figure 11-11.

The sextupole strengths are determined from tracking to optimize the momentum bandwidth of the system. This application of sextupoles for bandwidth-optimization was first proposed by Brinkmann at DESY [Brinkmann 1990]. Similar to Brinkmann's early results, the momentum bandwidth of the NLC final focus is at least doubled by means of the additional sextupoles. This beneficial effect of Brinkmann-sextupoles is explained by a reduced chromatic breakdown of the $-I$ sections between the main sextupoles and also of the FT: a Taylor-map analysis of the final-focus optics reveals a significant reduction of fifth-order chromo-geometric aberrations due to the additional sextupoles (Section 11.5.3).

Optimization

The length of the 1.5-TeV final-focus system was originally optimized with regard to nonlinear aberrations, such as third-order horizontal and vertical chromaticity, and chromo-geometric terms with generator $x'^2 y'^2 \delta$, and also with regard to the effect of synchrotron radiation in the bending magnets, octupole-like aberrations from long sextupoles, magnet vibration tolerances inside the CCY, and power-supply ripple. A general optimization procedure is described in [Zimmermann 1995], and is a modified version of an earlier proposal by Irwin [Irwin 1991]. Some specific side-constraints for the actual design are not included in this optimization scheme. In particular, the optimization assumes only one operating energy and detector backgrounds are not taken into account.

The final focus has been designed such that its total length is constant in the entire energy range between 350 GeV and 1.5 TeV. The length of the system is then determined by the 1.5-TeV case, and it may be interesting to compare the design at this energy with the shortest possible, or optimum, final focus. Table 11-6 lists the theoretical optimum and the actual design values of vertical beta function and dispersion at the Y-sextupoles, sextupole strength, and length.

Parameter	1.5 TeV	
	Design	Theor. optimum
β_D^y (km)	300	80
η_D (mm)	30	24
k_D (m^{-2})	2.2	8.3
Δx (nm)	300	300
$\Delta k/k$	5×10^{-5}	8×10^{-5}
$L_{\rm tot}$ (m)	1800	900

Table 11-6. *Comparison of the 1.5-TeV final focus with a hypothetical design optimized for minimum length, assuming $\beta_x^* = 10$ mm, $\beta_y^* = 125$ μm, and $\delta \approx 3 \times 10^{-3}$. The length L_{tot} denotes the total distance from the start of the final focus to the IP, $\Delta k/k$ is the maximum field ripple of quadrupoles in the CCY, and Δx the tolerable orbit drift at the second Y-sextupole due to perturbations internal to the CCY.*

The optimization assumes that the maximum tolerable horizontal orbit variation Δx at the second Y-sextupole caused by perturbations internal to the CCY is the same as for the actual design, *i.e.*, 300 nm.

The length of the 1.5-TeV final focus appears to be about a factor of 2 larger than the theoretical optimum. Not included in the optimization, however, are the geometry-adjustment section in front of the CCX, which holds the IP position constant at all energies, the soft-bend section, and the long final transformer which proved to be essential for reducing detector background due to synchrotron radiation. The geometry-adjustment section and final transformer in the 1.5-TeV design are about 230-m and 500-m long, respectively, and account for most of the additional length, compared with the theoretical optimum.

Apertures and Beam Stay-Clear

The collimation depth in the postlinac collimation section will be about 7 σ_x, 35 σ_y and $\Delta E/E \approx 4\%$. There are also four horizontal and vertical collimators in the final-focus system, close to the main sextupoles, with a slightly larger collimation depth. The beam stay-clear in the final-focus system has to exceed this collimation depth. A side-constraint is that there should be as few as possible variations of the vacuum-chamber dimension, since these generate geometric wakefields. The beam-pipe radius r of the present design fulfills

$$r^2 \geq \max\left[(20\sigma_{\beta,x})^2 + (\eta_x \times 0.04)^2\ , (45\sigma_{\beta,y})^2\right] \quad . \tag{11.8}$$

The contribution from the 4% energy spread is small compared with the 20-$\sigma_{\beta,x}$ betatron beam size. Figure 11-12 illustrates the variation of the 20 σ horizontal and 45 σ vertical beam envelopes, right-hand side of Eq. 11.8, along the 500-GeV (c.m.) final focus, assuming normalized emittances $\gamma\epsilon_x \approx 5 \times 10^{-6}$ m and $\gamma\epsilon_y \approx 8 \times 10^{-8}$ m, which are 10%–20% larger than the design value. The proposed beam-pipe radius is also depicted. In most of the system the radius is constant, equal to 9.5 mm. Magnet apertures are assumed to be 1 mm larger, *i.e.*, about 10.5 mm.

The largest beam size is encountered around the CCX sextupoles. Here the beam-pipe radius needs to be increased to 18.5 mm. Larger apertures of 19–20 mm are then required for the two SX1 sextupoles, for four quadrupoles (QE1, QX3A, QX3B, and QBX1) and for nine B2 bending magnets in the CCX. A larger beam-pipe radius, 14 mm, is also necessary in the final transformer, and in the adjacent soft bending magnets. In the figure, the beam-pipe radius was chosen as 14 mm for all soft bends.

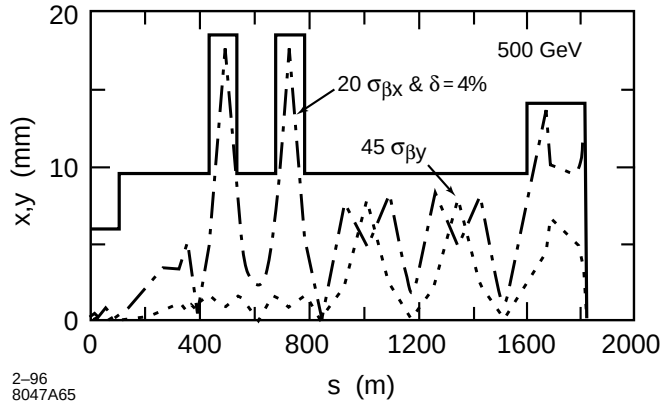

Figure 11-12. *Horizontal and vertical beam envelopes ($20\sigma_x$ and $45\sigma_y$) in the final-focus system for 500-GeV-c.m. energy, assuming normalized emittances of $\gamma\epsilon_x \approx 5 \times 10^{-6}$ m and $\gamma\epsilon_y \approx 8 \times 10^{-8}$ m. The beam-pipe radius is also depicted.*

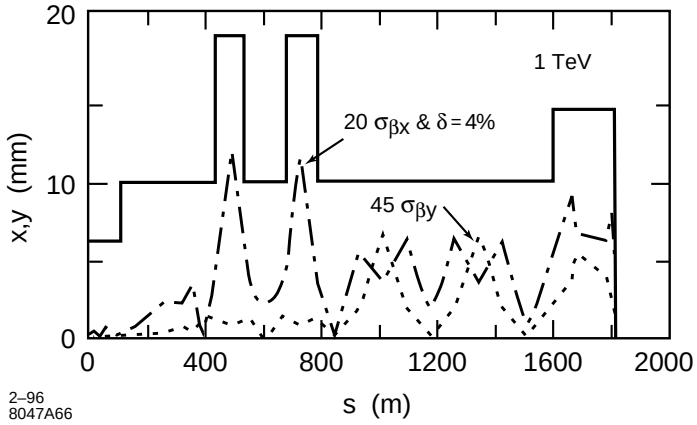

Figure 11-13. *Horizontal and vertical beam envelopes ($20\sigma_x$ and $45\sigma_y$) in the final-focus system for 1-TeV-c.m. energy, assuming normalized emittances of $\gamma\epsilon_x \approx 5 \times 10^{-6}$ m and $\gamma\epsilon_y \approx 8 \times 10^{-8}$ m. The beam-pipe radius is also depicted.*

In the 1-TeV final focus, the beam-pipe radii are still the same as for 500 GeV, and, because of the reduced beam sizes, the beam stay-clear becomes magnificent; see Figure 11-13.

An increased aperture could also be useful around the SY sextupoles, if the vertical emittance is much larger than the design value (for instance, during commissioning). In that case, the best luminosity would be achieved for constant vertical beta function (this is shown in Section 11.5.3), "Bunch Length," which implies larger IP divergence and larger aperture needs. Increased apertures in the CCY do make sense only, of course, if the aperture is not limited somewhere else, *i.e.*, in the final-doublet magnets.

The beam stay-clear at 500-GeV-c.m. energy for the 1-TeV final-doublet design is depicted in Figure 11-14. The beam-pipe radius is 11 mm inside the two conventional quadrupoles Q3 and Q2, as well as in the superconducting quadrupole Q1, and it decreases to 5 mm in the last, permanent-magnet quadrupole QA. The same doublet can operate in the entire energy range between 500-GeV and 1-TeV-c.m. energy. At 500 GeV the horizontal beam stay-clear in the final doublet is 23 σ_x; the vertical beam stay-clear is about 55 σ_y (see Figure 11-14). Again, at 1 TeV the beam

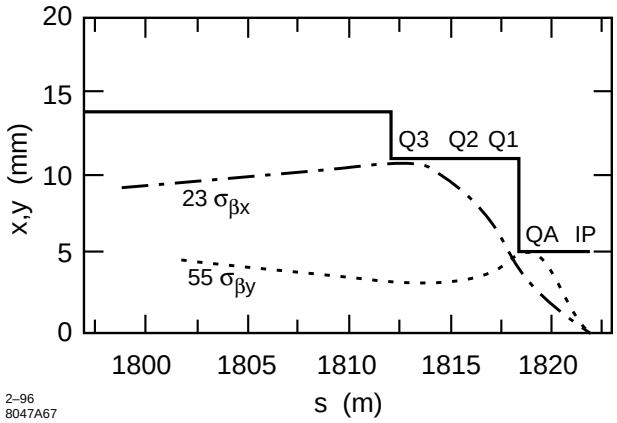

Figure 11-14. *Horizontal and vertical beam envelopes ($18\sigma_x$ and $45\sigma_y$) at the four quadrupoles of the final doublet, for 500-GeV-c.m. energy, assuming normalized emittances of $\gamma\epsilon_x \approx 5 \times 10^{-6}$ m and $\gamma\epsilon_y \approx 8 \times 10^{-8}$ m. The beam-pipe radius is also depicted.*

stay-clear of the doublet, in terms of beam size, is much larger than at 500 GeV. For a detailed discussion of the final doublet see Section 11.6.

To reduce background and to ease the collimation, the final-focus design will likely evolve towards even larger beam stay-clear. An overall vertical stay-clear of 55 σ_y at 500-GeV-c.m. energy is readily achieved by slightly increasing the sextupole apertures. Either by modifying the final doublet or by using a different doublet at 500 GeV and at 1 TeV , the vertical aperture at 500 GeV may be further increased to 60 σ_y.

In conclusion, the apertures of the final-focus design are very large, when viewed in terms of beam size and compared with the SLC (where the stay-clear is about $15\sigma_{x,y}$). A further increase of the vertical beam stay-clear from 55 σ_y to 60 σ_y would also not be difficult.

11.5.3 Performance

Beam Size at the Interaction Point

In this subsection, we discuss contributions to the spot-size from synchrotron radiation and from higher-order optical aberrations. The spot size, or luminosity, is further diluted by residual uncorrected low-order aberrations, which are described later in this section, by crab-crossing errors and by timing offsets between the two beams: A crab-crossing error arises when the phases of the two crab cavities vary with respect to each other. In that case the two beams do not collide head-on. The crab-cavity tolerances, which are discussed in Section 11.7.2, allow for a 2% luminosity loss from imperfect crab crossing. If there is a timing (or phase) error between the two bunch compressors, the collision occurs longitudinally offset from the IP waist, and the spot size at the collision point is increased by the effective waist shift. The proposed tolerance budget also assigns a 2% luminosity loss to this timing error (tolerances on bunch-compressor rf phases are discussed in Chapter 5).

The IP-spot-size increase due to higher-order chromatic aberrations and due to synchrotron radiation in bending magnets and quadrupoles is shown in Table 11-7, for the IP beam parameters of Table 11-1. Each entry in Table 11-7 was obtained by tracking 10,000 particles using the program DIMAD [Servranckx 1990]. Spot sizes for the 1.5-TeV

	500 GeV		1.0 TeV		1.0 TeV (1.5-TeV design)	
	σ_x (nm)	σ_y (nm)	σ_x (nm)	σ_y (nm)	σ_x (nm)	σ_y (nm)
Linear	252	4.18	200	3.35	200	3.35
$\delta_{\rm rms} = 0.3\%$	264	4.32	212	3.40	208	3.55
+ s. rad. in bends	264	4.32	232	3.47	210	3.56
+ s. rad. in quads	264	4.33	232	3.59	211	3.71

Table 11-7. *RMS IP spot sizes for 500 GeV and 1 TeV, as obtained by tracking 10,000 particles with DIMAD.*

	500 GeV		1.0 TeV		1.0 TeV (1.5 TeV design)	
	$\Delta\sigma_x/\sigma_{x0}$	$\Delta\sigma_y/\sigma_{y0}$	$\Delta\sigma_x/\sigma_{x0}$	$\Delta\sigma_y/\sigma_{y0}$	$\Delta\sigma_x/\sigma_{x0}$	$\Delta\sigma_y/\sigma_{y0}$
Chromo-geometric	3.5%	3.3%	**6.0%**	1.5%	4.0%	**6.0%**
Rad. in bends	0.0%	0.0%	**10.0%**	2.1%	1.0%	0.3%
Rad. in quads (tracking)	0.0%	0.2%	0.0%	**3.5%**	0.5%	**5.1%**
Total	**4%**	**3%**	**16%**	**7%**	**6%**	**11%**

Table 11-8. *Relative spot-size increases due to various effects, according to Table 11-7.*

final focus (Version III in Figure 11-10) operated at 1 TeV are also shown, in the far right column of the table. They are slightly better than those obtained with Version II at 1 TeV (second column from the right).

Table 11-8 compiles the relative spot size increases due to different sources as deduced from the above tracking results. At 500 GeV, the chromo-geometric blow-up is about 3.5% both horizontally and vertically. There is hardly any spot-size increase caused by synchrotron radiation.

At 1 TeV, the spot-size increase is considerably larger: 16% horizontally and 7% vertically for the 1-TeV design, and 6%/11% for the 1.5-TeV version operated at 1 TeV (Table 11-8). For the 1-TeV final focus, the largest contribution to the vertical spot-size arises from synchrotron radiation in the final doublet (Oide effect), which causes an rms spot-size increase by about 3.5%. In general, the Oide effect decreases with increasing length of QFT2/QFT3. In the proposed design, the total length of these two quadrupoles is about 4 m, and further improvement for greater length is negligible. (The Oide effect is discussed later in this section and in 11.6.4: "The Oide Effect Including Horizontal Motion".)

The horizontal blow-up at 1 TeV is primarily caused by radiation in the bending magnets (10%) and by chromo-geometric aberrations (6%), assuming a Gaussian momentum distribution of rms value 0.3%. The blow-up due to synchrotron radiation is proportional to the R_{16} matrix-element from the bending magnets to the IP. This blow-up could be reduced by either lowering the dispersion or by weakening the bending magnets. On the other hand, the chromo-geometric aberrations are enhanced by a reduced dispersion (and larger sextupole strength). Thus the present value of dispersion, at which the effects of synchrotron radiation and aberrations are roughly comparable, is about the optimum. One possibility to further reduce the residual horizontal spot-size increase due to radiation and aberrations would be to increase the length of the final-focus system.

The impact of dispersion on spot size and bandwidth can be understood by noting that most of the aberrations arise from the chromatic breakdown of the $-I$ between the main sextupoles. The aberrations affecting the vertical spot size

are then described by a Hamiltonian of the form

$$H \propto K_s^2 \eta_s^2 \left(y'^2 \delta^3 + 2\delta^2 x' y'^2 \frac{\beta_{x,s}^{\frac{1}{2}}}{\eta_s} + x'^2 y'^2 \delta \frac{\beta_{x,s}}{\eta_s^2} + \ldots \right) \quad , \tag{11.9}$$

where K_s is the sextupole strength, $\beta_{x,s}$ the beta function, and η_s the dispersion at the sextupole. The coordinates x', y' denote the normalized slopes at the IP (in units of $\sqrt{\mathrm{m}}$). The product $K_s \eta_s$ is a constant, determined by the doublet chromaticity. The Hamiltonian, Eq. 11.9, shows that most of the aberrations are reduced for increased values of η_s except for the first term which represents the third-order vertical chromaticity. Similarly, most of the important aberrations which influence the horizontal spot size are also smaller for increased dispersion. The third-order vertical chromaticity, which is independent of the dispersion, is canceled by the Brinkmann-sextupoles (Section 11.5.3, "Aberrations").

In summary, synchrotron radiation and high-order chromo-geometric aberrations lead to a total increase of the vertical rms spot size by about 3% and 7% at 500 GeV and 1 TeV, respectively. Since a large part of the blow-up at 1 TeV is due to the Oide effect, the actual luminosity loss will be smaller than quoted, because only few photons are radiated. This is elaborated in Section 11.6. Finally, the increase of the horizontal spot size due to synchrotron radiation could be compensated with a further reduction of β_x^*, but we have not made this assumption.

Momentum Bandwidth

A large momentum bandwidth of the final focus is very desirable considering beam dynamics in the linac, although a larger energy spread necessitates tighter tolerances in the final focus. The bandwidth of the final focus has been increased by introducing additional sextupoles, as suggested by Brinkmann. Examples of the achievable bandwidth are presented in Figure 11-15 and 11-16 for 500 GeV and 1 TeV, respectively, where in both cases three additional Brinkmann sextupoles have been used: one in each of CCX, CCY, and FT. A minimum of three sextupoles appears to be needed for achieving a decent bandwidth, but the further improvement in going from three to 12 Brinkmann-sextupoles is rather small. Therefore, the presently adopted design employs only three Brinkmann sextupoles.

Figure 11-15 shows the vertical and horizontal beam sizes at 500 GeV as a function of the momentum-offset Δ of a mono-energetic beam. The momentum bandwidth for a 10% blow-up of either spot size is $\pm 0.61\%$. As illustrated by Figure 11-16, at 1 TeV the bandwidth for a 10% spot-size increase is about the same. In both figures, the spot sizes are given in units of the values for zero momentum offset. If Brinkmann-sextupoles are not used, the momentum bandwidth is less than $\pm 0.35\%$.

Aberrations

In this subsection, we first discuss the importance of low-order aberrations. Although they can be tuned, these aberrations turn out to be significant for proper estimating the achievable luminosity. Towards the end of this subsection, we also describe the dominant higher-order aberrations.

The perhaps most important, yet often overlooked source of IP spot-size dilution are residual low-order aberrations. These are aberrations, such as waist shift, skew coupling, etc., for which tuning schemes exist, but which cannot be fully compensated, due to the finite accuracy of the beam-beam deflection scans, from which the IP beam size is inferred during tuning. In general, we allocate a 1–2% spot-size increase to each first-, second- and third-order aberration, including the spot-size increase occurring between two tuning scans. This appears to be a fairly conservative estimate of tuning accuracy and stability. For comparison, the actual tuning accuracy in the SLC is about 0.5% per aberration.

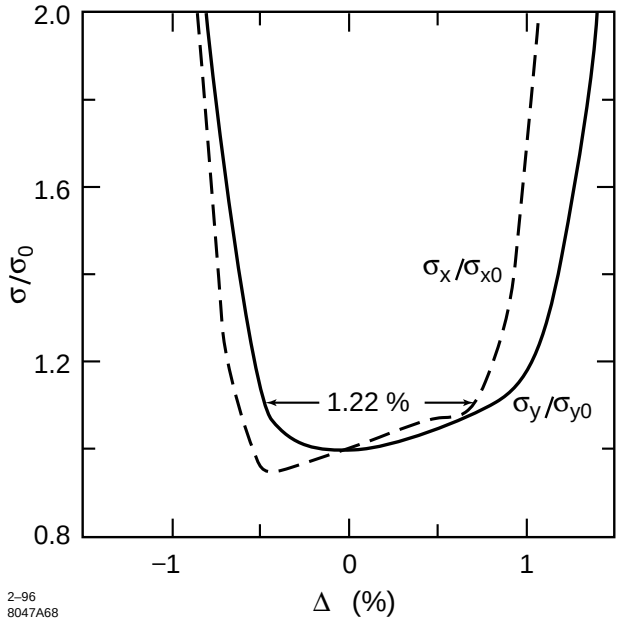

Figure 11-15. *Relative increase of spot sizes as a function of momentum-offset Δ for a monoenergetic beam at 500 GeV, using three Brinkmann-sextupoles. Effects of synchrotron radiation are not included.*

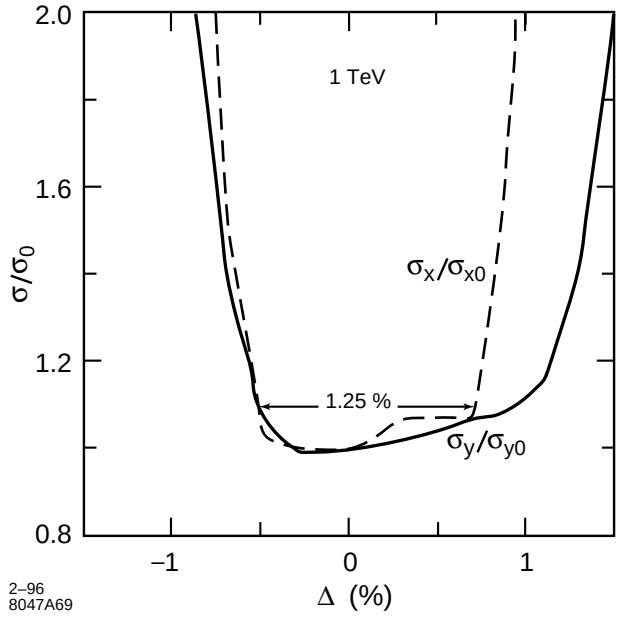

Figure 11-16. *Relative increase of spot sizes as a function of momentum-offset Δ for a monoenergetic beam at 1 TeV, using three Brinkmann-sextupoles. Effects of synchrotron radiation are not included.*

The aberration tuning in the NLC final focus can further be improved in a number of ways: A fast and precise luminosity monitor, *e.g.,* a detector for low-angle Bhabha scattering, will provide a more accurate luminosity measurement than the beam-beam deflection scans and will, therefore, allow a better fine-tuning of aberrations. For all energy-dependent aberrations, the tuning may also be bettered by temporarily increasing the energy spread. The horizontal blow-up will be compensated by reducing the horizontal IP beta function. In addition, if first- and second-order dispersion are continually monitored and corrected, using measured correlations between the beam position at the IP or at the pre-image point and the centroid energy, these two aberrations will become insignificant.

The effect of the low-order aberrations is summarized in Table 11-9 which lists all aberrations that will be tuned, including tuning procedure, tuning frequency, luminosity loss attributed to each aberration, and associated maintenance systems. The table shows that the total increase of the vertical spot size due to residual uncorrected tunable aberrations is expected to be about 13%. Thus, imperfectly-tuned vertical aberrations amount to about half the total vertical blow-up originating in the beam-delivery system; most of the rest being due to synchrotron radiation and to uncorrectable higher-order aberrations. Note that the assumed value for the average dilution per aberration is somewhat ambiguous, since it depends on tuning accuracy, tuning frequency and BPM stability, and can be improved in numerous ways. The assumptions in Table 11-9 differ from those made earlier in Table 11-5. The latter table was more optimistic and predicted a vertical blow-up due to tuned aberrations of only about 6%.

Optical aberrations of order 5 or higher (in the Hamiltonian) exist by design, and at present no tuning scheme is contemplated for any of these. Higher-order aberrations can be calculated from a Taylor map M representing the final-focus system to arbitrary order in (x, x', y, y', δ). Such a map is extracted from a standard MAD input file by methods of differential algebra [Berz 1989] (also called truncated power series algebra), using the program DESPOT [Forest] [3]. The Taylor map can be rewritten as a Dragt-Finn factorization, from which an approximate nonlinear Hamiltonian is determined. Formally we have

$$M = R\exp(-H_{\rm non}) + \text{ higher-order terms} \tag{11.10}$$

where the term R denotes the linear transfer matrix, and $H_{\rm non}$ represents the nonlinear Hamiltonian describing the aberrations. The spot-size increase caused by these aberrations is given by

$$\Delta\sigma^2_{x,y} \approx \left\langle \left(\frac{\partial H_{\rm non}}{\partial p_{x,y}} \right)^2 \right\rangle \quad . \tag{11.11}$$

The angular brackets indicate an average over the (linear) beam distribution at the IP, usually assumed as Gaussian.

An example of such an analysis is given in Table 11-10, which shows contributions to the spot size of some important fifth-order aberrations, to be added in quadrature. The largest aberration is the third-order vertical chromaticity (generator $y'^2\delta^3$), which in the absence of Brinkmann-sextupoles would cause a spot-size increase of 16–25%. In the optimized design, the effect of this aberration becomes negligible (see right column). There is still a considerable amount of third-order horizontal chromaticity, which seems to give rise to a spot-size increase of 5–10%. However, it is somewhat misleading to look at this term in isolation: to produce the desired optimum bandwidth, the third-order horizontal chromaticity has (empirically) been balanced against a nonzero first-order chromaticity which is of similar size and opposite sign. For the optimization of higher-order terms, evidently, a compromise had to be found between a large momentum bandwidth and a small chromo-geometric blow-up for a beam of certain finite momentum spread.

In summary, uncorrected lower-order aberrations cause a 6%–13% increase of the vertical spot size. The horizontal spot size may be recovered by reducing $\beta^\star_x$. The residual fifth-order chromo-geometric aberrations give rise to a vertical blow-up of 2%–10%.

[3] In the current installation, the MAD input first has to be converted into a DESPOT input with the help of the code TRACY.

Time	Name	Hamiltonian	Budget[e] (%)[a]	Tuning Knob	Diagnostic	Maint. System
1/5 s	Steering	y'	.5+.5	Corrector at FD	IP kick	FD anchor + seism. + steering
		x'	.5+.5 [b]			none
1 hr	Dispersion	$\delta y'$	N/A[d]	Weak SD Sexts. asym. hor. move	IP spot size scans	FF orbit control
		$\delta x'$	N/A [b,d]	Weak SF Sexts. asym. hor. move		
	Waist	y'^2	.5+.5	Weak SD Sexts. symm. hor. move		
		x'^2	1+1 [b]	Weak SF Sexts. symm. hor. move		
	Skew1	$x'y'$	1+1	Weak SD Sexts. asym. vert. move		
1 wk	Sextupole	$x'y'^2$	2	Sp. sext. in FT	IP spot size scans	Sext. strength & LT stability
		x'^3	2 [b]			
	Skew sextupole	y'^3	2	Sp. skew sexts. in FT		Sext roll, FD mult. & LT stability
		x'^2y'	2			
	Skew2	xy'	2	Sp. skew quad		LT stability & solenoid strength
	Chromaticity	$\delta y'^2$	1 [c]	SD sext strength		& sext. strength & roll
		$\delta x'^2$	1 [b,c]	SF sext strength		
	Chromatic Skew	$\delta x'y'$	1 [c]	CCY vert. disp.		Occasional FFS alignment studies
	2nd order disp.	$\delta^2 y'$	N/A [c,d]	QT6 and QT5 move		& LT stability
1 mo	Within range of aberration tuning knobs	All	N/A	Element movers	Beam-based alignment	FFS alignment studies & XLT stability
1 yr	Within range of bm based align. (capt. tol.)	N/A	N/A	Coarse element movers	Survey	XXLT stability

[a] .5+.5 means the budget is 1/2% for the final doublet and 1/2% for the remainder of the system; 1+1 means the budget is 1% for the final doublet and 1% for the remainder of the system; system being either the final focus (for steering) or the whole beam line from linac to IP (for all other aberrations).
[b] The pure x-aberrations can be compensated by a slight reduction of β_x^*.
[c] Chromatic aberrations can be enhanced by increasing the energy spread. We assume that these aberrations are tuned out with a doubled energy spread. The chromatic skew can be eliminated by canceling the vertical dispersion. The second-order dispersion at the IP could also be detected directly if there were a beam size monitor available at the IP.
[d] Dispersion and second-order dispersion can be continually corrected, using the correlation of beam-beam pulse-to-pulse deflection with pulse-to-pulse energy of both beams.
[e] Perhaps, because they are stable, the aberrations in the one-week timescale could, under steady beam conditions, be better compensated using a luminosity monitor. We have not made this assumption.

Table 11-9. *Low-order aberration tuning and maintenance. This table allocates a 1% spot-size increase to each δ-dependent aberration, except for dispersion which is assumed to be perfectly compensated, and it assigns a 2% spot-size increase to most other aberrations. The total increase of the vertical spot size is 13%. Note that in Table 11-5 different assumptions about tuning accuracy, frequency and stability were made (0.5% increase per aberration including dispersion), which resulted in about half the vertical blow-up.*

$(\Delta\sigma_y^2)^{\frac{1}{2}}/\sigma_{y0}$	500 GeV		1.0 TeV		1.0 TeV (1.5-TeV design)	
Generator	no B.-sext's.	3 B.-sext's.	no B.-sext's.	3 B.-sext's.	no B.-sext's.	3 B.-sext's.
$x'y'^2\delta^2$	0.31	0.21	0.27	0.29	0.52	0.63
$y'^2\delta^3$	0.52	0.02	0.58	0.03	0.78	0.12
$(\Delta\sigma_x^2)^{\frac{1}{2}}/\sigma_{x0}$	500 GeV		1.0 TeV		1.0 TeV (1.5-TeV design)	
generator	no B.-sext's.	3 B.-sext's.	no B.-sext's.	3 B.-sext's.	no B.-sext's.	3 B.-sext's.
$x'^4\delta$	0.12	0.08	0.06	0.22	0.25	0.30
$x'^2\delta^3$	0.25	0.27	0.33	0.47	0.28	0.33

Table 11-10. *Effect of fifth-order nonlinear aberrations in the final-focus system, with and without Brinkmann-sextupoles for the parameters listed in Table 11-1 and $\delta_{\rm rms}$ =0.3%. The contribution to the spot size quoted has to be added in quadrature.*

Synchrotron Radiation

Besides the effect of lower- and higher-order aberrations, further increases of the spot size arise from synchrotron radiation in final doublet and bending magnets. These are the subject of this section. The Oide effect is also treated, much more comprehensively, in Section 11.6.4.

Synchrotron radiation in the final-doublet quadrupoles causes different particles to be focused at a different distance from the last quadrupole, and, thereby, gives rise to an ultimate limit on the achievable spot size. This has first been pointed out by K. Oide [Oide 1988], after whom it is called "Oide limit". Generalizing Oide's original formula for the spot-size increase [Oide 1988] to two planes (horizontal and vertical) and both quadrupoles of the final doublet, the increase of the vertical spot size due to synchrotron radiation in the last two quadrupoles is given by

$$\Delta\sigma_y^2 = \frac{55 r_e \lambda_e \gamma^5}{48\pi\sqrt{3}} \left[\int_0^{l_1+l_2} \left[\int_0^s g_y(s_1)^2 K(s_1) ds_1 \right]^2 \cdot \right.$$
$$\left. \cdot |K(s)|^3 < \left[|g_x(s)^2 x_0'^{*2} + g_y(s)^2 y_0'^{*}2| \right]^{\frac{3}{2}} y_0'^{*2} > ds \right] \quad , \tag{11.12}$$

where the angle-brackets denote an average over the bunch distribution, the variable s is the longitudinal position measured backward from the exit face of the last quadrupole, and $K(s)$ is the quadrupole strength at position s. The Green's functions g_x and g_y are depicted in Figure 11-17 for an approximation to the NLC final doublet.

The figure shows that most of the spot-size increase occurs in the second pair of quadrupoles viewed from the IP (QFT2 and QFT3), and is due to the focusing in the horizontal plane, rather than to the final vertical focusing. In general, increasing the length of QFT2 and QFT3, while keeping the integrated quadrupole field $K_2 \cdot l_2$ constant, reduces the effect of synchrotron radiation in the final doublet. The length chosen is close to the optimum, in the sense that further improvement for still greater length is negligible. With the present final-doublet design, the increase of the rms spot size due to the Oide effect is less than 0.1% at 500 GeV and about 3.5% at 1 TeV; compare Table 11-8. A modification of the final-doublet design may be required to reduce the blow-up at 1 TeV. The reader is referred to Section 11.6 for a more detailed discussion of the Oide effect.

Synchrotron radiation in the bending magnets affects the beam size at the IP in two different ways. First, radiation in dispersive regions increases the horizontal spot size because of a nonvanishing R_{16}-matrix element between dispersive bend regions and the IP. Synchrotron radiation in the bending magnets causes a horizontal spot-size increase by about 0% and 1–10% at 500 GeV and 1 TeV, respectively (Table 11-8). The blow-up at 1 TeV could be reduced by lengthening the system. Second, for particles losing energy in the final and central bending sections of the CCY,

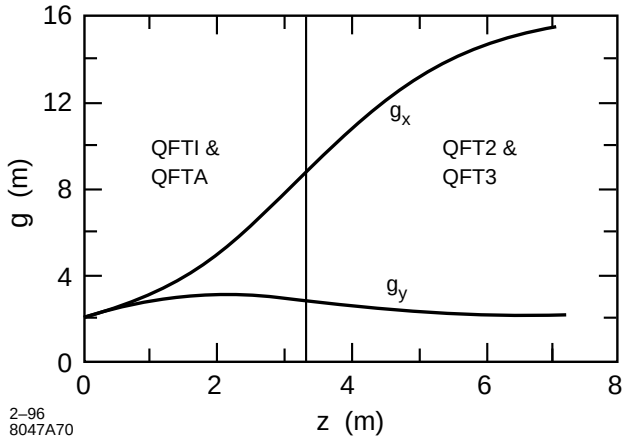

Figure 11-17. *Horizontal and vertical Green's functions as a function of longitudinal position s measured backward along the NLC final doublet. the zero point $s = 0$, refers to the exit face of the last quadrupole.*

	Energy	500 GeV	1 TeV	1 TeV[a]
Number of photons	N_γ	33	66	34
Critical energy	E_c (MeV) in bends	0.3	2.7	1.6
Critical energy	E_c (KeV) in soft bends	25	200	173
Average energy loss	$\Delta E_{\rm rad}$ (MeV)	3.3	52	17
Induced energy spread	$\Delta\delta_{\rm rms}$	0.6×10^{-5}	3.2×10^{-5}	1.2×10^{-5}
Emittance growth	$\Delta(\gamma\epsilon_x)$ (mr)	8×10^{-9}	4.1×10^{-7}	4.1×10^{-8}
Rel. emittance growth	$\Delta(\epsilon_x)/(\epsilon_{x\,0})$ (%)	0.2	9.6	1.0
Hor. spot-size increase	$\Delta\sigma_x/\sigma_{x0}$ (%) (tracking)	0.0	10.0	1.0
Vert. spot-size increase	$\Delta\sigma_y/\sigma_{y0}$ (%) (tracking)	0	2	0.3

[a] This column refers to the 1.5-TeV final focus operated at 1 TeV.

Table 11-11. *Characteristics of synchrotron radiation in the bending magnets.*

the vertical chromaticity of the final doublet is not or only partly compensated, and the particles are chromatically defocused, resulting in an increase of the vertical spot size. This second mechanism leads to a vertical blow-up by about 0.3–2% at 1 TeV (Table 11-8).

The spot-size increases due to synchrotron radiation in the final doublet and bending magnets have been listed in Table 11-8. Some related parameters such as the average energy loss $\Delta E_{\rm rad}$, the average number of photons emitted per electron N_γ, and the critical energy E_c in the bending magnets are given in Table 11-11.

We conclude that synchrotron radiation in bending magnets and quadrupoles is not important at 500 GeV and that at 1 TeV it reduces the luminosity by about 15%, assuming the same final-focus geometry as at 500 GeV (Version II in Figure 11-10). The luminosity decrease due to synchrotron radiation is less than half that, *i.e.*, 7% , if the 1.5-TeV final focus (Version III) is operated at 1 TeV.

Long-Sextupole Effect

A long sextupole magnet gives rise to an octupole-like fourth-order aberration (see, *e.g.*, [Irwin 1992]). For a certain strength, the maximum sextupole length causing a 2% spot-size increase is given by

$$l_{sext} \leq \frac{1.2}{\sqrt{3}\beta_x^s \beta_y^s \epsilon_{x,y} + \sqrt{15}\beta_{y,x}^{s\ 2}\epsilon_{y,x}} \frac{1}{k_{sext}^2} \tag{11.13}$$

where

$$k_{sext} \equiv \frac{2 l_{sext} B_T}{(B\rho)a^2} \tag{11.14}$$

denotes the integrated sextupole strength in units of m^{-2}, and the beta functions are those at the sextupole. Applying this formula to the 1-TeV final focus for normalized emittances of $\gamma\epsilon_x \approx 5 \times 10^{-6}$ m and $\gamma\epsilon_y \approx 8 \times 10^{-8}$ m, we find the maximum tolerable sextupole lengths

$$l_{SX1} \leq 27\,\mathrm{m} \quad \text{and} \quad l_{SY1} \leq 23\,\mathrm{m} \quad , \tag{11.15}$$

For the same optics at 500 GeVand normalized emittances of $\gamma\epsilon_x \approx 5 \times 10^{-6}$ m and $\gamma\epsilon_y \approx 10 \times 10^{-8}$ m, the limit on the sextupole length is

$$l_{SX1} \leq 9\,\mathrm{m} \quad \text{and} \quad l_{SY1} \leq 12\,\mathrm{m} \quad . \tag{11.16}$$

Thus, the fourth-order aberrations induced by the finite sextupole length are insignificant. Note that the 500-GeV limit is tighter, because both the emittances and the horizontal beta function are larger than at 1 TeV. By contrast, due to increased dispersion and lowered sextupole strength at 350 GeV, the maximum sextupole length for the 350-GeV optics will be larger than at 500 GeV.

At 500 GeV, the sextupole lengths may be chosen as 0.4 m, which, for the assumed magnet apertures of 20 mm and 10.5 mm, translates into a pole-tip field of 3.3 kGauss and 1.9 kGauss for SX1 and SY1, respectively. The upgrade to 1 TeV could be performed by adding more sextupoles, to increase the effective length of the two SX1 and SY1 magnets to 0.8 m. Alternatively, longer sextupoles could be installed from the beginning.

We conclude that the present design is far from the long-sextupole limit.

Bunch Length

It is interesting to study the dependence of luminosity on bunch length and vertical beta function. A larger bunch length would relax requirements on the bunch compressor or on the main linac, while an increase of the vertical beta function would reduce the spot-size blow-up due to aberrations and due to synchrotron radiation.

Figure 11-18 shows the luminosity as a function of bunch length, for three different values of β_y^* and a c.m. energy of 500 GeV. The luminosity is estimated from a scaling law for luminosity enhancement, derived by P. Chen [Chen 1993], assuming linear IP spot sizes. The figure illustrates that an increase of the bunch length from 125 μm to 140 μm would cause a luminosity loss by about 3%. A similar luminosity loss occurs if the vertical IP beta function is raised from 125 μm to 150 μm.

The conclusion here is that both bunch length and IP beta function can be changed over a wide parameter range with only marginal loss of luminosity.

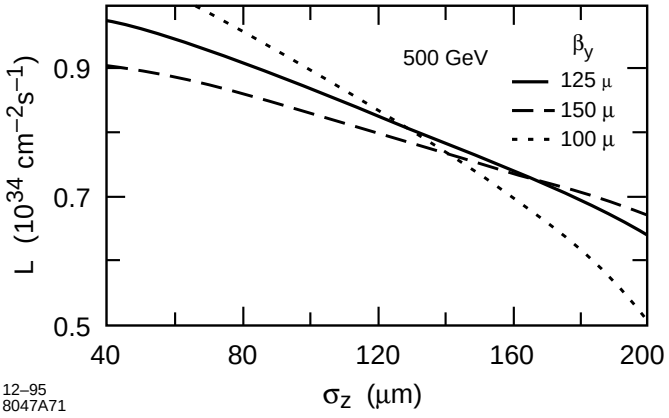

Figure 11-18. *Luminosity at 500-GeV-c.m. energy as a function of the bunch length, for three different values of β_y^*, 90 bunches with 0.65×10^{10} particles per bunch, and a repetition rate of 180 Hz; other parameters as listed in Table 11-1.*

IP Effect	Magnitude	Mover Symmetry	Mover Plane	$\Delta/\ \mu$m at SX1	$\Delta/\ \mu$m at SY1
Skew	$r_{32} = 0.20$	symmetric	y	0.85	0
x-waist	1.6 mm	symmetric	x	1.66	0
y-waist	25 μm	symmetric	x	0	0.28
x-dispersion	19 μm	asymmetric	x	4.30	0
y-dispersion	1.1 μm	asymmetric	y	1.07	0

Table 11-12. *IP tuning with CCX and CCY main-sextupole movers. The minimum displacement requirements, Δ, in the right two columns and the magnitude, in the second column, are for a 2% IP single spot size increase ($E_{\rm beam} = 250$ GeV, $\beta_x^* = 8$ mm, $\beta_y^* = 125\ \mu$m, $\gamma\varepsilon_x = 5 \times 10^{-6}$ m-rad, $\gamma\varepsilon_y = 5 \times 10^{-8}$ m-rad, $\sigma_\delta = 0.3\%$).*

11.5.4 Tuning

Control over IP horizontal and vertical dispersion, waist position, demagnification, chromaticity, and linear coupling, is provided by orthogonal magnet- or mover-knobs similar to those suggested by Irwin for the SLC [Walker 1993, Zimmermann 1995b] or the FFTB. Laser wires will measure the beam size at several locations in the final focus. Valuable experience will be gained from a first laser wire installed at the SLC [Ross 1994]. Decoupling, match of the incoming dispersion and emittance-measurements are performed upstream of the CCX (*e.g.*, in big bend, SCS and DS). The BMS-quadrupoles are used to correct a mismatch in phase space of the incoming beam and to adjust the demagnification at a pre-image point of the IP in the BX (the tuning on the pre-image point is described in Section 11.4), or at the IP itself.

Symmetric or asymmetric displacements of the main-sextupole pairs correct waist shifts, coupling and dispersion at the IP. A mover-based tuning is attractive, since a precise adjustment and control of sextupole positions is required regardless. A summary of main-sextupole mover requirements, their effect on the IP beam and minimum step-size specifications is given in Table 11-12. In all cases the SX1 or SY1 sextupole pairs are moved either symmetrically or asymmetrically.

The minimum mover step size should be $\sim$0.9 μm and $\sim$0.3 μm for the SX1 and SY1 sextupoles, respectively. The accuracy of the corrections is determined by mover precision, and can be improved by adding movable weak sextupoles

adjacent to the main ones. The minimum mover step size requirements can be increased a factor of ten by using a main to weak sextupole strength ratio of 9:1. This also allows the main sextupoles to remain aligned so that chromaticity adjustments do not couple to IP dispersion, skew or waist effects. The main-sextupole mover range should be $\pm$300–500 μm ($\pm$3 mm for the weak sextupoles).

Alternatively, instead of movable weak sextupoles, one could correct waist, dispersion and skew coupling with three pairs of normal and skew quadrupoles, as are being used in the SLC. An advantage is that field changes of such tuning quadrupoles could be implemented much faster than the equivalent sextupole moves. The maximum pole-tip fields required to correct a 100% spot-size increase are of the order 10–30 G at a 2-cm radius. A magnet-time constant of 50–100 ms would be sufficient to limit the luminosity loss due to tuning: assuming that seven aberrations per beam are tuned once per hour, that each aberration tuning consists of seven beam-beam deflection scans at different quadrupole settings, and that a settle time of four time constants is allocated to each quadrupole-field change, the total luminosity loss due to time spent on aberration tuning is estimated to be about 1%.

A correction limit is set by additional aberrations generated by using sextupole movers or tuning quadrupoles in the CCX or CCY to correct optical errors induced by the final quadrupole. For example, a 100-μr rolled final quadrupole (QFT1) generates skew which is correctable by moving the SX1 main-sextupole pair vertically by 60 μm. However, the vertical beam size remains 4% larger than nominal due to the non-local correction. For this reason it will be useful to include a small air-core skew quadrupole near the final doublet. A skew quadrupole of 10-cm length and 50-mm pole radius will require $\sim$4-Gauss pole-tip field step size and $\sim$500-Gauss range at 250 GeV/beam to correct up to 250-μr QFT1 rolls. Similarly, some vernier on the final quadrupole gradients of $\sim$2% will be useful for correcting large doublet induced waist errors.

Some preliminary tuning simulations have been performed on the final focus system simply to test the tuning concept. The incoming beam at the start of the BMS was unrealistically distorted ($\beta_x = 2\beta_{x0}$, $\Delta\alpha_y = 1$, $\Delta\eta_x = 10$ mm, $\Delta\eta_y = 1$ mm) and a final quadrupole gradient error of 0.3% was introduced. This degrades the luminosity by three orders of magnitude. Assuming an IP beam size and divergence measurement with precision of 5%, and using the BMS quadrupole strengths and main-sextupole movers, the final beam sizes achieved were within 10% of nominal. More realistic simulations will be performed in the future which include magnet misalignments, rolls and gradient errors. The beam-based alignment of quadrupoles and sextupoles will be similar to that performed in the SLC [Emma 1992] or FFTB [Tenenbaum 1995]. To monitor and maintain the alignment and orbit, conventional strip-line BPMs are used as well as high-resolution radio-frequency beam-position monitors (rf BPMs) [Hartman priv] which could be integrated into the structure of about 10 quadrupoles in the CCY and the FT. Alternatively each quadrupole and sextupole could be equipped with these rf BPMs, but this is not strictly necessary. The rf BPMs can detect small dispersion-generating drifts of magnet-positions and orbits over a minute timescale (Section 11.5.6, “CCY and FT Orbit Feedback.”)

11.5.5 Tolerances

Tolerance requirements are very tight for most parts of the NLC design. This is especially true for the final-focus system, in which the beta functions are largest and which has to generate and collide beams of minuscule transverse sizes. It is, therefore, necessary to evaluate all tolerances and to demonstrate that they can be met and how .

Variations of the incoming beam parameters, magnet motion, and changes of the magnetic fields will all affect the luminosity. Each change, drift, or vibration needs to be smaller than a certain tolerance value, in order that the design luminosity can be achieved. The timescale over which a tolerance has to be met depends on the type of aberrations generated and also on the tuning frequency or on the damping time of an automated feedback loop.

In accordance with Table 11-9, we distinguish between the following stability categories and associated timescales:

vibration/ripple:	$t <$ 1/5 s
stability/drift:	$t <$ 1 hr
long-term stability:	$t <$ 1 week
very long term stability:	$t <$ 1 month
extremely long term stability:	$t <$ 1 year

Each timescale corresponds to a tuning frequency. All tolerances studied in this section are specified relative to these timescales. Specifically, the tolerances and sensitivities discussed in this section pertain to vibration and ripple (steering tolerances), to stability (skew, waist, and dispersion effects), and to long-term stability (second-order dispersion, chromaticity, geometric aberrations).

Unless noted otherwise, all tolerances presented in this section will refer to a c.m. energy of 1 TeV , normalized emittances of $\gamma\epsilon_x \approx 5 \times 10^{-6}$ m and $\gamma\epsilon_y \approx 10 \times 10^{-8}$ m, and to IP spot sizes $\sigma_y \approx 3.6$ nm, $\sigma_x \approx 225$ nm. Both emittances and spot sizes are about 10% larger than the linear design values quoted in Table 11-1.

In the following, we first determine how sensitive the IP spot size is to incoming orbit variations and to increased emittances. We then look at how displacing a single magnet affects the IP beam position and beam size. Next, the field stability tolerances are discussed for bending magnets, quadrupoles and sextupoles, in Section 11.5.5, "Power Supply Tolerances." In Section 11.5.5, "Scaling of Tolerances," we briefly describe how the tolerances scale with beta function, emittance and energy. In Section 11.5.5, "Tolerance Budget and Luminosity Loss," the overall tolerance budget and the resulting luminosity loss are described, including the different contributions to various aberrations. If the magnet motion is due to ground waves, the individual displacements are not uncorrelated, and the tolerances for incoherent magnet motion do not apply. Instead the wavelength-dependent response of the final-focus system has to be calculated. The luminosity loss due to ground motion is computed in Section 11.5.5. "Ground Motion". Ground motion also plays a role in requirements on repetition rate of both IP spot-size tuning (waist correction, etc.) and beam-based alignment. These questions will be addressed in Section 11.5.5. "Capture Tolerances and Tuning Frequency". Collimator tolerances are discussed in Section 11.5.5, "Collimator Tolerances". Next, thermal stability and the required vacuum pressure are discussed in Sections 11.5.5, "Temperature", and 11.5.5, "Vacuum". Finally, some beam-loss mechanisms other than gas-scattering are described.

We will distinguish between sensitivities and tolerances. By sensitivity we mean the amount of displacement or field change of a single magnet which causes either a 0.1 σ_x (0.2 σ_y) steering error or a 1% spot-size increase. While the sensitivity can be calculated for every magnet, tolerances are assigned. The tolerances are chosen so as to restrict the total luminosity loss from each aberration, due to all magnets, to 1–2%. Thus tolerances translate directly into engineering specifications on power supplies or magnet supports, while the sensitivity has no immediate practical interpretation. The two notions are, however, closely related, since a tolerance is roughly equal to the sensitivity divided by the square root of the number of magnets.

Incoming Jitter Tolerance

Figure 11-19 shows the relative increase of the horizontal and vertical IP spot-size caused by a change of the incoming horizontal and vertical beam orbit. The orbit change is quoted in units of the design beam size (or divergence) at the entrance of the final focus, and the resulting blow-up represents an average over both position and slope changes of either sign.

The figure demonstrates that a horizontal or vertical orbit change by 0.5 σ would lead to an increase of the vertical or horizontal IP spot size by less than 1%. This sensitivity to orbit changes appears tolerable.

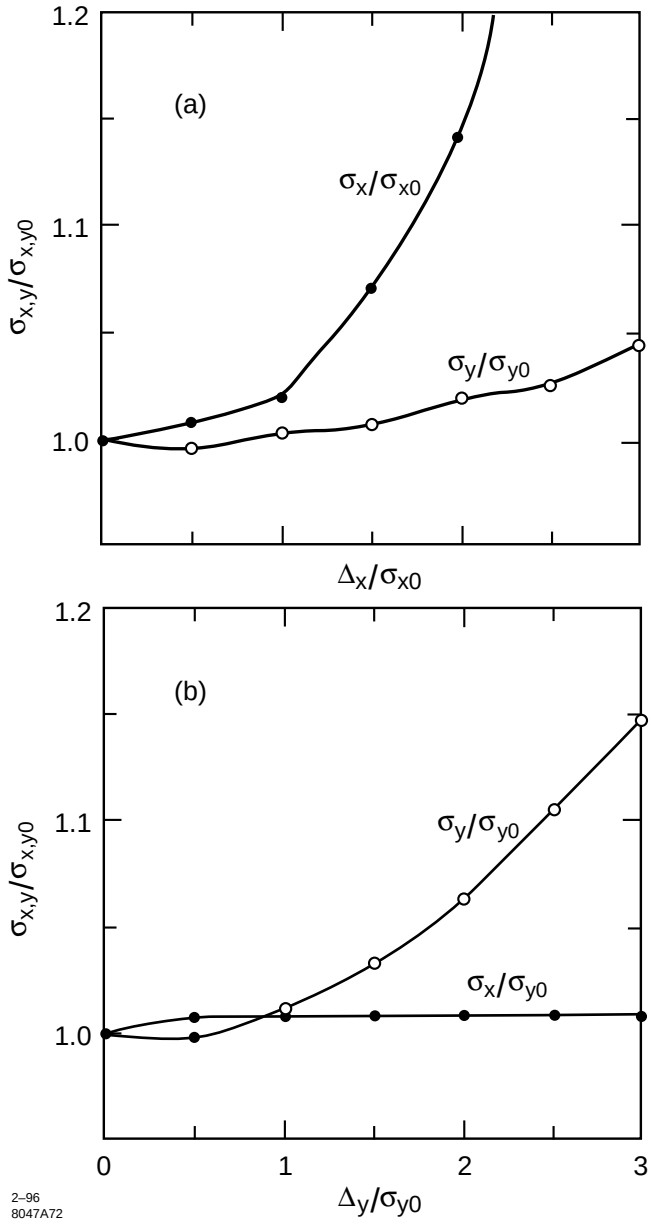

Figure 11-19. *Relative increases of the IP spot sizes as a function of horizontal or vertical incoming orbit variation in units of the design beam size. Effects of synchrotron radiation are not included.*

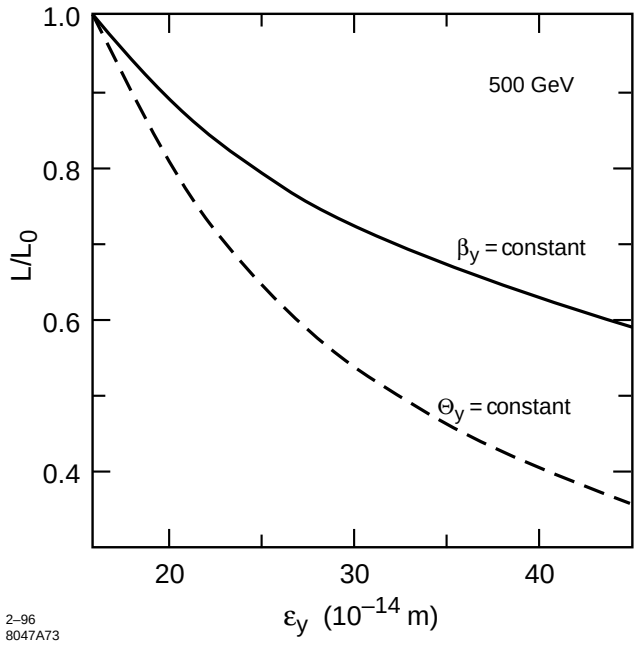

Figure 11-20. *Relative loss of luminosity for larger vertical emittances, keeping either IP beta function or divergence constant.*

Sensitivity to Emittance Increase

Figure 11-20 illustrates the relative loss in luminosity, disruption and hourglass effect not included, at 500 GeV as a function of the vertical emittance, for either constant β_y^* or constant θ_y^*. It is clearly advantageous to keep the beta function constant, and the importance of the chromo-geometric aberrations, relative to the linear spot size, does not appear to increase for the emittances considered. The reason is that the Lie generators of the dominant aberrations, $x'y'^2\delta^2$ and $y'^2\delta^3$ (compare Table 11-10), are proportional to y'^2 and thus increase in the same way as the linear spot size. If the vertical emittance is three times larger than the design, the luminosity is reduced by about 40%. The bandwidth for twice the vertical emittance is still the same as the design value.

A similar result is found if both the vertical and the horizontal emittances are increased together. When both emittances are doubled, to $\gamma\epsilon_x = 10^{-5}$ m and $\gamma\epsilon_y = 17.5 \times 10^{-8}$ m, the horizontal and vertical spot sizes for a 0.3% energy spread at 500-GeV-c.m. energy are 416 nm and 7.16 nm, respectively, if the beta functions are held constant (8 mm and 125 μm). This corresponds to a luminosity loss by about a factor of 2, so that again contributions from the nonlinear aberrations do not significantly increase. The bandwidth does not deteriorate, as it is shown in Figure 11-21.

Tolerances on Magnet Vibration and Position Drift

Steering Tolerance. *a) Quadrupole Vibration:* According to the jitter-budget proposed by J. Irwin (Table 9-3), the maximum tolerable incoming vertical orbit-jitter is about $0.44\sigma_y$ corresponding to a 2.4% loss of luminosity. The contributions to the IP position jitter from vertical and horizontal vibrations of magnets in the final focus (not including the final doublet) shall result in no more than an additional 0.5% luminosity reduction each.

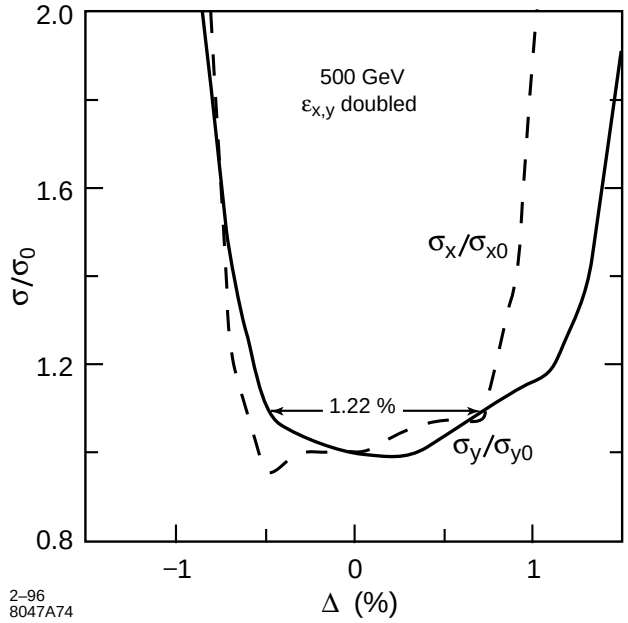

Figure 11-21. *Momentum bandwidth of the 500-GeV final-focus system, for increased emittances,* $\gamma\epsilon_x = 10^{-5}$ *m,* $\gamma\epsilon_y = 17.5 \times 10^{-8}$ *m, and constant IP beta functions,* $\beta_x^* = 8$ *mm,* $\beta_y^* = 125$ μ*m.*

The tolerance on the quadrupole vibration amplitude is thus calculated by requiring that the resulting change of the horizontal (vertical) IP beam position is not larger than $0.1\sigma_x$ ($0.2\sigma_y$). The vertical tolerance is looser by a factor of two, due to the large vertical disruption.

For a single quadrupole, the maximum vibration amplitude Δx, Δy is given by [Roy 1992]

$$\Delta x \quad < \quad \frac{\sigma_x^*}{10 R_{12} k_q} \tag{11.17}$$

$$\Delta y \quad < \quad \frac{\sigma_y^*}{5 R_{34} k_q} \tag{11.18}$$

where R_{12} and R_{34} are the R-matrix elements from the quadrupole to the IP and k_q denotes the integrated quadrupole strength. Sensitivities to both horizontal and vertical quadrupole vibrations are listed in Tables 11-13 and 11-14. Note that these numbers apply to each magnet individually, and that the actual vibration tolerance is given in Table 11-19. The tightest sensitivities (again not including the final doublet) for a 0.5 % luminosity loss, due to a single magnet, correspond to vibration amplitudes of about 70 nm horizontally and 14 nm vertically, for about seven magnets at 1-TeV-c.m. energy (Table 11-14, and Figures 11-23 and 11-24).

The sensitivity for skew-quadrupole vibrations can be calculated in a similar way. Some resulting tolerances for the correction skew-quadrupoles in the SCS can be found in Table 11-28.

b) Roll of Bending Magnet: If a bending magnet vibrates in the x-y plane, it can steer the beam vertically at the IP. The maximum allowed roll-angle θ_{xy}, for a $0.2\sigma_y$ change of the IP beam position, is

$$\theta_{xy} \leq \frac{\sigma_y^*}{5 R_{34}^{bIP} \theta} \tag{11.19}$$

where σ_y^* denotes the vertical IP beam size, R_{34}^{bIP} the (3,4)-R matrix element from the bending magnet to the IP, and θ the bending angle. The tolerances for most magnets are fairly tight (Table 11-16 and Figure 11-31), eg a change in roll by 2 μr of a single bend magnet in the BX can reduce the luminosity by 1%. This is a jitter tolerance, since steering errors at the IP will be corrected in less than 0.2s by a fast IP collision feedback, akin to that of the SLC.

Dispersion. A displaced or rolled magnet can generate dispersion at the IP. If the dispersion is tuned and corrected in hourly intervals, the corresponding tolerances are position-drift tolerances, which for some magnets may be difficult or expensive to meet. Fortunately, dispersion can be corrected continuously, if one utilizes the correlation of beam-beam pulse-to-pulse deflection with pulse-to-pulse energy for both beams. For this purpose, the pulse-to-pulse energy variation could be intentionally increased, by lowering the gain of one or more energy feedback loops.

a) Quadrupole-Position Drift: A displaced quadrupole increases the IP spot size due to dispersion, which is generated both directly by the chromatic kick from the displaced quadrupole and by the orbit change in the downstream elements. The spot-size increases by 1% or less, if the quadrupole-position drift Δx or Δy satisfies

$$\Delta x < \frac{\sigma_x^*}{5\sqrt{2}\delta \mid -R_{12}+T_{126}\mid k_q} \tag{11.20}$$

$$\Delta y < \frac{\sigma_y^*}{5\sqrt{2}\delta \mid -R_{34}+T_{346}\mid k_q} \tag{11.21}$$

where δ is the rms momentum spread ($\delta \approx 0.3\%$), and T_{126}, T_{346} denote the T-matrix elements (in TRANSPORT notation) from the quadrupole to the IP. For magnets inside or behind the CCY, the largest contribution to these two coefficients arises from the uncompensated chromaticity of the final doublet.

At 1 TeV, the maximum tolerable vertical dispersion at the IP is 160 nm, corresponding to a 1% blow-up of the vertical spot size for an intrabunch energy spread of $\delta \approx 0.3\%$. The vertical displacement corresponding to a 1% luminosity loss is about 40 nm for the first two quadrupoles in the FT (QFT5 and QFT6) and for QEI4, further upstream, and it is 140 nm for the two quadrupoles in the center of the CCY (Table 11-14). These sensitivities correspond to an orbit change by about 110 nm at the end of the first doublet magnet (QFT3), which needs to be detected and corrected by a fast orbit feedback. The orbit variation to be measured is small compared with the vertical rms beam size of 60 μm. Nevertheless, simulations show that orbit correction with the desired accuracy is possible in less than 2 s, based on four 1-μm-resolution BPMs. These simulations are presented in Section 11.5.6, "CCY and FT Orbit Feedback." The feedback response time could be further improved by using rf BPMs, which have much higher resolution.

Horizontal displacement sensitivities due to dispersion are 140 nm or larger.

b) Sextupole-Position Stability: Sextupole motion at a location with nonzero dispersion generates dispersion at the IP. The corresponding maximum motion for a 1% spot-size increase is

$$\Delta x_s^\eta < \frac{\sqrt{2}\sigma_x^*}{5k_s\delta\eta_s R_{12}} \tag{11.22}$$

$$\Delta y_s^\eta < \frac{\sigma_y^*}{5\sqrt{2}k_s\delta\eta_s R_{34}} \tag{11.23}$$

where δ denotes the rms momentum spread, $R_{12,34}$ are the R-matrix elements from the sextupole to the IP, $\sigma_{x,y}$ the IP beam sizes, η_s is the nominal dispersion at the sextupole, and k_s the integrated sextupole strength.

In case the dispersion is not corrected continually, this is both a vibration and a stability tolerance, which has to be met over 30–60 minutes.

c) Bend Roll: Also a rolled bending magnet generates dispersion at the IP. The bend roll causing a 1% luminosity loss is given by

$$\theta_{xy}^{b} \leq \frac{\sigma_y^*}{5\sqrt{2}|T_{346} - R_{34}|\theta\delta} \tag{11.24}$$

where θ is the bend angle, δ the rms momentum spread, and R_{34}, T_{346} denote the R- and T- matrix elements from the bending magnet to the IP.

Skew Coupling and Waist Shift. *a) Sextupole-Position Stability:* In addition to dispersion, sextupole motion causes waist shift or skew coupling, and also thereby increases the IP spot size. The corresponding maximum motion for a 1% luminosity loss is:

$$\Delta x_s^w \quad < \quad \frac{1}{5\sqrt{2}k_s \max(\beta_x, \beta_y)} \tag{11.25}$$

$$\Delta y_s^s \quad < \quad \frac{1}{5\sqrt{2}k_s\sqrt{\beta_x\beta_y}}\sqrt{\frac{\epsilon_y}{\epsilon_x}} \tag{11.26}$$

where ϵ_x, ϵ_y denote the emittances and k_s the integrated sextupole strength. Values for the 15 sextupoles in the 500-GeV final focus are listed in Table 11-15. The tightest sensitivities for a 1% luminosity loss are about 500 nm horizontally and vertically for the two main Y-sextupoles (Figures 11-28 and 11-29). Again the actual tolerances that have to be achieved are tighter than those quoted, in this case by roughly a factor of two assuming uncorrelated sextupole motion.

b) Quadrupole-Position Stability (or Drift): The same skew coupling or waist shift is generated when a quadrupole moves inside the CCX or CCY steering the beam off-center through the second sextupole. The maximum drift amplitudes due to this effect for a 1% luminosity loss are:

$$\Delta y_q \quad \leq \quad \frac{\sqrt{2}\Delta y_s^s}{R_{34}^{qs}k_q} \tag{11.27}$$

$$\Delta x_q \quad \leq \quad \frac{\sqrt{2}\Delta x_s^w}{R_{12}^{qs}k_q} \tag{11.28}$$

where Δx_q and Δy_q denote the motion tolerances, due to waist shift or skew coupling, R_{34}^{qs} and R_{12}^{qs} the R-matrix elements from the quadrupole to the next sextupole, and k_q the integrated quadrupole strength. The term Δy_s^s is the tolerance for sextupole movement giving rise to a skew aberration, and Δx_s^w is the tolerance for sextupole movement giving rise to a waist aberration. For a few quadrupoles in the CCY, the vertical (horizontal) displacement sensitivity due to this effect can be as tight as 110 (500) nm, for a spot size increase by 1% (Figures 11-25 and 11-26 present sensitivities for 1% luminosity loss).

c) Quadrupole Roll: A quadrupole rolling in the x-y plane may generate skew coupling at the IP. The tolerance on the x-y roll angle θ_{xy} for a 1% spot size increase is given by

$$\theta_{xy} \leq \frac{1}{10\sqrt{2}k_q\sqrt{\beta_x\beta_y}}\sqrt{\frac{\epsilon_y}{\epsilon_x}} \tag{11.29}$$

where β_x, β_y are the horizontal and vertical beta function at the quadrupole, and k_q is the integrated quadrupole strength. Roll sensitivities for all quadrupoles are listed in Table 11-14. The tightest actual tolerances are those for the final-doublet magnets QFT3–QFT1: about 1.5 μr in 1 h (compare Figure 11-27).

d) Bend Roll: A rolled bending magnet may steer the beam vertically at the next sextupole, thus generating skew coupling. This effect gives rise to a second drift tolerance on the bend roll angle, in addition to that arising from

vertical dispersion. The bend roll drift causing a 1% luminosity loss due to skew coupling is

$$\theta^b_{xy} \leq \frac{\Delta y^s_s}{\sqrt{25} R^{bSX}_{34} \theta} \tag{11.30}$$

where θ is the bend angle, Δy^s_s the drift tolerance for the downstream sextupole due to skew coupling, and R^{bSX}_{34} the R-element between bending magnet and sextupole.

Second-Order Dispersion. *a) Quadrupole Alignment:* The maximum tolerable second-order dispersion at the IP is about 35 μm, for a 1% luminosity loss and an rms energy spread of $\delta_{\rm rms} \approx 0.3\%$. If no tuning scheme for this aberration is implemented, the number above translates into a vertical alignment tolerance for quadrupole magnets in the final focus. Second-order dispersion is primarily generated by interaction of a chromatic kick from a displaced quadrupole with the doublet chromaticity. In the absence of a correction scheme, the absolute alignment tolerance for a single final-focus quadrupole due to generated second-order dispersion would be

$$\Delta y < \frac{\sigma^*_y}{10\ \delta^2\ |T_{346}|\ k_q}. \tag{11.31}$$

The tightest sensitivities of about 12 μm are those for the first two magnets in the FT (QFT6 and QFT5). Sensitivities for all quadrupoles are given in Tables 11-13 and 11-14.

One possibility for compensating the second-order dispersion is by vertical moves of quadrupoles QFT6 and QFT5. A quadrupole move will also create first-order dispersion, which is of similar magnitude as the second-order dispersion and which, therefore, will dominate the spot size during a scan. Specifically, we have the following relation between first- and second-order dispersion $\eta^{(1)}_y$, $\eta^{(2)}_y$ at the IP and the vertical quadrupole positions Δy_{QFT5}, Δy_{QFT6}:

$$\eta^{(1)}_y = 3.8 \times \Delta y_{QFT5} - 3.0 \times \Delta y_{QFT6} \tag{11.32}$$

$$\eta^{(2)}_y = -4.0 \times \Delta y_{QFT5} + 1.7 \times \Delta y_{QFT6} \tag{11.33}$$

In principle, the two quadrupoles can be moved simultaneously such that only second-order dispersion is generated, but no first-order dispersion. As an example, if QFT5 is moved by -18 μm and QFT6 by -23 μm, a second-order dispersion of 35 μm is produced, and the first-order dispersion is not changed. However, in order to realize such a pure $\eta^{(2)}_y$ tuning knob, the mover positions would need to be controlled with an unrealistic precision of 30 nm. Otherwise the measured spot sizes during an $\eta^{(2)}_y$-scan are still affected by residual first-order dispersion. Hence, the second-order dispersion cannot be tuned by a simple scan, but instead an iterative procedure is necessary: after each QFT5/QFT6 move the first-order dispersion is corrected by the standard procedure using sextupole movements in the CCY, before the vertical spot size can be measured. Such a 2-dim. scan (or a "scan of scans") would be a new type of procedure, not used at the SLC.

This complication can be avoided by utilizing the correlation of beam-beam pulse-to-pulse deflection with pulse-to-pulse energy, as it has already been proposed for correcting the regular dispersion. In this case, the second-order dispersion can be continually tuned, and it then causes no significant spot-size dilution.

Power Supply Tolerances

Steering Tolerance. *a) Bending Magnets:* A field change of a bending magnet steers the beam horizontally at the IP. To give a horizontal steering error smaller than $0.1\ \sigma_x$, the relative field-ripple of the bending magnets must satisfy

$$\frac{\Delta\theta}{\theta} \leq \frac{\sigma^*_x}{10\ R^{bIP}_{12}\theta} \tag{11.34}$$

where θ denotes the nominal bending angle, and R_{12}^{bIP} the R-matrix element from the bending magnet to the IP. Sensitivities for bending magnets in the different bending sections are listed in Table 11-16 (Figure 11-30). The actual tolerances which need to be achieved are quite tight, on the order of 3×10^{-6}. This is a "jitter" tolerance, which has to be met over 1/5 s.

Waist Shift. *a) Bending Magnets:* Similar to the effect of horizontally drifting quadrupoles (Eq. 11.27), a field change of the bending magnets inside the CCX or the CCY steers the beam horizontally off-center through the next sextupole, which causes a waist shift at the IP. The maximum allowed field ripple for a 1% luminosity loss is given by

$$\frac{\Delta\theta}{\theta} = \frac{\Delta x_s^w}{R_{12}^{bs}\theta} \tag{11.35}$$

where Δx_s^w denotes the horizontal vibration tolerance due to waist shift of the next sextupole (SX1b or SY1b), θ the nominal bending angle, and R_{12}^{bs} the R-matrix element from the bending magnet to the sextupole. Some numbers may be found in Table 11-16. Assuming 10-m-long bend sections inside the CCX or the CCY are fed by independent power supplies, the tolerable relative field ripple is about 2×10^{-5}. The tolerance decreases to 4×10^{-6}, if all magnets are powered as a string. This is a stability tolerance (timescale 1 hr), unless there is an orbit stabilization system such as discussed in Section 11.5.6: "CCY and FT Orbit Feedback."

b) Quadrupoles: The change of a quadrupole field also causes a waist shift at the IP. For an associated spot-size increase smaller than 1%, the maximum field change is written [Roy 1992]

$$\frac{\Delta k_q}{k_q} = \frac{1}{5\sqrt{2}\max(\beta_x, \beta_y)k_q} \tag{11.36}$$

where k_q is the integrated quadrupole strength, and $\beta_{x,y}$ the beta function at the quadrupole. The sensitivities for the quadrupoles of CCX, CCY, and FT are listed in Table 11-17. The tightest sensitivities (except for the final doublet) for a 1% luminosity loss are about 10^{-4}. Again, the final tolerance that actually needs to be achieved will be smaller than the quoted numbers, each of which refers to ripple in a single magnet only.

Dispersion. Field changes of magnets may give rise to dispersion at the IP. It is contemplated to continually monitor and correct the IP dispersion, using the correlation of beam-beam pulse-to-pulse deflection with pulse-to-pulse energy of both beams, so as to render the dilution due to dispersion as insignificant.

a) Quadrupoles: In addition to causing a waist shift, a field change of quadrupole magnets at locations with nonzero dispersion also generates horizontal dispersion at the IP. The relative field change for a 1% loss of luminosity due to the induced dispersion is given by

$$\frac{\Delta k_q}{k_q} = \frac{\sigma_x^*}{5\sqrt{2}\delta k_q \eta_x^q R_{12}} \tag{11.37}$$

where k_q is the integrated quadrupole field, R_{12} the R-matrix from the quadrupole to the IP, and η_x^q the value of the dispersion at the quadrupole. Sensitivities are listed in Table 11-17.

The relative field-drift sensitivity of four CCX quadrupoles is 4×10^{-4} for a 1% luminosity loss due to generated dispersion. Their sensitivity due to induced waist shift is about twice as tight.

b) Bending Magnets: Horizontal dispersion is also generated by a field change of a bending magnet which alters the downstream orbit. The change of bend angle $\Delta\theta$ causing a 1% luminosity loss is given by

$$\Delta\theta \leq \frac{\sigma_x^*}{5\sqrt{2}|T_{126} - R_{12}|\delta} \tag{11.38}$$

where θ denotes the bending angle, δ the rms momentum spread, σ_x^* the horizontal IP spot size, and T_{126}, R_{12} the T- and R-matrix elements from the bend to the IP (in TRANSPORT notation).

Chromaticity. *a) Sextupoles:* The sextupole field-drift sensitivity due to the induced chromaticity follows from

$$\frac{\Delta k_s}{k_s} \leq \frac{1}{5\sqrt{2}k_s \max(\beta_{s,x}, \beta_{s,y})\eta_{s,x}\delta} \tag{11.39}$$

where $\beta_{s,x,y}$ denotes the horizontal or vertical beta function at the sextupole, $\eta_{s,x}$ the dispersion and k_s the integrated sextupole strength in units of m^{-2}. Sensitivities are not very tight (Table 11-18).

Geometric Aberrations. *a) Sextupoles:* The sextupole field-drift sensitivity due to induced third-order geometric aberrations is approximately

$$\frac{\Delta k_s}{k_s} \leq \frac{1}{5\sqrt{2}k_s \sqrt{\beta_{s,x}\epsilon_x} \max\left(\frac{2}{\sqrt{3}}\beta_{s,x}, \beta_{s,y}\right)} \tag{11.40}$$

where $\beta_{s,x}$ and $\beta_{s,y}$ denote the horizontal and vertical beta function at the sextupole, and k_s the integrated sextupole strength. The resulting tolerances are loose and similar to those imposed by chromaticity (Table 11-18).

Magnet	Steering		Spot Size			
			disp. and skew		2nd o. disp.	roll
	Δx (nm)	Δy (nm)	Δx (μm)	Δy (μm)	Δy (μm)	θ_{xy} (mrad)
QDD	1700.	150.	7.	0.14	33.	4.9
QDF	600.	650.	11.	0.26	61.	7.6
QDD	660.	440.	37.	0.30	70.	4.3
QDF	400.	220.	6.	1.92	470.	2.5
QDD	640.	100.	6.	0.49	110.	2.2
QDF2	340.	80.	2.	0.20	46.	1.6
QDD2	2300.	50.	12.	0.09	22.	3.0
QDF2	240.	90.	4.	0.15	35.	1.3
QDD	640.	150.	6.	0.18	42.	4.0
QDF	550.	650.	3.	0.36	85.	10.0
QDD	1400.	440.	5.	0.51	120.	8.4
QDF	9200.	220.	4.	7.54	1600.	4.7
QDD	1700.	100.	7.	0.41	95.	2.7
QDF	600.	130.	8.	0.37	87.	1.9
QDD	660.	90.	65.	0.20	47.	1.8
QDF	400.	150.	12.	0.29	69.	22.3
QDD	640.	150.	9.	0.23	54.	4.0
QDF2	340.	720.	3.	0.35	81.	6.4
QDD2	2300.	240.	12.	0.49	116.	7.2
QDF2	240.	160.	11.	13.16	2290.	1.6
QDD	640.	100.	11.	0.52	120.	2.2
QDF	550.	130.	5.	0.52	120.	2.6
QDD	1400.	90.	6.	0.29	67.	3.6
QDF	9200.	150.	4.	0.45	104.	4.3
QDD	1700.	150.	7.	0.37	86.	4.9
QDF	600.	650.	7.	0.87	204.	7.6
QDD	660.	440.	17.	2.62	632.	4.3
QG1	430.	240.	122.	2.41	545.	2.6
QG2	1200.	70.	11.	0.36	82.	2.8
QG1	2300.	250.	3.	1.73	395.	4.5
QG2	1700.	3000.	8.	1.36	320.	6.8
QB1	2100.	1200.	39.	8.71	1993.	13.0
QB2	2700.	950.	147.	15.65	3450.	8.8
QB3	880.	370.	199.	19.44	3762.	1.3
QB4	280.	70.	32.	5.19	947.	0.2
QB5	84.	50.	9.	3.75	668.	0.1

Table 11-13. *Vibration, drift and roll sensitivity of quadrupoles between the SCS and BMS in the 1-TeV final focus; each number corresponds to a horizontal (vertical) position error of $0.1\sigma_x$ ($0.2\sigma_y$), or to a 1% spot-size increase, respectively.*

Magnet	Steering		Spot Size			
			disp. and skew		2nd o. disp.	roll
	Δx (nm)	Δy (nm)	Δx (μm)	Δy (μm)	Δy (μm)	θ_{xy} (μrad)
QE2	430.	89.	280.0	9.8	1600.	200.
QE2	400.	89.	240.0	9.8	1600.	200.
QE1	76.	97.	26.0	7.7	1400.	63.
QX3	76.	97.	26.0	7.7	1400.	63.
QX2	250.	57.	4.0	2.3	830.	120.
QX2	260.	58.	4.0	2.3	830.	130.
QX1	30000.	6800.	1.0	3.5	1300.	800000.
QX1	15000.	3400.	1.0	3.5	1300.	300000.
QX2	260.	58.	3.0	1.8	670.	130.
QX2	250.	57.	3.0	1.8	680.	120.
QX3	76.	98.	28.0	9.4	1600.	63.
QBX1	76.	97.	32.0	8.1	1400.	63.
QBX2	250.	57.	8.0	1.2	260.	120.
QBX2	260.	58.	7.0	1.2	260.	130.
QBX3	30000.	6800.	2.0	2.0	480.	800000.
QBX4	22000.	4900.	3.0	2.9	680.	480000.
QBX5	260.	58.	2.0	8.3	4800.	91.
QBX5	260.	56.	2.0	8.4	5200.	88.
QBX6	440.	17.	46.0	6.8	2400.	45.
QY3	440.	17.	47.0	7.0	2300.	45.
QY2	260.	57.	0.6	0.7	2500.	89.
QY2	260.	59.	0.6	0.7	2400.	92.
QY1	43000.	9600.	1.0	0.2	52.	—
QY1	22000.	4800.	1.0	0.2	52.	480000.
QY2	260.	58.	0.6	0.3	90.	90.
QY2	260.	56.	0.6	0.3	93.	88.
QY3	440.	17.	46.0	8.4	1800.	45.
QEI1	440.	17.	96.0	5.9	3100.	45.
QEI2	260.	57.	2.0	0.3	88.	89.
QEI2	260.	59.	2.0	0.4	85.	92.
QEI3	43000.	9700.	3.7	0.1	25.	—
QEI4	85000.	19000.	14.0	0.4	99.	—
QFT6	50.	11.	1.0	0.1	13.	9.
QFT5	70.	8.	1.5	0.1	11.	9.
QFT4	120.	17.	48.0	0.3	68.	20.
QFT3	12.	3.	2.2	0.7	85.	3.
QFT2	17.	2.	3.2	0.7	600.	3.
QFT1	21.	1.	4.6	0.1	79.	4.
QFTA	37.	1.	9.0	0.1	67.	9.

Table 11-14. *Vibration, drift, and roll sensitivity of quadrupoles between the CCX and IP in the 1-TeV final focus; each number corresponds to a horizontal (vertical) position error of $0.1\sigma_x$ ($0.2\sigma_y$), or to a 1% spot-size increase, respectively.*

Magnet	Δx (μm)	Δy (μm)
SX1	3.0	1.9
SX3	260000.0	46000.0
SX1	3.0	1.9
SY1	0.5	0.5
SY3	460000.0	81000.0
SY1	0.5	0.5
SI2	320000.	57000.0

Table 11-15. *Sextupole vibration sensitivity for the 1-TeV final focus due to induced skew coupling or waist shift, for a 1% spot-size increase.*

Name	$\Delta\rho/\rho$ (10^{-5}) (steering)	$\Delta\rho/\rho$ (10^{-4}) (beam size)	θ_{xy} (μrad)
BG	16.5	—	96.0
B1A	6.5	—	15.0
B1B	5.2	—	11.0
B2	1.7	2.3	11.0
B3A	3.5	—	8.0
B3B	3.5	—	1.7
B4	3.3	0.8	3.4
B5A	5.7	—	6.7
B5B	4.4	—	10.0
B5C	10.0	—	23.0

Table 11-16. *Field ripple and roll sensitivity for the bending magnets. Each number corresponds to a steering error by $0.1\sigma_x$, $0.2\sigma_y$ or to a spot-size increase by 1%, respectively.*

Magnet	Waist Shift $\Delta k/k$ (10^{-3})	Dispersion $\Delta k/k$ (10^{-3})	Total $\Delta k/k$ (10^{-3})
QE2	2.10	8.5	2.08
QE2	2.20	7.6	2.07
QE1	0.20	0.4	0.18
QX3	0.20	0.4	0.18
QX2	1.40	3.5	1.30
QX2	1.40	3.7	1.30
QX1	11000.00	240.0	240.00
QX1	4200.00	120.0	120.00
QX2	1.40	3.8	1.30
QX2	1.40	3.6	1.30
QX3	0.20	0.5	0.18
QBX1	0.20	0.5	0.18
QBX2	1.40	5.0	1.34
QBX2	1.40	5.0	1.37
QBX3	11000.00	72000.0	11000.00
QBX4	5900.00	25000.0	5800.00
QBX5	1.00	1.9	0.90
QBX5	1.00	1.9	0.86
QBX6	0.09	4.0	0.09
QY3	0.09	4.0	0.09
QY2	1.00	1.3	0.77
QY2	1.00	1.3	0.80
QY1	16000.00	460.0	460.00
QY1	5900.00	230.0	230.00
QY2	1.00	1.3	0.80
QY2	0.96	1.3	0.80
QY3	0.09	4.0	0.09
QEI1	0.09	4.0	0.09
QEI2	0.98	1.4	0.80
QEI2	1.00	1.4	0.80
QEI3	16000.00	890.0	890.00
QEI4	23000.00	1800.0	1800.00
QFT6	0.10	330000.0	0.10
QFT5	0.05	720000.0	0.05
QFT4	0.15	—	0.15
QFT3	0.04	200000.0	0.04
QFT2	0.02	390000.0	0.02
QFT1	0.01	990000.0	0.01
QFTA	0.02	—	0.02

Table 11-17. *Field ripple sensitivity for quadrupoles between the CCX and IP due to induced waist shift or due to horizontal dispersion generated at the IP. Each listed value corresponds to a 1% spot-size increase.*

Name	$\Delta k_S/k_S$ (10^{-3})		
	Chromaticity	Geom. aberrations	Total
SX1	12.0	4.7	4.4
SX3	—	—	—
SX1	12.0	4.7	4.4
SY1	2.9	3.4	2.2
SY3	—	—	—
SY1	2.9	3.4	2.2
SI2	—	—	—

Table 11-18. *Field ripple sensitivity due to chromaticity or due to geometric aberrations for the normal sextupoles in the CCX, BX, CCY, and FT: each number listed corresponds to a 1% (horizontal or vertical) beam-size increase.*

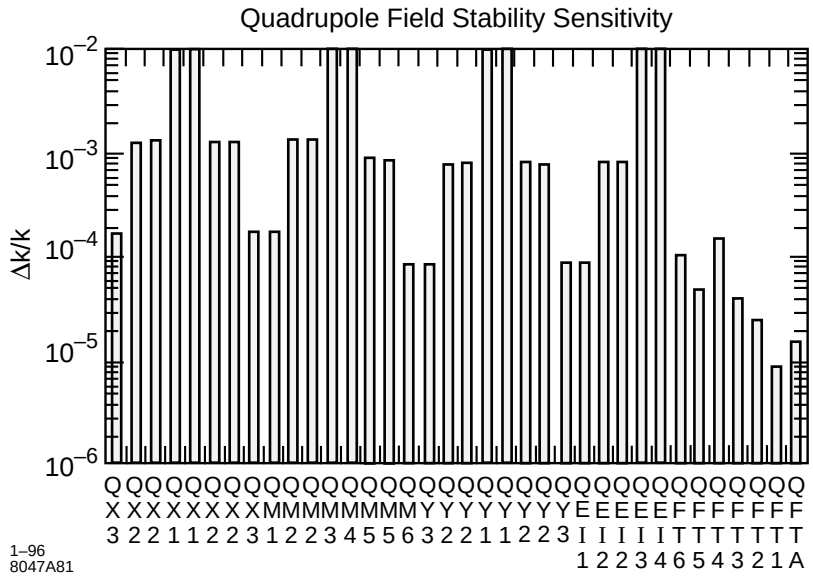

Figure 11-22. *Field-stability sensitivity of quadrupoles in the BMS, CCX, BX, CCY, and FT; each corresponding to a luminosity loss of 1%.*

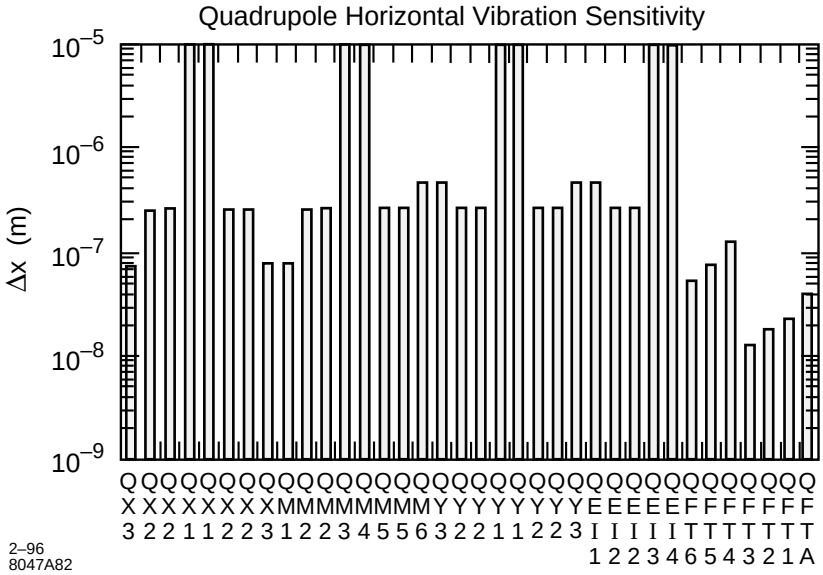

Figure 11-23. *Horizontal vibration sensitivity of quadrupoles in the CCX, BX, CCY, and FT; each corresponding to a luminosity loss of 1%.*

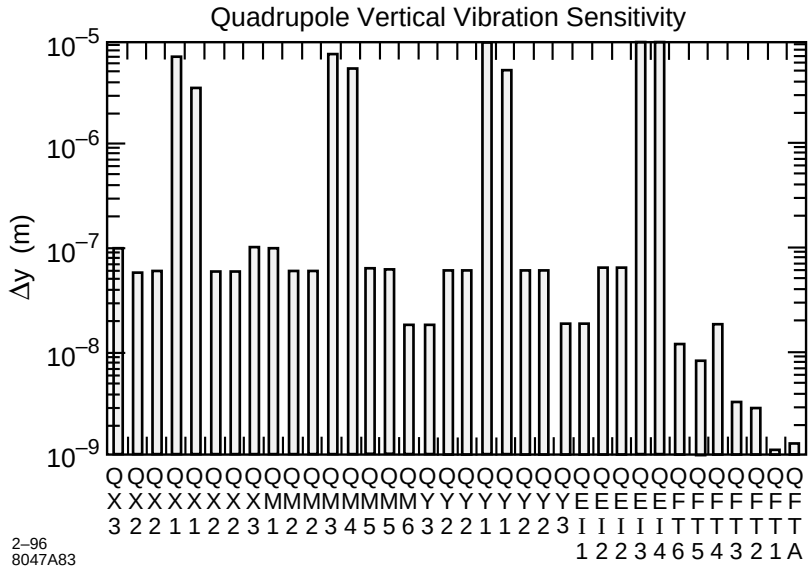

Figure 11-24. *Vertical vibration sensitivity of quadrupoles in the CCX, BX, CCY, and FT; each corresponding to a luminosity loss of 1%.*

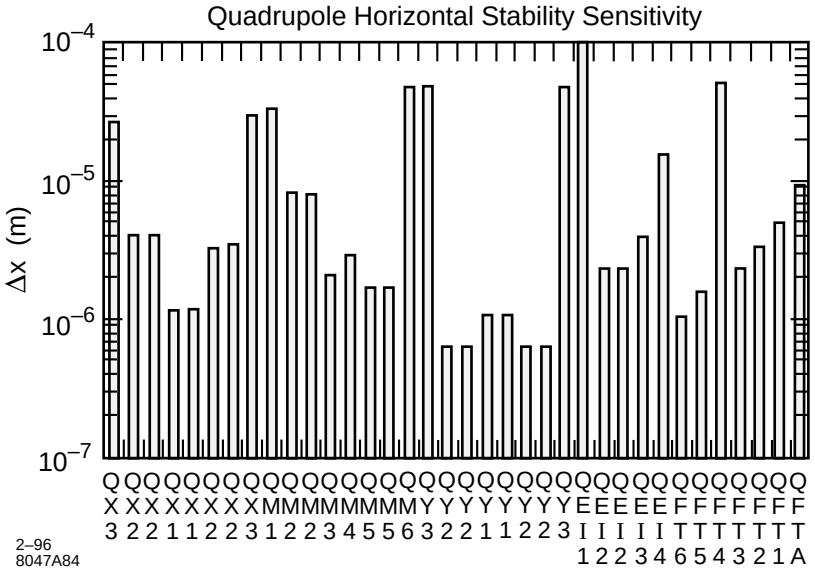

Figure 11-25. *Horizontal stability (or position-drift) sensitivity of quadrupoles in the CCX, BX, CCY, and FT; each corresponding to a luminosity loss of 1%.*

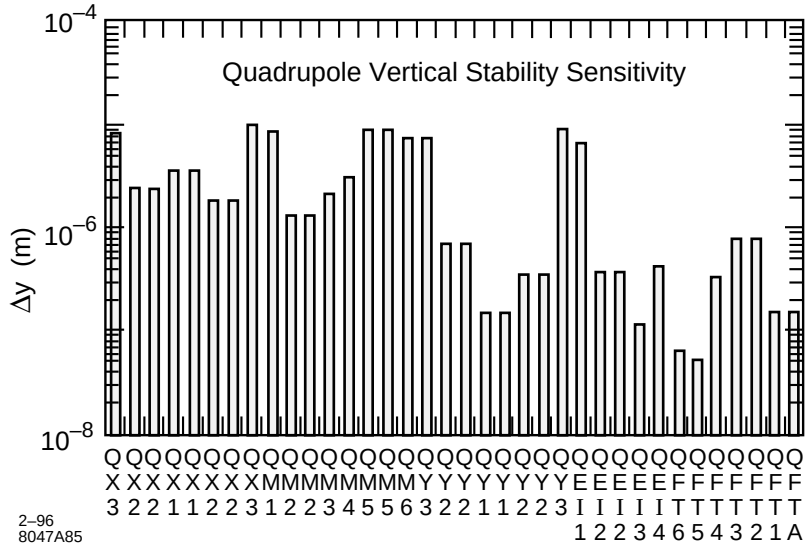

Figure 11-26. *Vertical stability (or position-drift) sensitivity of quadrupoles in CCX, BX, CCY and FT; each corresponding to a luminosity loss of 1%.*

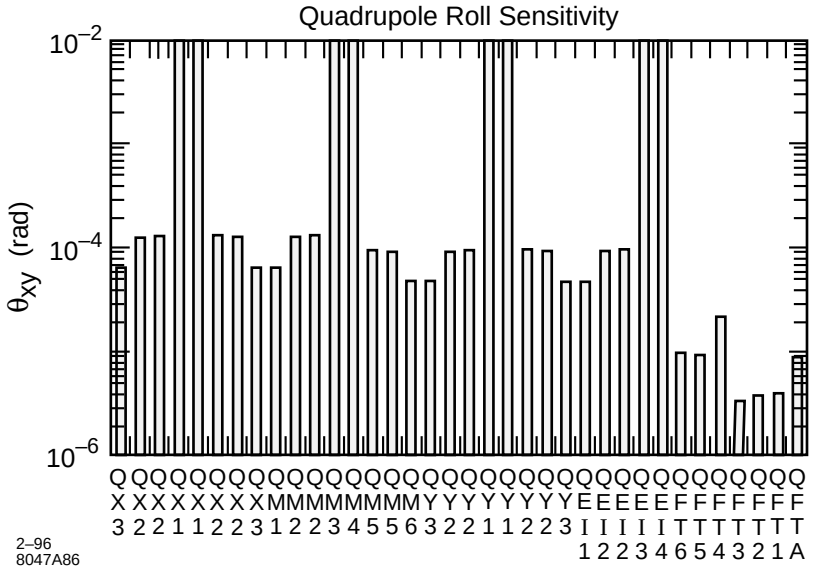

Figure 11-27. *Roll sensitivity of quadrupoles in the CCX, BX, CCY, and FT; each corresponding to a luminosity loss of 1%.*

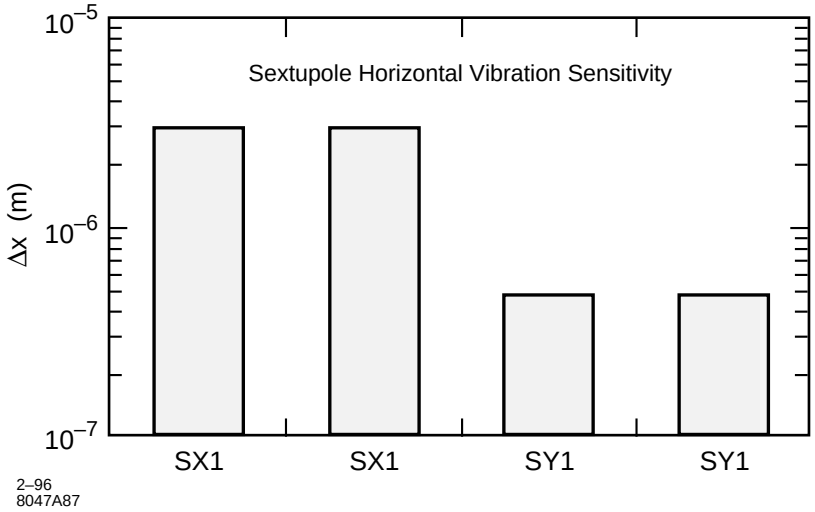

Figure 11-28. *Horizontal vibration sensitivity of main sextupoles in the final focus; each corresponding to a luminosity loss of 1%.*

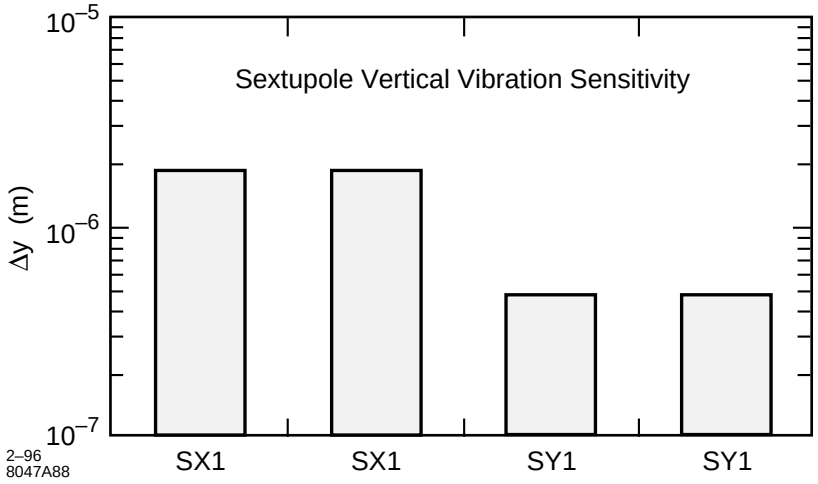

Figure 11-29. *Vertical vibration sensitivity of main sextupoles in the final focus; each corresponding to a luminosity loss of 1%.*

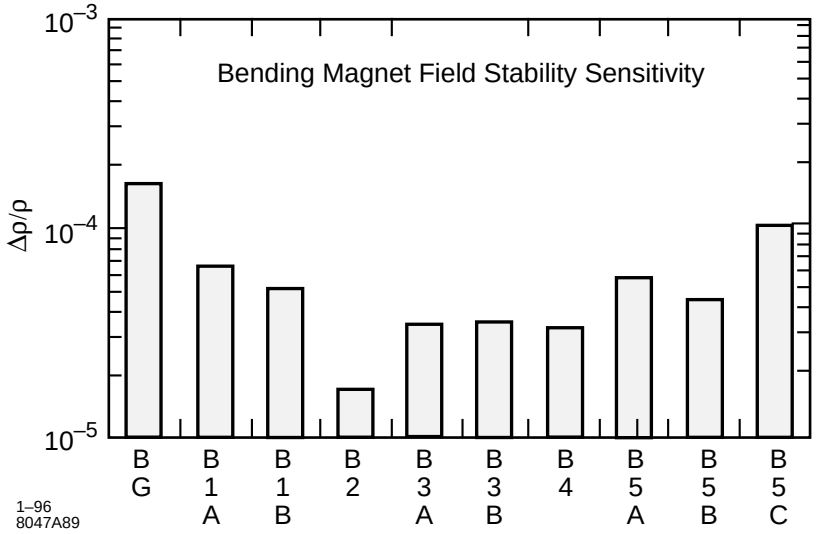

Figure 11-30. *Field-stability sensitivity for bending magnets in the final focus, assuming uncorrelated field ripple; each corresponding to a luminosity loss of 1%.*

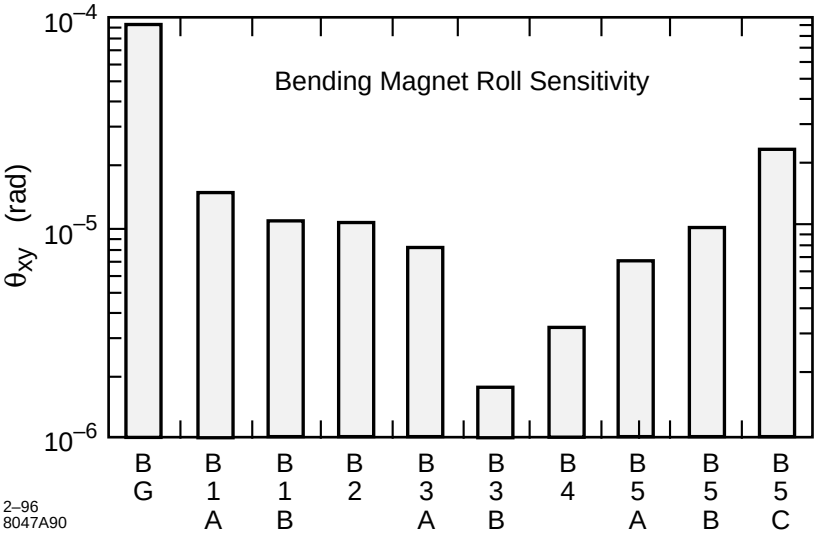

Figure 11-31. *Roll sensitivity of bending magnets in the final focus; each corresponding to a luminosity loss of 1%.*

Scaling of Tolerances

All vibration and stability (drift) tolerances presented in this section refer to a particular parameter set for 1-TeV-c.m. energy (Table 11-1). Most of the sensitivities scale directly with the IP beam size, independently of whether the latter changes due to an emittance variation or due to a different beta function. An exception are quadrupoles in front of the BMS, whose sensitivity is not affected by a change of the IP beta function. From a tolerance point of view, the operation at 500 GeV is equal to an emittance increase. Thus, almost all tolerances at 500 GeV will be a factor of $\sqrt{2}$ looser than those quoted in this chapter.

Tolerance Budget and Luminosity Loss

Beam-beam deflection scans will be used for correcting low-order aberrations which affect the IP spot size, such as waist shift, skew coupling etc.. Because of limited resolution of the deflection scans, these corrections cannot be perfect, but they are accurate to about 1%, implying a corresponding spot-size increase. Since this spot-size increase is dictated by the tuning method, it sets a lower limit on practicable tolerances, *e.g.,* for element strength changes and position drifts. Between two scans of the same aberration, the spot-size increase due to this aberration is assumed to grow from 1% to about 3%, because of magnet field and position drifts. On average (over time) the residual spot-size increase is then expected to be on the order of 2% for each tunable aberration, although various possibilities exist to reduce this number to 0.5% (see discussions in Section 11.5.3 and also Table 11-5). Thus, for consistency, a set of tolerances on magnet motion and field stability was chosen which roughly assigns a 2% spot-size increase caused by all components between linac and IP, or 1% generated in the final focus alone, to each such perturbation. Figure 11-32 illustrates that, for the tolerances chosen, various different effects may contribute by similar amounts to each aberration.

To facilitate design and cost estimates, we have grouped the magnets into different classes. The same tolerances then apply to all magnets of one class. Specifically, the quadrupoles are divided into four classes. The majority of the final-focus magnets is in Class 1. Four quadrupoles in the CCY with tighter tolerances form Class 2. Three quadrupoles at the entrance of the final transformer, with still tighter tolerances, are in Class 3, and the final-doublet magnets define Class 4. The sextupoles are split into two classes: main sextupoles and Brinkmann-sextupoles. The bending magnets are not further subdivided. A list of the different magnet types, along with relevant tolerances and the number of magnets of each type, is presented in Table 11-19. Table 11-20 describes the individual tolerances for each magnet class and how they can be met. The overall loss of luminosity corresponding to these magnet tolerances is 11%; see Table 11-21. This number assumes that dispersion is corrected at hourly intervals only, and not continually in which case the luminosity loss would be 1–2% smaller. Taking into account other residual aberrations, such as skew sextupole components and additional sources of aberrations, the estimated total loss of luminosity due to uncorrected tunable aberrations is about 13% (Table 11-9).

Ground Motion

Transverse quadrupole displacements due to ground motion may lead to a serious reduction of luminosity if the two beams are steered off collision faster than feedback systems are able to correct the IP beam position. There are several different approaches to treat the effect of ground motion on the final-focus system. Here, we base the analysis on a two-dimensional power spectrum following Juravlev and co-workers [Juravlev 1995]. A complete treatment of ground motion can be found in Appendix C.

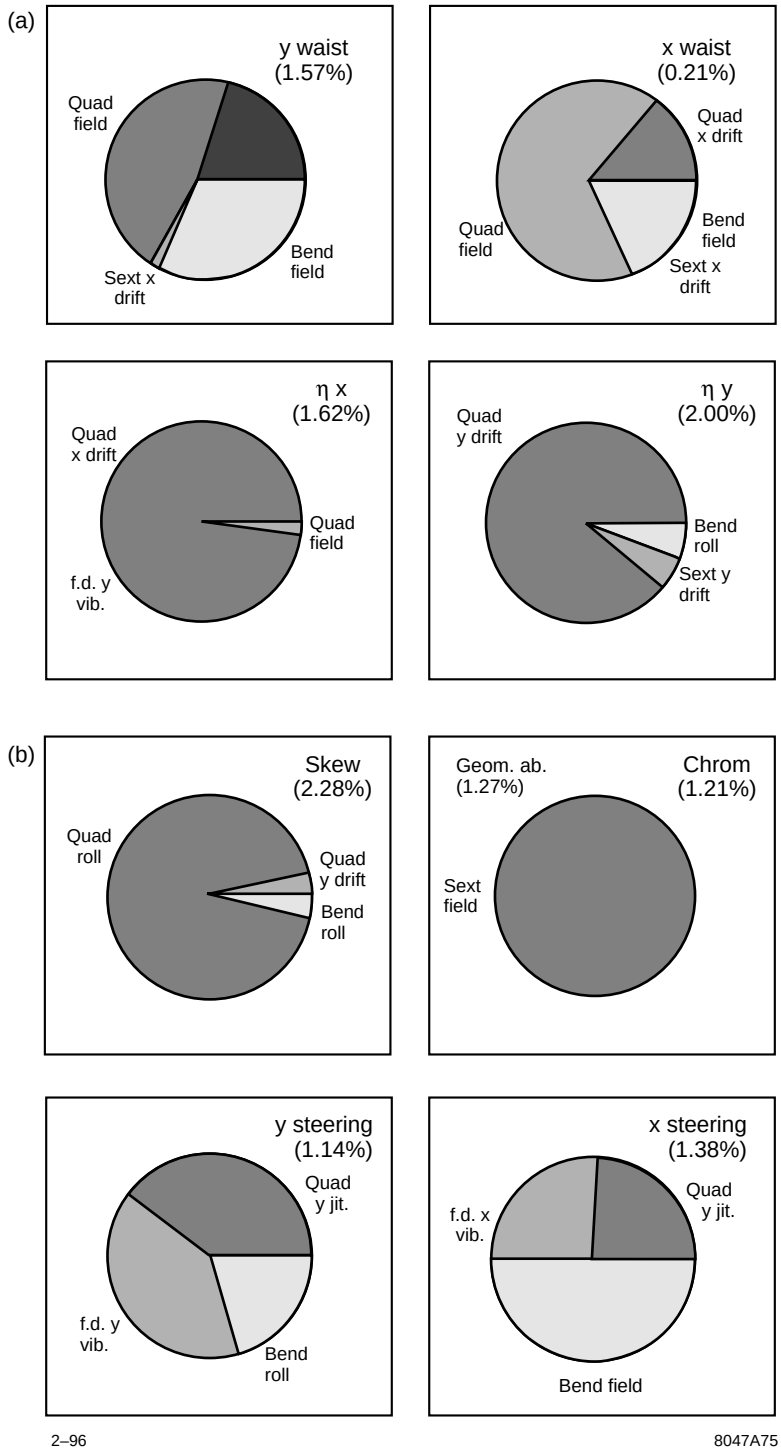

Figure 11-32. *Sources of important aberrations in the 1-TeV final-focus design, for the tolerances of Table 11-19. Numbers in parentheses refer to the overall luminosity loss due to a particular aberration.*
f.d.: final doublet; jit.: jitter; field: field ripple or drift.

Type	P #	Radius a (mm)	Length L (m)	Drift (10^{-5}) $\Delta K/K$	Vibration[a] (nm) Δx	Δy	Drift[a] Δx (nm)	Δy (nm)	θ_{xy} (μr)
Quad 1	33	10.50	0.5/1.0	3.3	6.8	7.3	144.0	33.0[b]	11.3
Quad 2	4	10.50	0.5/0.5	1.8	54.0	4.8	15000.0	2000.0	15.7
Quad 3	3	10.50	1.0/1.0	1.6	9.0	3.4	480.0	21.0[b]	3.4
Quad 4	4	4.00	1.5/2.0	0.4	3.6	0.7	1600.0	98.0	1.8
Skew q. 1	4	6.00	0.4/0.4	100.0	50.0	30.0	15000.0	15000.0	500.0
Sext. 1	4	10.50	0.4/0.4	220.0	50.0	50.0	50.0	50.0	20.0
Sext. 2	12	10.50	0.4/0.4	900.0	1000.0	1000.0	10000.0	10000.0	20.0
Bend 1	100	—	5.0/16.0	0.3	100.0	100.0	500.0	500.0	0.5

[a] With respect to ground.

[b] The vertical drift tolerance will be looser at least by a factor of 10, if the dispersion at the IP is continually corrected utilizing the correlation of beam-beam deflection and beam energy.

Table 11-19. *Magnet types and tolerances for 1-TeV-c.m. energy. Tolerances result in the luminosity loss of Table 11-21.*

If the vertical betatron phase advance from the entrance point e to the IP is a multiple of π, the offset of the two beams at the IP $\Delta y \equiv y_{\rm right} - y_{\rm left}$ due to an arbitrary vertical displacement $y(s)$ of the final-focus magnets is given by

$$\Delta y = -\sum_{i,\rm right} k_i R_{34}^{i\to IP} y(s_i) + R_{33}^{e\to IP} y(s_{e,\rm right}) + \sum_{i,\rm left} k_i R_{34}^{i\to IP} y(s_i) - R_{33}^{e\to IP} y(s_{e,\rm left}) \equiv \sum_j \mu_j y(s_j) \quad (11.41)$$

where $R_{34}^{i\to IP}$ denotes the (3,4) TRANSPORT-matrix element from the ith magnet to the IP, $R_{33}^{e\to IP}$ is the (3,3) matrix element from the entrance of the final focus to the IP, and k_i the integrated quadrupole strength of quadrupole i. For simplicity, we have replaced the $\pm k_i R_{34}$ and $\pm R_{33}$ by the generalized lattice parameters μ_j. The subindex i runs over only one side of the final focus system, while the subindex j runs over both sides. If we square the sum in Eq. 11.41, we will find mixed expressions of the form $y(s_i)y(s_j) \equiv y(s_i)y(s_i + \Delta s_{ji})$, whose expectation value over position s and over time t is given by

$$< y(s_i)y(s_j) >_{s,t} = \lim_{S\to\infty} \frac{1}{ST} \int_{-\frac{S}{2}}^{\frac{S}{2}} \int_{-\frac{T}{2}}^{\frac{T}{2}} y^*(s_i,t) y(s_i + \Delta s_{ji}, t)\, ds\, dt \quad (11.42)$$

$$= \int_0^\infty \frac{d\omega}{2\pi} \int_0^\infty \frac{dk}{2\pi} P(\omega,k) \cos(k\Delta s_{ji}) \quad (11.43)$$

where $\Delta s_{ji} \equiv s_j - s_i$. The term $P(\omega,k)$ denotes the two-dimensional power spectrum (regarding frequency and wave number) of the ground motion. The expectation value for the change of the beam-offset squared after time T can be written

$$< (\Delta y(t) - \Delta y(t+T))^2 >_t = 2 \int_0^\infty \frac{d\omega}{2\pi} \int_0^\infty \frac{dk}{2\pi} G(k) P(\omega,k)(1 - \cos(\omega T)) \quad . \quad (11.44)$$

The function $G(k)$ describes the response to a harmonic displacement of quadrupoles as a function of wavelength. It equals the average squared ratio of the beam-beam offset at the IP and the ground-motion amplitude at that wavelength, and is called the lattice response function. In terms of the lattice parameters μ_j and the positions s_j, this function can be written as:

$$G(k) \equiv \sum_{j1,j2} \mu_{j1}\mu_{j2} \cos(k(s_{j1} - s_{j2})) = 4 \left(\sum_j \mu_j \sin k s_j \right)^2 \quad (11.45)$$

Ripple:	
Quad1	Conventional
Quad2	10^{-5} commercially available, standard FFTB supply
Quad3	10^{-5} commercially available, standard FFTB supply
Quad4	Permanent magnet QA: SmCo with Erbium, see Sec. 11.6. Superconducting Q1: under design Q2 and Q3: if conventional, need special supply
Skew q1	Conventional power supply
Sext1	Conventional power supply
Sext2	Conventional power supply
Bend1	Special supply
Vibration:	
Quad1	8 nm, FFTB support: ground to quad diff. 1 nm
Quad2	5 nm, FFTB support: ground to quad diff. measured as 1 nm
Quad3	3.5 nm, FFTB support: ground to quad diff. 1 nm
Quad4	1 nm, optical anchor, plus seismometer on ground, to keep in line, See IR section
Skew q1	Conventional mount
Sext1	Conventional mount
Sext2	Conventional mount
Bend1	Conventional mount
Drift:	
All	Rf BPMs or orbit stabilization system. See Sec. 11.5.6. Thermal stabilization of tunnel ($<$0.1 μm/hr achieved in FFTB)
Drift (roll):	
All	Rf BPMs or orbit stabilization system. See Sec. 11.5.6.

Table 11-20. *Tolerances for magnet types from Table 11-19 and how they can be achieved.*

The lattice response function $G(k)$ for the present NLC final-focus design is shown in Figure 11-33. For large wave numbers k (above 0.6 m^{-1}) the response function $G(k)$ is about constant, equal to ten. The oscillations are due to the discrete distances between the supports of the four final-doublet magnets. The calculation assumes that all magnets are supported beneath their center.

For small values of the wave number k, that is for $k < 0.01$ m^{-1}, $G(k)$ increases as the sixth power of k. There are three reasons for this: First and second, each side of the final-focus optics fulfills the Irwin sum rules [Irwin 1995a]:

$$-\sum_i k_i R_{34}^{i\to IP} + R_{33}^{e\to IP} = 1 \tag{11.46}$$

$$-\sum_i k_i R_{34}^{i\to IP} s_i + R_{33}^{e\to IP} s_e = 0, \tag{11.47}$$

where Eq. (11.46) expresses that a constant displacement of the entire system, including incoming beam orbit, has no effect on the beam-beam offset at the IP, and Eq. 11.47 means that a displacement of constant slope also does not affect the beam-beam offset. Note that, in Eq. 11.47, the betatron phase advance from the final-focus entrance e to the IP was

Name	Tolerance	$\Delta L/L$ (%)
Quads	hor. vibr.	0.33
	vert. vibr.	0.50
	hor. stab.	1.00
	vert. stab.	1.00
	field ripple	0.50
	roll	1.10
	Total:	**4.23**
Final Doublet	hor. vibr.	0.36
	vert. vibr.	0.50
	hor. stab.	0.95
	vert. stab.	1.00
	field ripple	0.38
	roll	0.96
	Total:	**3.90**
Sextupoles	hor. vibr.	0.03
	vert. vibr.	0.05
	field ripple	2.40
	Total:	**2.50**
Bends	field ripple	0.69
	field stability	0.67
	roll vibration	0.24
	roll drift	0.13
	Total:	**1.71**
Overall	**Total:**	**10.9**

Table 11-21. *Overall luminosity loss corresponding to imposed magnet tolerances. Reference design luminosity (without pinch) is* 0.96×10^{34} *cm*$^{-2}$ *s*$^{-1}$*. Numbers correspond to tolerances listed in Table 11-19.*

assumed to be a multiple of π, but this assumption is not essential. The two conditions (11.46) and (11.47) imply at least a k^4 behavior at small k. In addition and third, the final-focus system consists of several paired π-modules, *i.e.*, of identical modules with phase advance π on either side of the IP. For large wavelengths, the effects of these modules cancel each other, giving rise to the observed k^6 asymptotics. In an intermediate wave number range, between 0.01 and 0.6 m^{-1}, the response function increases about linearly with k (Figure 11-33).

The frequency-dependent correlation of ground motion at different positions can be characterized by

$$R(\omega, \Delta s) \equiv \int_0^\infty \frac{dk}{2\pi} \mu(\omega, k)(1 - \cos k\Delta s) \tag{11.48}$$

where

$$\mu(\omega, k) \equiv \frac{P(\omega, k)}{P(\omega)}, \tag{11.49}$$

with

$$P(\omega) \equiv \int \frac{dk}{2\pi} P(\omega, k) \tag{11.50}$$

representing the local power density of the ground motion. The function $R(\omega, \Delta s)$ can be extracted from recent ground motion measurements at SLAC, performed with two STS-2 seismic sensors on the linac tunnel floor. The

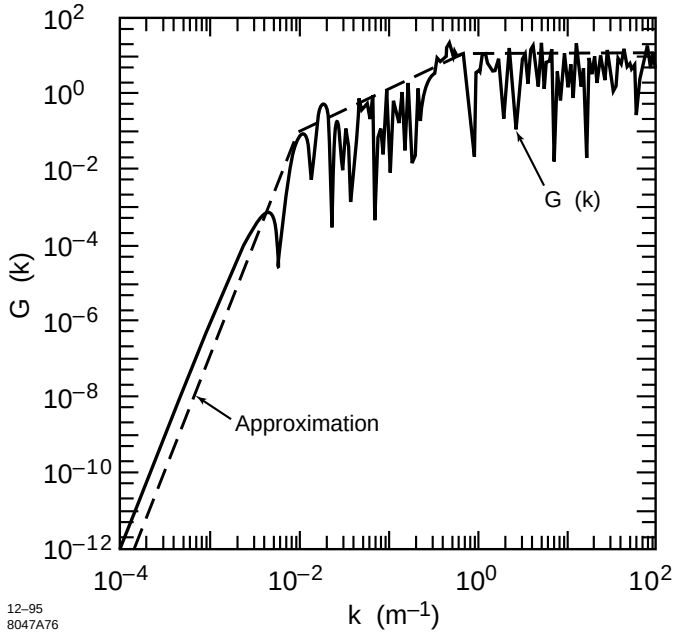

Figure 11-33. *Lattice response function for the NLC final-focus system.*

measurements suggest that R is parameterized quite well by the expression [Adolphsen 1995]

$$R(\omega, \Delta s) \approx 1 - J_0\left(k(\omega)\Delta s\right) \tag{11.51}$$

where J_0 denotes the zeroth-order Bessel function, $k(\omega) = \omega/v(\omega)$ with

$$v(\omega)\ [\,\mathrm{m\ s^{-1}}] \approx 450 + 1900 \exp\left(-\frac{\omega}{4\pi}\right) \tag{11.52}$$

and SI units are used throughout. The quantity $v(\omega)$ may be interpreted as the velocity of ground waves at frequency $f = \omega/(2\pi)$. The correlation function $R(\omega, \Delta s)$ is converted into the two-dimensional power spectrum $P(\omega, k)$ via Fourier transform:

$$P(\omega, k) = 4P(\omega) \times \int_0^\infty (1 - R(\omega, L)) \cos(kL) dL \cdot \tag{11.53}$$

or

$$P(\omega, k) = \begin{cases} \frac{4}{\sqrt{k(\omega)^2 - k^2}} P(\omega) & \text{if} \quad k(\omega) > k \\ 0 & \text{else} \end{cases} . \tag{11.54}$$

Interestingly, the same functional dependence is obtained if the ground motion is modeled by an ensemble of isotropic plane surface waves, for which each frequency is associated with a certain wavelength; longer wavelengths corresponding to lower frequencies [Irwin 1995b].

According to measurements at various locations [Juravlev 1995], a reasonable approximation to $P(\omega)$ for a "quiet" site is

$$P(\omega)[\,\mu\mathrm{m}^2/\mathrm{Hz}] \approx \frac{15.6 \cdot 10^{-3}}{\omega^4}. \tag{11.55}$$

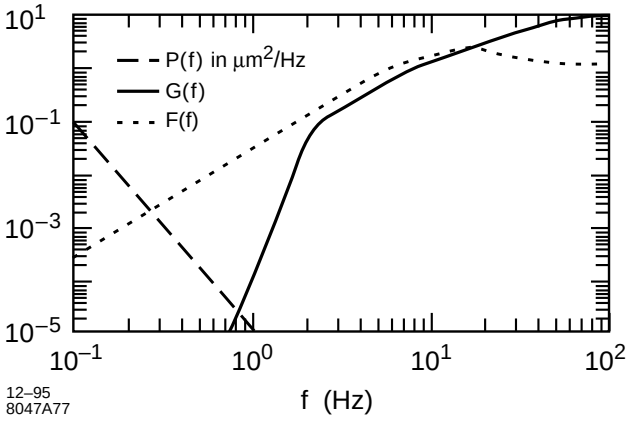

Figure 11-34. *Three functions which determine the rms beam-beam separation due to plane-wave ground motion: $F(f)$ — the feedback response [Hendrickson 1995]; $P(f)$ — the local power density; $G(f) \equiv \tilde{G}(2\pi f)$—defined by Eq. 11.57. The integral over the product of these functions gives the square of the rms beam-beam separation.*

where the angular frequency ω is given in s^{-1}, and only frequencies $\omega > 0$ are considered. The power density $P(\omega)$ decreases rapidly at high frequencies, while at low frequencies the response to ground motion is suppressed by the lattice-response function $G(k)$ in conjunction with the dispersion relation, Eq. (11.54). A further reduction may be achieved by orbit-feedback systems.

The ground-motion spectral density, Eq. (11.54), determines the rms separation $\Delta y_{\rm rms}$ of the two beams at the IP, as caused by the plane-wave ground motion. The rms separation can be written as

$$\Delta y_{\rm rms}^2 = \int_0^\infty \frac{d\omega}{2\pi} \tilde{G}(\omega) P(\omega) F(\omega), \tag{11.56}$$

where $F(\omega)$ denotes the feedback response, $P(\omega)$ is the power density, Eq. (11.55), and $\tilde{G}(\omega)$ represents the lattice response function converted into the frequency domain. It is defined as an integral of the product of $G(k)$ and the k-dependent part of $P(\omega, k)$ over k, *i.e.*,

$$\tilde{G}(\omega) \equiv \int_0^{k(\omega)} G(k) \frac{4}{\sqrt{k(\omega)^2 - k^2}} \frac{1}{2\pi}\, dk \quad . \tag{11.57}$$

The three functions $P(\omega)$, $\tilde{G}(\omega)$, and $F(\omega)$ are illustrated in Figure 11-34. The shape of $\tilde{G}(\omega)$ shows that the effect of ground motion is strongly suppressed by the lattice response. Numerical integration yields a value for the rms beam-beam separation of

$$\Delta y_{\rm rms} \approx 0.2 \text{ nm} \qquad \text{(with feedback)} \tag{11.58}$$

$$\Delta y_{\rm rms} \approx 0.3 \text{ nm} \qquad \text{(without feedback)} \tag{11.59}$$

and, thus, the plane-wave ground motion is insignificant, provided the magnet centers move exactly as the ground beneath them. If plane-wave ground motion were the only source of orbit-perturbation, no orbit-feedback would be needed at a quiet site. Above 6 Hz, the power spectrum of the SLAC measurements is considerably larger than that of Eq. (11.55), due to resonances of the linac support structures and also due to cultural noise. Assuming the SLAC power spectrum, one finds an expected rms beam-beam separation of about 1.1–1.3 nm, which still seems acceptable, but which is considerably larger than the 0.3 nm for a quiet site.

Some authors have argued that at low frequencies a component of ground motion exists which cannot be cast into the above framework, and which is of pure random character [Juravlev 1995]. They characterize this part of the ground motion by a so-called ATL law, according to which the change of the average squared relative displacement of two points is proportional to the distance between the points and to time. (An entirely different interpretation of ground motion as a systematic process was suggested by R. Pitthan [Pitthan 1995].) The two-dimensional spectral density describing the ATL law can be written

$$P_{ATL}(\omega, k) = \frac{4A}{\omega^2 k^2} \tag{11.60}$$

where $k > 0, \omega > 0$ is assumed, and $A \approx 10^{-8}$–10^{-5} μm^2 s^{-1} m^{-1} depending on location and on relevant timescale. The SLAC measurements over a timescale of seconds indicate $A < 6 \times 10^{-7}$ μm^2 s^{-1} m^{-1}.

Folding in the feedback response function, it is possible to determine the rms beam-beam separation due to ATL-like ground motion in the frequency range 0–0.01 Hz, where the ATL law might be applicable. For $A = 10^{-6}$ μm^2 m^{-1} s^{-1}, this rms separation is found to be 15 pm. Assuming as a worst case, that the size of uncorrelated motion is equal to the noise floor of the STS seismometer, the rms separation in the frequency range of 0.01–6 Hz is estimated to be no larger than 242 pm, and the contribution from frequencies above 6 Hz is about 124 pm at a quiet site. In total then, the rms separation from uncorrelated ATL-like ground motion does not exceed 0.3 nm, and the entire separation due to all ground motion (ATL-like and plane-wave motion) at a quiet site is about 0.4 nm, which would result in a luminosity loss of only 0.1%. The conclusion is that one can use the ground (bedrock) as a reference for stabilization.

Thus, magnet supports need to be designed which neither amplify nor damp the ground motion, but couple the magnet firmly to the ground. As discussed previously, the tightest tolerances on uncorrelated quadrupole-to-ground vibration above 5 Hz (vibration at lower frequency is compensated by the orbit feedback) are 1 nm (rms) for the final doublet and 3–4 nm for a few other quadrupoles (Table 11-19). These tolerances correspond to a total luminosity loss of about 2%. At DESY (SBLC-TF), relative rms vibrations above 1 Hz were measured to be smaller than 1 nm, which would meet all the NLC tolerances. Quadrupoles at the FFTB were found to vibrate by about 4 nm with respect to the ground, excited mainly by bad cooling pumps. These vibration amplitudes would still satisfy the tolerance criteria for all NLC magnets other than the final doublet. For the latter a special stabilization system based on an optical anchor and piezo-electric movers has been devised, which is described in Chapter 12.

Capture Tolerances and Tuning Frequency

The magnet pre-alignment tolerances required to steer the first beam through the final focus onto the dump will be loose. They are essentially determined by the magnet-mover ranges. A pre-alignment with an accuracy of 500 μm is expected to be sufficient. This is easily achieved by standard alignment techniques, which provide a typical accuracy of 100–200 μm. Once the beam reaches the NLC main dump, the actual alignment is performed using beam-based techniques, similar to those employed at the SLC or FFTB [Emma 1992, Raimondi 1993, Tenenbaum 1995].

More interesting is the question how often the beam-based alignment has to be performed, and how accurate it should be. The answer to this depends on the maximum range of the tuning elements, and on the IP spot-size increase due to ground motion. The recent progress in understanding ground motion (see previous section and Appendix C), and new work on tuning schemes shed light on this problem. A related question refers to the required frequency of aberration tuning and whether it is acceptable.

In complete analogy to the steering effect of ground motion, lattice-response functions may be defined for vertical dispersion and skew coupling, in an obvious way. The only difference is that, in this case, the two final foci on either side of the IP are treated independently. More precisely, the lattice-response functions are of the form

$$G_\delta(k) = \sum_{i,j} \mu_i^\delta \mu_j^\delta \cos(k \Delta s_{ij}) \tag{11.61}$$

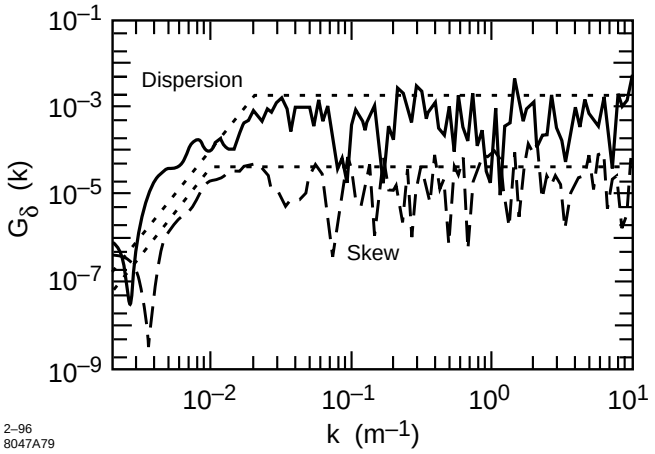

Figure 11-35. *Lattice response functions for vertical dispersion and skew coupling. Dotted lines represent approximations which are employed in the later analysis.*

where the subindices i, j run over only one side of the IP only, and the multipliers $\mu^{\delta}_{i,j}$ characterize the IP spot-size increase due to a displacement of quadrupole (or sextupole) i. The term Δs_{ij} denotes, as before, the distance between the two magnets i and j. The lattice response functions for dispersion and skew coupling are depicted in Figure 11-35, along with simple approximations which are used in the following studies. If the wavelengths are small, *i.e.*, at large k, the response is about constant, since the magnets move incoherently. For small k, the lattice response is strongly suppressed and decreases as the 4th power of k. As for the steering effect discussed earlier, this suppression represents the invariance of the luminosity with regard to displacements and tilts of the entire beam line. Unlike the steering, however, there is no cancellation between the two sides of the IP or between paired $-I$ modules, and this is the reason why the response here decreases as the 4th power of k, instead of k^6.

The spot-size increase due to ATL ground motion as a function of time T is described by the equation

$$< \Delta\sigma_y(T)^2 >= 2 \int_{-\infty}^{\infty} \frac{d\omega}{2\pi} \int_{-\infty}^{\infty} \frac{dk}{2\pi} G_\delta(k) P_{ATL}(\omega, k)(1 - \cos(\omega T)) \tag{11.62}$$

where $G_\delta(k)$ denotes the lattice-response function for dispersion or skew coupling (Figure 11-35). Figure 11-36 presents the increase of the spot size due to dispersion as a function of time, for three different magnitudes of ATL-type ground motion.

Even though this figure does not assume any orbit stabilization other than a beam-centroid correction at the IP, there would still be several minutes time to correct the dispersion. In reality, feedback systems which stabilize the orbit will reduce the generated dispersion. If the frequency-response curve of a typical SLC-style orbit feedback is included in the calculation, an ATL coefficient $A = 10^{-6}$ μm^2 m^{-1} s^{-1} is assumed, and the product spectrum is integrated over frequencies below 0.01 Hz, the spot size is found to reach a maximum value after about 100s and then to stay constant. The spot-size increase at that moment is less than a picometer, to be added in quadrature. Thus the effect of ATL-like ground motion on the IP spot size appears to be insignificant, assuming the orbit is stabilized by a typical SLC-style feedback system. The frequency at which the different aberrations need to be tuned, in order to keep the average luminosity loss per aberration below 1–2%, is thus not determined by the ground motion, but by the stability of the feedback BPMs. If the BPM stability were the same as measured in the FFTB, the aberrations would have to be tuned less than once per hour. Since the NLC BPMs will be located underground, and temperature and humidity much better controlled, the BPM stability is expected to surpass that in the FFTB.

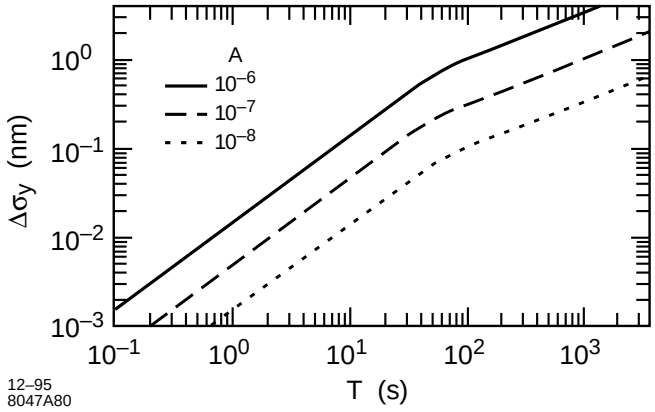

Figure 11-36. *Incoherent spot-size increase due to vertical dispersion, caused by ATL ground motion, as a function of time, for three different values of A (in units of μm^2 s^{-1} m^{-1}), and assuming $\delta \approx 3 \times 10^{-3}$.*

Collimator Tolerances

As a supplement to the two-phase collimation section upstream of the big bend, a last collimation of the final-doublet betatron phase is performed in the final focus itself. Its purpose is to reduce the number of electrons which may hit the final doublet to below ten, so that the detector background remains acceptable. The final-focus collimators remove the beam halo which is newly generated by gas scattering, bremsstrahlung and inverse Compton scattering downstream of the collimation section and by edge scattering in the IP-phase collimation. The ideal position for final-focus collimators are the high-beta points in CCX and CCY. Therefore, the two horizontal and two vertical collimators will be located close to the main horizontal and vertical sextupoles, respectively.

In addition to these four tungsten collimators, the final focus accommodates almost 200 wide-aperture titanium spoilers. These are placed upstream of each quadrupole and each dipole section, and protect the magnets against damage by a missteered beam.

Collimators do not only improve the background, but, as SLC experiments have demonstrated [Bane 1995], they can also adversely affect the beam quality by generating resistive-wall and geometric wakefields. To reduce the geometric wake, most or all of the NLC collimators will be tapered at a shallow angle, as discussed in Chapter 9, Adjustable collimators are usually flat and consist of two jaws (top and bottom, or left and right). Protection collimators are round.

Specifically, there are four main effects of collimators:

- If the incoming beam executes a betatron oscillation, the collimator wakes will cause an amplification of the oscillation in the orthogonal betatron phase. This effect is called jitter amplification, and occurs even when the collimators are perfectly aligned. If the collimator is located in the final-doublet phase, the position change at the IP Δy caused by the collimator is

$$\frac{\Delta y}{\sigma_y^*} = \xi \frac{y'}{\sigma_{y'}} \tag{11.63}$$

  for an initial betatron oscillation of size y', where all coordinates and rms values refer to the IP. The coefficient ξ is the relative jitter amplification, and is expressed in terms of collimator and beam parameters as

$$\xi \equiv \frac{\beta_y^{\rm coll} 2Nr_e}{\gamma\sigma_z}\left[\left(8 < f_r >< g_r > \frac{(b^2-g^2)(b-g)}{b^3}\right)^{\frac{1}{2}}\left(\frac{\lambda\sigma_z}{g^6}\right)^{\frac{1}{4}} + \frac{L}{g^3} < f_r > \sqrt{\lambda\sigma_z}\right] \tag{11.64}$$

where $< f_r > \approx 0.3$, $< g_r > \approx 0.82$, g is the half-aperture, b the beam-pipe radius, $\lambda = \rho/(120\pi)$ (ρ resistivity in Ωm), and L the length of the flat part of the collimator.

- In addition to jitter amplification, there is also an emittance growth arising from the variation of the wakefield kick across the bunch. Typically, this effect is smaller than the former.
- If the collimator jaws (of a flat collimator) are misaligned with respect to the center of the beam, they will also cause emittance growth, even if the incoming orbit is unperturbed. This emittance growth gives rise to an alignment tolerance. For a spot size increase by 2% or less the alignment tolerance of a single collimator is

$$\Delta y \approx \frac{\sigma_y^{\rm coll}}{4.5\,\xi} \quad . \tag{11.65}$$

- Finally, even if a flat collimator is perfectly aligned, and the beam unperturbed, the collimator still delivers a quadrupole wake-field to the beam, changing the focusing of particles in the bunch-tail halo and causing an emittance dilution. The magnitude of the quadrupole wakefield kick from a flat collimator is about a third of that of the dipole wake. Thus, for an expected orbit jitter larger than 0.5 σ_y, the quadrupole effect is small compared with the dipole kick.

The main horizontal and vertical final-focus collimators are located at the high beta points in CCX and CCY, respectively, where $\beta_x \approx 70$ km or $\beta_y \approx 200$ km. If we assume $N = 10^{10}$ particles per bunch, and $\sigma_z = 100\,\mu$m, the jitter amplification ξ for a 7-cm-long (about 20 r.l.) W collimator, and collimation at 17 σ_x or 43 σ_y, is 0.06 (0.01) in $y(x)$. The vertical alignment tolerance, Eq. (11.65), for a 2% spot-size increase caused by the two vertical collimators is 1.6 mm; the horizontal alignment tolerance for the CCX collimators is even larger. Thus, the required alignment accuracy will not be determined by emittance growth, but by the collimation efficiency. The latter probably demands that the vertical collimators are aligned to within 150 μm ($1\sigma_y$).

Temperature

The tolerances on position and field strength translate into tolerances on the temperature stability of magnets and magnet supports. The tolerances on medium-term stability are considerably relieved by the existence of an orbit stabilization system (*i.e.,* feedback) which corrects orbit distortions resulting from quadrupole drifts, bend-field changes and bend rolls.

In the FFTB, quadrupole motion due to temperature variation was measured to be smaller than 100 nm/h. This stability is an order of magnitude better than what is needed for the NLC.

Vacuum

The required vacuum pressure is determined by the tolerable background in the detector. The following discussion shows that the largest contributions to the vacuum-related background are due to bremsstrahlung. At an average pressure of 10 nTorr, less than 10 particles per bunch train will hit apertures in the final-doublet region. The background from these particles needs to be compared with that expected from synchrotron radiation generated in the bending and quadrupole magnets, and with that caused by beamstrahlung and pair-creation at the IP.

Coulomb Scattering. If an electron undergoes hard Coulomb scattering on a residual-gas nucleus, it may hit the pole faces or inner beam pipe of the final doublet. Following Irwin (Chapter 9), the relative number of scattered

particles hitting the doublet is given by

$$\frac{\Delta N}{N} = 2\pi\rho\left(\frac{r_e}{\gamma a_D}\right)^2\left(\sum_i Z_i^2\right)\left[\int_{SX1b}^{QFTA} ds\ R_{12}^2(s) + \int_{SX2b}^{QFTA} ds\ R_{34}^2(s)\right] \tag{11.66}$$

where $R_{12}(s)$ and $R_{34}(s)$ denote the R-matrix elements from point s to the entrance face of QFTA, r_e the classical electron radius, and a_D the inner radius of QFTA (assumed as 5 mm). The integrations are performed between the last sextupole in CCX and CCY, respectively,—these are the collimator positions—and QFTA. The sum over i runs over the different atoms of a molecule, and $\rho \approx 3.2 \times 10^{13}\mathrm{m}^{-3}p/$ nTorr is the molecule density. Evaluation yields

$$\left[\int_{SX1b}^{QFTA} ds\ R_{12}^2(s) + \int_{SX2b}^{QFTA} ds\ R_{34}^2(s)\right] \approx 7 \times 10^6\ \mathrm{m}^3. \tag{11.67}$$

Assuming carbon monoxide molecules and a beam energy of 500 GeV, we find

$$\frac{\Delta N}{N} \approx 4 \times 10^{-14}\frac{p}{\mathrm{nTorr}} \quad . \tag{11.68}$$

If we allow 10 electrons in each bunch train of 6×10^{11} particles to hit the doublet in the absence of final-focus collimators, a pressure of 400 nTorr is sufficient. The collimators in the final-focus system will intercept most of the scattered particles.

Bremsstrahlung. An electron may also get lost due to bremsstrahlung in the field of a nucleus. The cross section for an energy loss between ΔE_1 and ΔE_2 is [Piwinski 1985]

$$\sigma_{\mathrm{brems}} \approx \sum_i \frac{4r_E^2 Z_i^2}{137}\frac{4}{3}\ln\left(\frac{\Delta E_2}{\Delta E_1}\right)\ln\left(\frac{183}{Z_i^{\frac{1}{3}}}\right) \quad . \tag{11.69}$$

For CO molecules and an energy loss between 6% and 25%, we find $\sigma_{\mathrm{brems}} \approx 2$ barn. The fraction of particles suffering this energy loss is given by

$$\frac{\Delta N}{N} = \rho L \sigma_{\mathrm{brems}} \approx 6.4 \times 10^{-12}\frac{p}{\mathrm{nTorr}} \tag{11.70}$$

where $L \approx 1000$ m. In order that less than 10 particles per train lose 6–25% of their energy, we need to achieve a pressure of 4 nTorr. This value is two orders of magnitude smaller than that calculated before for particle loss due to hard Coulomb scattering. However, a large fraction of the electrons lost by bremsstrahlung do not hit the final-doublet apertures and will not contribute to the detector background. As a conservative estimate, we assume a pressure of 10 nTorr to be sufficient.

Inelastic Scattering. For simplicity, let us confine ourselves to hydrogen molecules, *i.e.*, we consider electron-proton collisions. In this case, using the Weizsäcker-Williams approximation, the differential cross section for leptoproduction $d\sigma_{ep}/dy$ reads [ZEUS/H1]

$$\frac{d\sigma_{ep}}{dy} = \sigma_{tot}^{\gamma p}(W_{\gamma p})\frac{\alpha}{2\pi}\frac{1+(1-y)^2}{y}\ln\frac{Q^2_{\max}}{Q^2_{\min}} \tag{11.71}$$

where $y \equiv 1 - E'/E$ is the photon energy in units of the incident electron energy. Approximating $\sigma_{tot}^{\gamma p} \approx 150\ \mu$barn, $Q^2_{\max} \approx 4E^2$, $Q^2_{min} = (m_e c^2 y)^2/(1-y)$, and integrating over photon energies from 500 keV to 250 GeV, we derive an upper bound for the relevant total cross section:

$$\sigma_{ep} \leq 180\ \mu\mathrm{barn} \quad . \tag{11.72}$$

Over a distance l of 100 m, the fraction of electrons undergoing inelastic reactions with the residual gas is then

$$\frac{\Delta N}{N} \approx \sigma_{ep} l \rho \leq 6 \times 10^{-17} \frac{p}{\text{nTorr}} \tag{11.73}$$

or $\Delta N \leq 0.003$ per bunch train for a pressure of 100 nTorr—a very small number.

Other Sources of Background

Inverse Compton Scattering. Electrons (or positrons) do not only scatter off residual-gas atoms, but can also suffer inverse Compton scattering on thermal radiation photons. The latter effect can limit the beam lifetime in high-energy electron storage rings [Telnov 1987], and it has been measured at LEP [Bini 1991] and at HERA [Lomperski 1993]. In this section, we estimate its importance for the NLC final-focus system.

The density of thermal photons increases as the third power of the temperature. For a temperature of 300 K, it is about

$$n_\gamma \approx 5 \times 10^{14}\ \text{m}^{-3}, \tag{11.74}$$

and thus equal to the density of residual-gas atoms at a pressure of 17 nTorr. The total Compton cross section can be expressed in terms of the dimensionless parameter x [Telnov 1987].

$$x \equiv \frac{4 E \omega_0}{m_e^2 c^4} \cos^2 \frac{\alpha_0}{2}, \tag{11.75}$$

where α_0 denotes the angle at which photons and electrons collide in the laboratory frame ($\alpha_0 = 0$ means head-on collision), E the beam energy, and ω_0 the photon energy. Assuming 500 GeV beam energy, an average photon energy of $\bar{\omega}_0 = 0.07$ eV and $\alpha_0 = 0$, we find $x \approx 0.56$, and a total Compton cross section not much different from the Thomson cross section $\sigma_t \approx 0.7$ barn. This cross section is an order of magnitude smaller than that for beam loss due to bremsstrahlung on residual-gas nuclei. However, the maximum energy loss of a Compton-scattered electron is quite large,

$$\left.\frac{\Delta E}{E}\right|_{\max} = \frac{x}{1+x} \approx 36\%, \tag{11.76}$$

which implies that almost all scattered electrons are lost so rapidly, that they do not make it to the final doublet. The total number of particles lost per bunch train is estimated as

$$\Delta N \approx \sigma_T L n_\gamma N \approx 36. \tag{11.77}$$

Here $N \approx 6 \times 10^{11}$ is the number of particles in the bunch train, and $L \approx 2000$ m the length of the final-focus system. The number of electrons suffering inverse Compton scattering on thermal photons is at least comparable to, if not larger than those lost due to bremsstrahlung or Coulomb scattering off the residual gas.

Touschek Effect. The scattering of two particles inside the same bunch off each other may lead to a particle loss due to the introduced change of longitudinal momentum. This effect limits the beam lifetime in many electron storage rings. It was first observed at AdA, in 1963 [Bernadini 1963].

The number of electrons scattered to energies larger than $\eta \equiv \left(\frac{\Delta E}{E}\right)_{\max}$ is given by [Walker 1987]

$$\Delta N = \frac{r_e^2 n_b N_b^2 L}{\gamma^2 \left.\frac{\Delta E}{E}\right|_{\max} 2\pi^{\frac{1}{2}} \sigma_x \sigma_y \sigma_z} J(\eta, \delta q) \quad . \tag{11.78}$$

Here, δq denotes the rms transverse momentum in units of $m_e c$, r_e the classical electron radius, n_b the number of bunches, N_b the number of particles per bunch, and L the length of the beam line considered. The loss rate is proportional to the second power of N_b, and inversely proportional to the square of the energy and to the beam size. An approximation to the function $J(\eta, \delta q)$ for $\delta q/\eta \geq 100$ is given in Eq. (7) of ref. [Walker 1987]. For the parameters of interest here, J is nearly equal to 1.

In the NLC final focus at 500-GeV-c.m. energy, transverse beam size and transverse momentum are $< \delta q >= 6.4\ \mu\text{rad}\times\gamma \approx 3.2$ and $< \sigma_x\sigma_y > \approx 148\ \mu\text{m}^2$. Assuming $N_b \approx 8.5 \times 10^9$ and $n_b = 90$, the number of scattered particles per bunch train is:

$$\Delta N \approx 2 \text{ for } \Delta E/E \geq 0.5\%, \qquad \text{and} \qquad \Delta N \approx 0.1 \text{ for } \Delta E/E \geq 2\% \tag{11.79}$$

This is a rather small effect.

11.5.6 Feedback and Stability

Overview of Feedback Systems

Several orbit feedback systems are envisioned to stabilize the beam orbit throughout the beam delivery system. In addition to feedbacks in the collimation section, the big bend, and the diagnostics section, there will be a "launch" feedback correcting the orbit in the beta-match section and CCX, and a feedback controlling the CCY and FT orbit. Each feedback system will use orbit readings from at least four BPMs to correct the orbit by moving quadrupoles of by adjusting dipole correctors. The CCY- and FT-orbit feedback, which is the most important of these feedback loops, is discussed in the next section.

A fast IP collision feedback is essential for correcting beam position and preserving collisions at the IP. This feedback will be very similar to the IP feedback at the SLC, which uses fast dither coils to maintain head-on collisions. The required dither changes are deduced from the measured beam-beam kick angle and the slope of the beam-beam deflection curve. The main difference to the SLC is that, because of the smallness of the required corrector strengths, the NLC feedback will use electrostatic vertical dither coils rather than magnetic. In addition, it may be possible to use a device similar to the crab cavity for compensating orbit changes along the bunch train, should that be desired.

Regarding control of emittance or spot size, a slow automatic skew-correction feedback is being contemplated, which may be based on DS wire scans and SCS skew correctors. Such a feedback will only be necessary if there are significant changes to the incoming x-y coupling over a few hours, and it would be straightforward to implement.

CCY and FT Orbit Feedback

The IP beam size is extremely sensitive to orbit variations which originate within the final focus. For example, a vertical displacement of QFT3 (see location on Figure 11-37; note that the design and the magnet names have changed since this was written and drawn!) by 44 nm kicks the vertical orbit in QFT1 by ∼200 nm which, for 0.3% rms energy spread, generates enough vertical dispersion at the IP to increase the beam size by 2%. A similar effect occurs for quadrupole displacements within the CCY where the orbit is steered off in the second CCY sextupole (SY1B). For these reasons it will be important to monitor and correct local orbit variations in the CCY and FT to a very high precision. The following describes a conceptual monitor and feedback system for CCY and FT local orbit distortions. Throughout, it is assumed that the IP beam-beam steering errors introduced by these orbit variations are corrected with a much faster (∼30 pulse) IP collision feedback which is not addressed here.

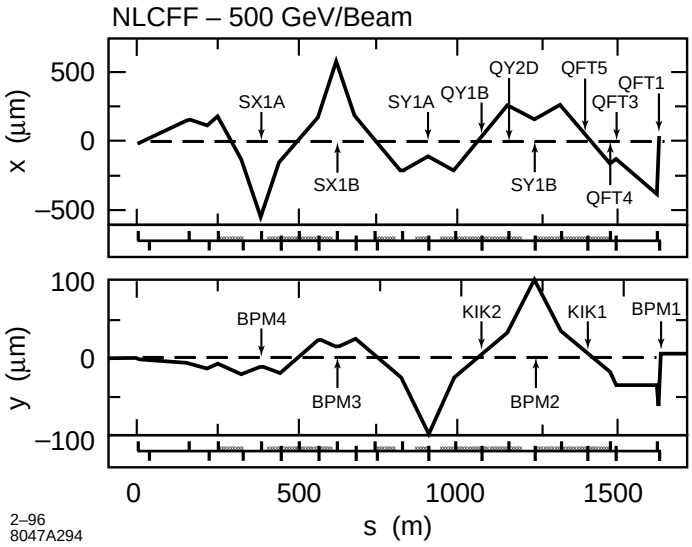

Figure 11-37. *Horizontal and vertical one-sigma IP angle betatron oscillation through the final focus (i.e., at the IP:* $\Delta x = 0$, $\Delta y = 0$, $\Delta x' = \sigma'_x$, $\Delta y' = \sigma'_y$*).*

The vertical beam size at the final doublet is quite large in comparison to the required orbit monitoring precision (60 μm compared with 200 nm). Therefore, local orbit distortion monitoring will be made in the presence of a large background signal of incoming trajectory jitter—which has much less impact on the IP beam size. The feedback system must suppress this incoming jitter signal reliably so that non-jitter related y-BPM reading variations of $\sim$200 nm are discernible. In order to accomplish this the feedback system must monitor BPMs in the CCX, CCY and FT. In the simplest case, two BPMs are placed in the CCX—each one adjacent to an SX1 sextupole (SX1A and SX1B)—in order to monitor both betatron and energy jitter (BPM-4 and BPM-3). A third BPM is placed in the CCY adjacent to the SY1B sextupole (BPM-2) to monitor CCY induced orbit changes, and a fourth BPM is placed just upstream of QFT1 (BPM-1) to monitor FT induced orbit changes. More BPMs may be added for redundancy.

A simplifying characteristic of the final focus is that only the IP angle betatron phase is visible with BPMs throughout the CCX, CCY and FT—a one-sigma IP angle oscillation generates a 60-μm BPM-1 reading while a one-sigma IP position oscillation generates a $\sim$3-nm BPM-1 reading. Figure 11-37 shows a one-sigma betatron oscillation at the IP angle phase in x and y, while Figure 11-38 shows a one-sigma oscillation at the IP position phase. The invisibility of the IP position betatron oscillation is clearly demonstrated.

For this reason each BPM reading can be broken down into a component of incoming IP angle jitter, energy jitter (for horizontal plane or vertical dispersion error), a CCY orbit kick, an FT orbit kick and a static offset. All other sources of BPM reading variations need to be $<$200 nm (BPM-1) over the scale of a few hours (time between re-tuning). A simple algorithm can then be devised where the four (or more) BPMs are used in a linear combination to determine the CCY- and FT-induced orbit changes so that corrections may be applied in both the CCY and the FT. The linear combination is determined by using the normal trajectory jitter to calibrate the BPM to BPM coefficients (assuming local orbit distortions are constant over the $\sim$200 pulses necessary for calibration). Each ith BPM is then fitted to the form

$$y_i(j) = \eta_i \cdot \delta(j) + \alpha_i \cdot y_\beta(j) + c_i \quad , \tag{11.80}$$

where $\delta(j)$ is the fractional energy deviation of the jth pulse, y_β is the incoming betatron amplitude (proportional to IP angle), and the three coefficients, α_i, η_i and c_i are the fit results. The energy deviation and betatron amplitude can then, given their $-I_{4\times4}$ transfer matrix separation, be conveniently parameterized as follows (actually any linear

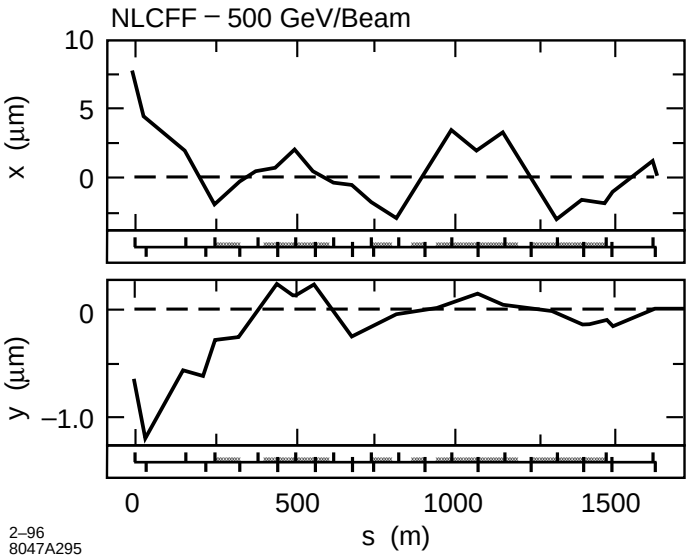

Figure 11-38. *Horizontal and vertical one-sigma IP position betatron oscillation through the final focus (i.e., at the IP:* $\Delta x = \sigma_x$, $\Delta y = \sigma_y$, $\Delta x' = 0$, $\Delta y' = 0$*).*

combination will suffice),

$$\delta(j) \equiv \frac{y_4(j) + y_3(j)}{R_{16}} \quad , y_\beta(j) \equiv \frac{y_4(j) - y_3(j)}{2} \quad . \tag{11.81}$$

where R_{16} ($\sim$150 mm) is a linear transfer matrix element between BPM-4 and 3.

This calibration is then performed after each IP re-tune. After a time necessary to generate local orbit distortions (must not be less than $\sim$10 seconds) a calculation is made using $\sim$200 more pulses and the same coefficients.

$$\begin{bmatrix} y_4 - c_4 \\ y_3 - c_3 \\ y_2 - c_2 \\ y_1 - c_1 \end{bmatrix} = \begin{bmatrix} \eta_4 & \alpha_4 & 0 & 0 \\ \eta_3 & \alpha_3 & 0 & 0 \\ \eta_2 & \alpha_2 & 1 & 0 \\ \eta_1 & \alpha_1 & \alpha_1/\alpha_2 & 1 \end{bmatrix} \cdot \begin{bmatrix} \delta \\ y_\beta \\ \Delta y_2 \\ \Delta y_1 \end{bmatrix} \tag{11.82}$$

Here the previously determined coefficients—assumed constant over the hour timescale—make up the matrix and the critical orbit distortion results, Δ_{y2} and Δ_{y1}, represent the local orbit distortions at BPM-2 (the second CCY sextupole SY1) and BPM-1 (the last quadrupole QFT1). This treatment assumes that all local orbit distortions are along the IP angle phase. This is generally true for the quadrupoles with the tightest tolerances (see Table 11-14). Corrections are then applied in order to maintain the CCY and FT orbit with respect to the incoming orbit. This is the only point in the algorithm where some knowledge of short sections of the optics is required. Static optical errors and BPM gain errors have been removed in the calibration process.

Simple simulations of this feedback have been run which include random BPM noise, IP position and angle jitter, energy jitter, BPM gain errors, BPM non-linearities and BPM offsets. Table 11-22 summarizes the simulation conditions.

For the simulation, two CCY quadrupoles and two FT quadrupoles (QY1B, QY2D, QFT4 and QFT3) were each displaced by 1 μm which, for QFT3, is >20 times tolerance. In the case of adjacent and opposite strength quadrupoles such as QFT3 and QFT4 the misalignments chosen were the worst case combination (*i.e.,* QFT3 $\Delta_{x,y} = +1\,\mu$m and

Number of pulses (cal. & cor.)	IP pos. rms jitter ($\sigma^*_{x,y}$)	IP ang. rms jitter ($\sigma^*_{x',y'}$)	Energy rms jitter (σ_δ)	BPM rms noise (μm)	BPM rms gain errors (%)	BPM non-linearity (% at 1 mm)	BPM rms offsets (μm)
200	0.5	0.5	0.25	1	5	2	250

Table 11-22. *Simulation conditions for CCY and FT local orbit distortion feedback system. With these conditions the feedback simulation successfully restored the IP beam size to within 2% for two CCY and two FT quadrupoles drifting 5 times their tolerance in x and y.*

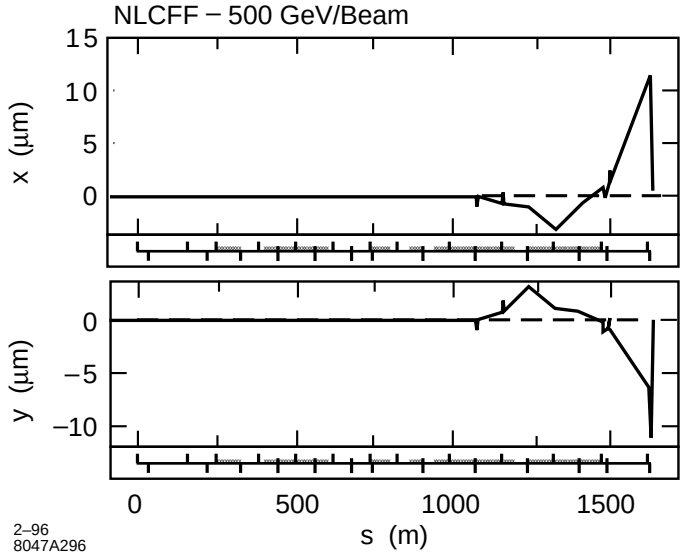

Figure 11-39. *Horizontal and vertical orbit through final focus after 1-μm alignment drift of four quadrupoles (before feedback correction). The luminosity is degraded by a factor of 10.*

QFT4 $\Delta_{x,y} = -1\,\mu$m). These sudden, uncompensated misalignments dramatically reduce the luminosity by a factor of ∼10 (assuming this drift occurs in only one of the two final-focus beam lines). In this case the vertical IP beam size increases to ∼13 times larger than nominal (2.5 nm) while the horizontal is only 6% larger. For the simulation, correctors were placed with one x and y pair (KIK2) at QY1B and one pair (KIK1) at QFT5 (each $\sim n\pi$ from the IP). Only one correction interval was applied (*i.e.*, no iterations were allowed). For these conditions the feedback successfully restored the luminosity to within 1% of nominal. Since there are only two correctors per plane and four misaligned quadrupoles the orbit is not everywhere restored. It is restored primarily at QFT1 (BPM-1) and SY1B (BPM-2) which, for this drift magnitude, is adequate. Figure 11-39 shows the difference orbit through the final focus, including the effect of the four displaced quadrupoles, before feedback correction is applied. Figure 11-40 shows the orbit after feedback correction. The horizontal feedback for this case is hardly necessary. However, further simulations have shown the horizontal feedback to work well at scales of up to ∼10 times the horizontal drift tolerances for these quadrupoles (10–30 μm).

The corrector strengths here are too small to be reliably applied by a simple dipole magnet (∼0.2 Gauss for a 10-cm length dipole). However, at this timescale (>10 seconds) a quadrupole mover could be used. In this case a 19-μm and 1.4-μm vertical displacement of QFT5 and QY1B, respectively will provide the necessary correction.

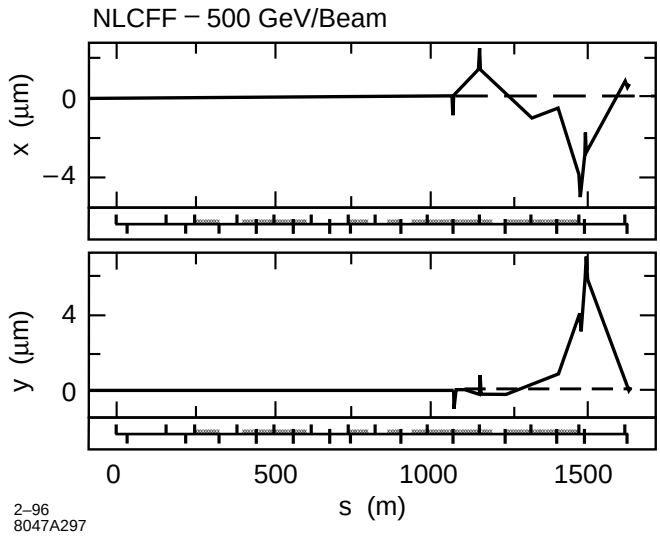

Figure 11-40. *Orbit through final focus after feedback correction. The feedback primarily restores the orbit at the final doublet and second y-sextupole. With more drifted quadrupoles than correctors, some orbit errors remain. The luminosity is restored to within 1% of nominal.*

Note that a BPM with 1-μm rms random noise was used successfully in this case. However, BPM offsets need to remain constant to $<$200-nm drift over a few hours which is probably the most challenging requirement and may be somewhat inconsistent with a 1-μm resolution BPM.

If high-resolution rf BPMs are required (a few nanometers), the dynamic range of these BPMs is limited, so that, in order to determine and correct magnet motion in the final focus, their readbacks must be averaged over a subset of orbits for which the incoming orbit jitter is small.

For these studies we have chosen to place only one corrector (per plane) in the CCY and one in the FT. It may also be possible to use more correctors so that the corrections are more closely associated with their original kick. This scheme probably allows a wider correction range, however it places much more stringent requirements on BPM resolution requirements in order that individual quadrupole drifts become measurably separable. This possibility has not been studied.

Finally, the linearity of the final-focus optics over both energy and betatron variations has been verified to be adequate (*i.e.,* $<$200-nm orbit change at BPM-1) over energy deviations of up to $\pm$0.25% and betatron oscillations more than twice the beam size. Therefore, if sampled orbit data is cut at $\pm$0.1% in energy deviation and $\pm$1-sigma in betatron jitter, the optics is completely linear.

The feedback system explored here looks promising. In the limited conditions simulated here the extraordinarily tight alignment drift tolerances in the final transformer can be greatly loosened with a local orbit feedback system by more than a factor of 20 which sets the quadrupole drift scale tolerances at the more livable level of 1 μm rather than 50 nm. Some of the important remaining issues not addressed here are summarized below.

- BPM offsets and gains need to be stable to $<$200 nm over a few hours.
- Tails in the beam distribution must not introduce a systematic position error.
- Optics need to be stable enough over a few hours (can be measured).

- BPMs must be insensitive to particle backgrounds.

11.5.7 Operations and Controls

Control System and Software

In general, the NLC control system will be based on the SLC experience and will adopt many grown features of the SLC control system. In certain aspects, however, it needs to surpass the SLC control system. Three features are particularly desirable: The control system has to be

- flexible, *i.e.,* accommodate to any unforeseen or changing demands,
- easy to modify and to augment, *i.e.,* allow accelerator physicists and operators to write applications themselves on the fly, and
- fast, *i.e.,* contain the luminosity loss due to tuning, magnet trimming, etc.

The last item is very important. As an illustration, let us consider the time required for scanning an aberration: if we only count a minimum number of 50 pulses per beam-beam deflection scan and take a settle time of 200 ms equal to four magnet time constants for each magnet trimming, we find that a seven-step aberration scan can be performed in less than 5 s. Since during an aberration scan the luminosity is close to zero, a tuning time of 5 s results in an average luminosity loss of 1.0%, assuming 10 scans per hour. To contain the luminosity loss, the processing time of the control system during a scan should be shorter than the 5-s time needed for tuning and steering. At the SLC, a tuning scan presently takes about a minute, which is almost entirely devoted to processing by the control system. The NLC control system needs to allow for a much faster tuning speed; if necessary this can be accomplished by postponing any analysis or data processing to after the aberration scan is completed and the tuning quadrupoles or sextupoles have been reset to their nominal value.

11.5.8 Components

Main Magnets

The skew correction, diagnostic and geometry sections contain 31 normal and four skew quadrupoles. Parameters are listed in Tables 11-23 and 11-28, respectively, along with power-supply ripple, vibration, and slow drift (stability) tolerances. BMS, CCX, BX, CCY, and FT comprise 40 normal quadrupoles, whose parameters are listed in Table 11-24, and the four quadrupoles of the final doublet, in Table 11-25. Field-stability sensitivities for these magnets are graphically displayed in Figure 11-22, vibration sensitivities in Figures 11-23 and 11-24, stability (or position-drift) sensitivities in Figures 11-25 and 11-26, and, finally, roll sensitivities in Figure 11-27.

Most of the quadrupoles are 0.5-m-long, and their pole-tip field is 3–7 kGauss at 1 TeV, for a typical half-aperture of 10.5 mm. Four quadrupoles in the CCX need a larger half-aperture of 19.5 mm to ensure sufficient beam stay-clear. The largest field gradients are those in the final doublet. Assuming that the half-aperture of the four final-doublet quadrupoles decreases from 11 to 5 mm (Figure 11-14), the required pole-tip fields are about 11 kGauss for the first two, conventional quadrupoles, 34 kGauss for the superconducting magnet QFT1, and 13.5 kGauss for the last quadrupole, QFTA, which is a permanent magnet (see also Section 11.6 and Chapter 12).

At least seven sextupole magnets are foreseen for correcting the horizontal and vertical chromaticity and for increasing the momentum bandwidth of the system. Parameters are given in Table 11-26. The main-sextupole vibration sensitivities are depicted in Figures 11-28 and 11-29. Note that the tolerances for the Brinkmann-sextupoles are extremely loose. The main CCX sextupoles SX1 and SX1b need reversible power supplies, since they will be used to minimize the vertical or horizontal spot size at the pre-image point during initial tune up.

More than half of the final focus is occupied by bending magnets (Table 11-27). Field-stability and roll sensitivities for 7–16-m-long sections of bending magnets are shown in Figures 11-30 and 11-31, respectively. The field-ripple sensitivities appear fairly tight for most of them. However, these ripple sensitivities correspond to jitter tolerances, which have to be met only over a time period of about 1 s, since thereafter orbit-stabilization feedbacks will correct the steering errors.

All sextupoles, quadrupoles, and dipole sections are installed on remotely controlled movers and fed by independent power supplies to facilitate beam-based alignment, orbit feedback and tuning.

Steering and Tuning Elements

All magnets in the final focus are mounted on remotely-controlled movers, which is exploited for beam-based alignment, for orbit stabilization (feedback), and for steering and tuning procedures. Regardless, there is still need for certain special correction elements: one additional skew quadrupole upstream of the final doublet will be used for correcting the residual y–x' coupling at the IP. Two normal and two skew sextupoles in the final transformer allow complete control over those second-order geometric aberrations which affect the vertical spot size. In addition, four small movable tuning sextupoles are foreseen adjacent to the main sextupoles. For this purpose, used FFTB sextupoles could be employed.

A magnetic dither coil is needed for horizontal beam-beam deflection scans. For vertical beam-beam scans and vertical orbit-feedback at the IP, an electrostatic dither is envisioned, since only tiny deflection angles are required. In addition, two horizontal and two vertical steering correctors are installed at each bend function (for instance, between the two main sextupoles of the CCY) to correct for bend-field drifts and bend rolls.

The tuning and correction elements are summarized in Table 11-29.

Diagnostics, Protection and Tune-Up Elements

The region between the entrance of the SCS and the IP comprises 75 main quadrupoles, 15 sextupoles, and five skew quadrupoles. This probably requires the installation of 75–95 conventional beam position monitors with wide dynamic range (*i.e.,* a few mm) for global alignment, initial tuning, and to diagnose "flyers." In addition about 10 rf BPMs [Hartman priv] will be integrated into the structure of some critical magnets to allow stabilization of the average orbit. This is not strictly necessary (see discussion of FT and CCY feedback in this chapter), but the rf BPMs promise very high resolution (*i.e.,* 10 nm) and correspondingly faster feedback response. A particular rf BPM will be installed at the IP pre-image point in the beta-exchanger. This BPM will detect betatron oscillations in the IP phase and, thereby, will allow to correct the beam-beam deflection scans for pulse-to-pulse orbit variations. Performance and reliability of exemplary rf BPMs is being tested at the FFTB.

Beam sizes and emittances are measured in the diagnostic section by means of six laser-wire scanners, each equipped with laser wires at three different angles. For redundancy, an equal number of conventional wire scanners will be installed. The conventional wires can be recycled from the SLC and/or FFTB. They will be useful only during tune up with single bunches and enhanced emittances. A further laser wire is used to infer the beam divergence at the pre-image point of the IP in the BX section (see the discussion in Section 11.4), and a last laser wire, located upstream

Name	Pole-tip field B_T (kGauss)	Radius a (mm)	Length L (m)	Ripple $\Delta K/K(10^{-4})$	Vibration[a] Δx	Δy	Drift[a] Δx	Δy	Roll θ_{xy} (μrad)
QDD	7.00	7.	1.	10.	25.	15.	550.	30.00	200.00
QDF	7.14	7.	1.	10.	25.	15.	550.	30.00	200.00
QDD	7.14	7.	1.	10.	25.	15.	550.	30.00	200.00
QDF	7.14	7.	1.	10.	25.	15.	550.	30.00	200.00
QDD	7.14	7.	1.	10.	25.	15.	550.	30.00	200.00
QDF2	5.85	7.	2.	10.	25.	15.	550.	30.00	200.00
QDD2	4.96	7.	2.	10.	25.	15.	550.	30.00	200.00
QDF2	5.85	7.	2.	10.	25.	15.	550.	30.00	200.00
QDD	7.14	7.	1.	10.	25.	15.	550.	30.00	200.00
QDF	7.14	7.	1.	10.	25.	15.	550.	30.00	200.00
QDD	7.14	7.	1.	10.	25.	15.	550.	30.00	200.00
QDF	7.14	7.	1.	10.	25.	15.	550.	30.00	200.00
QDD	7.14	7.	1.	10.	25.	15.	550.	30.00	200.00
QDF	7.14	7.	1.	10.	25.	15.	550.	30.00	200.00
QDD	7.14	7.	1.	10.	25.	15.	550.	30.00	200.00
QDF	7.14	7.	1.	10.	25.	15.	550.	30.00	200.00
QDD	7.14	7.	1.	10.	25.	15.	550.	30.00	200.00
QDF2	5.85	7.	2.	10.	25.	15.	550.	30.00	200.00
QDD2	4.96	7.	2.	10.	25.	15.	550.	30.00	200.00
QDF2	5.85	7.	2.	10.	25.	15.	550.	30.00	200.00
QDD	7.14	7.	1.	10.	25.	15.	550.	30.00	200.00
QDF	7.14	7.	1.	10.	25.	15.	550.	30.00	200.00
QDD	7.14	7.	1.	10.	25.	15.	550.	30.00	200.00
QDF	7.14	7.	1.	10.	25.	15.	550.	30.00	200.00
QDD	7.14	7.	1.	10.	25.	15.	550.	30.00	200.00
QDF	7.14	7.	1.	10.	25.	15.	550.	30.00	200.00
QDD	7.14	7.	1.	10.	25.	15.	550.	30.00	200.00
QG1	7.14	7.	1.	10.	25.	15.	550.	30.00	200.00
QG2	7.14	7.	1.	10.	25.	15.	550.	30.00	200.00
QG1	7.14	7.	1.	10.	25.	15.	550.	30.00	200.00
QG2	7.14	7.	1.	10.	25.	15.	550.	30.00	200.00

[a] (nm), with respect to ground.

Table 11-23. *Normal quadrupoles in skew correction, diagnostic, and geometry sections.*

Name	Pole-tip field B_T (kGauss)	Radius a (mm)	Length L (m)	Ripple $\Delta K/K$ (10^{-5})	Vibration[a] Δx	Δy	Drift[a] Δx	Δy	Roll θ_{xy} (μrad)
QB1	2.09	10.5	1.0	3.3	6.80	7.30	144.0	33.00	11.30
QB2	0.95	10.5	1.0	3.3	6.80	7.30	144.0	33.00	11.30
QB3	0.95	10.5	1.0	3.3	6.80	7.30	144.0	33.00	11.30
QB4	2.95	10.5	1.0	3.3	6.80	7.30	144.0	33.00	11.30
QB5	6.54	10.5	1.0	3.3	6.80	7.30	144.0	33.00	11.30
QE2	2.71	10.5	0.5	3.3	6.80	7.30	144.0	33.00	11.30
QE2	2.71	10.5	0.5	3.3	6.80	7.30	144.0	33.00	11.30
QE1	7.89	19.5	0.5	3.3	6.80	7.30	144.0	33.00	11.30
QX3	7.88	19.5	0.5	3.3	6.80	7.30	144.0	33.00	11.30
QX2	4.24	10.5	0.5	3.3	6.80	7.30	144.0	33.00	11.30
QX2	4.24	10.5	0.5	3.3	6.80	7.30	144.0	33.00	11.30
QX1	4.24	10.5	0.5	3.3	6.80	7.30	144.0	33.00	11.30
QX1	4.24	10.5	0.5	3.3	6.80	7.30	144.0	33.00	11.30
QX2	4.24	10.5	0.5	3.3	6.80	7.30	144.0	33.00	11.30
QX2	4.24	10.5	0.5	3.3	6.80	7.30	144.0	33.00	11.30
QX3	7.88	19.5	0.5	3.3	6.80	7.30	144.0	33.00	11.30
QBX1	7.88	19.5	0.5	3.3	6.80	7.30	144.0	33.00	11.30
QBX2	4.24	10.5	0.5	3.3	6.80	7.30	144.0	33.00	11.30
QBX2	4.24	10.5	0.5	3.3	6.80	7.30	144.0	33.00	11.30
QBX3	4.24	10.5	0.5	3.3	6.80	7.30	144.0	33.00	11.30
QBX4	3.01	10.5	0.5	3.3	6.80	7.30	144.0	33.00	11.30
QBX5	3.01	10.5	0.5	3.3	6.80	7.30	144.0	33.00	11.30
QBX5	3.01	10.5	0.5	3.3	6.80	7.30	144.0	33.00	11.30
QBX6	3.01	10.5	0.5	1.8	54.00	4.80	15000.	2000.00	15.70
QY3	3.01	10.5	0.5	1.8	54.00	4.80	15000.	2000.00	15.70
QY2	3.01	10.5	0.5	3.3	6.80	7.30	144.0	33.00	11.30
QY2	3.01	10.5	0.5	3.3	6.80	7.30	144.0	33.00	11.30
QY1	3.01	10.5	0.5	3.3	6.80	7.30	144.0	33.00	11.30
QY1	3.01	10.5	0.5	3.3	6.80	7.30	144.0	33.00	11.30
QY2	3.01	10.5	0.5	3.3	6.80	7.30	144.0	33.00	11.30
QY2	3.01	10.5	0.5	3.3	6.80	7.30	144.0	33.00	11.30
QY3	3.01	10.5	0.5	1.8	54.00	4.80	15000.	2000.00	15.70
QEI1	3.01	10.5	0.5	1.8	54.00	4.80	15000.	2000.00	15.70
QEI2	3.01	10.5	0.5	3.3	6.80	7.30	144.0	33.00	11.30
QEI2	3.01	10.5	0.5	3.3	6.80	7.30	144.0	33.00	11.30
QEI3	3.01	10.5	0.5	3.3	6.80	7.30	144.0	33.00	11.30
QEI4	0.76	10.5	0.5	3.3	6.80	7.30	144.0	33.00	11.30
QFT6	4.12	10.5	1.0	1.6	9.00	3.40	480.	21.00	3.40
QFT5	4.01	10.5	1.0	1.6	9.00	3.40	480.	21.00	3.40
QFT4	2.51	10.5	1.0	1.6	9.00	3.40	480.	21.00	3.40

[a] (nm), with respect to ground.

Table 11-24. *Normal quadrupoles in the CCX, BX, CCY, and FT.*

Name	Pole-tip field B_T (kGauss)	Radius a (mm)	Length L (m)	Ripple $\Delta K/K$ (10^{-5})	Vibration[a] Δx	Δy	Drift[a] Δx	Δy	Roll θ_{xy} (μrad)
QFT3	11.20	11.	2.00	.42	3.60	.70	1600.	98.00	1.80
QFT2	11.20	11.	2.00	.42	3.60	.70	1600.	98.00	1.80
QFT1	34.70	11.	1.50	.42	3.60	.70	1600.	98.00	1.80
QFTA	13.50	5.	1.50	.42	3.60	.70	1600.	98.00	1.80

[a] (nm), with respect to ground.

Table 11-25. *The quadrupoles of the final doublet. QFTA is a permanent magnet, QFT1 superconducting, and QFT2 and QFT3 are conventional.*

Name	Pole-tip field B_T (kGauss)	Radius a (mm)	Length L (m)	Ripple $\Delta K/K$ (10^{-3})	Vibration/drift Δx	Δy
SX1	6.66	20.00	0.40	2.20	50.	50.
SX3	1.80	10.50	0.40	9.00	1000.	1000.
SX1	6.66	20.00	0.40	2.20	50.	50.
SY1	3.71	10.50	0.40	2.20	50.	50.
SY3	1.02	10.50	0.40	9.00	1000.	1000.
SY1	3.71	10.50	0.40	2.20	50.	50.
SI2	1.47	10.50	0.40	9.00	1000.	1000.

[a] (nm), with respect to ground.

Table 11-26. *Normal sextupoles in the CCX, BX, CCY, and FT.*

Name	#	B [G]	L (m)	θ (μrad)	$\Delta\rho/\rho$ (Δx) (10^{-6})	$\Delta\rho/\rho$ ($\sigma_{x,y}$) (10^{-6})	$\theta_{x,y}$ (μrad)
BG	2	538.7	5.00	0.5	2.8	15.	0.5
B1A	5	157.5	7.00	0.5	2.8	15.	0.5
B1B	5	157.5	7.00	0.5	2.8	15.	0.5
B2	28	157.5	7.00	0.5	2.8	15.	0.5
B3A	8	157.5	8.28	0.5	2.8	15.	0.5
B3B	4	157.5	9.19	0.5	2.8	15.	0.5
B4	24	112.5	10.00	0.5	2.8	15.	0.5
B5A	12	65.0	10.00	0.5	2.8	15.	0.5
B5B	8	65.0	11.46	0.5	2.8	15.	0.5
B5C	4	12.0	16.00	0.5	2.8	15.	0.5

Table 11-27. *Bending magnets in the final focus. In reality, each bending magnet listed here represents 3–5 shorter magnets on a common power supply, and possibly common support.*

Name	Pole-tip field B_T (kGauss)	Radius a (mm)	Length L (m)	Ripple $\Delta K/K$ (10^{-4})	Vibration/drift Δx (nm)	Δy (nm)
SQ1	4.	6.	0.4	10.	50.	30.
SQ2	4.	6.	0.4	10.	50.	30.
SQ3	4.	6.	0.4	10.	50.	30.
SQ4	4.	6.	0.4	10.	50.	30.

[a] With respect to ground.

Table 11-28. *Skew quadrupoles in skew correction section.*

Type	#	Location
Geom. sextupoles	4	FT
Tuning sextupoles	4	CCX, CCY
Skew quad	1 (4)	FT (SCS)
Magnetic dither	1	at IP
Electrostatic dither	1	at IP
Steering correctors (x or y)	20	at each bend function

Table 11-29. *Steering and tuning elements in the final focus.*

or inside of the final doublet, measures the IP beam divergence. Finally, a laser-interferometer is foreseen for the pre-image point itself. It needs to be determined if a variant of such a monitor could also be installed inside the detector close to the IP.

Two insertible single-bunch stoppers will be convenient during commissioning and for tune up. One is located behind the DS and facilitates coupling correction prior to bringing beam through the final focus. The second insertible stopper, in the final transformer, allows tuning of the final focus, using single bunches with enlarged emittance at 10-Hz repetition rate, before the nominal beam is sent through final doublet and detector. A conventional profile monitor will be placed in front of each beam stopper.

Magnet sensors in each quadrupole and each dipole detect fast field changes and are part of the machine-protection system. Machine protection is also served by two toroids which measure beam losses in the final-focus region. At the high-beta points close to the main sextupoles, four tungsten collimators are installed. These collimators are important for controlling the detector background. There are also about 176 1/4 r.l. Ti spoilers which will protect quadrupoles and bends from missteered beams. Finally, three muon spoilers located at appropriate positions ensure that the muon background remains acceptable [Keller 1993]. Muon spoilers are treated in Chapter 12.

Tables 11-30 and 11-31 summarize the diagnostics and protection elements, respectively, between the SCS and the IP.

11.5.9 Summary

The proposed final-focus design delivers spot sizes not too far from the linear values, in the entire ZDR operating plane, and it has a sufficiently large momentum bandwidth of 1.2–1.3%, both at 500 GeV and at 1 TeV. Motivated by SLC experience, considerable effort was devoted to evaluating and budgeting all possible sources of spot-size dilution. The budgets for tolerances and aberrations are an integral part of the NLC design. Dedicated stabilization systems and tuning procedures throughout the system ensure that most tolerances can easily be met and maintained.

Type	#	Resolution	Comment
Conventional BPMs	84	1 μm	at each magnet
Rf BPMs	10	10–100 nm	at critical locations
Laser-wire scanners	8	10 % of beam size	3 wires at each scanner
Laser-interferometer	1 (or 2)	10 % of beam size	in BX (and close to IP)
Conv. wires	8	20 % of beam size	
Toroids	2	1 % of beam current	in SCS and FT
Profile monitor	2	30 % of beam size	in front of dump

Table 11-30. *Diagnostics elements between the SCS and IP.*

Type	#	Comment
Collimators W	4	at sextupoles
Prot. collimators 1/4 r.l. Ti	176	one per quad and dipole
Insertible single-bunch stopper	1	in FT and after DS
Muon spoilers	3	at strategic locations
Magnet sensors	176	in each quadrupole and dipole

Table 11-31. *Protection and tune-up elements between SCS and IP.*

The requirements on ground motion and on magnet-to-ground vibrations are less severe than what has already been achieved at the FFTB. A possible exception is the final doublet, whose vibration tolerances are comparable to measured quadrupole-vibration amplitudes. Therefore, the final doublet will be further stabilized by means of an optical anchor and a seismometer. In general, the final-focus system is very tolerant with regard to parameter changes, and it lends itself to an uncomplicated upgrade from 350 GeV to 1.5-TeV-c.m. energy.

Outstanding questions that still need some work include a simulation of beam-based alignment, and a description of commissioning and operation. None of these items is expected to be difficult. Further studies may also be devoted to the odd-dispersion design proposed by Oide, which could offer cost savings due to its smaller number of magnets and shorter length without compromising the performance. Tunability, tolerances, and operational flexibility of this scheme, in comparison with the present design, remain to be evaluated.

11.6 The Final Doublet

It is the function of final-focus systems to demagnify the beam. Systems using only quadrupoles are limited by a fundamental, unavoidable chromatic aberration in each plane. In present generation final-focus systems, this aberration is compensated by adding sextupoles at dispersive points in the beam line (K. Brown). The amount of chromatic aberration from quadrupoles, to be compensated by the sextupoles, remains a fundamental parameter determining the characteristics of the system, including length, optical functions, and tolerances. One wishes to start with a quadrupole configuration that has the smallest possible chromaticity.

Given a specification for the demagnification, one can show that the smallest chromaticities arise from placing strong quadrupoles as close as physically possible to the focal point. The strength of the quadrupoles is determined by magnet technology and aperture considerations. The free distance from the first quadrupole to the focal point is denoted by the symbol L^*. Factors determining L^* involve background and detector solid-angle considerations.

The function of the final strong quadrupoles then is to match rays having divergences that, on the one side are determined by the proximity of the focal point, and on the other side, are characterized by the remainder of the final focal system. Since the focal system modules are usually much larger than L^* (hundreds of meters compared to one or two meters), the function of the final quadrupoles is simply to focus to a point those particles whose trajectories are parallel to the beam direction.

The simplest such system consists of two quadrupoles and is referred to as the final doublet. The systems described in this section function as a doublet though, for reasons that will be clarified, it is beneficial to use four separate magnets, which we will call the final quartet. Since from an optical point of view the important parameters will be the horizontal and vertical chromaticities, we will seek final doublet designs that meet other criteria and limitations, keeping the chromaticities as small as possible.

The other criteria to be met include:

- L^* is large enough to meet detector solid-angle and background requirements.
- The magnetic material is suitable for a large solenoidal field environment (3 T).
- The magnetic field strength is able to meet stability requirements.
- The magnets can be constructed, supported, and monitored so as to meet alignment tolerances.
- The system satisfies geometric constraints arising from crossing exit and entrance beam lines.
- Synchrotron radiation is below the Oide limit.
- The system has acceptable energy adjustability.

The purpose of this section will be to show how chromaticity varies with doublet parameter choices, and how one may meet the above criteria with a minimum impact on chromaticity. Then, the important tolerances of the system will be explored, and some operational guidelines presented.

Since the final quartet in the beam line will not exactly focus parallel to point, they will vary somewhat from the designs presented in this chapter. If one wishes to know the parameters exactly, consult the lattice "decks." The purpose of this chapter is to clarify the principles underlying the design of the final doublet (quartet), and to give a sense of the trade-offs that were made in arriving at the present design, and could be made if further changes in quartet parameters were desirable to meet additional or modified criteria.

11.6.1 Doublet Parameters

For the purposes of studying the final doublet (FD) as a system independent of the final-focus system, it is a very good approximation to assume that its function is to focus parallel rays to a point at the IP. This can be confirmed by looking at the plots of $\sqrt{\beta(s)}$ for final-focus systems. The ratio of the slope of this function before and after the FD is less than 0.1, both horizontally and vertically.

To begin we will limit pole-tip fields for final doublet quadrupoles to 1.2 T, (the permanent-magnet material of choice, SmCo with Erbium, for a ratio of inner to outer radius of 1/4, has a pole-tip field of 1.35 T), and assume the pole-tip radius is greater than 3 mm. The latter limit arises from resistive-wall wakefields. This means for the quadrupole $Q1, \kappa_1 = B_{T1}/(a_1 B\rho) \leq 120/E(\text{GeV}) = \{0.48, 0.24, 0.16\}\text{m}^{-2}$ for beam energies of {250, 500, 750} GeV respectively. In general, $\kappa_2 < \kappa_1$, since a somewhat larger Q2 aperture is usually desirable, but more importantly

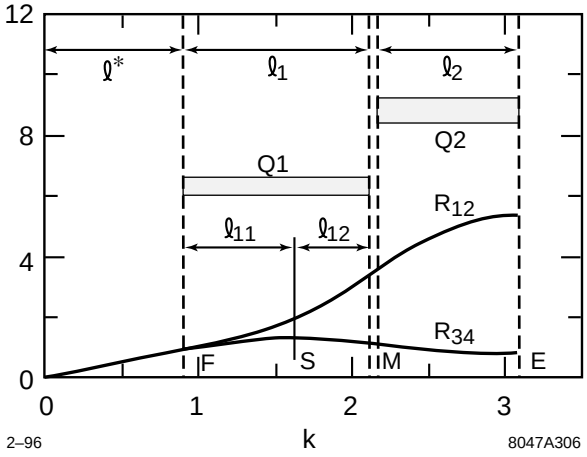

Figure 11-41. *A diagram of a model final doublet.*

the contribution to the Oide effect that arises from horizontal betatron motion through the final doublet can be reduced by taking a smaller κ_2.

Given κ_1, κ_2, and the free length, L^* (from the IP face of Q1 to the IP), the lengths L_1 and L_2 of Q1 and Q2 are determined by the parallel-to-point focusing condition. (There is one other parameter, the free space between Q1 and Q2 which we will denote by d. For purposes of this discussion we take $d = 0$.) Since κ_1 will be chosen as large as possible, and its limit is being fixed by magnet technology and resistive-wall limits, we use $k_1 = \sqrt{\kappa_1}\,\mathrm{m}^{-1}$ to scale all lengths and define $\ell^* = k_1 L^*,\ \ell_1 = k_1 L_1,\ \ell_2 = k_1 L_2$, and $\tilde{k} = k_2/k_1$.

There are now two parameters determining the system: L^* and $\tilde{\kappa}$. A sketch of a model final doublet is shown in Figure 11-41.

The IP end of Q1 is denoted by F (front face), the split between Q1 and Q2 by M (middle), and the entrance to Q2 by E (entrance). Rays have been drawn with unit slope at the IP. This implies that these rays will be the R_{12} and R_{34} functions for horizontal and vertical motion respectively. The magnet Q1 has been split into two parts at S where the R_{34} function is a maximum, defining lengths ℓ_{11} and ℓ_{12}. Note that with $k_1 \approx \{0.7, 0.5, \text{and } 0.4\}$ and $L^* = 2\,\mathrm{m}$, we have $l^* \approx \{1.4, 1.0, \text{and } 0.8\}$ for beam energies $E = \{250, 500, \text{and } 750\}$ GeV, respectively.

11.6.2 An Analytical Model of the Doublet

Element Lengths and Strengths

Letting $x = R_{12}$ and $y = R_{34}$ be the rays originating from the IP, the condition $y/y' = \ell^*$ at F implies $\ell_{11} = \cot^{-1}\ell^*$ and, at S, $y_{\max} = \sqrt{(\ell^{*2}+1)}$. We have

$$\ell_{11} = \cot^{-1}\ell^* \approx \frac{\pi}{4} - \frac{(\ell^*-1)}{2} \quad \text{for} \quad \ell^* \approx 1 \quad . \tag{11.83}$$

At boundary M, we may derive that the ratio $x/x' = (1+m)/(1-m)$ where $m = (\ell^*-1)/(\ell^*+1)\exp(-2\ell_1)$. From the nature of the y function in the ℓ_{12} region, we can make a rough estimate of $\ell_{12} \approx \pi/6$ and adding this to

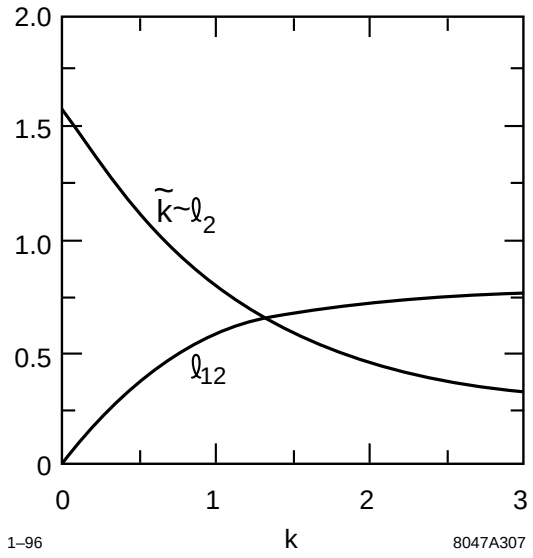

Figure 11-42. *The functions $\ell_{12}(\tilde{k})$ and $\tilde{k}\ell_2(\tilde{k})$.*

$\ell_{11} \approx \pi/4$ from above, find $\ell_1 \approx 1.3$, implying an estimate for m < 0.01 even for $\ell^* = 1.4$. (Even if $\ell_{12} \to 0$ which can occur for very small k, we have $m < 0.05$.) In other words, for all parameters under consideration, x/x' is within a few percent of unity at M. This fact makes it possible to find an analytical model for the doublet by setting $x/x' = 1$ at M.

Since for $\tilde{k} = 1$, and m small, $\ell_2 = \pi/4 = 0.79$, it follows that at M $y/y' = \coth(\pi/4) = 1.52$, hence $\ell_{12} = 0.58$. For general $\tilde{k}$, and m small, $\tilde{k}\ell_2 = \cot^{-1}\tilde{k}$. At M, $y/y' = \coth(\tilde{k}\ell_2)/\tilde{k} = \cot(\ell_{12})$ determines ℓ_{12}.

We will define a function $c(\tilde{k}) = \coth(\tilde{k}\ell_2) = \coth(\cot^{-1}\tilde{k})$. As $\tilde{k} \to \infty$, $c(\tilde{k}) \to \tilde{k}$, and as $\tilde{k} \to 0$, $c(\tilde{k}) \to \coth(\pi/2)$.

$$\ell_{12}(\tilde{k}) = \cot^{-1}\left[\frac{\coth(\tilde{k}\ell_2)}{\tilde{k}}\right] = \cot^{-1}\left[\frac{c(\tilde{k})}{\tilde{k}}\right] \tag{11.84}$$

The functions $\ell_{12}(\tilde{k})$ and $\tilde{k}\ell_2(\tilde{k})$ are shown in Figure 11-42. As $\tilde{k} \to 0$, $\tilde{k}\ell_2 \to \pi/2$ and $\cot \ell_{12} \to \infty$, hence $\ell_{12} \to 0$. As $\tilde{k} \to \infty$, $\tilde{k}\ell_2 \to 1/\tilde{k}$.

The R_{12} and R_{34} Functions

The values of R_{12} and R_{34} at M and E can now be determined.

$$\begin{aligned} R_{34}^M(\tilde{k}) &= \sqrt{\ell^{*2}+1}\,\frac{c(\tilde{k})}{\sqrt{c(\tilde{k})^2+\tilde{k}^2}} & R_{34}^E(\tilde{k}) &= \sqrt{\ell^{*2}+1}\sqrt{\frac{c(\tilde{k})^2-1}{c(\tilde{k})^2+\tilde{k}^2}} \\ R_{12}^M(\tilde{k}) &\approx \tfrac{1}{2}(\ell^*+1)e^{\ell_{11}}e^{\ell_{12}(\tilde{k})} & R_{12}^E(\tilde{k}) &\approx \tfrac{1}{2}(\ell^*+1)e^{\ell_{11}}e^{\ell_{12}(\tilde{k})}\frac{\sqrt{\tilde{k}^2+1}}{\tilde{k}} \end{aligned} \tag{11.85}$$

These functions are shown in Figure 11-43a and 11-43b.

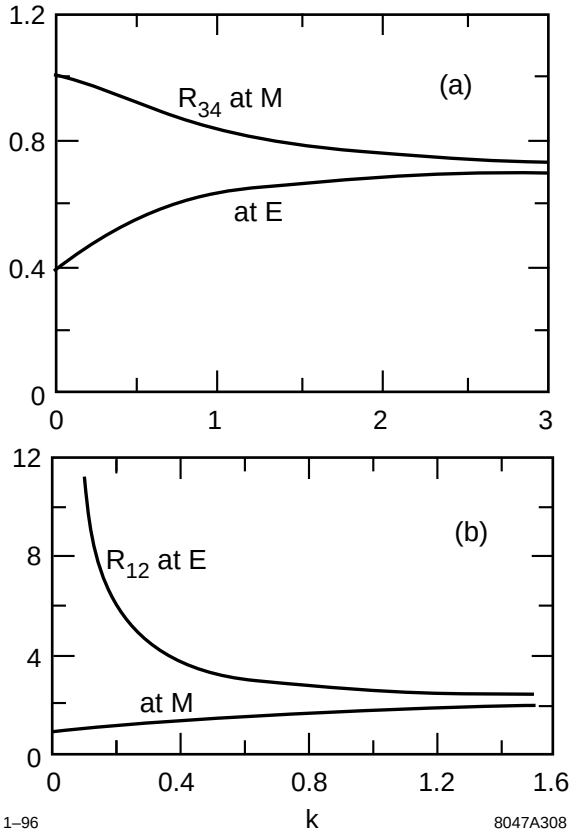

Figure 11-43. *(a) The ray $R_{34}(\tilde{k})$ at M and E. (b) The ray $R_{12}(\tilde{k})$ at M and E.*

Chromaticity

An important parameter for final-focus system design and operational tolerances is the chromaticity, which is given by

$$\int ds\, \kappa_2(s)\beta_z(s) = \frac{1}{\beta_2^*}\int ds\, \kappa_2(s) R_{12}^{z^2}(s) \equiv \frac{L_z^c}{\beta_z^*} \quad . \tag{11.86}$$

The subscript z here can be x or y. $\kappa_z = |\kappa|$ if the quadrupole is focusing in z plane, and $\kappa_z = -|\kappa|$ otherwise.

It is best to consider separately the contributions from the integration of regions specified by ℓ_{11}, ℓ_{12}, and ℓ_2. For the vertical plane, the integral for the regions ℓ_{11}, ℓ_{12} is given by

$$\frac{(\ell^{*2}+1)}{2}\left(\ell + \frac{\cot\ell}{\cot^2\ell + 1}\right) \tag{11.87}$$

where $\ell = \ell_{11}$ or $\ell = \ell_{12}$. The contribution of region ℓ_{11} is independent of $\tilde{k}$ and given by

$$\ell_{11}^{cy} = \frac{\ell^{*2}+1}{2}\cot^{-1}\ell^* + \frac{\ell^*}{2} \quad . \tag{11.88}$$

The contribution from regions ℓ_{12} and ℓ_{l2} is given by

$$\ell_{12}^{cy} + \ell_2^{cy} = \frac{(\ell^{*2}+1)}{2}\left(\ell_{12} + \tilde{k}^2\ell_2\frac{c^2(\tilde{k})-1}{c^2(\tilde{k})+\tilde{k}^2}\right) \quad . \tag{11.89}$$

$\ell_{12}^{cy} + \ell_2^{cy} = 0.13(\ell^{*2}+1)$ at $\tilde{k}=1$ and approaches 0 as $\tilde{k}\to 0$. These two contributions to the vertical chromatic length add up to a function of ℓ^* plus $(\ell^{*2}+1)/2$ times a function of $\tilde{k}$. At $\tilde{k}=1$

$$\ell^{cy} = \frac{\ell^{*2}+1}{2}\left(\cot^{-1}\ell^* + 0.27\right) + \frac{\ell^*}{2} \quad . \tag{11.90}$$

The chromatic length $L^{cy} = \ell^{cy}/\tilde{k}$. Multiplying and dividing by L^* gives

$$L^{cy} = \frac{L^*}{\ell^*}\left[\frac{(\ell^{*2}+1)}{2}\left(\cot^{-1}\ell^* + 0.27\right) + \frac{\ell^*}{2}\right] \tag{11.91}$$

This expression diverges to $+\infty$ for $\ell^*\to 0$ and as $\ell^*\to\infty$ it goes to $L^*(1.0+0.135\ell^*)$. There should be a minimum value somewhere. For $\tilde{k}=1$, the minimum occurs at $\ell^*=1.85$; the chromaticity at $\ell^*=1.0$ is 12% larger and at $\ell^*=0.8$ is 24% larger than this minimum. In Figure 11-44a, we show a plot of L^{cy}/L^* for $\tilde{k}=1$ and $\tilde{k}=0.5$. The large crosses marked 250, 500, and 750 show the parameters for doublets at these three beam energies with $d=0.3$ m (Section 11.6.5). These solutions were done by numerical interaction on the value of x/x' at M, and do not make the assumption that $x/x'=1$ as in the analytic case. Note how well they fall in the analytic approximative curves!

For the horizontal plane, the chromatic contribution from Q1 is given by

$$\ell_1^{cx} = -\frac{1}{8}(L^*+1)^2e^{2\ell_1} - \frac{1}{2}(L^{*2}-1) + \frac{1}{2}\ell^* \tag{11.92}$$

and the contribution from Q2 by

$$\ell_1^{cx} = \frac{1}{8}(L^*+1)^2e^{2\ell_1}\left[\frac{\tilde{k}^2+1}{\tilde{k}}\cot^{-1}\tilde{k} + \tilde{k}\right] \quad . \tag{11.93}$$

The horizontal chromatic length can also be written as the sum of two terms: one which is a function of ℓ^*, and another which is a function of ℓ^* times a function of $\tilde{k}$. We show L^{cx}/L^* for $\tilde{k}=1$ and $\tilde{k}=0.5$ in Figure 11-44b. It also has a minimum (at $\ell^*=6.5$) equal to 5.3. At $\ell^*=2$, it is 1.24 times this minimum, at $\ell^*=1.5$, 1.53 times, and at $\ell^*=1$, a factor of 2.3 times the minimum. Since the β_x^* is a 100 times larger than β_y^*, the horizontal chromaticity is less critical than the vertical.

At this point we can draw the following conclusions:

- The analytic solution based on the R_{12} value-to-slope ratio (x/x') being one between quadrupoles gives the same doublet parameters as the numerical solution (within a few percent).
- There is a minimum horizontal and vertical chromatic length that can be achieved by a final doublet.
- Since the chromaticity is the chromatic length divided by the appropriate β^*, and the desired β_x^*/β_y^* ratio is about 100, the minimum horizontal chromaticity is twenty times smaller than the minimum vertical chromaticity.
- For an L^* of 2 m, field strengths based on a 1.2-T pole-tip field strength, and a beam energy of 250 GeV, the minimum is achieved for the vertical chromatic length and the horizontal chromatic length is about 40% larger than the minimum.

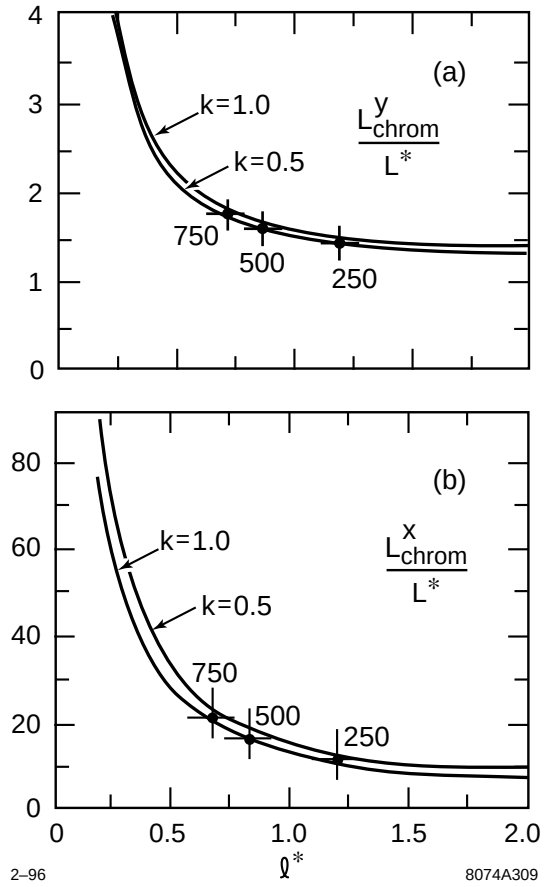

Figure 11-44. *(a) The vertical chromatic length for $\tilde{k} = 1$ and $\tilde{k} = 0.5$ as a function of $k_1 L^* = \ell^*$. (b) The horizontal chromatic length for $\tilde{k} = 1$ and $\tilde{k} = 0.5$ as a function of $k_1 L^* = \ell^*$.*

- The worst situation occurs at 750-GeV beam energy where the vertical chromatic length is 25% larger than the minimum and the horizontal chromatic length is three times the minimum.
- These solutions are surprisingly insensitive to changes in the strength of Q2 (Figure 11-44 shows chromatic lengths for equal field strengths and with the Q2 field strength reduced by a factor of 4).

We now turn our attention to the impact of increasing the separation between the magnetic elements Q1 and Q2. We will show that the chromatic lengths are also surprisingly insensitive to this parameter.

Doublets with Large Q1-Q2 Separations

In Table 11-32, we show the chromatic lengths for three cases with parameters appropriate for the 250-GeV beam energy. The pole-tip field was set at 1.35 T, the aperture of Q1 was chosen to be 5 mm, and L^* remains equal to 2 m. The separations were $d = 0.3$ m, 1.5 m, and 3.0 m.

Figure 11-45 shows the doublet solutions corresponding to the smallest and largest separation, $d = 0.3$ m and $d = 3.0$ m. The vertical chromatic length changes very little: in fact, it decreases slightly with increasing separation. The

Q1-Q2 separation (d)	Vertical chromatic length (L_y^c/L^*)	Horizontal chromatic length (L_x^c/L^*)
0.3 m	1.17	14
1.5 m	1.14	16
3.0 m	1.11	19

Table 11-32. *Chromatic lengths for several Q1-Q2 separations.*

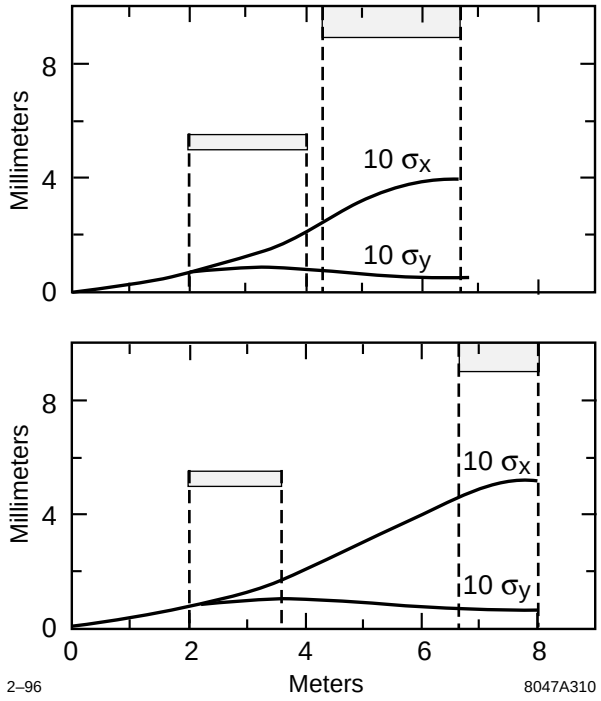

Figure 11-45. *Doublets for separations $d = 0.3\,m$ and $d = 3.0\,m$ with field strengths and L^* held constant.*

major effect is on the horizontal chromaticity which increases by about 33%, and on the R_{12}^E which increases in Q2 by about 25%. It is interesting to note that the length of both Q1 and Q2 decreases as d increases.

A large separation between Q1 and Q2 can be advantageous: i) the region of the detector fringe can be avoided, and ii) space is available for an adjustable magnet to allow for energy variability. For example, a superconducting magnet could be placed in the fringe region, since there the beam separations are sufficient that the entrance beam-line quadrupole not interfere with the exit beam line.

Skew Quadrupole from Tilt

The vertical displacement of an incoming ray due to the tilt of one or both of the quadrupoles is given by

$$\begin{aligned} \Delta y^* &= 2\int R_{34}(s)\,\theta(s)\,\kappa(s)\,x(s)\,ds \\ &= 2x'^*\int R_{34}(s)\,\theta(s)\,\kappa(s)\,R_{12}(s)\,ds \end{aligned} \tag{11.94}$$

where $\theta(s)$ is the quadrupole tilt specified as a function of s. If we suppose that $\theta(s)$ is constant over some range of s, we can substitute $\kappa(s)\,R_{12}(s) = -R_{12}(s)''$, integrate twice by parts and use $\kappa(s)\,R_{34}(s) = R_{34}(s)''$ to get

$$\Delta y^* = \theta x'^*\,[R_{34}(s)\,R'_{12}(s) - R'_{34}(s)\,R_{12}(s)]_{s_1}^{s_2} \quad . \tag{11.95}$$

We note that because of the boundary conditions $R_{12} = R_{34}$ and $R_{12'} = R_{34'}$ at $s = L^*$, and $R_{12'} = R_{34'} = 0$ at the doublet exit, that $\Delta y^* = 0$ if the whole doublet is rotated. If only parts of the doublet are rotated this term is quite large. For example, by requiring $\Delta y^*/y^* < 1/5$ (for 2% luminosity loss), we get the condition

$$\theta < \frac{1}{5}\sqrt{\frac{\varepsilon_y}{\varepsilon_x}}\,\frac{\sqrt{\beta_x^*\beta_y^*}}{[R_{34}(s)\,R'_{12} - R'_{34}(s)\,R_{12}(s)]_{s_1}^{s_2}} \quad . \tag{11.96}$$

Inserting a typical emittance ratio of 1/100 and a $\sqrt{(\beta_x^*\beta_y^*)} \approx 1$ mm, and assuming the bracket can be on the order of 1 m, we find the requirement that $\theta < 20\ \mu$r. Of course, the skew quadrupole aberration can be corrected globally, and this should not be interpreted as an absolute requirement. It does indicate that extreme care should be taken in controlling the tilt of the doublet elements, to the order of 0.1 mr if possible.

11.6.3 Final Doublet Wake Effects

Resistive-wall Wake

We use the standard resistive-wall wake formula (described in Chapter 9, Section 11.8.10).

$$\Delta y'^T_R = 2\,\frac{N r_e}{\gamma\sigma_z}\,\frac{L}{g^3} < f_R > \sqrt{\lambda\sigma_z}\,\Delta y \tag{11.97}$$

where $< f_R >= 0.82$ is the average of the longitudinal shape function of the wake distribution, r_e is the classical electron radius, $\lambda = \rho/(120\pi)$ is called the skin depth (ρ being the resistivity), N is the number of particles per bunch, σ_z is the bunch length, L is the length of the section, g is the beam-pipe radius, and Δy is the offset of the beam from the center. It is the jitter we are primarily concerned with, because a constant steering can be corrected, as long as it is not so large as to effect the beam emittance. In estimating the importance of this term, we use a beam jitter of 1 sigma and integrate the kick along the trajectory of the particle. Since the absolute alignment of the doublet can not be much worse than the maximum of this 1-sigma trajectory (from Oide and second-order dispersion effects), and this term must give a kick that displaces the beam at the IP by less than 0.2 σ_y^*, emittance growth will not be a concern (see Section 9.2.4 for a comparison of emittance growth with centroid kicks).

The contribution of the resistive-wall wake can be compensated quite easily by increasing the aperture of the quadrupole Q1. The $1/g^3$ is a strong fall-off and apertures of 4 mm are adequate for the 1-TeV-c.m. parameter set. In fact we may take an aperture somewhat larger than this to minimize background effects.

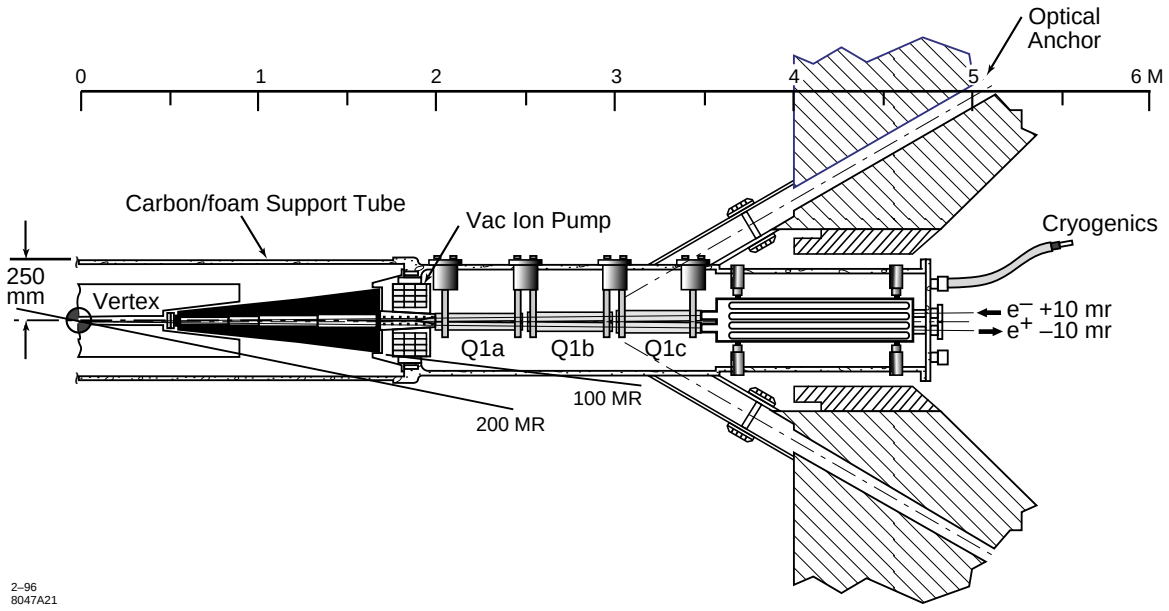

Figure 11-46. *Current final doublet layout with 20-mr crossing angle.*

Geometric Wakes

To minimize geometric wakes we suppose that the walls will be tapered anywhere the beam pipe diameter changes. This could presumably occur at the entrance to the final doublet, at the transition between Q1 and Q2, and at the IP end of Q1. In the collimation section, Section 9.2.4, it was shown that there is a broad optimum taper angle at

$$\Theta_T^{opt} \approx 1.1 \left(\frac{\lambda \sigma_z}{g^2} \right)^{\frac{1}{4}} \tag{11.98}$$

which equals about 10 mr for $g = 5$ mm. Hence the 0.3-m free space between Q1 and Q2 optimally accommodates a 3-mm change of beam-pipe radius. Since radii changes between quadrupoles are less than 4 mm, the total wake from the between-quadrupole region will not be much more than twice the resistive wall part, hence negligible.

At the IP end of Q1, the beam pipe will presumably taper up to the tungsten mask and proceed across the IP along the inner radius of the vertex chamber. This section of beam pipe is marked HOM shield in Figure 11-46.

The surface of the beam pipe at the end of Q1 will be complex since there are two holes here, one from the exit beam line and one from the entrance beam line. Though not explicitly considered in the calculations, we imagine that the beam-pipe surface is defined by two cones, each centered on one of the beam-line quadrupole bores, and that these cones terminate either at their intersection with one another or at the inner surface of the tungsten mask. (We have not considered any multibunch effects which might result from resonances of this IP region cavity.) The geometric wake is given by (see Eq. 9.27)

$$\Delta y'^T_G = 2 \frac{N r_e}{\gamma \sigma_x} \frac{(b-g)^2}{g b L_T} < f_G > \Delta y \quad . \tag{11.99}$$

Using $< f_G >= 0.28$, and $N r_e/(\gamma \sigma_z) \approx 2 \times 10^{-7}$ we have

$$\Delta y^* = L^* \Delta y'^T_G \approx 10^{-7} L^* \frac{b}{L_T} \frac{\Delta y}{g} \quad . \tag{11.100}$$

Δy at the face of the quadrupole (the smallest part of the cone) is given by $L^* y'_{\rm IP}$. Assuming we have about 1-sigma jitter, this becomes

$$\frac{\Delta y^*_{\rm rms}}{y^*_{\rm rms}} \approx 10^{-7} L^* \frac{b}{L_T} \frac{L^* y\prime^*_{\rm rms}}{g y^*_{\rm rms}} = 10^{-7} \frac{b}{L_T} \frac{L^{*2}}{g\beta^*_y} \quad . \tag{11.101}$$

Taking $\beta^*_y = 100\,\mu$m, $L^* = 2$ m and $g = 4$ mm, we obtain $\Delta y^*_{\rm rms}/y^*_{\rm rms} \approx b/L_T$. Parameters foreseen for b (2 cm) and L_T (35 cm) would be adequate.

11.6.4 Synchrotron Radiation Effects

The Oide Effect Including Horizontal Motion

The Oide effect [Oide 1988] begins with a calculation of the change in the IP position due to the change of energy of a particle at point s in the beam line. This is determined by the integral

$$R^{z6}_p(s) = \int_0^s ds' \, \frac{d\theta^z}{ds'}\,(s') R^z_{12}(s') \tag{11.102}$$

where the subscript p indicates the integral is to be taken along the path followed by the particle from the point s to the origin. For a particle following a betatron trajectory in an aligned quadrupole

$$\frac{d\theta^z}{ds} = -\kappa^z(s) z(s) = -\kappa^z(s) R^z_{12}(s) z'_{\rm IP} \tag{11.103}$$

hence

$$R^{z6}_p(s) = -z'_{\rm IP} \int_0^s ds' \kappa^z(s') R^2_{12}(s') = -z'_{\rm IP} L^{cz}(s) \quad . \tag{11.104}$$

If at the position s a photon of energy u is emitted, the change of the IP position for this particle will be

$$\Delta z_{\rm IP}(s) = R^{z6}_p(s) \frac{u}{E} \quad . \tag{11.105}$$

With a correct accounting of statistics [Sands 1985], the spread in the spot size for an ensemble of particles following this path will then be given by

$$(\Delta z_{\rm IP})^2 = \int ds\, \Delta z_{\rm IP}(s)^2 n(u,s) du = \int ds\, R^{z6}_p(s)^2 \int du \left(\frac{u}{E}\right)^2 n(u,s) \tag{11.106}$$

where $n(u,s)$ is the probability of emitting a photon with energy u (per unit length and energy.) The last integral can be performed and equals

$$\int du \left(\frac{u}{E}\right)^2 n(u,s) = c_s r_e \lambda\!\!\!^{-}_e \frac{\gamma^5}{|\rho(s)^3|} \quad . \tag{11.107}$$

Since $\frac{1}{|\rho|} = \frac{|B|}{p/q} = \frac{\sqrt{B_x^2+B_y^2}}{p/q} = \left[\frac{1}{\rho_x^2} + \frac{1}{\rho_y^2}\right]^{\frac{1}{2}}$, this integral can be written

$$(\Delta z_{\rm IP})^2 = c_u r_e \lambda\!\!\!^{-}_e \gamma^5 z'^2_{\rm IP} \int ds L^{cz}(s)^2 |\kappa(s)^3| \left[x'^2_{\rm IP} R_{12}(s)^2 + y'^2_{\rm IP} R_{34}(s)^2\right]^{\frac{3}{2}} \quad . \tag{11.108}$$

The integral in Eq. 11.101 becomes a triple integral where one integrates over a Gaussian distribution in $x'_{\rm IP}$ and $y'_{\rm IP}$. We change variables to $x'_{\rm IP} = t\,\sigma^*_{x'}$ and $y'_{\rm IP} = v\,\sigma^*_{y'}$, then in the $(t\,,v)$ space introduce polar coordinates r and ψ. The radial integral in this space is $\int\limits_0^\infty dr\, r^6\, e^{-\frac{r^2}{2}} = 15\sqrt{\frac{\pi}{2}}$. The angular integral for the vertical direction is

$$\begin{aligned} I(s) &= \frac{1}{2\pi}\int_0^{2\kappa} d\psi \sin^2\psi \left[\cos^2\psi\,\sigma^{*\,2}_{x'}\,R_{12}(s)^2 + \sin^2\psi\,\sigma^{*\,2}_{y'}\,R_{34}(s)^2\right]^{\frac{3}{2}} \\ &= \left[\frac{\sigma^{*\,2}_{x'}\,R_{12}(s)^2 + \sigma^{*\,2}_{y'}\,R_{34}(s)^2}{2}\right]^{\frac{3}{2}} \frac{1}{2\pi}\int_0^{2\kappa} d\psi \sin^2\psi\,[1+\lambda(s)\cos(2\psi)]^{\frac{3}{2}} \\ \text{where}\qquad & \lambda(s) = \frac{\sigma^{*\,2}_{x'}\,R_{12}(s)^2 - \sigma^{*\,2}_{y'}R_{34}(s)^2}{\sigma^{*\,2}_{x'}\,R_{12}(s)^2 + \sigma^{*\,2}_{y'}R_{34}(s)^2} \le 1. \end{aligned} \tag{11.109}$$

It is possible to find a good approximation to the final integral by expanding the bracket in a power series. When the integral is carried out on the series, the terms converge very rapidly. Keeping the leading terms, the resulting expression for $I(s)$ is

$$I(s) \approx \frac{1}{16\sqrt{2}}\left[\sigma^{*\,2}_{x'}\,R^2_{12}(s) + \sigma^{*\,2}_{y'}\,R^2_{34}(s)\right]^{\frac{1}{2}}\left[\sigma^{*\,2}_{x'}\,R^2_{12}(s) + 7\sigma^{*\,2}_{y'}\,R^2_{34}(s)\right] \quad . \tag{11.110}$$

The integral for the horizontal moves the coefficient 7 to the first term in the final bracket. Inserting the result of Eq. 11.110 into Eq. 11.108 we have, for the vertical direction

$$(\Delta y_{\rm IP})^2 \approx \frac{15\sqrt{\pi}\,c_u r_e \lambda_e \gamma^5 \sigma^{*\,2}_{y'}}{32}\int ds\, L^{cz}(s)^2 |\kappa(s)|^3 \left[\sigma^{*\,2}_{x'}\,R^2_{12}(s) + \sigma^{*\,2}_{y'}\,R^2_{34}(s)\right]^{\frac{1}{2}}\left[\sigma^{*\,2}_{x'}\,R^2_{12}(s) + 7\sigma^{*\,2}_{y'}\,R^2_{34}(s)\right] \quad . \tag{11.111}$$

Thus a good indicator for the importance of the Oide effect, taking into account both the horizontal and vertical motion in the final doublet, can be obtained from a single quadrature.

It is appropriate to first look at the situation described by Oide [Oide 1988] when $\sigma^*_{x'} = 0$. Then

$$I(s) = \sigma^{*\,3}_{y'}\,R_{34}(s)^3 \frac{1}{\pi}\int\limits_0^\kappa d\psi \sin^3\psi = \frac{8}{15\pi}\,\sigma^{*\,3}_{y'}\,R^3_{34}(s) \tag{11.112}$$

and

$$(\Delta y_{\rm IP})^2 = 4.2 r_e\,\lambda_e\,\gamma^5 \sigma^{*\,5}_{y'}\int ds\, L^{cy}(s)^2\,|\kappa(s)|^3\,R_{34}(s)^3 \quad . \tag{11.113}$$

For a vertical IP divergence angle of 22 mr and $E = 500$ GeV, the constant in front of the integral in Eq. (11.113) evaluates to $0.02\,\text{nm}^2$. Hence for a 2% contribution to spot size we need the (dimensionless) integral to remain below 8. The integral over Q2 can be made small by choosing a small value of $\tilde{k}$. The value of $\Delta y^2_{\rm IP}/\sigma^2_y$ is given for each of the doublets in the doublet designs of Section 11.6.5.

Oide Effect with Jitter

In the integral over the Gaussian distribution of $y'_{\rm IP}$, it is possible to offset the distribution assuming a nonzero centroid $y'_{0,\,IP}$. With no centroid offset, the average value of $< y'^5_{\rm IP} >= 6.8\sigma'^5_y$. With a centroid offset, the average values are given in Table 11-33.

Centroid offset $y'_{0\ IP}/\sigma_{y'}$	$\left\langle (y'_{\rm IP} + y'_{0\ IP})^5 \right\rangle / \left\langle y'^5_{\rm IP} \right\rangle$
0.00	1.00
0.25	1.16
0.50	1.70
0.75	2.60
1.00	4.00
1.50	10.00
2.00	22.00
3.00	87.00

Table 11-33. *Growth of synchrotron radiation with centroid offsets.*

Photons radiated per electron (in Q1)	σ/σ_0	L_0/L	Luminosity loss was overestimated by:
0.22	1.012	1.006	2.0
0.25	1.036	1.014	2.6
0.29	1.090	1.025	3.6
0.35	1.330	1.050	6.6
0.46	3.170	1.140	15.6
0.71	10.620	1.380	25.3
1.00	37.700	1.860	42.7

Table 11-34. *Beam-shape modifications due to synchrotron radiation in Q1 are very non-Gaussian. Here we compare luminosity loss that would be estimated from rms beam size increase with proper luminosity integrals (based on [Hirata 1989]).*

At an orbit displacement corresponding to 1 sigma, the rms of the vertical displacement due to synchrotron radiation effects in the final doublet are doubled. The conclusions that one would derive from looking at Table 11-33 are considerably tempered when one takes into account the non-Gaussian nature of the bunch distribution. Table 11-33 indicates that if we limit the rms beam size increase as an on-axis beam to 2%, then when missteered by 1 σ, the rms would be 4%. However, according to Table 11-34, an rms increase of 4% in reality implies a 2% luminosity loss. (Table 11-34 is based on information taken from Table 1 in [Hirata 1989]. In that study, β^* was varied, keeping the doublet configuration fixed. This is a bit unrealistic. The appropriate studies must be carried out to correctly evaluate the effects of large synchrotron radiation for our parameter configuration.)

11.6.5 Nominal Final Doublet Designs

A Doublet for 250 GeV

A possible doublet for the 250-GeV beam energy is shown in Figure 11-47. The IP parameters are: $E = 250\,\text{GeV}$, $\varepsilon_x = 10^{-11}$ m-rad, $\varepsilon_y = 10^{-13}$ m-rad, $\beta_x^* = 10^{-2}$ m, $\beta_y^* = 10^{-4}$ m. The pole-tip field of Q1 equaling 1.5 T was calculated for a SmCo magnet with an outer radius of 20 mm. The pole-tip field in Q2 is 1.2 T. The steering from the end of Q2 is given by $R_{12} = 10.6$ m and $R_{34} = 1.5$ m. The stay-clears are 27 σ_x and 60 σ_y. For 1-σ_y jitter, the resistive-wall wake would contribute about 0.1% to the vertical beam size. The synchrotron radiation, assuming a final

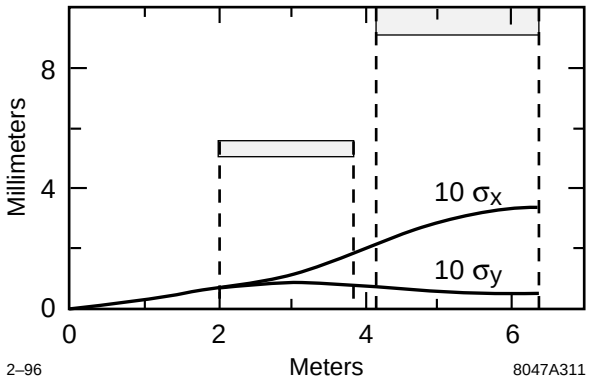

Figure 11-47. *A final doublet diagram for a 250-GeV beam energy showing 10-σ_x and 10-σ_y ray trajectories. The doublet parameters are: $L^* = 2$ m, $d = 0.3$ m, $B_{T1} = 1.5$ T, $B_{T2} = 1.2$ T, $a_1 = 5$ mm, $a_2 = 9$ mm. The chromaticities are $\xi_x = 2200$ and $\xi_y = 29,000$.*

Gaussian shape from the photon emission, would contribute 1% to the beam size. In fact, the shape is not Gaussian, and the luminosity degradation will be less than this number for an aligned doublet. Two-thirds of the beam size growth from synchrotron radiation comes from the vertical motion alone. By choosing a weaker Q2, the horizontal motion contribution was held to 1/2 the vertical contribution.

A Doublet for 500 GeV

A final doublet for a 500-GeV beam energy is shown in Figure 11-48. The IP parameters are: $E = 500$ GeV, $\varepsilon_x = 510^{-12}$ m-rad, $\varepsilon_y = 5\,10^{-14}$ mr, $\beta_x^* = 2.5\,10^{-2}$ m, $\beta_y^* = 10^{-4}$ m. Note that the beta function ratio is now enlarged to 240 from 100 for the 250-GeV design. This was to keep the parameter n_γ, the number of beamstrahlung photons per electron, to about 1.0. It is also a help for us in reducing the horizontal chromaticity and the contribution of the horizontal motion to synchrotron radiation.

The steering from the end of Q2 is given by $R_{12} = 15$ m and $R_{34} = 1.8$ m. The stay-clears are 42 σ_x and 73 σ_y. For 1-σ_y jitter, the resistive-wall wake would contribute 0.2% to the vertical beam size. The synchrotron radiation, assuming a Gaussian shape for the final beam after photon emission, contributes 2% to the beam size. The horizontal contribution is now less than 1/4 of the vertical.

A Doublet for 750 GeV

Figure 11-49 shows a final doublet for a beam energy of 750 GeV. The assumed IP parameters are: $E = 750$ GeV, $\varepsilon_x = 3.410^{-12}$ m-rad, $\varepsilon_y = 3.4 \times 10^{-14}$ mr, $\beta_x^* = 3.8 \times 10^{-2}$ m, $\beta_y^* = 1.6 \times 10^{-4}$ m. The steering from the end of Q2 is given by $R_{12} = 19$ m and $R_{34} = 2.0$ m. The stay-clears are 51 σ_x and 96 σ_y. For 1-σ_y jitter, the resistive-wall wake would contribute 0.1% to the vertical beam size. The synchrotron radiation, assuming a Gaussian-shape beam after photon emission, contributes 2% to the beam size.

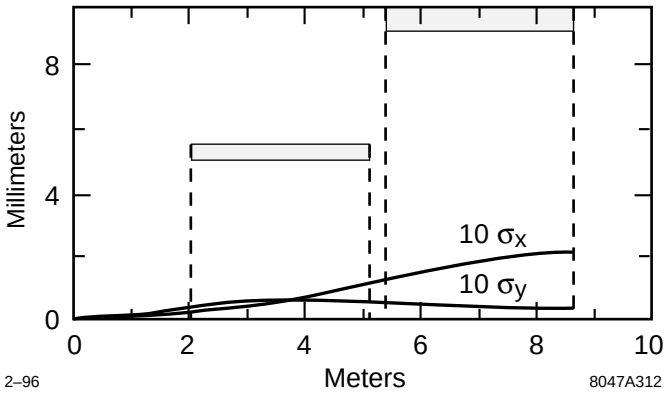

Figure 11-48. *A final doublet diagram for a 1-TeV-c.m. energy showing 10-σ_x and 10-σ_y ray trajectories. The doublet parameters are: $L^* = 2$ m, $d = 0.3$ m, $B_{T1} = 1.5$ T, $B_{T2} = 1.2$ T, $a_1 = 5$ mm, $a_2 = 9$ mm. The chromaticities are $\xi_x = 1300$ and $\xi_y = 31,000$.*

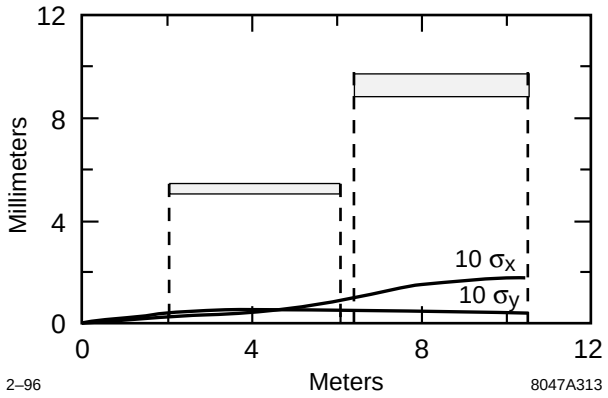

Figure 11-49. *A final doublet diagram for a beam energy of 750 GeV showing 10-σ_x and 10-σ_y ray trajectories. The doublet parameters are: $L^* = 2$ m, $d = 0.3$ m, $B_{T1} = 1.5$ T, $B_{T2} = 1.2$ T, $a_1 = 5$ mm, $a_2 = 9$ mm. The chromaticities are $\xi_x = 1100$ and $\xi_y = 23,000$.*

Final Quartets

Since the doublet performance is not a sensitive function of the distance between Q1 and Q2 (in fact separations of a couple of meters appear satisfactory: the vertical chromaticity decreases slightly, while the horizontal chromaticity increases about 20%) we may place a variable element between Q1 and Q2 to obtain energy adjustability.

We propose to place a variable superconducting quadrupole (Q1.5) between Q1 and Q2 in the region of the detector fringe. This quadrupole provides adjustability, and avoids permanent magnet material in the fringe region where the perpendicular components of the solenoidal field become large, and can cause demagnetization.

The quadrupole Q2 is now outside the solenoid and easy to support and adjust. Because of its length, it may be practical to divide it into two pieces. Thus we arrive at the "final quartet."

Figure 11-50 shows two possible final quartets for 250 and 500 GeV beam energy, respectively. Q2 was not divided into two parts so only three elements appear in this figure.

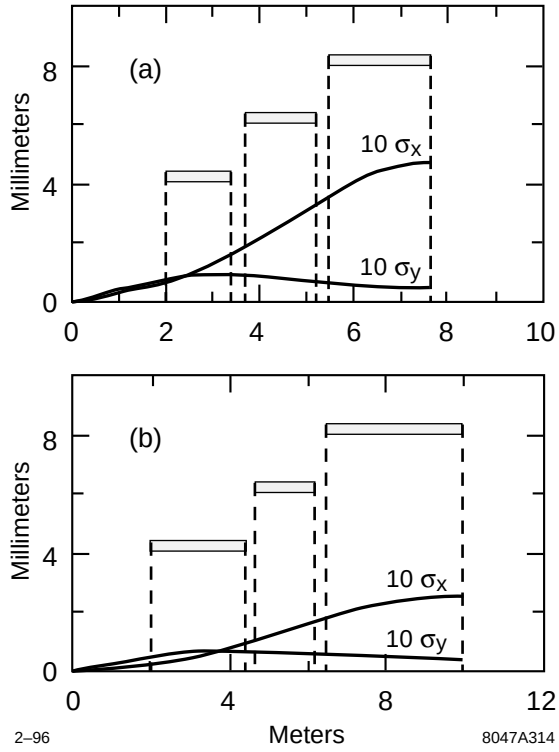

Figure 11-50. *Final quartets at 250- and 500-GeV beam energy.*

11.6.6 Tolerances

Steering Jitter Tolerances

Luminosity Loss

The luminosity for missteered beams, without disruption, goes as

$$L \propto \frac{1}{\sqrt{\sigma_R^2 + \sigma_L^2}} \exp\left(-\frac{\Delta y^2}{2\left(\sigma_R^2 + \sigma_L^2\right)}\right) \tag{11.114}$$

where Δy is the distance between the two beams. The beam separation Δy may arise from random uncorrelated missteering of the two beams, in which case the average displacements satisfy $\Delta y^2 = \Delta y_R^2 + \Delta y_L^2$. Assuming the right and left σ are equal, and the right and left error budget is the same, 2% luminosity loss occurs at rms values $\Delta y_L = \Delta y_R = (1/5)\sigma$.

If the offset is arising from correlated motion of elements to the right and left of the IP, then a 2% loss occurs at an rms $\Delta y = \sqrt{2}/5\sigma$. If the motion is correlated and sinusoidal in nature, then $< \Delta y^2 >= 0.5\ \Delta y_{\max}^2$, hence a 2% loss occurs at $\Delta y_{\max} = (2/5)\sigma$.

There is considerable vertical disruption for all NLC parameters, which means that the separated beams are steered toward one another during the collision. The luminosity formula follows the same relation with σ replaced by 3 σ in

Machine Section	Steering Budget	Accumulated Jitter	Luminosity Loss
To end of linac	$\sqrt{2}/5\sigma$	$\sqrt{2}/5\sigma = 0.28\sigma$	1%
Collimation system:	$1/5\sigma$	$\sqrt{3}/5\sigma = 0.35\sigma$	1.5%
w/ amplification:		$\sqrt{3}/4\sigma = 0.43\sigma$	2.3%
Big bend	$1/10\sigma$	0.44σ	2.4%
Final focus	$1/5\sigma$	0.48σ	2.9%
Final doublet	$1/5\sigma$	0.52σ	3.4%

Table 11-35. *Proposed NLC jitter budget.*

Aberration	Displacement					
	y_{Q1}	y_{Q2}	y_{Q1T}	y_{Q2T}	y_E	$R_{Ey'E}$
$y_{\rm IP}$	1.63	-0.63	0.04	0.04	0	-1.00
$\eta_{\rm IP}$	-1.33	-0.55	0.11	-0.23	1.88	-2.29
$\eta_{2,IP}$	1.35	0.47	-0.09	0.25	-1.07	2.20
$\eta_{{\rm IP}\vert S}$	2.40	-1.99	0.21	-0.15		
$\eta_{2,IP\vert S}$	-2.32	1.85	0.19	0.17		
$\eta_{{\rm IP}\vert SD}$	-0.85	0.72	-0.07	0.08		

Table 11-36. *The strength of aberrations for a variety of doublet displacements and incoming beam errors. This table was compiled for the 250-GeV final doublet of Figure 11-47.*

the exponent of Eq. 11.114 at design intensities. If the intensity is one-half the design, it is appropriate to replace σ by 2 σ in the exponent. To be conservative, we make the latter assumption.

11.6.7 Steering Jitter Budget

So that 2% luminosity losses do not proliferate to an unacceptable sum, we have assigned the budgets indicated in Table 11-35. A budget is also necessary because with a large beam jitter it becomes difficult to carry out beam-based alignment, wakefield effects are enhanced, and synchrotron radiation in the final doublet is enhanced (Section 11.6.4).

Steering Coefficients. With this section, we begin a discussion of aberrations which arise from the displacement of the doublet elements or from an incoming beam that has a nonzero position or slope. The aberration strength can be related to the displacement by a set of dimensionless coefficients, such as are given for the 250-GeV beam energy in Table 11-36. We will discuss the meaning of each of these coefficients, beginning with the steering coefficients.

There are potentially two coefficients relating IP motion to incoming beam centroid parameters. Since the final doublet focuses parallel rays to the IP, one of them is zero. The minus sign in Eq. 11.115 comes from the convention we use that the longitudinal distance is increasing, moving away from the IP.

$$\frac{\partial y_{\rm IP}}{\partial y_E} = 0 \qquad \text{and} \qquad \frac{\partial y_{\rm IP}}{R_{34}^{E\to{\rm IP}}\partial y'_E} = -1 \tag{11.115}$$

We include the R_{34}^E ($1.5\,\text{m} < R_{34}^E < 1.8\,\text{m}$) with the y'_E so that steering and dispersion coefficients are dimensionless.

There are two coefficients relating IP beam-position change to quadrupole displacements,

$$\frac{\partial y_{\rm IP}}{\partial y_{Q1}} \approx 1.6 \qquad \text{and} \qquad \frac{\partial y_{IP}}{\partial y_{Q2}} \approx -0.6 \quad , \tag{11.116}$$

which must add to one because a displacement of both elements shifts the focal point by the same distance. There are two coefficients relating IP motion to quadrupole pitch angle. The subscript T designates "tilt." $y_{Q1T} \equiv 0.5\, L_{Q1}\, y'_{Q1}$ is defined as the displacement of the end of the quadrupole farthest from the IP.

$$\frac{\partial y_{\rm IP}}{0.5 L_1 \partial y'_{Q1}} \approx 0.04 \qquad \text{and} \qquad \frac{\partial y_{\rm IP}}{0.5 L_2 \partial y'_{Q2}} \approx -0.04 \quad . \tag{11.117}$$

These are quite small because the R_{34} function is symmetric in Q1 and rather flat in Q2.

We can draw the following conclusions from these steering coefficients:

- If each quad is supported as a rigid unit, the tilt of this unit is less important by more than an order of magnitude than its position.
- Mounting both quadrupoles in a single long barrel should be avoided. In such a case, for the Π-mode vibration of the barrel, Q1 would be moving upward while Q2 was moving downward, and both would move the IP position in the same direction.
- Mounting the Q1 quadrupoles in a single barrel would be better. In such a case, the support of the barrel should be directly beneath Q1. Then the Π-mode would consist of a rotation of the Q1 quadrupole as a whole, and as noted above, this has a very small effect on the IP position.

Steering Jitter Tolerances. We assume, that at about 5 Hz, the steering feedback can reduce the impact of jitter. At frequencies above 5 Hz, element changes in the IP position could be measured and compensated by steering.

With the Q2 quadrupoles in separate barrels, it is appropriate to consider the four degrees (four is enough since we can neglect tilt) to be specified by the four linear combinations: i) $y_{Q1R} + y_{Q1L}$, ii) $y_{Q1R} - y_{Q1L}$, iii) $y_{Q2R} + y_{Q2L}$, and iv) $y_{Q2R} - y_{Q2L}$. The symmetric combinations move the IP symmetrically, so the beams remain in collision. Only the two antisymmetric motions are significant. The Q2 coordinates are less important than the Q1 by a factor of 2.7, so the jitter tolerance on the system is determined by the combination $y_{Q1R} - y_{Q1L}$. If it is 1 nm, the beams will miss by 1.6 nm. Assuming a doublet jitter budget of 1/2% luminosity loss, and assuming a factor of 2 from disruption (valid at 1/2 the design intensity), the tolerance on $y_{Q1R} - y_{Q1L}$ is $\sigma^*_y/5$.

We note that the motion of Q1R and Q1L should be highly correlated because they are separated by only 6 m. This is a fraction of a wavelength for motions up to 15 Hz. At these frequencies, seismic motion is very small (<0.1 nm) at most locations. Thus it is the cultural noise that must be carefully controlled at these frequencies.

Stability Tolerances from Dispersion

Dispersion Budget. It is assumed that dispersion is being tuned at regular intervals, every hour or less. Since the dispersion aberration is the most sensitive to beam position, it will likely require the most tuning. Ideally, the dispersion tuning would be automated. Dispersion at the IP implies a centroid off-set that is correlated with pulse-to-pulse energy. This correlation could be detected in the steering feedback data, and continuously minimized.

Dispersion at the IP can arise from several sources; the largest source is from the beam position in the final doublet and at the CCY sextupoles. However, this beam position in the final doublet is with respect to the beam position in the

Machine Section	Dispersion Budget	Luminosity Loss
To end of linac	1/5 σ	3% tent.
Collimation system	1/10 σ	0.5%
IP switch/big bend	1/10 σ	0.5%
Final focus/final doublet	1/5 σ	2%

Table 11-37. *Proposed NLC dispersion budget.*

final-focus system, because incoming jitter will not give rise to dispersion. It is the final-focus system, especially the CCY and the final telescope that must be stabilized. A proposed dispersion budget is shown in Table 11-37.

Allowing a 2% loss in luminosity from residual dispersion, the rms value of the dispersion aberration at the IP must be less than 1/5 the beam size, $< \eta_1\delta >_{\rm rms} \leq \sigma y^*/5$. Using a square distribution of width $\pm\Delta$, the rms of $\eta_1\delta$ is $< \eta_1\delta >_{\rm rms} = \eta_1\Delta/\sqrt{3}$. Thus, for $\Delta = 510^{-3}$ ($\delta_{\rm rms} \approx 3\times10^{-3}$) the first-order dispersion must satisfy $\eta_1 < 67\sigma_y^*$. At 1 TeV and $\sigma_y^* = 3$ nm, we must have $\eta_1 \leq 200$ nm. This sets the first-order dispersion scale.

11.6.8 Sources of First-order Dispersion in the Doublet

Dispersion arises from a change of beam position at the doublet entrance or a change of beam position at the IP. These are given in Table 11-36 as

$$\frac{\partial\eta_1}{\partial y_E} \approx 1.9 \qquad \text{and} \qquad \frac{\partial\eta_1}{R_{34}^{E\to IP}\partial y'_E} \approx -2.3 \quad . \tag{11.118}$$

The first term, corresponding to a displacement of the incoming beam or a vertical motion of the doublet system as a whole, indicates a tolerance of 200/1.9 = 105 nm for the 1-TeV machine. The vertical beam size at this point is about 33 μm, so this tolerance is about 1/300 of the beam size. This deserves some explanation.

The tolerance arises from the fact that passing off-axis through large chromaticity gives rise to dispersion. Since the chromaticity is compensated by the sextupoles in the CCY section of the final-focus system, an incoming jitter of the beam will pass off-axis through three large chromaticity points (the two sextupoles and the final doublet). Since the chromaticity has been adjusted to cancel, the dispersion will cancel as well. However, if the final doublet moves with respect to the final-focus system, or a quadrupole in the final telescope moves, or if the strength of one of the dipoles in the final telescope changes, then the dispersion will not cancel. So this problem can be approached in three ways:

- Control all systems to meet the stability requirements for time intervals equal to the time between dispersion tunings (this amounts to 20 nm for a few quadrupoles in the final telescope). For the FFTB, the observed motion (measured relative to a wire alignment system) is less than a micron per hour. This is a ground surface installation, and one might expect to do better underground.
- Have very sensitive BPMs ("rf BPMs") located at crucial positions, such as at the main CCY sextupoles and final doublet quadrupoles, and use all BPMs in the final-focus system to determine the incoming jitter of any pulse. Then with a minute's worth of pulses (10,800), select 1% (108 pulses) with the smallest jitter amplitude for further analysis. The amplitudes of these pulses are small enough so that the higher sensitivity rf BPMs can be used, since for these selected pulses the distribution width at the final doublet entrance will be 330 nm. Now, if the rf BPM had the required sensitivity (<100 nm), any one of these pulses would determine if something in

the beam line had moved, because it is a change in relative readings in the system that is of consequence. 100 pulses is an abundance.

- Use the fact that the presence of dispersion at the IP implies energy dependent steering. A correlation of IP position (as determined by beam-beam pulse-to-pulse deflections) with pulse-to-pulse energy from both right and left beams can be used to continuously correct the dispersion.

The second equation in Eq. 11.118 is of importance if the IP collision point wanders. A proper analysis requires consideration of the two doublets and the optimal method for their operation as a pair. In addition to holding the entry position (or the position in Q2) to each doublet constant, some other measurement must be used. One might imagine a good choice would be to minimize the change in the absolute sums of BPM readings in the two exit quadrupoles. This is not a good choice, because the ray that begins at the corrector in front of Q2 has a small value at the exit quadrupole in comparison to the size of this ray in Q1, where the dispersion is created. A better choice is to minimize the sum of the absolute changes of BPM readings in the two Q1s.

So let us imagine that this absolute sum is minimized and the beams are held in collision. To begin with, we could assume that the IP position does not change. The dispersion which arises from a small change in Q1, subject to this constraint, is:

$$\left.\frac{\partial \eta_1}{\partial y_{Q1}}\right|_s = \frac{\partial \eta_1}{\partial y_{Q1}} - \frac{\partial \eta_1}{R^{E\to IP}\partial y'_E}\,\frac{\partial y_{\rm IP}}{\partial y_{Q1}} \quad . \tag{11.119}$$

The values for these quantities are also shown in Table 11-36

$$\left.\frac{\partial \eta_1}{\partial y_{Q1}}\right|_s = 2.4 \qquad \text{and} \qquad \left.\frac{\partial \eta_1}{\partial y_{Q2}}\right|_s = -2.0 \tag{11.120}$$

The size of these coefficients emphasizes the importance of keeping the beam passing through the centers of these quadrupoles. In other words, misalignments of 200/2.4 = 83 nm is the maximum displacement of Q1 before the dispersion becomes unacceptable. As mentioned, this must be diagnosed and continually tuned or compensated. The beams must be held in collision, and the dispersion of each beam must remain unchanged. The latter can be arranged by changing the position at E (the IP position does not change, but the dispersion does.)

Stability Tolerances from Waist Motion

The strength aberration is also given by the chromaticity function. If the strength of both magnets in the doublet changed together, the tolerance on the strength would be:

$$\frac{\Delta k}{k} \le \frac{1}{10\xi} \approx 3.3 \times 10^{-6} \tag{11.121}$$

where we have budgeted a 1/2% luminosity loss for this aberration to the final doublet, and used 30,000 for the vertical chromaticity. If only the strength of Q1 changed, this tolerance is about 20% smaller.

Thermal Stability for Permanent Magnets. The material SmCo has a strength coefficient of $-4 \times 10^{-4}/^\circ$C, which would lead to the conclusion that the magnets should be stable to $10^{-2}\,^\circ$C in times that are on the order of waist tuning times (which we would like to have at one-hour intervals). This could conceivably be accomplished by providing a controlled thermal environment for the magnets. Temperature deviations of this order could be measured and small waist corrections introduced to compensate thermal drift.

Another possibility is to use a permanent magnet material that is more stable. There exists permanent magnet materials, $Sm_xEr_{l-x}Co$, containing erbium, that have very flat temperature coefficients, down to 10^{-6}/°C. In fact there are even materials which increase in strength with increasing temperature, at 10^{-5}/°C which could be chosen so as to compensate for the thermal expansion of the doublet. The remnant field of these materials is about 0.9 T, whereas the straight $SmCo$ remnant field can be as high as 1.06 T. However, 0.9 T seems adequate, and can give a pole-tip field of 1.35 T.

Temporal Stability of Permanent Magnets. The temporal stability of permanent magnet materials has been measured to be about $10^{-6}/hr$. Our experience with permanent magnets in accelerator environments also confirms this number [Spencer 1995]. Thus the temporal stability of permanent magnets is acceptable. The temporal stability of the $Sm_xEr_{l-x}Co$ needs to be checked.

Static Alignment Tolerances

Static Tolerances from Second-Order Dispersion. If we suppose that there is no knob in the final-focus system to adjust second-order dispersion, then this aberration will establish limits on static alignment tolerances. Synchrotron radiation also sets a limit on static alignment. The lowest of these two limits must be taken as the static alignment specification.

In calculating this tolerance, we assume that steering errors arising from static misalignments are being corrected by steering elements at E (the entrance end of Q2), and the dispersion is being corrected by adjusting the beam position at E. The appropriate coefficients are of the form:

$$\frac{\partial \eta_2}{\partial y_{Q1}}\Big|_{sd} = \frac{\partial \eta_2}{\partial y_{Q1}}\Big|_{s} - \frac{\partial \eta_2}{\partial y_E}\,\frac{\frac{\partial \eta_1}{\partial y_{Q1}}\Big|_{s}}{\frac{\partial \eta_1}{\partial y_E}\Big|_{s}} \quad . \tag{11.122}$$

The aberration term $\eta_2\delta^2$ contains a steering aberration, $\eta_2 < \delta^2 >$. After subtracting this steering, the rms spot size growth is $\eta_2\sqrt{\left(\left\langle\delta^4\right\rangle - \left\langle\delta^2\right\rangle^2\right)}$. For a square distribution of width $\pm\Delta$, this quantity equals $0.3\eta_2\Delta^2$. If the limit on luminosity loss from the second-order dispersion is taken to be 2% and $\Delta = 5\times10^{-3}$, then the second-order dispersion must satisfy $\eta_2 \le 3\times10^4\sigma_y^*$. At 1 TeV for $\sigma_y^* = 3$ nm, $\eta_2 \le 90\,\mu$m. This distance sets the scale of the static alignment tolerances arising from second-order dispersion effects.

Referring to Table 11-36, we see

$$\left.\frac{\partial \eta_2}{\partial y_{Q1}}\right|_{SD} = -0.85 \qquad \left.\frac{\partial \eta_2}{\partial y_{Q1}}\right|_{SD} = -0.72 \qquad \left.\frac{\partial \eta_2}{\partial y_E}\right|_{SD} = -1.0p7 \quad . \tag{11.123}$$

The fact that all of these coefficients are close to unity, indicates the absolute alignment tolerances arising from second-order dispersion are on the order of 90 μm. A smaller absolute alignment tolerance comes from synchrotron radiation considerations.

Static Tolerances from Synchrotron Radiation. Table 11-33 indicates that for a 0.5-sigma vertically-missteered beam, the synchrotron radiation integral is larger by a factor of 1.7. That means that a displacement of the incoming beam by about 16 μm results in an additional 1.4% spot size increase. (This estimate may be a factor of two too high. See Table 11-34). Though we have not computed the synchrotron radiation increase from element misalignments, this tolerance arises from the integral in Q1, hence it is the orbit in Q1 which sets this number. Since the missteered beam

has an orbit maximum which is somewhat larger in Q1, the misalignment tolerance will be somewhat larger than the 16-μm number deduced above. This number is a factor of five smaller than the static tolerance limits arising from second-order dispersion.

Meeting Static Alignment Tolerances. To meet absolute (static) alignment tolerances, it will be necessary to locate the beam with respect to the magnetic centers in the final doublet system. One must either provide for beam alignment based on varying quadrupole strengths, or in the case of permanent magnets, provide BPMs with appropriate absolute alignment accuracy. For permanent magnet systems, we will assume that BPMs are located at all element centers and determine the position of the magnetic centers with an absolute accuracy denoted by $\Delta y_{\rm BPM}$. For example, rf BPMs may be integrated into the permanent magnet quadrupole structure.

We begin by assuming the BPM centers are coincident with the magnetic centers. Thus they establish the two doublet center lines (say right and left) to which the incoming beam may be steered. Let us begin by neglecting the steering that may be required to arrange that each incident beam is traveling along this center line. The IP separation of these beams will be given by

$$\Delta y = \frac{s_2}{s_2 - s_1}\left(y_{1R} - y_{1L}\right) - \frac{s_1}{s_2 - s_1}\left(y_{2R} - y_{2L}\right) \quad . \tag{11.124}$$

As steering is introduced to collide the beams, it should be done with equal corrector strength on each side. Then magnets Q1 or dipole coils around Q1 should be equally adjusted so that the required steering from correctors is zero on each side. If the BPM centers were equal to the magnetic centers, the doublet would now be perfectly aligned. However, there will be BPM error. Synchrotron radiation, as noted in the previous paragraph, sets the limit on the absolute accuracy of these BPMs to be $\Delta y_{\rm BPM} \leq 16\ \mu$m.

11.6.9 Superconducting Quadrupole Q1.5

We propose to place a superconducting quadrupole, Q1.5, upstream of the permanent magnet Q1. This quadrupole serves three purposes: It, first, can provide a high gradient up to about 300 Tm^{-1}; it, second, allows operating the same doublet over a wide range of beam energies; and, third, it avoids permanent-magnet material in the solenoid-fringe region. The exit face of Q1.5 is located 3.85 m from the IP, where the incoming and outgoing beam lines are separated by about 7.7 cm. The inner bore is 11–14. mm, and the pole-tip field at 1-TeV-c.m. energy is 3–4 T.

Using a regular superconducting quadrupole would lead to a considerable field in the region where the second beam will pass, which is not desirable. We, therefore, intend to use a special magnet configuration: the current distribution will be arranged in an inner and outer shell so as to approximate two concentric $\cos 2\theta$ distributions with opposite polarity. While such a magnet can generate about the same field gradient as a conventional superconducting magnet, it has the additional advantage that the stray field experienced by the other beam is essentially zero (it is about 2–3 G).

Figure 11-51 illustrates the proposed current distribution and magnetic field pattern at the front face of the superconducting quadrupole pair viewed from the IP. Figure 11-52 shows the field-strength variation along the centerline of the two magnets on a linear scale, assuming a pole-tip field of 2 T and an inner-bore radius of 14 mm. The field falls off rapidly outside of and between the two quadrupoles, and it is very linear inside of each magnet. Finally, in Figure 11-53 the absolute value of the field is depicted on a logarithmic scale. Note that the field should go through zero at the center of the magnet, and that the finite value shown is an artifact of the drawing.

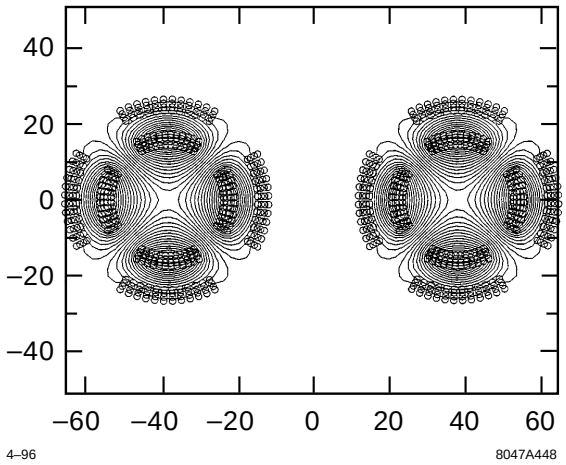

Figure 11-51. *Current and field distributions for the superconducting quadrupole pair Q1.5.*

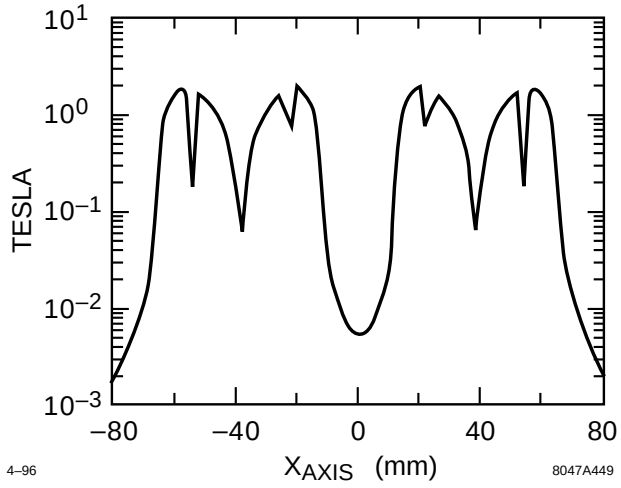

Figure 11-52. *Field strength along the centerline of the superconducting quadrupole pair Q1.5 on a linear scale.*

11.6.10 Summary

We have presented doublet designs for beam energies of 250, 500, and 750 GeV, whose chromaticities are close to the theoretical minimum and additionally

- have acceptable Oide effect synchrotron radiation,
- have acceptable resistive-wall and geometric wakes,
- have sufficient beam stay-clear,
- provide for a large range of adjustment to changing beam energy (about a factor of 2),
- are sufficiently stable thermally and temporally,

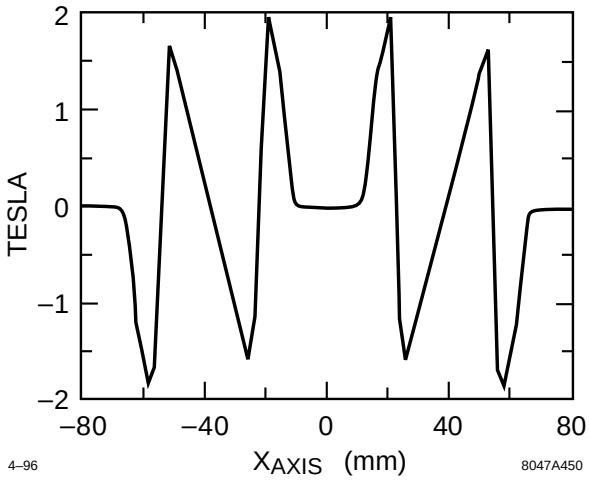

Figure 11-53. *Absolute field value along the centerline of the superconducting quadrupole pair Q1.5 on a logarithmic scale.*

- have no permanent-magnet material in solenoid fringe region,
- provide sufficient space for an exit beam path, exit beam-line elements and instrumentation at the 20mr crossing angle, and
- provide a mechanism (dipole coils) to achieve the required absolute alignment and to compensate solenoid field changes.

Final-doublet support is discussed in Section 12.4.2.

11.7 Crossing Angle, Crab Cavity, and Solenoid

Section 11.7 begins with a discussion of the factors involved in the choice of 20 mr as the IP crossing angle. Such a relatively large crossing angle implies the need for a crab cavity. The crab-cavity parameters and tolerances are discussed in Section 11.7.2. The crab cavity is placed either at the entrance of the final doublet, or if a quartet is used to obtain energy variability, then the crab cavity will be placed between the second and third element of the quartet so that the aperture of the cavity better conforms to the apertures of the quadrupoles. The crab cavity can be six $\lambda/3$ X-band cells with a total length of 5.2 cm.

This section concludes with a discussion of the effects of the detector solenoidal field including the skew aberrations, steering and dispersion effects, and synchrotron radiation.

11.7.1 Determination of Crossing Angle

The crossing angle must be large enough so that:

- There is no multibunch instability from parasitic beam-beam interactions.
- There is physical room for the final doublet and the exit beam port.
- The big bend angle provides sufficient muon protection for the detectors.
- The IPs are sufficiently separated to provide radiation and ground noise isolation.

The last two items are necessary only for beam-line geometries that interrelate the big bend angle with the crossing angle, as in the geometry we have chosen.

The crossing angle should be chosen as small as possible to minimize:

- The impact of the solenoidal field on steering, dispersion, and synchrotron radiation.
- The power requirements of the crab cavity.
- The voltage and phase stability tolerances of the crab cavity.
- The length of the big bend (especially at 750-GeV beam energy).

The NLC crossing angle parameter has been chosen to be $\theta_c = 20$ mr and the corresponding big bend angle is 10 mr (Figure 11-46).

11.7.2 Crab Cavity

The purpose of the crab cavity is to provide a transverse displacement within the bunch that varies with longitudinal distance according to

$$\frac{\partial x^*}{\partial z} = \frac{\theta_c}{2} \quad . \tag{11.125}$$

Using $\Delta x^* = R_{12}^E \Delta x'_E$ and $\Delta x'_E = \text{ eV}/E_0$, we find

$$\frac{\theta_c}{2} = \frac{\partial x^*}{\partial z} = R_{12}^E \frac{e\,\partial V(z)}{E\;\partial z} = R_{12}^E \frac{\text{eV}_{\max}}{E} k\cos(kz) \approx R_{12}^E \frac{\text{eV}_{\max}}{E}\frac{2\pi}{\lambda} \tag{11.126}$$

where in the last step we assumed the bunch was traveling through the cavity at the zero of the rf wave. R_{12}^E, which is the R_{12} matrix element from the entrance of the doublet to the IP, can vary somewhat with doublet design and machine energy, but it is in the range of 10 m to 20 m.

Crab Cavity Parameters

We have chosen the rf wavelength at X-band to keep the power requirements low and the structure length short. Table 11-38 compares X-band with S-band [Wilson 1995]. The parameters of the S-band cavity are "LOLA-III" taken from SLAC Report 17 (1963) and SLAC-PUB-135 (1965). The X-band parameters we will refer to as LOLA-X. Lolita-X is six cells of LOLA- X.

The required values for $V_{\max}$ and corresponding power are given in Table 11-39. We see that for the LOLA-X structure, the required input power is close to 0.25 MW for all energies. Since this is a very small power, the structure

Parameter	Symbol	Unit	Scaling	S-Band LOLA-III	X-band LOLA-X	X-band Lolita-X
Transverse shunt impedance	$r_\perp$	MΩ/m	$\omega^{1/2}$	11.7	23.4	23.4
Structure length	L	m	$\omega^{-3/2}$	3	0.375	0.0523
Attenuation	τ	none	1	1.04	1.04	0.15
Iris diameter	$2\,a$	mm	ω^{-1}	47	11.8	11.8
Q value	Q	1	$\omega^{-1/2}$	11,000	5,500	5,500
Group velocity	v_g/c	1	1	-0.0078	-0.0078	-0.0078
Fill time	TF	ns	$\omega^{-3/2}$	1,280	160	22
Number of $\lambda/3$ cells	N_c	1	$\omega^{-1/2}$	86	43	6
Deflection volts/$\sqrt{\text{MW}}$	$p_\perp c/\sqrt{P_0}$	MeV/$\sqrt{\text{MW}}$	$\omega^{-1/2}$	5.3	2.65	0.55

Table 11-38. *Scaling of crab-cavity parameters with wavelength.*

Beam Energy (GeV)	R_{12}^E (m)	θ_c (mr)	V (MV) S-band	V (MV) X-band	Power (MW) LOLA-III	Power (MW) LOLA-X	Power (MW) Lolita-X
250	8.9	20	4.8	1.2	0.8	0.20	4.8
500	17	20	5.0	1.3	0.9	0.24	5.6
750	21	20	6.0	1.5	1.3	0.32	7.4

Table 11-39. *Required values of maximum crab-cavity voltage for three energies.*

can be substantially decreased in length. The X-band structure with six cells (Lolita-X, 5.23-cm long) would suffice if driven with 7.4 MW of power. Shortening the structure also greatly reduces wakefield effects (almost as the square of the length).

A potential problem with the X-band structures is the iris aperture of radius 5.9 mm. We have chosen a somewhat larger Q2 aperture, to minimize resistive-wall wakes as well as provide a large beam stay-clear. At 250-GeV beam energy, the 23-σ_x aperture at the end of Q2 (see Figure 11-14) is about 11 mm for the parameter set with an 8-mm β_x^*. However, it is also possible to place the crab cavity between Q1 and Q2. For this parameter set R_{12} is still about 8 m, due to the space occupied by the superconducting Q1.

Crab Cavity Tolerances

We discuss five tolerance issues:

- Crab cavity voltage stability.
- Crab cavity pulse-to-pulse phase difference jitter.
- Crab cavity phase difference short-term stability (1 hour).

- Beam phase jitter.
- Crab cavity alignment.

Crab Cavity Voltage Stability. If the crab-cavity voltage changes, the "crabbed" angle changes. A 2% luminosity loss would occur for a crab angle error of $\theta_d/5 \approx 0.2\sigma_x/\sigma_z \approx 0.6\,\text{mr}$. For $\theta_c/2 = 10\,\text{mr}$, the permissible voltage error would be $\Delta\,\text{V}/\,\text{V} = (\theta_d/5)/(\theta_c/2) \approx 0.06$. This estimate yields a permissible 6% voltage error.

Crab Cavity Phase Difference Jitter. If the phase of the crab cavity on the left jitters with respect to the crab cavity on the right, the beams will not collide head-on. A 2% luminosity loss occurs at $\Delta x = (2/5)\,\sigma_x$ (right beam minus left beam). Since $\Delta x = (\theta_c/2)\Delta z$, the allowed $\Delta z = (4/5)\,(\sigma_x/\theta_c)$, which for $\theta_c = 20\,\text{mr}$ has the value $\Delta z = 12.8\,\mu$m, corresponding at X-band to about 0.2°. At S-band, the number of degrees would be an intimidating factor of four smaller.

It should be noted that this tolerance is a phase difference tolerance between the two crab cavities. It is a jitter tolerance, since steering correctors would compensate for any error in crab cavity phase difference which occurs for times greater than 1/5 s. To minimize phase difference jitter, both cavities should be driven by the same klystron. The phase jitter for an X-band system in such a circumstance has yet to be experimentally determined, but a simple experiment which uses a phase mixer to measure the relative phase in two rf transport lines coming from a splitter, driven by one klystron, can provide the required information. (Note: It is routine in the SLC klystron gallery to compare the S-band phase of the output from a SLED-I cavity with the rf reference phase driving that klystron. There the phase jitter is known to be less than or the order of 0.1°.)

It is interesting to estimate the thermal change on the transmission line on one side that would be result in a 0.2° phase change. The phase change is given by $\Delta\phi = \Delta(k_g L) = k_g L(\Delta k_g/k_g + \Delta L/L)$. Using $k_g = 2\pi/\lambda_g = 2\pi/\lambda(1-y^2)^{1/2}$ where $y = 0.61\lambda/a$ we have $\Delta k_g/k_g = (y^2/(1-y^2))\Delta a/a$. And $\Delta a/a = \Delta L/L = \alpha\Delta T$ with $\alpha = 1.8\,10^{-5}$, leads to $\Delta\phi = 2\pi L/\lambda\alpha\Delta T(1-y^2)^{-1/2} = 2.7°$ per °C (taking $L = 10\,\text{m}$, $\lambda = 0.026$). In other words, the temperature must be stable to 1/15°C in times of 1/5 s, or drifts should be smaller than 20°C per minute. It is expected that the temperature will be more stable than this.

A concern is that the phase difference may creep, so that the steering corrector kicks become large. Phases should be monitored for this, and a system installed to maintain the phase of the rf reaching each cavity to be the same, and at a null at the beam phase. 0.5 degrees corresponds to a horizontal steering at the IP of 1 σ_x. Probably 40-σ_x steering, corresponding to a crab-cavity-to-beam phase difference of 20°, is possible before unacceptable dispersion is created. The phase of the cavity with respect to the beam can be monitored by observing steering of the beam at a post-IP BPM as the power of the cavity is ramped. There will be no steering if the beam-pulse arrives at the rf null.

Incoming Beam Phase Jitter. Although the crab-cavity jitter tolerance is only 0.2°, this does not imply a need for a corresponding phase stability of bunches in the incoming beam. The function of the crab cavity is to align the bunch for a complete collision no matter how long. Hence the limits on beam phase stability arise from considerations of luminosity loss due to hourglass effects at the IP. If we can have $\Delta z_{\text{collision}} = \frac{1}{5}\beta_y^*$, and if the arrival of each beam is taken to be statistically unrelated, then we can have $\Delta z_{\text{beam}} = \sqrt{2}(100)\,\mu$m, which is about 1.9 degrees of X-band.

Crab Cavity Alignment for Multi-bunch Effects. If the beam passes through the cavity on-axis, no dipole mode is induced, even if the bunches are not at the zero phase. This is because the cavity does not put energy into the beam when steering it. So beam loading is entirely associated with misaligned cavities. We will assume a misalignment of 100 μm for numerical estimates.

Even if the cavity is misaligned, the induced fundamental field has a null at the longitudinal phase where the charge passes. As a result, if all particles are passing through the cavity at the same phase (modulo 2π), the induced field will change the slope of the field, but not its magnitude at the location of the bunches. We need an estimate for the change of the fundamental (dipole) mode and for the higher-order dipole modes which could steer the beam.

An estimate for the induced transverse field of 90 bunches traveling through the Lolita-X cavity off-axis by 100 μm can be found from the formula (P. Wilson)

$$V_{\perp}^{\rm ind}(n) = \frac{1}{2} I\, r_{\perp}\, L_s\, kx \left(\frac{1 - e^{-2\tau'} - 2\tau' e^{-2\tau}}{1 - e^{-2\tau}} \right) \quad \text{where} \quad \tau' = \tau\; Min\left[1,\; \frac{n\,\tau_{\rm sep}}{T_F}\right] \quad , \tag{11.127}$$

where n equals the bunch number and $\tau_{\rm sep}$ is the separation time between bunches. The expression in brackets reaches its maximum value of 0.15 at $n = 16$. The corresponding maximum induced voltage is 2.5 kV. Dividing by 1.2 MV, the crab-cavity voltage at 250 GeV, gives $V_{\rm ind}/V_{\rm crab} = 0.002$, or 0.2% change. This is comfortably smaller than the allowed 6% calculated in Section 11.7.2.

A rough estimate for higher-order dipole modes is that they might be about 10% of the induced fundamental, or about 0.25 kV for Lolita-X. This voltage could cause a missteering at the IP of $R_{12}(\text{ eV})/E = 17(9\ 10^3)/(500\ 10^9) = 8.3$ nm which is just about equal to 1/40 σ_x. This is also negligible.

Stability Tolerance from Energy Change. The Hamiltonian that gives the desired crab-cavity kick is of the form

$$H = \frac{\theta_c}{2R_{12}}\, x\, z \quad , \tag{11.128}$$

where the kick $\Delta x'$ is given by the derivative with respect to x, and has the linear z-dependence desired. However, there is also a change in energy implied by this Hamiltonian given by the derivative with respect to z. It is

$$\Delta\delta = \frac{\theta_c}{2R_{12}}\, x \quad . \tag{11.129}$$

The change in energy could be $\delta \approx 6 \times 10^{-6}$, which is also the stability tolerance of the final doublet. Inserting values for the crossing angle and R_{12}, we find the condition $x < 6$ mm. This is of no concern as an alignment stability requirement. This number also places a limit on the beam size at the crab cavity. This limit is met since the beam size is on the order of $R_{12}\sigma_{x'} < 0.3$ mm.

Feedback Systems

The physical quantities to be monitored and stabilized are i) the crab-cavity phases with respect to beam arrival times, ii) the crab-cavity voltage, iii) the crab-cavity phase difference between the two crab cavities, and iv) the crab-cavity alignment. The phase with respect to the beam, as pointed out above, can be checked by changing the crab voltage and looking for steering in the outgoing beam. The voltage itself must be set to minimize the horizontal beam size, which one should be able to monitor by vertical and horizontal beam deflection scans. It is equivalent to a beam size measurement.

By installing an insulated return line from each crab cavity to the tee (following the klystron) and comparing the phase of the two return lines, a phase correction can be introduced to keep the return phases stable. A schematic of this stabilizing system is depicted in Figure 11-54. The system is designed to keep large drifts from occurring in the phase difference. In addition, phase jitter must be small, and short-term phase stability will be taken care of by the IP steering feedback system.

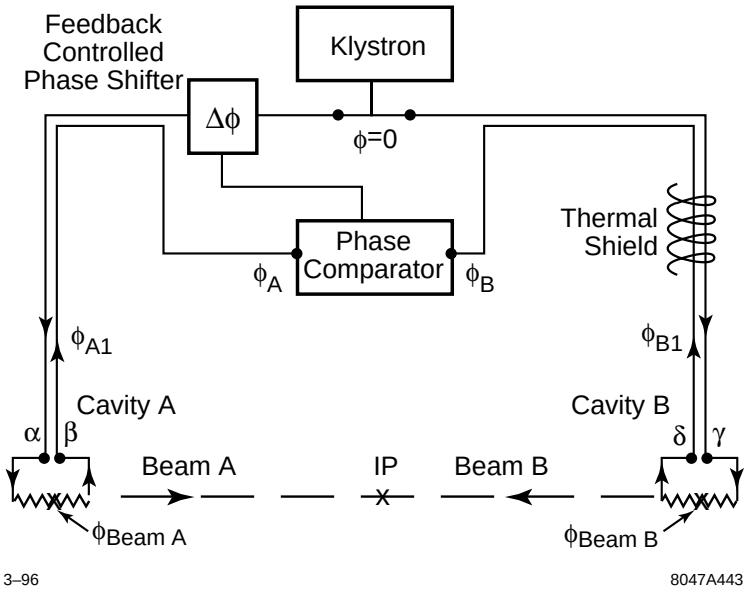

Figure 11-54. *Schematic of a system which stabilizes the phase difference between the two crab cavities.*

11.7.3 Solenoid Effects

We will assume that the maximum solenoidal field strength will be 3 T, and that the maximum crossing angle to be considered is 30 mr. Under these assumptions, the maximum field perpendicular to the beam trajectory is $B_\perp = 450$ Gauss. For this field, $B_\perp/B\rho = \{0.5\times10^{-4}, 0.25\times10^{-4}, 0.2\times10^{-4}\}m^{-1}$ at $E = \{250, 500, 750\}$ GeV respectively.

Skew Quadrupole Aberrations

The skew quadrupole term in the solenoid Hamiltonian is $1/2\, k_s(xp_y - yp_x)$ with $k = B_s/B\rho$. If there were no quadrupole within the solenoid, then this term is a constant (by rotational symmetry) and can be evaluated at the IP, to give an integrated beam-line generator of

$$G = LH = \frac{1}{2}\,\frac{B_s L}{B\rho}\left(x^*\, p_y^* - y^*\, p_y^*\right) \tag{11.130}$$

giving $\Delta y^* = (B_s L_s/B\rho)\, x^*$. Taking $B_x = 3$ T and $L_s = 4$ m leads to $B_s L_s/(B\rho) = \{0.014, 0.007, \text{and } 0.005\}$ for $E = \{250, 500, \text{and } 750\}$ GeV. Since $\sigma_x^* = \{100, 160, 160\}\ \sigma_y^*$, $\Delta y^*_{\rm rms}/\sigma_y^* = \{0.7, 0.6, 0.4\}$. So this term of the generator is small, but still too large by a factor of about five, and must be compensated with a skew quadrupole. We note that it is not the generator $p_x p_y$, which is the main term generated and corrected in the final-focus system. This skew quadrupole may have to precede the final-focus system, or be obtained from two skew quadrupoles on the opposite sides of an IP image in the final-focus system.

The interaction of Q1 and the solenoid will also produce the skew quadrupole generator $p_x p_y$, which may readily be compensated by the final-focus system skew quadrupole.

Steering and Dispersion

The solenoidal field in the region between Q1 and the IP will have a component $B_s\theta_c/2$, and will steer the beam by $\Delta y^* = B_s L^*/B\rho\ \theta_c/2$. For $\theta_c = 20\,\text{mr}$, this has the value $\Delta y^* = \{70,\ 35,\ \text{and}\ 25\}\ \mu\text{m}$ at $E = \{\ 250,\ 500,\ \text{and}\ 750\}$ GeV. This will also be the magnitude of the dispersion generated.

The two beams are deflected apart so steering must be introduced to correct this displacement. If this is done with a corrector at the Q2 end of the doublet, then because (see Table 11-36)

$$\frac{\partial \eta_1}{R_{34}^E \partial y\prime_E} = -2.3 \quad , \tag{11.131}$$

the dispersion generated by the doublet adds to the dispersion generated by the solenoidal field, giving a net dispersion 3.3 times the amount from the solenoidal field alone. This is a huge dispersion, and attempts to correct it will create unacceptable second-order dispersion terms and synchrotron radiation.

The only available alternative is to displace Q1 by $\Delta y_{\text{Q1}} = -\Delta y^*/1.6$ or to introduce an equivalent dipole field in the region of Q1. This will create dispersion which has the opposite sign but does not totally cancel the original. Theoretically, a small section at the IP end of Q1 could be displaced to re-steer the beam, in which case the dispersion would almost totally cancel. This does not work because the synchrotron radiation in such a corrector would be unacceptable. The remaining dispersion is $(1.63 - 1.33)/1.63 \approx$ 1/5 of the original (from Table 11-36: $\Delta\eta = -1.33\Delta y_{\text{Q1}}$).

The remaining residual dispersion of $\{21,\ 11,\ \text{and}\ 9\}\ \mu$m at $E = \{250,\ 500,\ \text{and}\ 750\}$ GeV can be corrected by displacing the incoming beam by $\{11,\ 5,\ \text{and}\ 4\}\ \mu$m. This is at the edge of acceptability vis-a-vis the generation of synchrotron radiation. For 20-mr crossing angles, these numbers are reduced by a factor of 1.5, and are acceptable.

Synchrotron Radiation

We first calculate the additional synchrotron radiation created by the solenoid for the on-axis particles. Then we calculate the effects of the increased dispersion function on the final doublet synchrotron radiation for focused particles (Oide effect + solenoid).

Solenoid Field Alone. The $R_{36}(s)$ function generated by the solenoid in the L^* region is given by

$$R_{36}(s) = \int R_{34}(s) d\theta = \int R_{34}(s) \frac{B_s \frac{\theta_c}{2}}{B\rho}\, ds = \frac{B_s \theta_c}{4B\rho}\, s^2 \quad . \tag{11.132}$$

The synchrotron radiation from this region results in

$$\frac{\Delta y_{\text{IP}}^2}{\sigma_{\text{IP}}^{y2}} = \frac{c_u r_e \lambda_e \gamma^5}{\sigma_{\text{IP}}^{y2}} \int ds\, R_{36}(s)^2 \left|\frac{1}{\rho(s)^3}\right| = \frac{c_u r_e \lambda_e \gamma^5}{\sigma_{\text{IP}}^{y2}} \int ds \left(\frac{B_s\theta_c}{4B\rho}\, s^2\right)^2 \left|\frac{B_s\theta_c}{2B\rho}\right|^3 = \frac{1}{20}\, \frac{c_u r_e \lambda_e}{\sigma_{\text{IP}}^{y2}} \left(\frac{B_s\theta_c L^* \gamma}{2B\rho}\right)^5 \tag{11.133}$$

Assuming $L^* = 2\,\text{m}$, $B_s = 3\,\text{T}$, and $\theta_c = 40\,\text{mr}$, $[\Delta y_{\text{IP}}/\sigma_{y^*}]^2 = \{0.04,\ 0.06,\ 0.06\}$. Fortunately, this term goes like $(B_s\theta_c)^5$, and can be reduced by reducing the crossing angle or the solenoidal field. For $\theta_c = 30\,\text{mr}$, the coefficients are reduced by a factor of 7.6, and $[\Delta y_{\text{IP}}/\sigma_{y^*}]^2 = \{0.005,\ 0.008,\ 0.008\}$. These are already acceptable values.

The contribution from the compensation of the solenoidal steering that lies within Q1 must be added. Here the value of $1/\rho$ is smaller and the R_{36} function from the solenoid plus quadrupole is becoming smaller. This term adds an additional 15% to the above coefficients (at $E = 250\,\text{GeV}$).

Solenoid Field Plus Final Doublet. The effect of the synchrotron radiation (Oide effect) in the quadrupole is enhanced by the presence of the solenoidal field because of the increased dispersion function to the IP. This will be negligible at a 20-mr crossing angle.

Tolerance on Solenoidal Field Strength Stability

If the solenoid field were to change, the orbit to the IP would change and the beams would not collide. With the beam separation proportional to the solenoidal field and between 200 and 80 μm, and a tolerance on the beam separation for a 1/2% luminosity loss of about 2.4 nm, the field must be stable to one part in 10^5. Because the effect is a steering effect, this is a jitter tolerance and should be met quite easily.

11.7.4 Summary

From the point of view of the requirements on the crab cavity and the solenoidal field, the considerations of this section suggest that the 20-mr crossing angle is acceptable. This allows us to couple the big bend angle (used to obtain IP separation and reduce muon backgrounds) with the crossing angle, and to have the space to use permanent magnets for the first entrance and exit quadrupoles. The permanent magnet exit quadrupole is helpful by providing focusing close to the IP (which is necessary because of the large exit beam divergence) securing the high-quality beam removal optical path crucial for post-IP diagnostics. Permanent magnet fields can be quite stable under thermal change.

It is an important result that the first quadrupole must be displaced by up to 45 μm when the solenoidal field is turned on to correct the dispersion. This is a large movement compared to the nanometer stability required for this quadrupole under colliding conditions.

An experiment with an X-band phase mixer should be undertaken to confirm the possibility of maintaining a 0.2° relative phase tolerance between the two crab cavities.

11.8 The Beam Extraction and Diagnostic System (The Dump Line)

The main functions of this system are to optimize luminosity, to characterize beam properties at the interaction point, and to transport beams from that point to a dump with minimal backgrounds in the detector from these or any secondary functions that may occur. Beam characterization includes the measurement of current, position, profile, polarization, energy, and low-order correlations on a bunch-to-bunch basis for feedback and stabilization. A magneto-optical and diagnostic layout is described that provides such functions. We also consider the possibilities for e, μ, n, and γ secondary lines and dump experiments as well as energy recovery and local reuse of an assumed 10 MW of power in each 500-GeV beam. An earlier condensed version of this section was given in [Spencer 1995b].

To accomplish all of this, we need to know the detailed composition and characteristics of the outgoing beam(s) under different, possible circumstances. Clearly, these characteristics depend on those assumed for the incoming beam. Based on an assumed set of incoming beam parameters and transport optics we then make predictions for the outgoing beams that are used to guide the design of the outgoing, dump line optics. Typically, these beams have a significant number of pairs and more photons than leptons. Thus, if background simulations for the detector then imply an unacceptable situation, this procedure has to be iterated until a consistent solution is achieved.

Our approach was to develop a "straw man" design, *i.e.*, to assume a set of upstream characteristics that are reasonable but conservative to provide a worst-case scenario that emphasizes the major problems in constructing the transport system. The current design is a reasonably versatile one that takes the primary, outgoing disrupted beam (including photons) from the IP to the dump with minimal loss of particles. We have also included the low-energy pairs that are produced during the strong beam-beam interaction. We have found no basic limitations on the achievable luminosity imposed by the dump line. Furthermore, it provides a range of configurations that allow a variety of options.

While our primary goal was to optimize the luminosity while disposing of the various secondary beam components, it is also important to provide any monitoring and feedback that can optimize the average, usable collision rate at the IP. Thus, beyond simply dumping the beam, there are other functions that run from the necessary to the desirable that will be considered a part of the dump line:

- Beam control and stabilization,
- Diagnostics and monitoring - including luminosity and polarization,
- e, μ, n, γ secondary beams and parasitic experiments,
- Polarized sources for γ, μ and e^+ beams, and
- Energy recovery.

Due to the high power in the outgoing photon beam and the cost of beam dumps, we decided that the photons and primary leptons should share a common beam dump. This implies an available distance for beam studies of $\approx$150 m before the outgoing, high-energy photons begin to cause problems for the present dump design.

Because the SLC was a prototype for the NLC, we begin by reviewing the SLC and the FFTB experience relative to the NLC design. Next, we summarize the more important working assumptions in terms of a table of parameters characterizing the input and the output optics and beam characteristics at the IP. Next we describe the design procedure and give some intermediate results that were used to arrive at the final design. A horizontal chicane is used to separate the outgoing photon and electron beams, which are comparable in number and density, to allow separate experiments, before both beams are recombined into a common dump. Some rather sophisticated measurements and capabilities are possible over the available distance that are compatible with a low-background dump. We have also tried to accommodate the possibility of beam dump experiments. However, various additional simulations need to be done to confirm this and certify specific designs. Certain hardware is discussed where relevant. Finally, we summarize our conclusions and discuss the work that still needs to be done.

11.8.1 Comparison with the SLC

One advantage for the NLC dump design relative to that for the SLC is a horizontal crossing angle ($\theta_{c,x}$=2$\times$10 mr) at the IP that allows us to avoid kickers and septa for separating the counterpropagating beams. A related but more subtle advantage of this is that it allows us to reverse the polarities between the ingoing and outgoing IP doublets for better control of the larger outgoing horizontal disruption angle and emittance.

The much smaller vertical spot sizes assumed for the NLC overcome other differences to make its disruption larger. Although this complicates the disposal problem, it still allows all of the SLC measurements to be done as well as others that may not be practical there. For example, we can measure the energy loss distribution and use precise rf BPMs in the beginning of the line to measure position, angle, and timing of individual bunches where this may be impractical for the SLC due to its larger peak deflection angles that produce rms outgoing angular spreads that are four times larger than our worst case.

However, the outgoing, disrupted energy spreads and energy offsets calculated for the NLC are more than a factor of twenty larger. The outgoing beam also includes a significant number of synchrotron radiation photons that can produce low-energy pairs quite apart from the beamstrahlung. Because the emittance and disruption angle is largest in the horizontal, this implies that we want our analyzing magnets to bend horizontally which should also simplify any beam dump experiments.

Rather than 30 kW in each SLC beam, one has to deal with nearly 10 MW in each NLC beam. There is a factor of ten in energy for 500-GeV beams in the NLC, the same rf pulse repetition rate of 120/s, and a factor of twenty or so in beam current per rf pulse from accelerating a multibunch train in each pulse. This increased beam power poses certain problems for intercepting detectors and implies significantly higher operating costs. For 10¢/kWh, this represents a potential refund of as much as $45K/day if energy is restored to the grid or otherwise recycled before it is dissipated in the dump.

11.8.2 Basic Design Procedures, Constraints, and Assumptions

The optics can only be realized after we know the characteristics of the outgoing beam from the IP. The procedure was to take the upstream final-focus design in the form of TRANSPORT [Brown 1977] and convert this to DIMAD [Servranckx 1990] for predicting the spot characteristics at the IP due to emittance growth from synchrotron radiation in the dipoles and quadrupoles. One assumption was that the effect of the energy loss on the optics, especially in the quadrupoles, can be neglected. The predicted beam parameters resulting from DIMAD were then used in ABEL91 [Yokoya 1986] to predict the composition and characteristics of the outgoing beam as well as to produce ray sets for all particle types for tracking. The ABEL results were checked against analytic calculations where possible and used to simulate the dump line with TRANSPORT (for design) and TURTLE (for tracking) [Carey 1982]. Table 11-40 gives several configurations that were used with those labelled `A' the current ones for 250- and 500-GeV incident beams.

In the Table, $\mathcal{L}_{e^\pm}$ and $\mathcal{L}_{e^-e^-}$ are the predicted incident channel luminosities for these parameters whereas $\mathcal{L}_{\rm Compton}$ and $\mathcal{L}_{\gamma\gamma}$ are secondary to the e^+e^- channel. $\mathcal{L}_{\gamma\gamma}$ is rather large because it includes contributions from real and virtual photons and the beamstrahlung parameter Υ is fairly large. Υ is an important measure of the QED and QCD backgrounds expressed in terms of $\gamma\gamma \rightarrow e^+e^-$ pairs and minijets ($\gamma\gamma \rightarrow$ X + anything). Such parameters are described in more detail below. Because there is still debate on how to calculate the hadronic backgrounds in terms of the various possible quark and gluon contributions at these energies, they are not listed. There is interesting physics available here if it could be measured but an upgraded SLC would be a better place to find new hadrons, quark molecules or glueballs.

Because electrons and positrons are generally interchangeable, we will often talk about electrons but all parameters such as N_B, the number of electrons (or positrons) per bunch apply equally to both beams unless otherwise stated. In fact, N_B can also be the number of photons per bunch [Spencer 1995c] in a general linear collider (GLC). The last column for 500-GeV beams was our primary case for the optics design. In the absence of other input, we used only the **disrupted** beam from this worst case having the lowest $\beta^*_{x,y}$ and highest Υ. The numbers in the table and the ray sets that were used were predicted using a modified version of ABEL that was made operational on the SLAC VM system. Calculations were done for all of the columns shown and the output was archived for general use.

The length of the extraction line was set by the outgoing beamstrahlung photons and their predicted size at the dump:

$$12\sigma^\gamma_{x'} \times L_D \leq 2R_D \ , \tag{11.134}$$

where L_D is the distance from the IP to the dump face and R_D is its radius. For a dump window of 20 cm in diameter and outgoing angular spreads of $\sigma_{x',y'}$=92,43 μr, taken from Figure 11-58, we have ≈150 m of usable length available. The apertures of the outgoing magnets were sized to pass these photons (and pairs) outside the detector so that the outgoing photons pass through the system into the dump without serious loss.

$\sqrt{s}_{\rm NLC}$	(GeV)	500	500A	1000	1000A	`Worst'
$f_{\rm rep}$	(Hz)	180	180	120	120	120
n_B		90	90	75	90	75
$\gamma\epsilon_y$	(10^{-8} m)	5	8	5	10	5
N_B	(10^{10})	0.65	0.65	1.1	0.95	1.1
σ_x^*/σ_y^*	(nm)	319.7/3.2	285.9/4.52	360/2.3	226.1/3.57	245/2.5
σ_z	(μm)	100	100	100	125	125
β_x^*/β_y^*	(mm)	10/0.1	8/0.125	25/0.1	10/0.125	10/0.1
$\mathcal{L}_G$	($10^{34}{\rm cm}^{-2}{\rm sec}^{-1}$)	0.53	0.42	1.05	0.96	1.42
D_x/D_y		0.073/7.3	0.090/5.70	0.049/7.60	0.132/8.33	0.104/10.2
$\theta_D = \theta_{x,\max}$	(μrad)	233	257	175	238	256
Υ		0.09	0.10	0.27	0.30	0.32
$\mathrm{H}_D \equiv \mathcal{L}/\mathcal{L}_G$		1.37	1.42	1.30	1.36	1.56
$\mathcal{L}_{e^\pm}$	($10^{34}{\rm cm}^{-2}{\rm sec}^{-1}$)	0.73	0.60	1.37	1.30	2.20
$\langle s\rangle/s_{\rm NLC}$			0.972		0.913	
$\langle \mathrm{E}_e - \mathrm{E}_\diamond\rangle/\mathrm{E}_\diamond$		0.019	0.032	0.0711	0.103	0.127
$\delta_B \equiv \delta\mathrm{E}_e^{\rm rms}/\mathrm{E}_\diamond$		0.042	0.065	0.120	0.143	0.167
$\mathcal{L}_{100}/\mathcal{L}_{e^\pm}$		0.441	0.376(0.405)	0.305(0.323)	0.195(0.218)	0.182(0.206)
$\mathcal{L}_{90}/\mathcal{L}_{e^\pm}$		(0.83)	(0.80)	(0.84)	(0.75)	(0.69)
N_γ/N_B		0.88	0.98	1.21	1.67	1.77
$\langle \mathrm{E}_\gamma\rangle/\mathrm{E}_\diamond$		0.027	0.033	0.059	0.062	0.072
N_p/N_B	(10^{-7})[a]		3.95		8.69	
$\langle \mathrm{E}_p\rangle$	(MeV)[a]		23.4		25.8	
$\mathcal{L}_{\rm Compton}$			0.23		0.80	
$\mathcal{L}_{\gamma\gamma}$	($10^{34}{\rm cm}^{-2}{\rm sec}^{-1}$)		0.10		0.56	
$\mathcal{L}_{e^-e^-}$			0.23		0.45	

[a] N_p/N_B is the ratio of outgoing positrons per incident electron for energies $\mathrm{E}_p > 2$ MeV and angles $\theta \geq 10$ mr.

Table 11-40. *Beam-beam effects for e^+e^- at $E_{\rm cm} = 0.5$, 1.0 TeV and $\gamma\epsilon_x = 5 \times 10^{-6}$ m. Quantities enclosed in (...) are calculated analytically rather than from the simulations.*

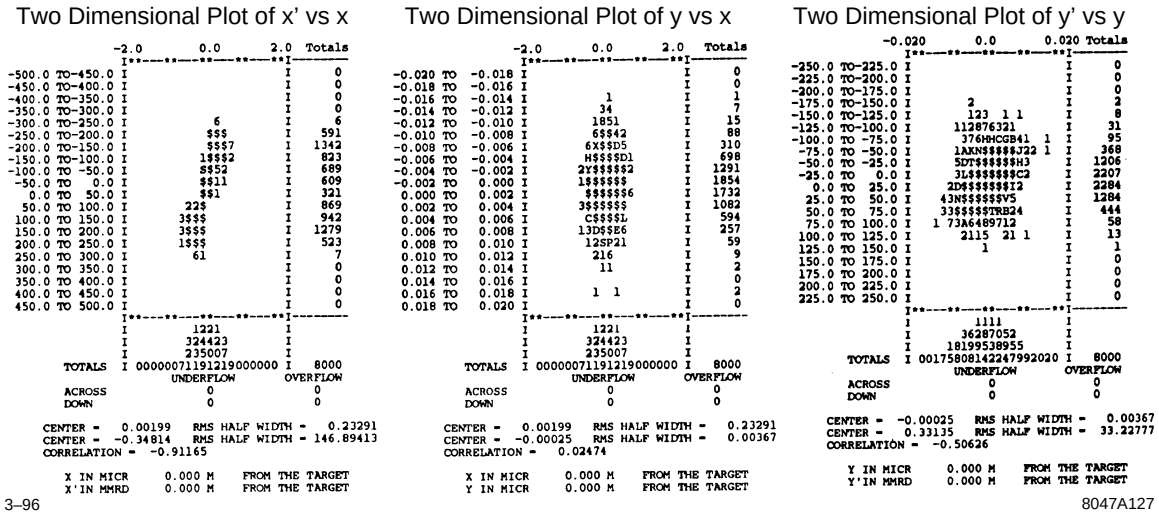

Figure 11-55. *Disrupted beam distribution at the IP for the `Worst' case in Table 11-40*

11.8.3 The Beam-Beam Calculations

Histograms of our initial working set of 8000 disrupted particles are shown in Figures 11-55 and 11-56. From these figures we see the shearing of the upright ellipses from the focusing by the other beam just after the interaction as well as emittance growth in both transverse and longitudinal directions. However, the energy loss and spreading with a very long tail extending nearly down to the Compton edge (50 GeV for 500-GeV beams and a Nd:YAG laser) is probably the most significant effect. These and the subsequent histograms based on them were taken directly from third-order TURTLE. The beamstrahlung distributions that are shown next were also done with TURTLE for uniformity.

Figures 11-57 and 11-58 show the outgoing photon ray set for the same input beam. From the Table there are actually more outgoing photons than electrons but a thinning factor was used. When the configurations are frozen we will enlarge the ray sets and also characterize them analytically. The average photon energy and distribution looks very much like a bremsstrahlung spectrum and relates directly to that for the outgoing disrupted electrons.

The effective, transverse photon emittances are typically smaller than the disrupted, charged particle beam because of the differing effects of disruption. Although this is discussed later, we note that the photon spot size provides a better, realtime measure of the incoming, unperturbed beam profile than the disrupted electrons. The outgoing photons were important in determining the length and acceptance of the extraction line because they can't be controlled in the same way as charged beams and because they have enough high energy photons to allow a good, nonintercepting profile monitor for bunch-to-bunch measurements outside of the solenoid. Figures 11-59 and 11-60 show the TURTLE output at various distances from the IP after tracking the beams through the quadrupoles inside the detector. From these figures and Figure 11-65 below, we see from the rms beam sizes and the numbers of particles outside the picture frame, that the disrupted primary beams and their associated beamstrahlung should clear the quadrupole apertures and solenoid with negligible loss.

From these figures, the primary disrupted beam is still the determinant of the magnet apertures but neither beam imposes any severe restrictions—at least while they are in the solenoid. The most damaging effect is then expected to come from the low-energy pairs. We have calculated their spectrum and detector simulations are now being done. This is complicated by the low energies, the crossing angles, and the strong solenoidal fields at the IP that necessarily couple the transverse coordinates.

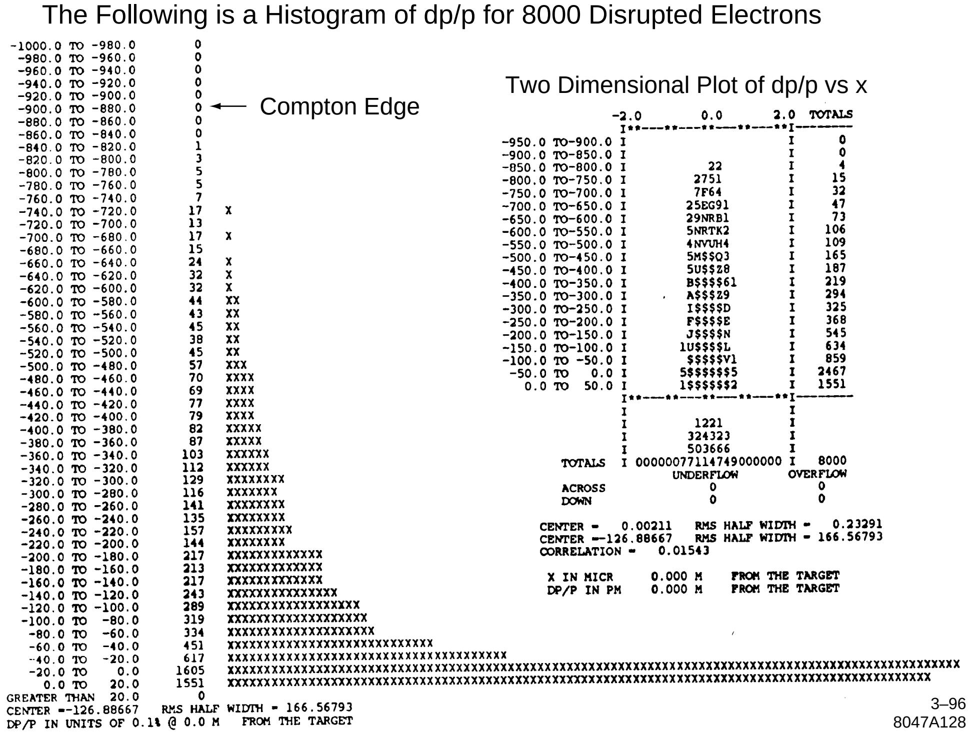

The Following is a Histogram of dp/p for 8000 Disrupted Electrons

```
-1000.0 TO -980.0          0
 -980.0 TO -960.0          0
 -960.0 TO -940.0          0
 -940.0 TO -920.0          0
 -920.0 TO -900.0          0
 -900.0 TO -880.0          0
 -880.0 TO -860.0          0
 -860.0 TO -840.0          0
 -840.0 TO -820.0          1
 -820.0 TO -800.0          3
 -800.0 TO -780.0          5
 -780.0 TO -760.0          5
 -760.0 TO -740.0          7
 -740.0 TO -720.0         17   X
 -720.0 TO -700.0         13
 -700.0 TO -680.0         17   X
 -680.0 TO -660.0         15
 -660.0 TO -640.0         24   X
 -640.0 TO -620.0         32   X
 -620.0 TO -600.0         32   X
 -600.0 TO -580.0         44   XX
 -580.0 TO -560.0         43   XX
 -560.0 TO -540.0         45   XX
 -540.0 TO -520.0         38   XX
 -520.0 TO -500.0         45   XX
 -500.0 TO -480.0         57   XXX
 -480.0 TO -460.0         70   XXXX
 -460.0 TO -440.0         69   XXXX
 -440.0 TO -420.0         77   XXXX
 -420.0 TO -400.0         79   XXXX
 -400.0 TO -380.0         82   XXXXX
 -380.0 TO -360.0         87   XXXXX
 -360.0 TO -340.0        103   XXXXXX
 -340.0 TO -320.0        112   XXXXXX
 -320.0 TO -300.0        129   XXXXXXXX
 -300.0 TO -280.0        116   XXXXXXX
 -280.0 TO -260.0        141   XXXXXXXX
 -260.0 TO -240.0        135   XXXXXXXX
 -240.0 TO -220.0        157   XXXXXXXXX
 -220.0 TO -200.0        144   XXXXXXXX
 -200.0 TO -180.0        217   XXXXXXXXXXXXX
 -180.0 TO -160.0        213   XXXXXXXXXXXXX
 -160.0 TO -140.0        217   XXXXXXXXXXXXX
 -140.0 TO -120.0        243   XXXXXXXXXXXXXXX
 -120.0 TO -100.0        289   XXXXXXXXXXXXXXXXXX
 -100.0 TO  -80.0        319   XXXXXXXXXXXXXXXXXXX
  -80.0 TO  -60.0        334   XXXXXXXXXXXXXXXXXXXX
  -60.0 TO  -40.0        451   XXXXXXXXXXXXXXXXXXXXXXXXXXXX
  -40.0 TO  -20.0        617   XXXXXXXXXXXXXXXXXXXXXXXXXXXXXXXXXXXXXX
  -20.0 TO    0.0       1605   XXXXXXXXXXXXXXXXXXXXXXXXXXXXXXXXXXXXXXXXXXXXXXXXXXXXXXXXXXXXXXXXXXXXXXXXXXXXXXXXXXXXXXXXXXXXXXXXXXXXX
    0.0 TO   20.0       1551   XXXXXXXXXXXXXXXXXXXXXXXXXXXXXXXXXXXXXXXXXXXXXXXXXXXXXXXXXXXXXXXXXXXXXXXXXXXXXXXXXXXXXXXXXXXXXXXX
GREATER THAN  20.0         0
CENTER =-126.88667   RMS HALF WIDTH = 166.56793
DP/P IN UNITS OF 0.1% @ 0.0 M   FROM THE TARGET
```

Compton Edge

Two Dimensional Plot of dp/p vs x

```
                   -2.0         0.0         2.0  TOTALS
                   I**----**----**----**----**I--------
-950.0 TO-900.0 I                          I        0
-900.0 TO-850.0 I                          I        0
-850.0 TO-800.0 I            22            I        4
-800.0 TO-750.0 I           2751           I       15
-750.0 TO-700.0 I           7F64           I       32
-700.0 TO-650.0 I          25EG91          I       47
-650.0 TO-600.0 I          29NRB1          I       73
-600.0 TO-550.0 I          5NRTK2          I      106
-550.0 TO-500.0 I          4NVUH4          I      109
-500.0 TO-450.0 I          5M$$Q3          I      165
-450.0 TO-400.0 I          5U$$Z8          I      187
-400.0 TO-350.0 I          B$$$$61         I      219
-350.0 TO-300.0 I       .  A$$$Z9          I      294
-300.0 TO-250.0 I          I$$$$D          I      325
-250.0 TO-200.0 I          F$$$$E          I      368
-200.0 TO-150.0 I          J$$$$N          I      545
-150.0 TO-100.0 I         1U$$$$L          I      634
-100.0 TO -50.0 I          $$$$$V1         I      859
 -50.0 TO   0.0 I         5$$$$$$$5        I     2467
   0.0 TO  50.0 I         1$$$$$$$2        I     1551
                I**----**----**----**----**I--------
                I                          I
                I           1221           I
                I          324323          I
                I          503666          I
         TOTALS I 00000077114749000000     I     8000
                          UNDERFLOW        OVERFLOW
         ACROSS               0               0
         DOWN                 0               0

CENTER =    0.00211   RMS HALF WIDTH =    0.23291
CENTER =-126.88667   RMS HALF WIDTH = 166.56793
CORRELATION =    0.01543

 X IN MICR      0.000 M     FROM THE TARGET
 DP/P IN PM     0.000 M     FROM THE TARGET
```

3–96
8047A128

Figure 11-56. *Disrupted energy distribution at the IP in units of 0.1% for the `Worst' case in Table 11-40. The insert shows the correlation with the horizontal position x.*

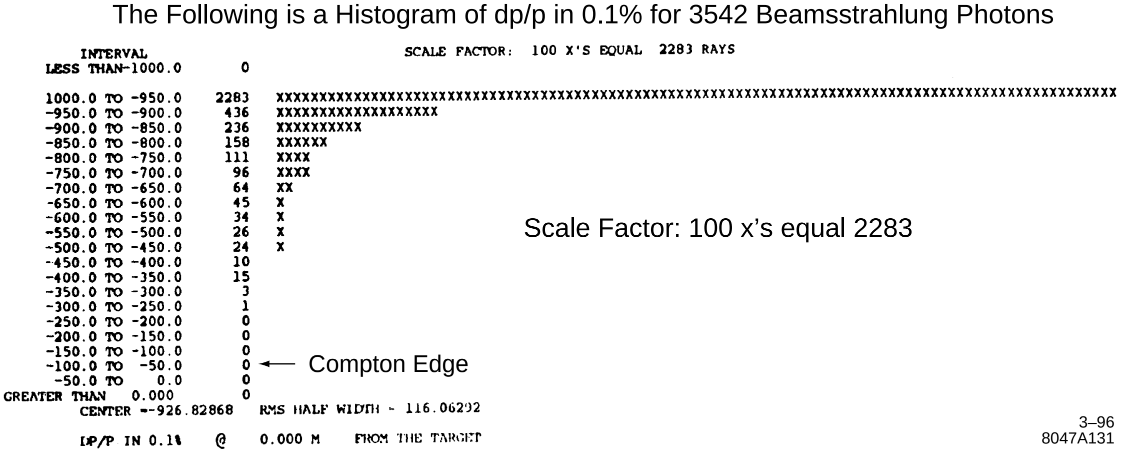

The Following is a Histogram of dp/p in 0.1% for 3542 Beamsstrahlung Photons

```
     INTERVAL                                  SCALE FACTOR:  100 X'S EQUAL  2283 RAYS
LESS THAN-1000.0        0

1000.0 TO -950.0     2283    XXXXXXXXXXXXXXXXXXXXXXXXXXXXXXXXXXXXXXXXXXXXXXXXXXXXXXXXXXXXXXXXXXXXXXXXXXXXXXXXXXXXXXXXXXXXXXXXXX
-950.0 TO -900.0      436    XXXXXXXXXXXXXXXXXXX
-900.0 TO -850.0      236    XXXXXXXXXX
-850.0 TO -800.0      158    XXXXXX
-800.0 TO -750.0      111    XXXX
-750.0 TO -700.0       96    XXXX
-700.0 TO -650.0       64    XX
-650.0 TO -600.0       45    X
-600.0 TO -550.0       34    X
-550.0 TO -500.0       26    X
-500.0 TO -450.0       24    X
-450.0 TO -400.0       10
-400.0 TO -350.0       15
-350.0 TO -300.0        3
-300.0 TO -250.0        1
-250.0 TO -200.0        0
-200.0 TO -150.0        0
-150.0 TO -100.0        0
-100.0 TO  -50.0        0
 -50.0 TO    0.0        0
GREATER THAN   0.000    0
      CENTER =-926.82868   RMS HALF WIDTH = 116.06292

      DP/P IN 0.1%    @    0.000 M    FROM THE TARGET
```

Scale Factor: 100 x’s equal 2283

Compton Edge

3–96
8047A131

Figure 11-57. *“Worst” case outgoing photon energy distribution from Table 11-40.*

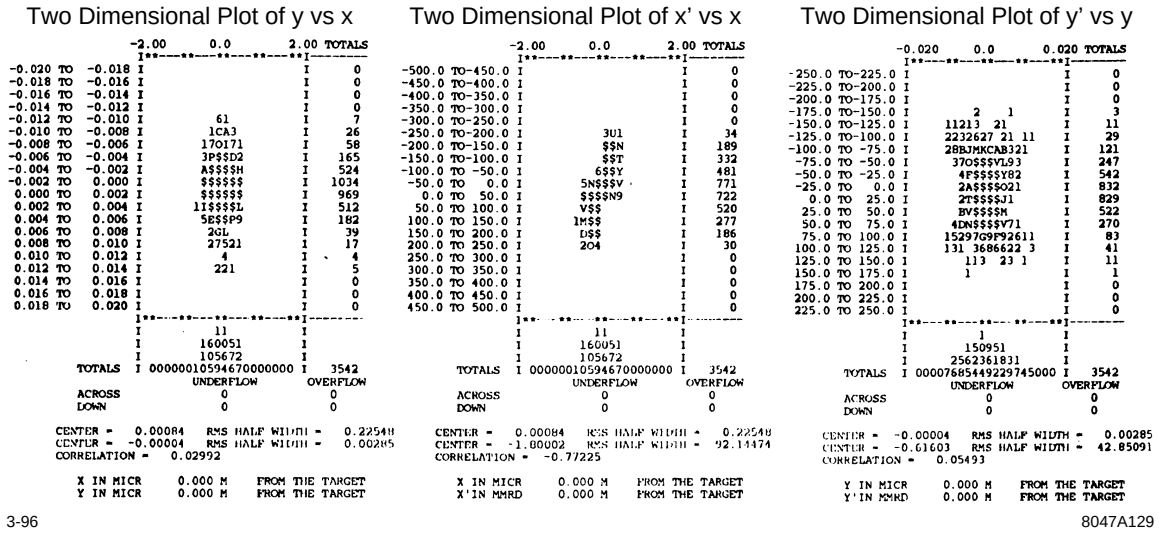

Figure 11-58. *`Worst' case transverse, outgoing photon distribution from Table 11-40.*

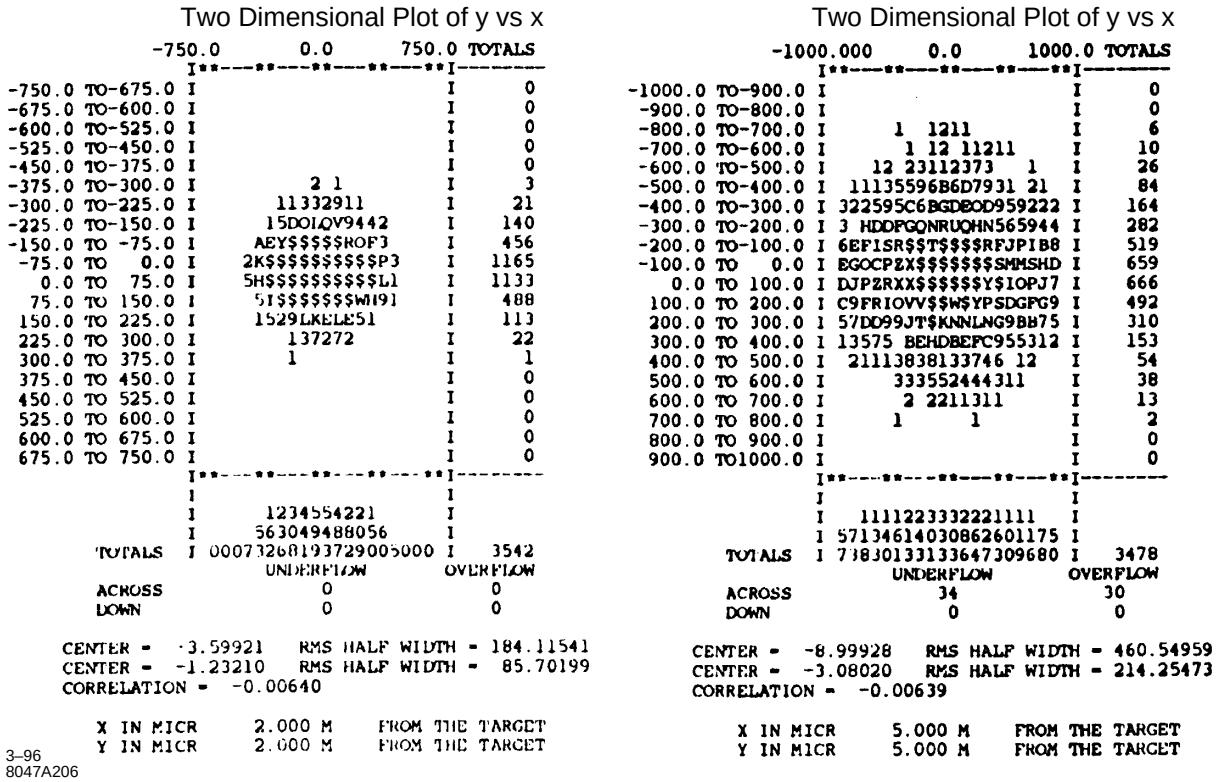

Figure 11-59. *Transverse, outgoing photon distribution at various distances from the IP in the solenoid (L_{sol}=5 m). The picture frame is ≥1/8 of the relevant quadrupole aperture.*

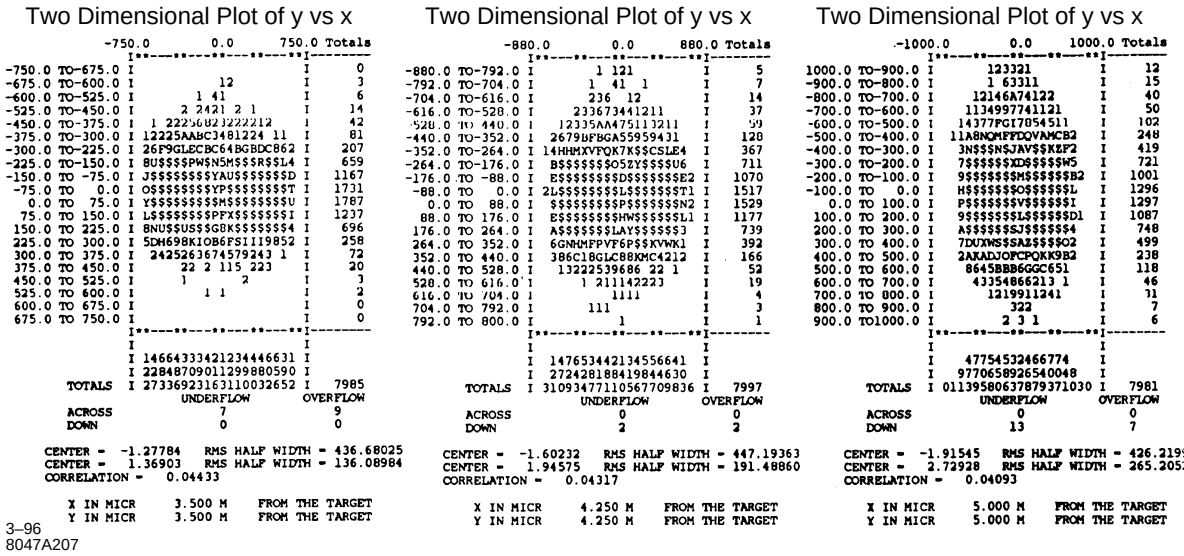

Figure 11-60. *Transverse, disrupted beam distribution at various distances from the IP in the solenoid. The picture frames are always ≥ 1/8 of the nearest quadrupole aperture.*

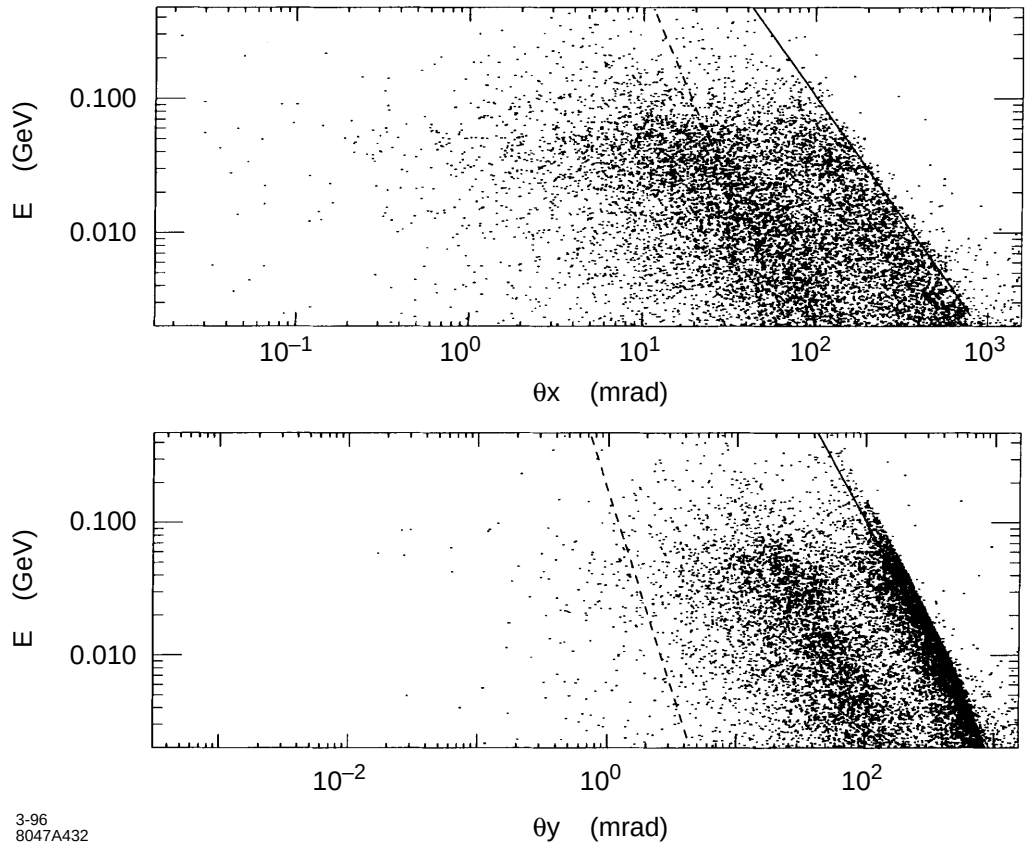

Figure 11-61. *Outgoing charged pairs at 1 Tev for Case 1000A in Table 11-40.*

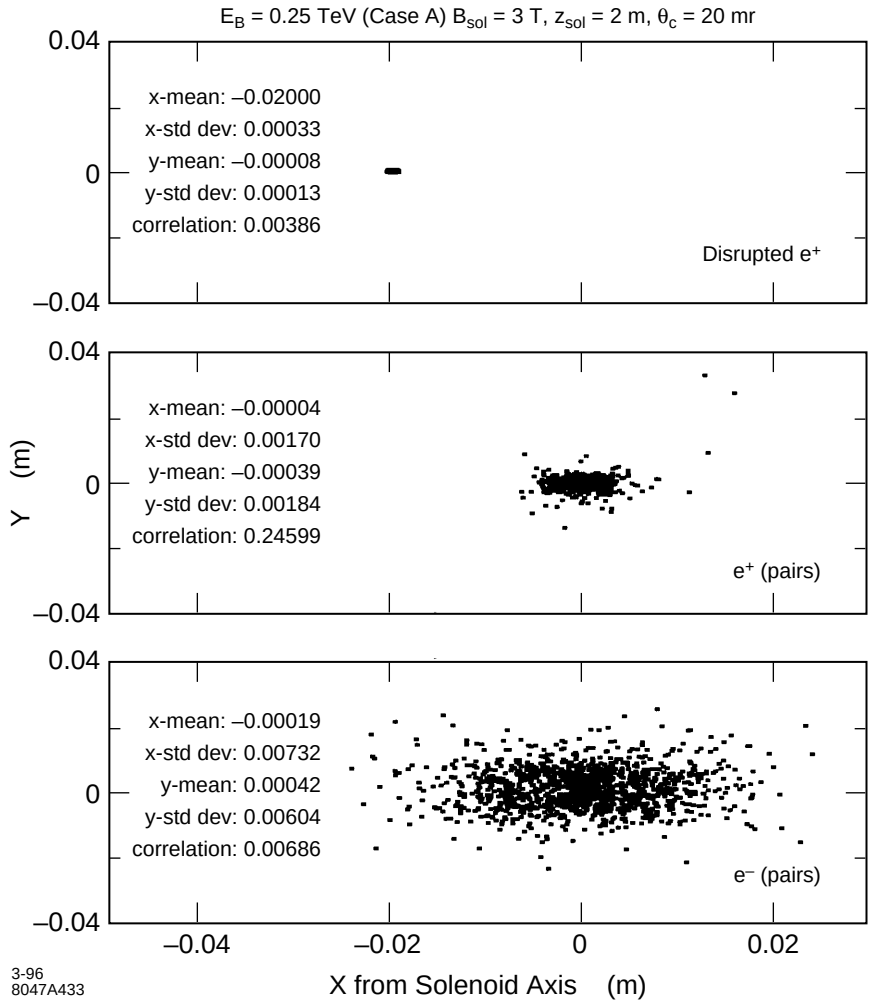

Figure 11-62. *Outgoing charged beams at 2 m from the IP in a strong solenoidal field.*

Such beams necessarily experience and are influenced by nonlinear fields in both the transverse and longitudinal directions before exiting the solenoid. Of equal importance, the response of an outgoing pair to the collective beam field after they are produced depends drastically on the charge and energy of each component.

Figures 11-61–11-64 show some characteristic predictions for the Case A columns in Table 11-40 corresponding to cuts $10 \leq E \leq 500$ MeV and $\theta \geq 10$ mr. The figures illustrate how the different species of outgoing particles complicate the design of the line—especially when it is desired to pass them without intercepting any (except via the required magneto-optical fields). While there are comparatively large angular and energy spreads between the incoming and outgoing electron and photon beams as shown above, the pairs are much worse and also include two opposite charge states. Figure 11-61 and 11-64 show this when we allow the pairs to drift 10 m after leaving the solenoid. In these figures, we assumed two different solenoid lengths for comparison. The results can be compared to the previous estimate of the length of the extraction line based on the outgoing photon beam characteristics. Fortunately, the pairs do not change our previous design in any essential way as we will discuss.

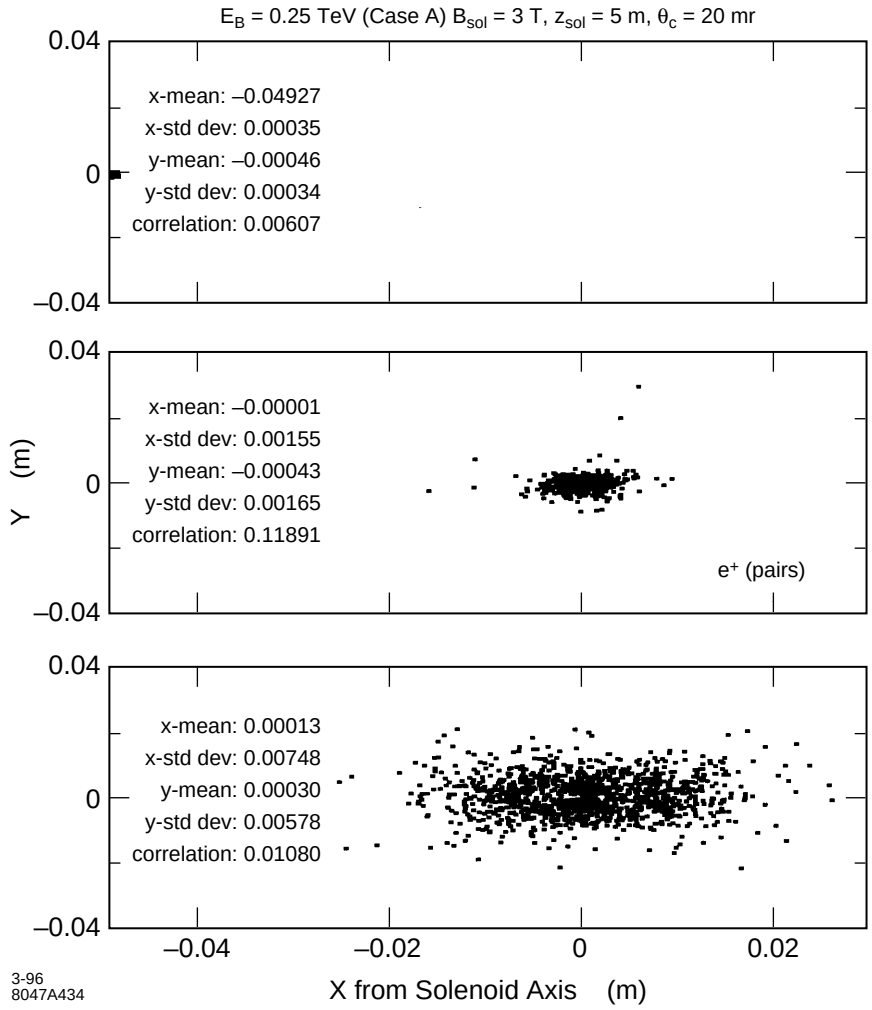

Figure 11-63. *Outgoing charged beams at 5 m from the IP in a strong solenoidal field.*

Besides constraining our optical and hardware design options, this forced us to continually constrain the apertures as well as the field integrals during the design optimization to ensure viable magnets that allow all of these beams to pass. Other constraints were related to the requirements imposed by the different possible measurements and experiments that might be required. For example, the electron spin rotation and depolarization from the bends and the beam-beam interaction as well as the energy resolution necessary to resolve the low-energy electrons near the Compton edge (the most sensitive ones for monitoring beam polarization) constrained the strength and disposition of the dipoles. A related constraint was the need to capture off-energy bunches from the linac or ones that did not collide and therefore lose any energy from the strong beam-beam interaction. Lastly, because the pairs also carry information about the luminosity in terms of the beam sizes at the IP, we wanted to pass them outside the solenoid to make measurements on them before dumping them in separate, reentrant dumps.

The simplest procedure is to sample the higher energy part of the pair spectrum because this is the most accessible and easiest to measure with the necessary resolution. The pair dumps are modest in both size and cost as indicated in

Table 11-40. The relative proportion of Breit-Wheeler, Bethe-Heitler and Landau-Lifshitz pairs depends on the cuts, but Breit-Wheeler production from two real photons is generally negligible at those energies.

We have laid out the essential assumptions and presented the results of calculations that provided the various input beams required for the detector simulations and the optics design. On the assumption that the detector studies show no irreconcilable conflicts with the ingoing or outgoing IR optics, the problems to be solved become reasonably well defined.

For example, given that l^*=2 m, we showed what the distributions of the outgoing beam components look like along the solenoid axis, *i.e.*, what the masking, the magnets, and the diagnostics within the detector must look like to accommodate such beams and provide the required beam stay-clear. For these outgoing beams, we anticipated the optics design and showed that we can get all the beam components out of the solenoid with virtually no loss if we can design rather strong quadrupoles with an open structure that can achieve their assumed characteristics in a strong solenoidal field ($\approx$3 T). A stronger solenoid for containment of the lower energy pairs appears desirable but this depends on the topology of the aperture, the crossing angles, etc. Ultimately, it is a question of the cost of the ideal structure *vs.* the practical question of what the detector design can accommodate. The next section gives the complete optics design from the IP to the dump that allows a variety of configurations and hardware for the options discussed in the introduction. Subsequent sections discuss these options and their hardware.

11.8.4 Beam Line Optics

In the SLC, the angular distribution predicted for the outgoing disrupted beam due to the strong focusing from the counterpropagating beam at the IP was a major factor in sizing the apertures of the strong IR quadrupoles. This was $\approx 10\ \sigma^*_{x'}$ for round beams which translates to $\approx 10\ \sigma_x$ at the exit of the last quadrupole adjacent to the IP. For the NLC, a closely analogous situation exists concerning the outgoing angles but perhaps the most important characteristic that dictates the optics is the energy spread in the outgoing beam. This also complicates the energy recovery for various methods such as rf deceleration where we might want the beam to pass through an accelerating structure where the energy-phase structure of the bunch at the cavities becomes important as does the transverse size. In the NLC, there will also be a significant number of lower-energy particles from beamstrahlung as well as pair production and the effective disruption parameter for such particles, that scales inversely with their energy, can become very large.

We note that the primary problem of transporting the outgoing beam to the dump is much simpler after it exits the detector. Figures 11-59 to 11-64 show the outgoing electrons, positrons and photons after various quadrupoles for various assumptions about the detector—typically assumed to end at 5.0 m from the IP. These results were computed through third-order with TURTLE and are dominated by the low order, chromo-geometric terms. In each Figure, the picture frame is $\leq$1/8 of the magnet aperture and the beam σ's are given in μm and μr. In all cases, the pole-tip fields and apertures of the magnets (including the beam dump) were sized to give $R_M \geq 12\sigma_{x,y}$ for the outgoing photons and disrupted electrons. In the initial doublet, that extends beyond 10 m from the IP, the apertures are $\geq 15\sigma_{x,y}$.

A number of configurations were tested and shown to be adequate under the stated assumption that we must take **all** photons and electrons to the beam dump with the stated size limit. Figure 11-65 shows one possible configuration that has space available for experiments, monitoring, and higher-order multipoles. It satisfies our criteria using only dipoles and quadrupoles. Further, some of the quadrupoles that are shown here were not excited for this particular optics. They act as potential tuning elements, *e.g.*, if QDD3 is turned off, the full energy, undisrupted beam will propagate to the dump in a point-to-parallel configuration. Lower energy particles will be overfocused so that the envelope of electrons tracked with TURTLE intersects that for the photons near 19 m from the IP. Thus, our first space available for beam size and polarization measurements comes between 10.5–16.2 m.

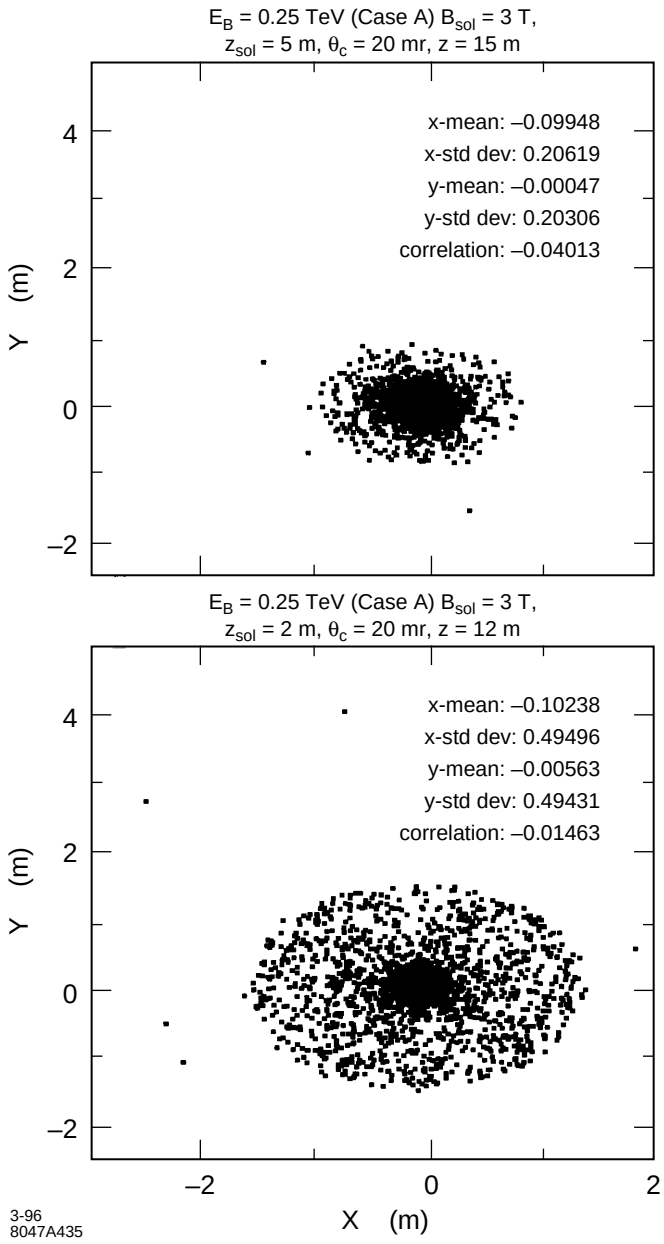

Figure 11-64. *Outgoing beams 10 m after a strong solenoidal field with $L_{\rm sol} = 2$ and 5 m.*

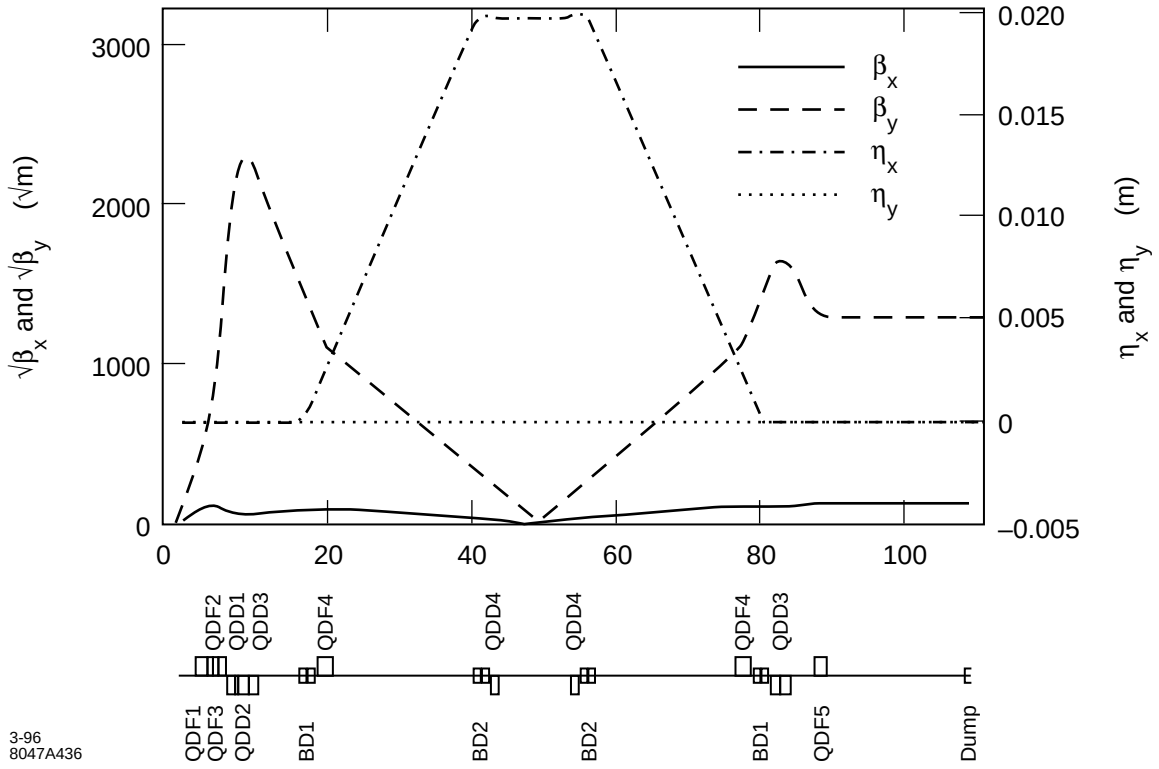

Figure 11-65. *Optical layout for the NLC dump line for the `worst' case in Table 11-40.*

The first dipole of the horizontal chicane, used to separate the outgoing photon and electron beams, begins at 16 m. It allows separate e and γ measurements or experiments before recombining both beams into a common dump at 110 m. The various bends in the chicane can serve as spectrometers as well as the chicane itself. Figure 11-65 shows the Twiss functions when the four bends are sized to separate the two beams by 12 sigma. Their maximum separation is

$$\Delta x = 2\rho_B(1-\cos\theta_B) + L_1\tan\theta_B \ , \tag{11.135}$$

where θ_B is the bend angle for the full energy of any one rectangular dipole of length L_B=$\rho_B sin\theta_B$ and L_1 is the separation between bends BD1 and BD2. Notice that this is just the dispersion η_x in the center of the chicane. This separation requires a minimum distance of

$$L_{\min} = 2\rho_B\sin\theta_B + L_1 \ . \tag{11.136}$$

The change in the bunch separation, due to the chicane, after this point in the central region is

$$R_{56} = \frac{\delta l_z}{\delta p/p} = 2\rho_B(\tan\theta_B - \theta_B) + L_1\tan^2\theta_B \ . \tag{11.137}$$

This is proportional to the rf phase shift [Spencer 1995a]. Thus we have a common beam pipe and sufficient dispersion to measure the energy and spread of the undisrupted beam.

For example, if we want to use the first bend for analyzing low-energy particles from the IP or from a laser interaction before this bend, then the first-order resolving power for some downstream location L is

$$R_1(\rho,\theta,L) = \frac{\rho(1-\cos\theta) + L\cdot\tan\theta}{[x_i\cos\theta + x_i'(\rho\sin\theta + L/\cos\theta)]} \ . \tag{11.138}$$

In the middle of the chicane R depends on the optics we impose. $R_{12}\rightarrow$0 for point-to-point so R=$\Delta x/10\sigma_x^*$=8000 for a magnification of 10. This region of the chicane can then resolve a single-beam, undisrupted energy spread of δp/p=0.0125% while the region directly in front of BD2 gives $R\approx$800 or a 0.13% capability.

Notice that there were several factors that constrained the bends: electron spin rotation as well as the energy resolution necessary to resolve low-energy electrons near the Compton edge (required for monitoring beam polarization). Further, dipoles drive many higher-order aberrations that act to blow the beam up that require higher multipoles to correct. These were not needed to get the beams into the dump with the 12-sigma constraint through the line.

Characteristic Angles and Some Related Disruption Effects

There are several processes that influence the beam and various characteristic angles that deserve discussion. The typical emission angle for most high-energy radiative processes such as incoherent bremsstrahlung is $\theta_r \approx 1/\gamma \approx 1\,\mu$r at 500 GeV. As the photon energy decreases, the angles begin to grow compared to θ_r as does the interaction volume of the electron. When the electron interacts with the collective field of the other bunch, it sees transverse electric and magnetic fields that are nearly equal. It is easy to show that these fields can bend an electron by angles significantly greater than θ_r so this angle is physically interesting. The resulting radiation, similar to synchrotron radiation, is called beamstrahlung.

A characteristic angle for the "full energy" primary, disrupted electrons is [Hollebeek 1981]:

$$\theta_d \equiv \frac{2Nr_e}{\gamma(\sigma_x+\sigma_y)} = \frac{D_{x,y}\sigma_{x,y}}{\sigma_z} \quad , \tag{11.139}$$

where $\sigma_{x,y}/\sigma_z$ is sometimes called the diagonal angle and equals θ_d for $D_{x,y}$=1. Typically, in the e^+e^- channel, the maximum disruption angle is $\theta_{x,max}$=θ_d because the disruption parameter in the vertical is so large that one gets overfocusing or a thick lens effect whereas the focusing over the length of the beam in x is weaker but cumulative or more like a thin lens. The rms angles are $<\sigma_{x,y}>= 0.550\theta_d$. For , the situation reverses and the vertical disruption angle dominates as expected.

Beyond θ^*=$\sigma_{x',y'}\ll\theta_d$, another angle of relevance here is the spin precession angle θ_s. This can be expressed in terms of the spin tune

$$\nu_s = \frac{E[GeV]}{0.44065}\cdot\frac{\Theta}{2\pi} \quad , \tag{11.140}$$

where Θ is some deflection angle in radians. For the bends used here, this is typically twice the maximum disruption angle θ_d=256 μr according to Table 11-40. Further, the bends rotate the polarization in a correlated way in the bend plane between the input and output rather than depolarize the beam assuming that radiative effects (spin flip) are small and that the emittance is small and that there are no significant orbit distortions. The effective polarization after such a bend is $P_{\rm eff} = P_{\rm inc}\cos(2\pi\nu_s)$=0.42–0.84.

There are still several depolarizing effects to be considered. The rms disruption angles cause a net depolarization. A previous section gives another due to an rms gaussian energy spread δ. Clearly, an energy spread will give rise to a spread in precession frequencies that can cause some depolarization but this appears small for the disruption angles and bend angles used here which is about 0.1 % for θ_d=256 μr and <2 % for a 1 mr of bend even at 500 GeV. This classical effect can be avoided insofar as the beam polarization measurement is concerned because the beam is dispersed with sufficient resolution to emphasize the undisrupted portion of the beam. A worse effect, pointed out by Yokoya and Chen, relates to spin-flip during the beamstrahlung process. This can be related to n_γ in Table 11-40. and was one constraint on our bend angles of 1 mr or so but this is not an intrinsic limitation and could prove useful to monitor beam overlap.

The final angle of relevance is the crossing angle θ_c at the IR. For multibunch trains, we may need to introduce a crossing angle and design the FF quadrupoles accordingly. This can decrease the collision efficiency ζ so that we have to introduce variable, crab-crossing cavities [Palmer 1990] that rotate the beams to the appropriate orientation at the IP or CP (the $e\gamma$ conversion point) to restore ζ. We have shown that such cavities will be required for all incident channels [Spencer 1995c] so we will assume that they exist.

Optical Considerations on Energy Recovery

For energy recovery, we want the purely transverse dispersive as well as the **mixed** transverse-longitudinal terms in the optics to be zero to all orders in $\delta \equiv (E-E_o)/E_o$. However, for energy recovery, we want to add another constraint that would not be important otherwise—the synchronicity or time (phase) variation with energy that makes different energy electrons arrive with the correct but differing phases required to lose (or gain) the correct energy. Until otherwise noted, this implies that a high-order achromat is desired (that is not otherwise required), with the corollary condition that we want a first-order or linear R_{56} term that we would like to make variable while otherwise maintaining the high-order achromatic behavior.

In practice, it is the energy-angle correlations as well as the purely angular and chromatic terms that are of most importance because of the small spots and the strong disruption at the IP. The most relevant terms without bending magnets, in standard notation, are:

Second Order:	$(1\|26), (3\|46)$	$(1\|16), (3\|36)$
Third Order:	$(1\|266), (3\|466)$	$(1\|166), (3\|366)$

where the second set of terms in each row is less important. The $(1|26)$ and $(3|46)$ terms are dominant but would not require correction if we only wanted to take the beam to the dump. In fact, they would help the loading on the dump window. The bunch length terms $(5|22)$ and $(5|44)$ enter at the level of 0.1 μm or 0.1 % of σ_z. If we add bending magnets, the only additional terms of importance are $(1|66)$ and $(1|666)$.

Although not essential for most of the other applications, reducing such terms improves things—especially the spectrometer resolving power that is important for the Compton measurements as well as measuring the energy distribution of the outgoing disrupted beam which in turn measures the overlap and distribution of the incoming beams. We should note that it appears more practical to use the 10 MW of power than to recover it to the grid.

Configurations for Beam Monitoring and Experiments

We have already discussed the point-to-parallel configuration for the primary beam. Of course, the undisrupted portion of the beam goes to the dump anyway but this has several different single-beam applications with differing focal points along the way to the dump. Some of these possibilities are discussed below and shown schematically in Figure 11-66.

11.8.5 Beam Control Hardware

The initial quadrupoles are assumed to be permanent magnets (PMs) made from SmCo and NdFe. We have actually made and used such multipoles at SLAC since 1982. Prototypes for the SLC final-focus quadrupoles were made and tested under a variety of conditions such as very strong transverse fields [delCorral 1982]. Figure 11-67 shows several PM systems including the SLC prototype, an SLC split-ring sextupole and an NLC prototype quadrupole with

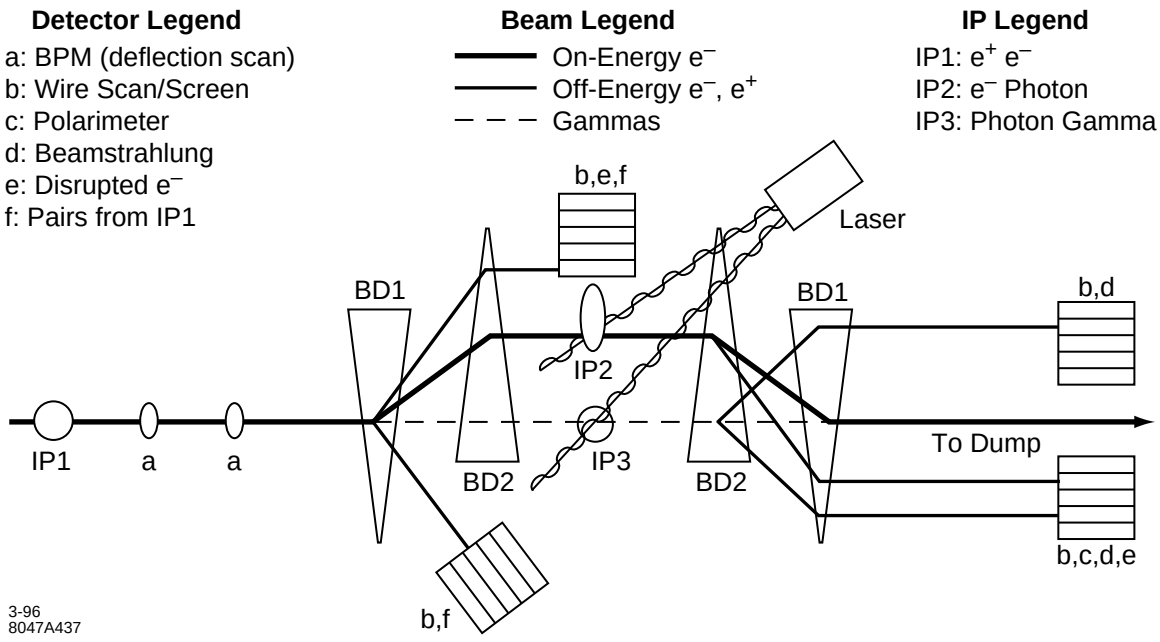

Figure 11-66. *NLC extraction line and diagnostic layout.*

a gradient G>500 T/m that was made in 1989. More recently our experience with the permanent magnet sextupoles used in the SLC damping rings since 1985 was reported [Gross 1994].

An important characteristic demonstrated by these sextupoles, applicable to any PM multipole that has symmetry about the median plane, is that there does not have to be any material in the median plane of the magnet. Thus, the large number of low-energy pairs that spread out from the solenoid axis to the position of the primary outgoing beam can be passed without necessarily intercepting any material. While it appears that conventional PMs can be used in the IR, some sample calculations using a new technique by which magnets with open structures can be designed and still achieve very strong fields also appear to be possible. Additionally, some of the dipoles are combined function magnets (dipoles/quadrupoles) to simplify the transmission of the larger energy spreads and emittances in the outgoing beam from the IP.

Finally, to avoid the nonlinearities in the end-field of the detector solenoid, we propose using a special wiggler in that region that is driven by the strong solenoid field itself. This element serves as a different kind of mirror plate for the detector field that shields the beam from the nonlinear transverse and longitudinal fields that occur in the end region by rerouting and reshaping the flux there. Ultimately that flux must be returned to the detector's conventional endcap by topologically distorting the wiggler's exterior mirror plate. Currently, a superconducting quadrupole (300 T/m) occupies this region and accomplishes a similar result.

11.8.6 Beam Monitors and Diagnostics

One of our primary goals is to provide diagnostics to help put the beams into collision, to maintain this state, and to measure and optimize luminosity. The latter involves diagnostics to characterize the beams: polarization, energy,

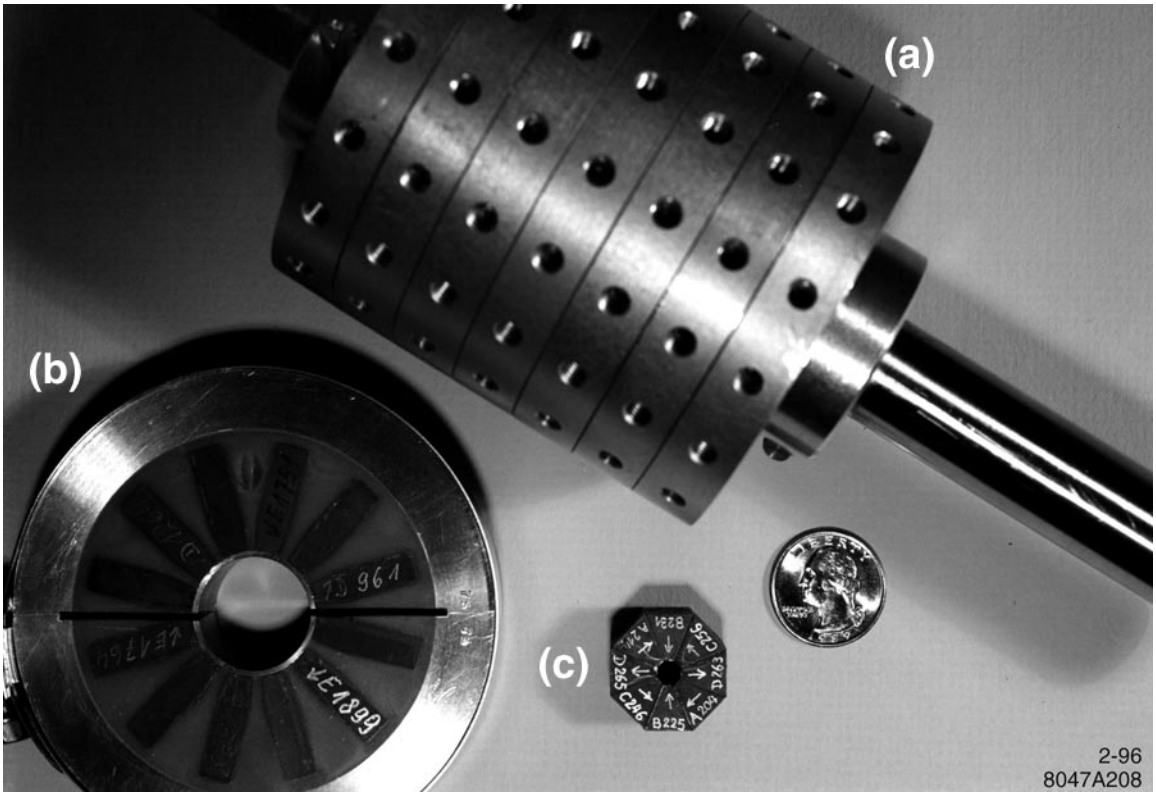

Figure 11-67. *Representative permanent magnet multipoles: (a) a 7-layer quadrupole for the SLC, (b) an SLC damping ring sextupole, and (c) a 500 T/m NLC quadrupole prototype.*

intensity, profile, positions (both absolute and relative), and the disruption of such quantities from the beam-beam and environmental factors.

We also need to dump the beams cleanly and safely. This involves the possibility of other functions such as secondary beams: e, μ, n and γ as well as other forms of energy recovery before final disposal.

The guiding principle in the instrument layout shown in Figure 11-66 was to minimize the material in the high-power beams. Thus, there is a significant use of lasers to control the production of additional particles. Rf BPMs for both position, angle, and timing information are assumed to begin near 5 m where the outgoing beams are still small and C-band cavities [Hartman priv] can have apertures comparable to the quadrupoles ($\approx \lambda/4$). Nevertheless, since beamstrahlung is unavoidable, there are possibilities [Norem 1995] to use either Compton or beamstrahlung photons that could prove useful for monitoring the position, size, and correlations of the bunches at the IP on a bunch-to-bunch basis. Clearly, beamstrahlung is quite sensitive to any changes in these parameters at the IP. In fact, the photon distribution is a better measure of the bunch profile at the IP than the outgoing, disrupted electrons as shown by Figures 11-55 to 11-60. We also assume BPMs, wire scanners, and screens similar to those used for the SLC [Field NIM].

The usual monitors such as BPMs and wire scanners are deployed at key locations for stabilization and feedback for position and energy control. It is understood that the BPMs include both amplitude and phase sensing. There are also more arcane monitors that look at the beamstrahlung from the IP as well as Compton backscattering that have

nanometer resolutions [Norem 1995] and can function on a bunch-to-bunch basis during colliding beam operation or with single beams.

Luminosity Measurements

To estimate the difficulty of this measurement, one can begin by looking at what the Bhabha rate might be for an "annular" detector subtending some angular range $\delta\theta$ near the front face of the first quadrupole in the dump line after the IP. Because this quadrupole (QDF1) is located at l^*=2 m with a radius of 7.5 mm, a reasonable minimum angle θ_1 occurs in the range $\theta_1 \approx$1–3 mr. If the predicted rate is reasonable for a bunch or even a train, we can then consider the backgrounds predicted in the beam-beam simulations to get an estimate of the signal-to-noise ratio. One can then consider the necessary characteristics required for the detector based on the characteristics of the backgrounds.

For unpolarized Bhabha scattering, a good approximation for the angles of interest here (a few hundred mr or less) is

$$\sigma(\delta\theta) = \int_0^{2\pi}\int_{\theta_1}^{\theta_2} \frac{d\sigma}{d\Omega}(e^+e^- \to e^+e^-) \approx \frac{4\pi\alpha^2}{s}\left[\frac{1}{\sin^2(\frac{\theta}{2})} + 4\ln\left(\sin\frac{\theta}{2}\right)\right]_{\theta_2}^{\theta_1} \quad . \tag{11.141}$$

Using $4\pi\alpha^2 = 261\,\mathrm{GeV}^2\,\mathrm{nb}$ with 250-GeV beams at very forward angles we have

$$\sigma(\delta\theta)|_{\theta_1}^{\theta_2} \approx 1.05\left(\frac{2}{\theta_1\theta_2}\right)^2(\theta_2-\theta_1)(\theta_2+\theta_1)\ \mathrm{pb} = 4.2\frac{1}{\theta_1(mr)}\frac{1}{\theta_2(mr)}\left[\frac{(\theta_2-\theta_1)(\theta_2+\theta_1)}{\theta_1\theta_2}\right]\mu\mathrm{b} \quad . \tag{11.142}$$

Assuming $\mathcal{L} = 6\cdot 10^{33}$ at 250 GeV for the 500-A column in Table 11-40 implies a Bhabha rate

$$R_B^{500A} = \mathcal{L}\sigma(\delta\theta)\Big|_{\theta_1=1mr}^{\theta_2=3mr} \approx 22,400/\mathrm{s} = 125/\mathrm{train} = 1.4/bunch \tag{11.143}$$

for a rep-rate of 180 pps in the linac with 90 bunches/train. Increasing θ_2 to 100 mr increases this rate by less than 15%. Again, using the column for 1000 A in the Table for 500-GeV beams, the corresponding numbers are

$$R_B^{1000A} = \mathcal{L}\sigma(\delta\theta)\Big|_{\theta_1=1mr}^{\theta_2=3mr} \approx 12,100/\mathrm{s} = 101/\mathrm{train} = 1.1/\mathrm{bunch} \quad . \tag{11.144}$$

Increasing θ_2 to 100 mr increases the rate to 114/train or 1.3/bunch. θ_2 was made small to be compatible with an rf shield that would extend from the last quadrupole toward the IP with a radius comparable to that of the quadrupole. While such a shield is not as important for the outgoing beam lines, there are no serious penalties imposed on the luminosity monitor for having one.

The value of θ_1=1 mr is reasonable from Figures 11-55, 11-58, and 11-59 for the typical beams of outgoing photons and electrons that we expect. While these two beams have comparably high intensities and are not expected to limit the measurement, the pairs are clearly a problem even though we expect on the order of 10^4/bunch crossing or 10^6 less than for the incident beams (or photons) per crossing. This is demonstrated in Figure 11-62 for the 500-A configuration. However, because these particles are predominantly below 1 GeV, some form of energy discrimination should be sufficient to deal with them.

However, because the pairs that are relevant here are in the higher-energy part of the pair spectrum, two important points can now be made. First, a sampling measurement of these particular pairs is itself a measure of the luminosity and is therefore a useful adjunct with a distinctly different signature. Further, this pair rate, in this location, is a problem that has to be dealt with anyway. Second, we can avoid this problem, at least for the Bhabha luminosity measurement, by going further downstream. This is clearly demonstrated in Figure 11-63 that shows the different beams at 5-m from the IP. However, from Figures 11-59 and 11-60 showing the x and y profiles for both the photons and electrons, this

is not the preferred location. Clearly, the optimal location is somewhere in between but a location near 2 m appears acceptable for making both measurements—especially because this allows the possibility of varying the solid angle subtended by the detector via tromboning or moving it longitudinally toward the IP. We expect almost 100 pairs within the quad aperture there.

Because halving the angle θ_1 quadruples the rate, the main questions are then how small we can make this angle, and whether it is practical to move the detector longitudinally to vary the subtended solid angle for different operating conditions such as beam scans. There are a number of interesting questions concerning the detector and its energy and timing discrimination for individual bunches.

Polarization Measurements

We propose to measure the longitudinal electron beam polarization (P_e) with a Compton polarimeter as shown in Figure 11-56 similar to how it is done for the SLC [Woods 1994]. The polarimeter will detect Compton-scattered electrons from the collision of the longitudinally polarized electron beam with a circularly polarized photon beam. The detector will be a segmented threshold Cherenkov counter similar to that in use at the SLC.

The counting rates in each Cherenkov channel are measured for parallel and anti-parallel combinations of the photon and electron beam helicities. The asymmetry formed from these rates is given by

$$A(E) = \frac{R(\rightarrow\rightarrow) - R(\rightarrow\leftarrow)}{R(\rightarrow\rightarrow) + R(\rightarrow\leftarrow)} = P_e P_\gamma A_C(E) \tag{11.145}$$

where P_γ is the circular polarization of the laser beam at the CIP at IP2 in Figure 11-66 and $A_C(E)$ is the Compton asymmetry function. $A_C(E)$ and the unpolarized Compton cross section are shown in Figure 11-68 for an electron beam energy of 250 GeV and a photon energy of 1.17 eV. The linear Compton spectrum is characterized by a kinematic edge at 46 GeV (180°) backscatter in the center of mass frame, and the zero-asymmetry point at 77 GeV (90° scattering in the center of mass frame).

The photon energy of 1.165 eV corresponds to using an Nd:YAG laser operating at 1064 nm. The long wavelength is chosen to avoid background from the reaction $e^-\gamma \rightarrow e^+e^-e^-$ that opens for

$$E_\gamma(\mathrm{eV}) > \frac{522}{E_e(\mathrm{GeV})} \quad . \tag{11.146}$$

However, this channel is mediated by a second photon and lower thresholds are possible when the second photon is real as from a secondary process such as Compton backscattering. Another laser photon can then produce a Breit-Wheeler pair. This cross channel process opens, in lowest order ($\eta \rightarrow 0$), for:

$$E_\gamma(\mathrm{eV}) > \frac{315}{E_e(\mathrm{GeV})} \tag{11.147}$$

and clearly depends on laser intensity and wavelength. Similarly, for beamstrahlung photons, the threshold is related to the Schwinger critical field by the laser's intensity and wavelength for a given incident electron energy.

The kinematics for Compton scattering gives the location of the Compton edge, $E_C(\mathrm{edge})$, and the edge asymmetry, $A_C(\mathrm{edge})$, as

$$\begin{aligned} E_C(\mathrm{edge}) &= E_e \cdot y \\ A_C(\mathrm{edge}) &= \frac{y^2 - 1}{y^2 + 1} \end{aligned} \tag{11.148}$$

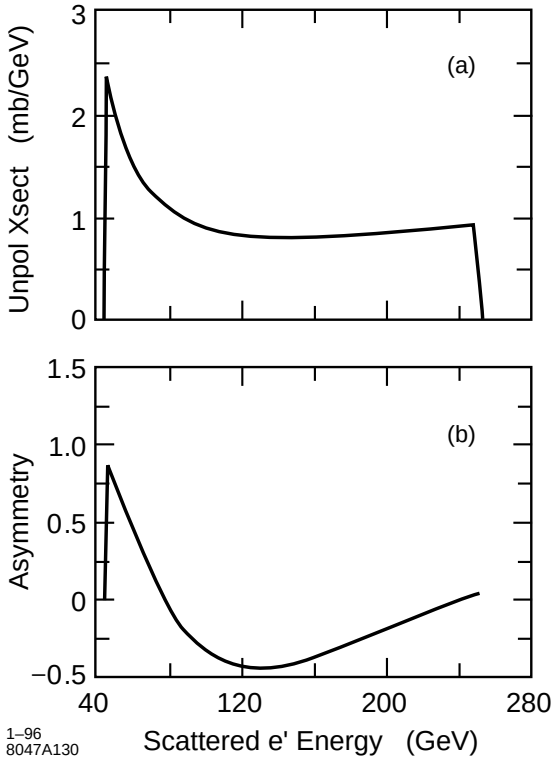

Figure 11-68. *(a) Linear Compton scattering and (b) asymmetry A_c for 250-GeV electrons.*

$$y = \frac{1}{1+\frac{4E_e E_\gamma}{m_e^2}} \tag{11.149}$$

where this is again in the limit that the classical, strong field parameter $\eta \ll 1$. The operant dimensionless, classical, strong field parameter is:

$$\eta = \frac{e\mathcal{E}_{\rm rms}\lambda\!\!\!^{-}_{\gamma}}{mc^2} = \frac{e\sqrt{\langle A_\mu A^\mu\rangle}}{mc^2} \quad . \tag{11.150}$$

This is described elsewhere [Bula 1995] where one sees the smearing effect on the edge from the nonlinear and multiple scattering effects due to high laser intensity. We have calculated this for an NLC example at 250 GeV using YACC, a variant of CAIN. A sample result is shown in Figure 11-69 and discussed further in the section on secondary beams.

Disruption of the electron beam during the collision process can have a significant effect on both the effective polarization of the electron beam during the collision process [Yokoya 1988] and on the measurement of beam polarization. The polarization of the undisrupted incoming beam can easily be determined by measuring the electron polarization when the positrons are absent. The effective polarization of the disrupted electron beam can be determined from Compton asymmetry measurements during collisions with studies of this asymmetry for different targeting of the the laser beam on the electrons at IP2. Corrections for the effects of jitter in the offsets between the beams at the IP can be made using multiple BPM measurements near the IP which is one objective of the spectrometer. Good knowledge of the disrupted electron beam energy spectrum will be required and this can be measured with a wire scanner near IP2.

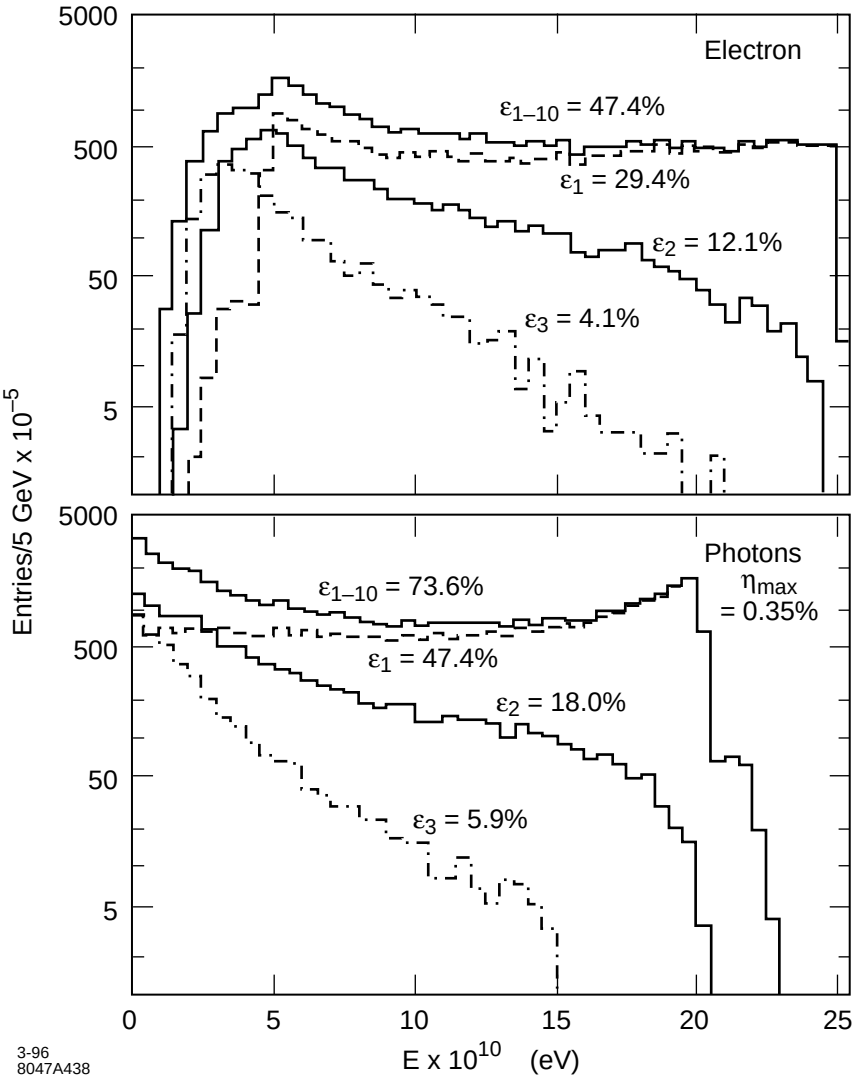

Figure 11-69. *Compton spectra for undisrupted beams at IP2 for high laser intensities.*

Because these electrons are quite low in energy and fall on the far out tail of the disrupted beam distribution, the only requirement is the ability to resolve their energy to within a few GeV, *i.e.,* we would like a resolving power at 500 GeV of:

$$R = \frac{P}{\Delta P} \geq 500.$$

We have provided $R > 2000$ for the full energy beam so there is no problem. We have pointed out before that the nonlinear effects are quite interesting in this regime but this will be discussed elsewhere.

Beam-Beam Deflection Scans

At the SLC, measurement of the deflection of one beam by the opposing beam at the IP, when they are offset, provides an important diagnostic which allows measuring, optimizing, and maintaining luminosity [Bambade 1989]. At the NLC, deflection angle measurements could prove just as valuable. For undisrupted beams, the luminosity varies exponentially with the square of the separation or offset between beams:

$$\frac{\mathcal{L}(\Delta_{x,y})}{\mathcal{L}(0)} = e^{-\Delta^2_{x,y}/2\Sigma^2_{x,y}} \tag{11.151}$$

where $\Delta_{x,y}$ is the transverse offset of the two beams and Σ_y (Σ_x) is the quadrature sum of the rms vertical (horizontal) beam size for the two colliding beams. A good test of our ABEL code is to compare to this prediction for a relevant set of NLC design parameters (Case A) while calculating a deflection scan. The results are shown in Figure 11-70 and are labeled by H_D but are more appropriately termed a collision efficiency factor ζ [Spencer 1995c] especially because the analytic calculations do not include disruption effects.

The deflection angles can be determined from BPM measurements before and after the IP. For flat, upright Gaussian beams which are centered on the x axis, the mean y deflection angle is given by:

$$< \theta_y >= \frac{2r_e N}{\gamma}\Delta_y \int_0^\infty dt \frac{e^{-\Delta^2_y/(t+2\Sigma^2_y)}}{(t+2\Sigma^2_y)^{3/2}(t+2\Sigma^2_x)^{1/2}} \tag{11.152}$$

where r_e is the classical electron radius, N is the number of target particles, and γ is the beam energy divided by the electron mass. Sample deflection scans for the NLC design parameters of Case A corresponding to Figure 11-70 are given in Figure 11-71.

According to Ref. [Raimondi 1995], the effect of beam-beam disruption will cause larger deflection angles than given in the above formula for y deflection angles, but will have a negligible effect on horizontal deflection angles. Our results indicate observable differences in both transverse directions, *e.g.,* 6–7% in the peak deflection angle in x and 9–10% in y. In both cases, the location of the peak deflection is pushed outwards but one sees that the predominant effect of the disruption is to push the location of the y peak outwards beyond 10σ or so for the chosen parameters. In fact, we can summarize the results of a number of calculations as follows: 1) small disruptions ($D_{x,y} \ll 1$) can use the analytic results while large Ds need simulations, 2) for a given set of parameters typical of Case A, the Y deflection angle converges to the same value ($\approx$220 μr) independent of σ_y, 3) the location at which this value is achieved comes at about $10\sigma_y$ in Figure 11-71, 4) this is true for a large range in σ_y, but 5) this value depends on the the value of σ_x assumed.

We can understand these results as due to the significant disruption/focusing of the beam in the collision region. A 200-μr angle over a 200-μm bunch length can give an offset of 40 nm or $\geq$ 10 σ. It seems advisable to test the characterizations made above with real experiments on the SLC where practical.

Because the maximum deflection angle will be comparable to or less than θ_d in Table 11-40, we may conclude that a radially uniform aperture in the outgoing quadrupoles should be acceptable for doing this diagnostic test even though

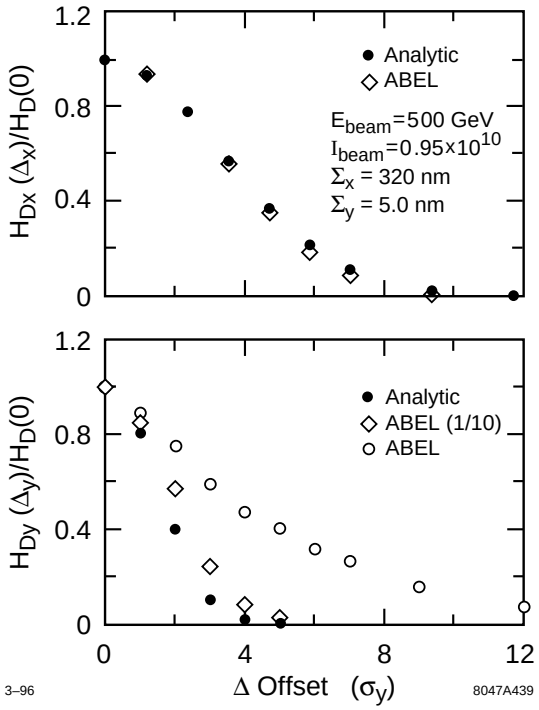

Figure 11-70. *Comparison of beam-beam enhancement factors H_D (or efficiencies ζ).*

the outgoing beamstrahlung now has a pointing angle that can sweep out angular apertures of nearly half a mr. This is not a problem because the apertures were sized to allow such angles. Rather, it provides another reason to place the primary beam dump closer to 100 m rather than the 150–200-m distance that would otherwise be allowed. Pair production is a worse problem for the quadrupole acceptances.

Another signature for disruption could come from measuring the photon moments as well as those of the electrons according to Refs. [Norem 1995, Field NIM]. The drawbacks of the deflection scan are obvious so that other alternatives, involving less beam time overhead and aperture, are being considered. This is one reason for the good energy resolution at IP1 in Figure 11-66. However, regardless of the method of choice, the deflection scan can be expected to provide a well-understood comparison that can be used for the NLC.

11.8.7 Beam Dump

The primary beam dumps have to dispose of essentially all of the power at the highest beam energy (750 GeV). Appendix 11.A argues that water should be the primary absorber in a cylindrical vessel housing a vortex-like flow of water with vortex velocity ≈1–1.5 m/s normal to the beam momentum. The vessel is 1.5-m, diameter and has a 6.5-m-long water section, followed by ≈1 m of water-cooled solids to attenuate a 750-GeV EM cascade shower. The beam enters through a thin window ≈1-mm thick and 20-cm diameter. Production of ≈5 l H_2/16 MW beam power from radiolysis [Walz, 1967] can be mitigated with a catalytic H_2/O_2 recombiner that has a closed-loop system that contains all radioisotopes.

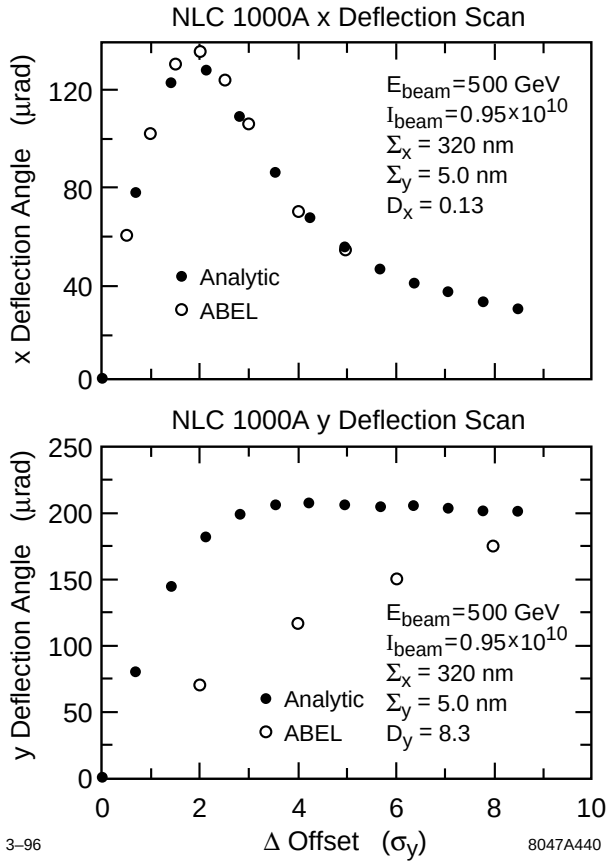

Figure 11-71. *Comparison of beam deflection scans corresponding to Figure 11-70*

The reader is referred to Appendix 11.A for the complete details. Here we only summarize the main characteristics and point out that a window size of 20 cm appears practical from all standpoints. We also note that there is the possibility to do some classical beam dump experiments after the dump which may be facilitated by dispersing the beams horizontally.

11.8.8 Secondary Beams

Beyond the usual possibilities, there are interesting opportunities to produce intense beams of higher mass leptons and hadrons as well as neutrons that haven't really been explored yet but could provide both a unique and comparatively inexpensive alternative source to nuclear reactors for some applications.

Muon Possibilities

Discussions on muon colliders have been resurrected recently so that the associated possibility of muon beams and colliders based on very high-energy, high-quality electron beams naturally arises. In fact, this is almost unavoidable

when one considers the backgrounds from muons that are also unavoidable and other questions of energy recycling and beam disposal.

Most discussions about muons use proton beams to produce the muons but Barletta and Sessler have looked at electroproduction recently. They concluded it was not viable but also did not consider the kinds of beams we will assume here. An important aspect is that we can use all the cooling tricks that have been discussed to cool the very large emittances from proton production although our assumption is that we can make them in a way that avoids many of the steps (and problems) normally required because we start at higher energies where there are several intrinsic advantages. The procedure is to produce high-energy photons as in the preceding section which are then used to produce the muon beams. Photoproduction was proposed previously for producing high-energy polarized positrons and there are a number of variants including the use of crystals and high-power lasers or FELs.

Photon Possibilities

This possibility relates to the second interaction region (IP2) and to the nonlinear QED experiment on the FFTB line at SLAC (E144). Clearly, similar problems are encountered with the Compton polarimeter and profile monitors based on photons. Related questions concern beam stability and synchronization so that much of the hardware has a number of interrelated uses. In Figure 11-69, we gave a worst-case scenario for IP2 assuming we were limited in both laser wavelength and power to the specified quantities. We point out that ignoring nonlinearities in the laser-electron interaction so that we can use unlimited laser power if we could get it, we could conceive of higher luminosity in this channel than currently appears slated for IP1. Table 11-41 gives some characteristic numbers. Additional results can be found in the section on the second IP and elsewhere [Spencer 1995c].

11.8.9 Energy Recovery and Its Applications

Following the introductory discussion, we note that it costs a significant amount to build and continuously dispose of such high-power beams in an environmentally acceptable way. Depending on the options that are pursued, there are at least four beam dumps required—not counting possible secondary lines. If we suppose that it takes another 4% of the total beam power just to dispose of the beams, this is another $1,000/day in power costs per dump. Clearly, this is worth pursuing if, in fact, one can find some nondisruptive means that are themselves environmentally acceptable. This question has been raised in the past at SLAC but the power involved and its subsequent uses implied it was not economically feasible.

Some ways to look at rf recovery methods are to remember how klystrons produce rf power from an electron beam, how recirculating systems work, and how high-frequency colliders such as CLIC propose to produce its rf power. If we want to store it or use it in some associated storage rings then we should consider superconducting systems. Any subsequent physics application should justify the cost. Ideally, whatever the sequence, one would end up with a final, dumped beam that has been reduced to an energy below the neutron production threshold to minimize activation of long-lived isotopes.

One obvious synergistic application is to try to drive an FEL with this beam in such a way that the same FEL can be used to produce variable, high-energy photon beams. It is interesting to point out that the Stanford recirculating SCA proposed and tested energy recovery to improve FEL efficiency [Rohatgi 1987]. One can expect such methods to provide up to 25 MV/m.

c.m. Energy (TeV)	0.5	1.0	1.5	TeV
Bunch Current, N_{max}	0.70	1.45	1.45	$\times 10^{10}$
Bunches/Train	100	75	75	
Bunch Separation	42	42	42	cm
Trains/s	180	120	120	s^{-1}
Coupling, $K \equiv \epsilon_y/\epsilon_x$	1.0	1.0	1.0	%
IR Beta, β_x^*/β_y^*	10/0.1	10/0.1	30/0.3	mm
IR Size, σ_x^*/σ_y^*	316/3.16	224/2.24	316/3.16	nm
Sizes at δz=4 cm	1.31/1.27	0.93/0.89	0.53/0.42	μm
Sizes at δz=8 cm	2.56/2.53	1.81/1.79	0.90/0.84	μm
Sizes at δz=12 cm	3.82/3.80	2.70/2.68	1.30/1.26	μm
Sizes at δz=20 cm	6.53/6.33	4.48/4.47	2.13/2.10	μm
Divergences, $\sigma_{x'}^*/\sigma_{y'}^*$	31.6/31.6	22.4/22.4	10.5/10.5	μrad
Laser $\lambda(\mu)$	1.05	2.1	3.2	μm
$< \delta t >_L$	0.1	0.1	0.1	ps
$< \delta l >_L$	0.3	0.3	0.3	ps
σ_C[b]	0.197	0.197	0.197	$\times 10^{-24}\mathrm{cm}^2$
Photons/Pulse, N_λ	4.2	4.7	2.9	10^{18}

Table 11-41. *Parameters for 0.5, 1 and 1.5 TeV. Electron emittances are $\gamma\epsilon_x$=5 $\times$ 10^{-6} m and $\gamma\epsilon_y$=5 $\times$ 10^{-8} m. The energy spread is σ_E/E=0.20 % and the bunch length is σ_z=100μ.*

11.8.10 Other Questions and Problems

There is a question concerning the sufficient separation between the various beams. This is especially relevant for the primary e and γ beams that are to be monitored and that have comparable densities and power. Another question is the e^- depolarization that we have not thought much about except for measuring it. Finally, there are all the alternatives for monitoring the luminosity, beam sizes, and offsets at the IP under normal operating conditions. We have proposed several methods in each case, and that work is still in progress. We have shown that there are significant differences between the SLC and NLC and that the NLC has more possibilities than the SLC because of the greater disruption and its secondary effects. We have also verified that virtually all of the corresponding diagnostic tools that are used for the SLC such as conventional deflection scans can be accommodated by the extraction optics and diagnostic devices even in the presence of pairs. However, this subject is a fertile area for exploration and it is being pursued together with that of strong PMs having open structures that are matched to the outgoing beam distributions and characteristics under differing diagnostic conditions. Finally, we strongly emphasize the importance of testing as many of the various calculations that have been presented here as practically possible. This could benefit the SLC as well as any future generation machine.

11.9 Conclusions and Comments

The NLC final-focus design fulfills all specifications, and achieves the desired IP spot sizes of about 300 nm$\times$4 nm, in the entire c.m. energy range between 350 GeV and 1.5 TeV, while maintaining a reasonable momentum bandwidth of $\pm 0.60\%$ or larger. The proposed design lends itself to an easy and straightforward upgrade to 1.5-TeV-c.m. energy, requiring only minor changes in geometry. The price to be paid for this flexibility is a final-focus length of about 2 km.

All possible sources of spot-size dilution, which are relevant on different timescales, have been budgeted, and are controlled by stabilization, tuning and maintenance systems. These systems also ease the tolerances on element vibrations, position drifts, and field stability. Most of the tolerances are not particularly tight, and have already been achieved at the FFTB or at other places. It is interesting that the luminosity loss caused by ground motion appears to be insignificant and that, therefore, the ground (bedrock) provides an ideal reference for magnet alignment and stabilization. In order not to destroy the coherence of the ground, care will be needed in the mechanical design of components and magnet supports. The primary engineering task will be to contain the effect of cultural noise.

The design of the NLC final focus profited greatly from experience with SLC and FFTB operation, whose influence is clearly exhibited by optical layout, aberration and tolerance budgets, tuning schemes, sensitivity studies, diagnostics, and operational procedures.

In conclusion, the NLC beam delivery system will not only produce small spot sizes at the IP, but it also promises redundant tunability, adjustability over a wide energy range, and, last not least, tolerable detector background.

11.A The Beam Dumps

If the efforts to economically recover a significant fraction of the spent electron beam energy are not successful, we will be faced with the tasks of safely disposing and dissipating these 10-MW beams. The working beam parameters are either:

90 Bunches/Train($\equiv n_B$) at $N_B \leq 0.85 \cdot 10^{10} \equiv 76.5 \cdot 10^{10}$/Train and $f_{\rm rep}$=180 Hz

or

90 Bunches/Train($\equiv n_B$) at $N_B \leq 1.25 \cdot 10^{10} \equiv 112.5 \cdot 10^{10}$/Train and $f_{\rm rep}$=120 Hz.

Then the beam energies and average power per beam are:

$E_\circ$ (GeV)	40	80	150	250	500	750
$P_{av,90/180}$ (MW)	0.88	1.76	3.30	5.51	11.02	16.52
$P_{av,90/120}$ (MW)	0.86	1.73	3.24	5.40	10.80	16.20

To assess the magnitude of the task, let us examine some engineering materials commonly used at accelerators. Specifically, we will look at the energy deposited in such materials at the beginning of an electromagnetic cascade and also in the region of peak energy deposition at shower maximum. At the beginning of the cascade (before any shower multiplicity), the average energy loss is approximately given by the ionization loss and can be written as

$$P'_{\rm av} \sim 1.6 \cdot 10^{-19} (-\rho \frac{dE}{dx}) f_{\rm rep} N_B n_B \tag{11.153}$$

and at shower maximum

$$P'_{\rm av,max} \sim \Pi_{\rm max} P'_{\rm av} \tag{11.154}$$

where $P'_{\rm av}$ and $P'_{{\rm av},max}$ are the average power depositions per unit length at the beginning and at shower maximum. ρ is the specific gravity of the material, dE/dx is the minimum ionization loss, and the other quantities are defined in Table 11-40.

For electrons, the location of the shower maximum $T^{e^-}_{\rm max}$, in units of radiation lengths $X_\circ$, and the maximum shower multiplicity $\Pi_{\rm max}$ are given by Rossi [Rossi 1952] as

$$T^{e^-}_{\rm max} = 1.01[\ln \frac{E}{\epsilon_\circ} - 1] \tag{11.155}$$

and

$$\Pi^{e^-}_{\rm max} = 0.31(\frac{E}{\epsilon_\circ})[\ln \frac{E}{\epsilon_\circ} - 0.37]^{-\frac{1}{2}} \tag{11.156}$$

where the critical energy $\epsilon_\circ$ of an absorber material is the unit of measure that makes these expressions independent of material. Typical values for carbon and lead are 76 and 7.6 MeV when one includes the effect of density variation, otherwise $\epsilon_\circ$ goes inversely with atomic number. The following tables give various quantities derived from the equations given above to judge the suitability of various materials for this application.

Table 11-42 gives the location of $T_{\rm max}$ as a function of beam energy. Table 11-43 gives the shower multiplicity $\Pi_{\rm max}$ at $T_{\rm max}$ as a function of beam energy. Table 11-44 gives the average power deposition per unit length at the beginning of the cascade (Π=1) for the two bunch train configurations (to first approximation energy independent). Table 11-45

Material	Be	C	H_2O	Al	Ti	Fe	Cu	W	Pb
E_0 =40	4.9	5.3	5.4	6.0	6.5	6.6	6.7	7.6	7.7
80	5.6	6.0	6.1	6.7	7.2	7.3	7.4	8.3	8.4
150	6.3	6.6	6.7	7.3	7.8	8.0	8.1	8.9	9.0
250	6.8	7.1	7.2	7.8	8.3	8.5	8.6	9.4	9.5
500	7.5	7.8	7.9	8.5	9.0	9.2	9.3	10.1	10.2
750	7.9	8.2	8.3	8.9	9.4	9.6	9.7	10.5	10.6

Table 11-42. *Location of $T^{e^-}_{max}$ for various materials (in units of X_0).*

Material	Be	C	H_2O	Al	Ti	Fe	Cu	W	Pb
E_0 =40	48	65	74	121	195	224	244	537	584
80	90	123	132	231	371	428	467	1030	1122
150	162	220	237	415	670	773	843	1867	2034
250	260	350	382	670	1084	1252	1365	3031	3302
500	497	678	732	1287	2087	2413	2631	5793	6390
750	727	993	1072	1889	3067	3546	3868	8630	9407

Table 11-43. *The shower multiplicity $\Pi^{e^-}_{max}$ at $T^{e^-}_{max}$ for various materials.*

Material	Be	C	H_2O	Al	Ti	Fe	Cu	W	Pb
$P_{av-90/180}$	68	80	44	98	158	255	282	500	284
$P_{av-90/120}$	67	79	43	96	154	250	277	490	279

Table 11-44. *Power deposition per unit length P'_{av} (W/cm) for the two bunch train configurations and various materials before shower development.*

give the same values for the two bunch train configurations at T_{max} as a function of beam energy. Note that the values in the two tables are very similar to each other.

It should be pointed out that calculations using the Monte Carlo code EGS gave power deposition values P'_{max} which are about 25–50% below those given in the tables using the equation for the shower maximum, whereas at the beginning of the shower, they are in very close agreement with the results obtained using P'_{av}.

As is readily apparent from the values presented in Table 11-45, removal of the vast amounts of thermal energy generated in solid materials in the region of shower maximum looks nearly impossible for the higher energy cases and the higher Z materials. Therefore, we will concentrate on examining the pros and cons of using water as the principal power absorption and dissipation medium in the beam dump.

11.A.1 The Beam Dump Vessel

For pulse- or bunch-train repetition rates of 180 Hz and 120 Hz, the train spacings are 5.6 ms and 8.3 ms, respectively. For a bunch spacing of 1.4 ns, the length of one train is 125 ns for 90 bunches and 105 ns for 75 bunches. Since energy

Material	Be	C	H_2O	Al	Ti	Fe	Cu	W	Pb
E_o=40	3.3	5.2	3.3	11.9	30.8	57.1	68.8	268	166
80	6.1	9.8	5.8	22.6	58.6	109.0	132.0	515	319
150	11.0	17.6	10.4	40.7	106	197.0	238.0	933	578
250	17.7	28.0	16.8	65.7	171	319.0	385.0	1516	938
500	33.8	54.2	32.2	126	330	615.0	742.0	2896	1815
750	49.4	79.4	47.2	185	485	904.0	1090	4315	2672

Table 11-45. *A. Maximum power deposition per unit length $P'_{\mathrm{av,max}}$ (kW/cm) for various materials as a function of beam energy with 90 bunches/180 Hz/0.85·$10^{10}e$.*

Material	Be	C	H_2O	Al	Ti	Fe	Cu	W	Pb
E_o=40	3.2	5.1	3.2	11.6	30.0	57.1	67.6	263	163
80	6.0	9.7	5.7	22.1	57.1	107.0	129.0	505	313
150	10.9	17.4	10.2	39.8	103.0	193.0	234.0	915	567
250	17.4	27.7	16.4	64.3	167.0	313.0	378.0	1485	921
500	33.3	53.6	31.5	124.0	321.0	603.0	729.0	2839	1783
750	48.7	78.4	46.1	181.0	472.0	886.0	1071.0	4229	2625

Table 11-45. *B. Maximum power deposition per unit length $P'_{\mathrm{av,max}}$ (kW/cm) for various materials as a function of beam energy with 90 bunches/120 Hz/1.25·$10^{10}e$.*

is principally lost by ionization from the primary electrons and secondary electrons or delta rays which are highly relativistic, the local microvolume exposed to these rays will have reached final temperature in the time frame of about 10^{-15} s after an individual bunch has passed. This is some three orders of magnitude less than the bunch width, some six orders of magnitude less than the bunch spacing, and some eight orders less than the length of one bunch train. Therefore, in the time frames of the bunch and the bunch train final temperature is reached instantaneously. On the other hand, significant thermal relaxation takes place on a timescale which is long compared to the approximately 100-ns length of a bunch train (and, incidentally, the pressure or shock waves generated by the sudden thermal expansion of the beam-heated microvolume will propagate outward at the velocity of sound in the local medium [∼1450 m/s], which is also on a timescale very long compared to the bunch spacing and long compared to the length of the bunch train). So, the pertinent question to ask at the onset of this examination is "What is the expected temperature rise due to one bunch train at $\mathrm{T_{max}}$?".

From experience and from simulations with the Monte Carlo code EGS, we can expect a beam size at $\mathrm{T_{max}}$ of $2\sigma_b$ ∼0.8 cm for an input size of $2\sigma_b$ ∼1 mm and the higher beam energies under consideration. Let us define a heat source term for the region of 0≤r≤σ at $\mathrm{T_{max}}$ and E_o=500 GeV

$$\mathrm{S} \stackrel{\mathrm{def}}{=} \frac{P'_{\mathrm{av,max}}\mathrm{C}}{(2\sigma_b)^2\pi/4} \tag{11.157}$$

where $C = 0.393$ is a constant to reflect the assumed transverse Gaussian beam intensity distribution. Numerically, we find

$$\mathrm{S} = \frac{32.2 \cdot 0.393}{0.8\pi/4} \sim 25.2 \ \frac{\mathrm{kW}}{\mathrm{cm}^3} \tag{11.158}$$

for the 90-bunch/180-Hz case. Then the temperature rise per bunch train is

$$\Delta T_T = \frac{\mathrm{S}}{\rho c_P f_{\mathrm{rep}}} \tag{11.159}$$

where ρc_P=4.22 J/cm^3°C is the specific heat capacity for water. This is approximately constant over the temperature interval of interest (it only decreases ∼1.5 %). We then find $\Delta T_T \approx$33°C for the 90-bunch train/180-Hz case at 500 GeV and ≈50° C for 750 GeV.

For comparison, the maximum water inlet temperature in mid-summer at the SLC is ≈30° C (≡ 90° F). So, peak bunch train temperatures at T_{max} would be ≈65 and 80°C. We should recall that the heat source term was defined as an average for the body of rotation bounded by $2\sigma_b$, and therefore somewhat higher values can be expected for a Gaussian distribution near r=0. On the other hand, EGS simulations with a Gaussian input often show a double-humped distribution at a depth of several radiation lengths with a small depression at r=0 resulting from the transverse spread of the electromagnetic cascade. Averaging over 2σ is a reasonable approximation. As a matter of fact, peak temperatures which are somewhat higher than the ones calculated at T_{max} are consistently found at a depth short of T_{max}. The reason for this is that in the early part of the electromagnetic cascade, the increase in shower multiplicity dominates over the increase in the transverse size of the beam on account of the higher average energy of the shower particles and consequential smaller scattering angles. At a depth short of T_{max}, this role is reversed and it is at that depth where peak temperatures are found. The discrepancy appears to be larger in low-Z materials.

The next question which needs to be asked is, "What is the significance of a temperature of 80° C, for example, in the beam-heated microvolume of water?" We can make a categorical statement that volume boiling of water needs to be avoided at all cost. The consequences would be a great reduction in the density of the power absorption medium and therefore a downbeam shift of T_{max}, perhaps no longer fully containing the longitudinal cascade shower within the dump itself. The boiling point of water at, for example, 7 atmospheres (≡100 psig) is ≈160° C. So, assuming for the moment that there is no thermal relaxation during the interbunch train period of 6–8 ms, one could accept a second bunch train and not reach the boiling point at the local pressure; with thermal relaxation, it would be at least three trains. But for continuous operation at 120–180 Hz, we must move the water transverse to the beam momentum vector, fast enough, with some element of conservatism, that no two successive bunch trains target on the same microvolume of water. Suppose we use a water velocity of ∼1 m/s, then the distance traveled by the lump of water during the interbunch train period is $V_w \geq 10^3$ mm/s$\times 5.6 \cdot 10^{-3}$s≈ 5.5 mm. This is almost what we need to avoid significant overlap of the microvolume element bounded by 2σ from two successive bunch trains.

The next question which we need to answer is, "What are the longitudinal and transverse dimensions to guarantee complete containment of the electro-magnetic cascade of a 750 GeV/16-MW electron beam in water?" From EGS and analytical work, we find ∼40 $X_\circ$ are needed to sufficiently attenuate the beam longitudinally. This does not address containment of 750-GeV muons. Of this total, ∼15–18 $X_\circ$ should be water. The remainder could be water-cooled solid materials. For water, 1$X_\circ$≡35.7 cm. Thus, the beam would first take a cold bath in ∼5.5–6.5 m of water. An additional 1 m of solids would complete the attenuation of the longitudinal cascade. The total dump length would then be ∼7.5 m.

The dump diameter needs to be large enough to attenuate the radial shower. Based on EGS and experience, $D_\circ$ ∼1.5 m of water should be sufficient. The next question to be answered is, "How much flow rate is required to keep the bulk water temperature rise from exceeding ∼30–35° C?" From simple calorimetry, we find ∼6800 l/min (≡1750 gpm). This should not present any great logistics problems.

Two beam dumps were originally designed and built at SLAC which use a vortex-like flow arrangement to economically dissipate the power from 2.2-MW, 25-GeV electron beams [Walz 1967a]. A schematic of such a dump is shown in Figure 11-72. Water is injected approximately tangential to the dump wall through a series of evenly-spaced holes from an inlet flow header located at the periphery of the cylindrical shell of the dump vessel. The water then flows spirally toward the center of the dump vessel where the exit manifold is located. In the region of interest, the velocity follows the laws of potential flow theory, namely V×r=const. Introducing the electron beam at a radius of ∼0.3 m guarantees a flow velocity transverse to the beam of ∼1 m/s for the flow rate of 2000 l/min (≡550 gpm). After traveling one complete revolution in the vortex, the heated microvolume of water has undergone complete mixing and is returning at a lower orbit. No danger exists for volume boiling.

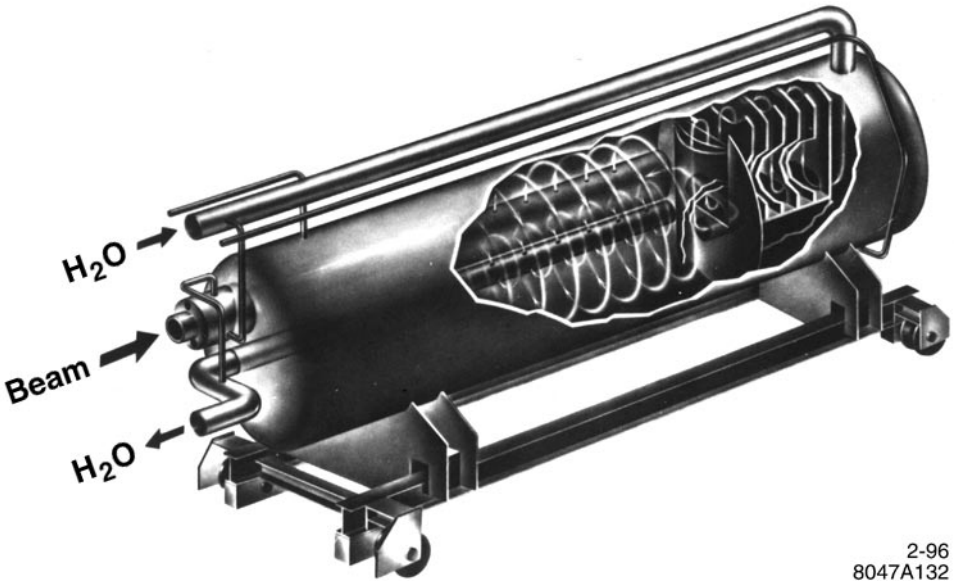

Figure 11-72. *Schematic representation of the primary beam dumps.*

11.A.2 The Window

The electron beam would enter the dump through a thin window separating the water from either vacuum or atmosphere. A number of materials such as aluminum, titanium, or copper appear suitable for this application, the latter being the most attractive. Since beam size and beam excursion from a nominal trajectory are expected to be small for an NLC, the window diameter can be small, say 10–15 cm. A reasonable wall thickness might then be δ=1 mm for a hemispherically-shaped window. The power deposited in the window can then readily be computed by multiplying $P'_{\rm av}$ by the window thickness and using the minimum ionization loss in copper $(-\rho\frac{dE}{dx})$ ~12.8 MeV/cm:

$$\mathrm{P}_w = \mathrm{P}'_{\rm av}\delta = 12.8\cdot 10^6(112.5\cdot 10^{10})120(1.6\cdot 10^{19})0.1 \sim 28\,\mathrm{W} \tag{11.160}$$

for the 90-bunch/120-Hz case. An EGS simulation at 50 GeV gave a value ~3% higher. To first approximation, we can neglect heat losses from the window by thermal radiation (and natural convection if there is atmosphere) to the upbeam world. We assume then that all heat is conducted through the window and removed by forced convection by water on the inside. Let us correct for a double convoluted Gaussian and obtain $\mathrm{P}_{\rm w,corr}$=28·0.393=10.9 W for the region 0≤r≤σ_b. After averaging over $2\sigma_b$ the effective heat flux into the water, neglecting lateral conduction for the moment, becomes q″=$\mathrm{P}_{w,corr}/\mathrm{A}_b$ = 10.86/0.01π/4≡1.38 kW/cm^2. This is in the nucleate boiling heat transfer range and, depending on flow velocity and subcooling, could be close to the transition from nucleate to film boiling. The latter is defined as a burnout condition.

Still neglecting lateral conduction, we find for the maximum temperature difference from the outside to the inside of the window (δ=1-mm thickness and k=3.9 Ws/mm^2°C/cm for copper).

$$\Delta T = \frac{q''\delta}{2}\mathrm{k} = \frac{1.38\cdot 10^3\cdot 0.1}{2\cdot 3.9} \sim 18°\mathrm{C} \quad . \tag{11.161}$$

To get an idea by how much lateral conduction reduces this temperature difference and the heat flux into the water, we use Fourier's Law of conduction

$$k\nabla^2 T + S = \rho c\frac{\partial T}{\partial \tau} \quad . \tag{11.162}$$

For steady state and internal heat generation, this reduces to the familiar Poisson equation

$$\nabla^2 T + \frac{S}{k} = 0 \quad . \tag{11.163}$$

For the axisymmetric case, the Laplacian ∇^2 can be written as

$$\frac{\partial^2 T}{\partial r^2} + \frac{1\partial T}{r\partial r} + \frac{\partial^2 T}{\partial z^2} + \frac{S}{k} = 0 \quad . \tag{11.164}$$

For finite cylinder boundary conditions with 0<z ≤2δ, 0<r≤σ_b and with heat production at a constant rate S per unit volume per unit time, a solution was given by Carlslaw [Carlslaw 1959] as

$$T = \frac{Sz(2\delta - z)}{2k} - \frac{16\delta^2 S}{k\pi^2} \sum_{n=0}^{\infty} \frac{I_\circ[(2n+1)\pi r/2\delta]}{(2n+1)^3 I_\circ\left[(2n+1)\,\frac{\pi\sigma}{2\delta}\right]} \sin\frac{(2n+1)\pi z}{2\delta} \quad . \tag{11.165}$$

The maximum temperature occurs at r=0, z=δ. Using only the first term (n=0) this reduces (assuming an adiabatic interface on the upbeam face of the window) to

$$\Delta T = \frac{s\delta^2}{2k}\left[1 - \frac{1.032}{I_\circ\left(\frac{\pi\sigma}{2\delta}\right)}\right] \tag{11.166}$$

where $I_\circ$ is a modified Bessel function of order zero. S=$0.393 \cdot P'_{\rm av}$=$13.9\,{\rm kW}/cm^3$. Then, we find

$$\Delta T_{\max} = \frac{13.86 \times 10^3 \times 0.1^2}{2 \times 3.9}\left[1 - \frac{1.032}{I_0\left(\frac{\pi \times 0.05}{2 \times 0.1}\right)}\right] \sim 2^\circ{\rm C} \quad . \tag{11.167}$$

Thus, for this case, lateral conduction is of great help and there are no worries about the heat flux into the water approaching the critical heat flux for the transition from nucleate to film boiling, even if we did not average over 2σ_b and instead used the real Gaussian distribution.

The last item to be checked for the window is the temperature rise per one bunch train (since we have already concluded that thermal relaxation is too slow to have any effect on individual bunches). Again, we find S=13.9 kW/ cm^3 and $\rho c|_{\rm Cu}$=3.45 J/ cm$^3{}^\circ$C

$$\Delta T_{{\rm T},W} = \frac{S}{\rho c f_{\rm rep}} = \frac{13.9 \times 10^3}{3.45 \times 120} \sim 33^\circ{\rm C} \quad . \tag{11.168}$$

In a fully restrained body and for E$\alpha|_{Cu}$= 282 psi/°C, we obtain a thermal stress rise

$$\sigma_{th} \approx E\alpha\Delta T = 282 \times 33 \approx 9330\ {\rm psi} \quad . \tag{11.169}$$

This would be excessive for fully annealed copper but should not lead to thermal fatigue in semi-hard or hard copper with fatigue strengths ranging from ~13,000 to 18,000 psi for N>10^8 cycles. Of some concern is the effect of cumulative radiation damage in the copper lattice due to the formation of clusters of vacancies and interstices with resultant embrittlement. For the expected current densities every atom in the lattice will "play musical chairs" and change its lattice site several times daily. It may be prudent to schedule a window change on a regular basis and not wait for a perforation to occur.

11.A.3 Isotope Production

The dominant radioisotopes produced in water by these high-energy electron beams are by photospallation on ^{16}O [Neal 1968]. They are in order of decreasing abundance and increasing half life:

$$
\begin{array}{ll}
^{16}\mathrm{O} \rightarrow {}^{15}\mathrm{O} & \mathrm{T}_{1/2} \sim \ 2 \text{ min} \\
\rightarrow {}^{13}\mathrm{N(small)} & \sim \ 10 \text{ min} \\
\rightarrow {}^{11}\mathrm{C} & \sim \ 20 \text{ min} \\
\rightarrow \ {}^{7}\mathrm{Be} & \sim \ 53 \text{ day} \\
\rightarrow \ {}^{3}\mathrm{H} & \sim 12.3 \text{ year}
\end{array}
$$

For practical purposes, we can neglect ^{15}O since it has mostly disappeared in ∼20 min. The isotope which influences tunnel entry and maintenance work the most is ^{11}C. A delay of three hours will allow most maintenance work. ^{7}Be is primarily removed by filtration in the demineralizer loop (not by ion exchange). Tritium builds up very slowly as $^{3}H_2O$ and can be managed by regularly planned disposal of the water as radioactive waste, albeit at a cost. Clearly, compared to solid power absorption materials (metals), water has significant advantages when viewed in light of residual radioactivity.

11.A.4 Radiolysis and Hydrogen Evolution

The deposition of the electron beam's energy in water causes radiolysis and dissociates the water molecule, thereby producing hydrogen, hydrogen peroxide, and oxygen per the following two relationships

$$
\begin{aligned}
\mathrm{H_2O} \xrightarrow{e^-} H_2^{\uparrow} \ &+ \ \mathrm{H_2O_2} \\
\mathrm{H_2O_2} \xrightarrow{e^-} O_2^{\uparrow} \ &+ \ \mathrm{H_2O} \quad .
\end{aligned}
\tag{11.170}
$$

After saturation and in the absence of oxygen removal processes such as corrosion, hydrogen and oxygen will evolve in gaseous form in places like the surge tank at the stoichiometric mixture ratio.

The measured rate of evolution of free hydrogen [Walz, 1967] is ∼0.3l H_2/MW-s [G(H_2)∼0.14 molecules H_2/100 eV]. Thus, for P_{av} ∼16 MW, the expected rate of evolution would be ∼5l H_2, less an allowance for power not directly deposited and dissipated in water or lost from the dump boundaries. The lower explosive limit (LEL) of hydrogen in air is 4%. A conservative maximum allowable concentration would be ∼1%. Thus, some 500l of the 1% H_2 in-air mixture has to be disposed of or processed per second. Since this gas contains most of the radioisotopes given above, release into the atmosphere is not an option.

One could build a delay line including holding tanks which would take care of the ^{15}O isotope. But ^{11}C with its $T_{1/2}$=20.3 min which evolves in the form of $^{11}CO_2$ is not manageable in a cost-effective way by this method. We have also studied the absorption of $^{11}CO_2$ in regenerative lime columns, but that method also proved to be cumbersome. Therefore, we developed at SLAC a catalytic H_2-O_2 recombiner with a capacity to process the radiolytically-evolved hydrogen for average beam powers up to 2 MW [Neal 1968, Walz 1969]. Four such recombiner facilities have been in use for more than 25 years with very low maintenance. Such a recombiner can be readily scaled up to process the gas from a 16-MW beam.

The recombiner uses a platinum-palladium catalyst through which the gases are pumped. The water vapor generated in the recombination of H_2 and O_2 is condensed out in the water spray which is generated by an ejector pump that provides the motive power to recirculate the gases. It is a closed-loop system and all gases and radioisotopes are always fully contained.

11.A.5 Summary

We showed that a beam dump to absorb and dissipate the power of 750 GeV/16-MW NLC beams is feasible using water as the primary power absorption medium. Such a dump could be a cylindrical vessel housing a potential vortex-like flow of water with the beam impinging at a radius of ∼0.3 m and a vortex flow velocity ∼1–1.5 m/s normal to the direction of the beam momentum vector. The vessel dimensions might be on the order of 1.5-m diameter and ∼6.5 m (∼18 X_o)-long for the water section followed by ∼1 m of water-cooled solid materials of higher Z to adequately attenuate the electro-magnetic cascade. The beam would enter the dump through a thin window (∼1-mm-thick copper would do). Isotope production in the water appears manageable relative to tunnel access requirements for maintenance and seems preferable to what can be expected for solid materials. The only drawback is production of ∼5l H_2/16 MW from radiolysis in water, but solutions exist to deal with this, notably the catalytic recombination of H_2 and O_2 into water, allowing for a closed-loop system containing all the radioisotopes.

References

[Burke 1995] D. Burke, "Proposal for New NLC Operating Plane", SLAC memorandum, unpublished (1995).

[Adolphsen 1995] C. Adolphsen, private communication (1995).

[Bernadini 1963] C. Bernadini *et al., Phys. Rev. Lett.* **10**, 407 (1963).

[Bambade 1989] P. Bambade *et al.,* "Observation of Beam-Beam Deflections at the SLAC Linear Collider", *Phys. Rev. Lett.* **62**, 2949 (1989); F. Zimmermann *et al.,* "Performance of the 1994/95 SLC Final Focus System", SLAC–PUB–95–6790, in *Proc. of the 1995 Part. Acc. Conf.* (1995).

[Bane 1995] K. Bane, C. Adolphsen, F.-J. Decker, P. Emma, P. Krejcik, F. Zimmermann, "Measurement of the Effect of Collimator Generated Wakes on the Beams in the SLC", SLAC–PUB–95–6865, in *Proc. of the 1995 Part. Acc. Conf.* (1995).

[Berz 1989] M. Berz, "Differential-algebraic description of beam dynamics to very high orders", *Particle Acclerators* **24**, 109 (1989).

[Bini 1991] C. Bini *et al., Phys. Lett.* **B** 135 (1991).

[Brinkmann 1990] R. Brinkmann, "Optimization of a Final Focus System for Large Momentum Bandwidth", DESY–M–90–14 (1990).

[Brown 1977] K. Brown, F. Rothacker, D. Carey, C. Iselin, "TRANSPORT - A Computer Program for Designing Charged Particle Beam Transport Systems", SLAC–91 (1977).

[Brown 1979] K. Brown and R. Servranckx, "Chromatic Correction for Large Storage Rings," SLAC–PUB–2270, in *IEEE Trans. Nucl. Sci.* **26**, 3598 (1979).

[Bula 1995] C. Bula, K.T. McDonald, E.J. Prebys (Princeton U.), C. Bamber, S. Boege, T. Kotseroglou, A.C. Melissinos, D.D. Meyerhofer and W. Ragg (Rochester U.), D.L. Burke, R.C. Field, G. Horton-Smith, A.C. Odian, J.E. Spencer, D. Walz (SLAC), S.C. Berridge, W.M. Bugg, K. Smakov and A.W. Wiedemann (Tennessee), "Observation of Nonlinear Effects in Compton Scattering", Submitted to *Phys. Rev. Lett.* , (Nov. 1995).

[Carlslaw 1959] Carlslaw, H.S. and Jaeger, J.C., "Conduction of Heat in Solids", (Oxford University Press, London, 1959).

[Carey 1982] D.C. Carey *et al.,* "DECAY TURTLE", SLAC Report 246 (March 1982).

[Chen 1993] P. Chen, "Disruption Effects from the Collision of Quasi-Flat Beams", SLAC–PUB–6215 (1993).

[delCorral 1982] J. del Corral, J.E. Spencer, S. St. Lorant, "Effects of Strong Transverse Fields on Permanent Magnets", SLC-CN-189 (1982).

[Dragt 1976] A.J. Dragt and J.M. Finn, "Lie Series and Invariant Functions for Analytic Symplectic Maps", *J. Math. Phys.* **17**, 2215–2227 (1976).

[Emma 1992] P. Emma, "Beam-Based Alignment of Sector-1 of the SLC Linac", *Proc. of 3rd EPAC*, Berlin (1992)

[Field NIM] Clive Field, "Wire Scanner System for the FFTB", NIM, To Be Published. See also SLAC–PUB–6717.

[Forest 1989] É. Forest, M. Berz and J. Irwin, "Normal form methods for complicated periodic systems: a complete solution using differential algebra and Lie operators", *Particle Acclerators* **24**, 91 (1989).

[Forest] The code DESPOT was written by É. Forest; the code TRACY by J. Bengtsson.

[Gross 1994] G. Gross, J. Spencer and SLAC's MMG, "Experience with the SLC Permanent Magnet Multipoles", Fourth European Part. Acc. Conf., London, England (1994). Also see SLAC–PUB–6558.

[Hartman priv] S. Hartman and T. Shintake, private communication.

[Hartman priv] S. Hartman, T. Shintake, N. Akasaka "Nanometer Resolution BPM Using Damped Slot Resonator", SLAC–PUB–95–6908, presented at 1995 Part. Acc. Conf., (1995).

[Hendrickson 1995] L. Hendrickson, private communication and this ZDR, Appendix D (1995).

[Hertzbach 1995] S. Hertzbach, private communication (1995).

[Hirata 1989] K. Hirata, B. Zotter, and K. Oide, *Phys. Lett. B* **224**, 437 (1989).

[Hollebeek 1981] The primary reference on disruption effects and their simulations is: Robert Hollebeek, "Disruption Limits for Linear Colliders", *Nucl. Instr. and Methods* **184**, 333 (1981).

[Irwin 1991] J. Irwin, "Final Focus System Optimization", *Proc. of Linear Colliders. 3rd International Workshop*, LC 91, Protvino, USSR, **Vol. 3**, V. Balakin *et al.*, (ed.) (1991).

[Irwin 1992] J. Irwin, "The Application of Lie Algebra Techniques to Beam Transport Design", SLAC–PUB–5315, published in *Nucl. Instr. and Methods* **A298**, 460 (1990).

[Irwin 1995a] These conditions were derived by J. Irwin (1995).

[Irwin 1995b] J. Irwin, presentation at SLAC (1995).

[Juravlev 1995] V.M. Juravlev, P.A. Lunev, A.A. Sery, A.I. Sleptsov, K. Honkavaara, R. Orava, E. Pietarinen, "Seismic Conditions in Finland and Stability Requirements for the Future Linear Collider", (1995).

[Keller 1993] L. Keller, "Muon Background in a 1-TeV Linear Collider", SLAC–PUB–6385 (1993).

[Lomperski 1993] M. Lomperski, "Compton Scattering off Blackbody Radiation and other Backgrounds of the HERA Polarimeter", *DESY* **93-045** (1993).

[Neal 1968] Neal, R.B., Editor, "The Stanford Two-Mile Accelerator", Chapter 20, (W.A. Benjamin, Inc., New York, 1968).

[Norem 1995] J. Norem *et al.*, "Tests of a High Resolution Beam Profile Monitor", *Proc. of the 1995 Part. Accel. Conf.*, Dallas, Texas, (1995).

[Oide 1988] K. Oide, "Synchrotron-Radiation Limit on the Focusing of Electron Beams", *Phys. Rev. Lett.* **61**, 15 (1988) 1713.

[Oide 1992] K. Oide, "Final Focus System with Odd-Dispersion Scheme", *KEK Preprint* **92**–58 (1992).

[Palmer 1990] R.B. Palmer, "Prospects for High Energy e^+e^- Linear Colliders", *Ann. Rev. Nucl. Sci.* **40**, 529 (1990).

[Pitthan 1995] R. Pitthan, "Re-Alignment: It is the Tunnel Floor which Moves, isn't It?", SLAC–PUB–95–7043, invited talk at 4th Int. Workshop on Acc. Alignment, Tsukuba (1995).

[Piwinski 1985] A. Piwinski, "Beam Losses and Lifetime", in CERN Accelerator School, Gif-sur-Yvette, France, *CERN* **85–19** Vol. II (1985).

[Raimondi 1995] P. Raimondi, F.J. Decker, P. Chen, "Disruption Effects on the Beam Size Measurement," SLAC–PUB–95–6882.

[Raimondi 1993] P. Raimondi, P.J. Emma, N. Toge, N.J. Walker, V. Ziemann, "Beam Based Alignment of the SLC Final Focus Superconducting Final Triplets", SLAC–PUB–95–6212. in *Proc. 1993 Part. Accel. Conf.*, Washington, DC (1993).

[Raimondi 1995] P. Raimondi, private communication (1995).

[Rohatgi 1987] R. Rohatgi, H.A. Schwettman and T.I Smith, "A Compact Energy Recovered FEL for Biomedical and Material Science Applications", *Proc. 1987 Part. Accel. Conf.*, Washington, DC, 1, 230 (1987).

[Rossi 1952] B. Rossi, *High-Energy Particles* (Prentice Hall, New York, 1952).

[Ross 1991] M.C. Ross *et al.*, "Wire Scanners for Beam Size and Emittance Measurements at the SLC", SLAC–PUB–5556 (May 1991).

[Ross 1994] M. Ross, *Proc. of Advanced Accelerator Concepts Workshop*, Lake Geneva (1994).

[Roy 1992] G. Roy, "Analysis of the Optics of the Final Focus Test Beam Using Lie Algebra Based Techniques", SLAC–397 (1992).

[Sands 1985] M. Sands, SLAC/AP–47 (1985).

[Servranckx 1990] R. Servranckx, K.L. Brown, L. Schachinger and D. Douglas, "User's Guide to the Program DIMAD", SLAC–0285 (1990).

[Shintake 1994] T. Shintake, "First Beam Test of Nanometer Spot Size Monitor Using Laser Interferometry", KEK-PREPRINT–94–129 (1994).

[Spencer 1995] J.E. Spencer, private communication (1995).

[Spencer 1995a] J.E. Spencer, "The SLC as a Second Generation Linear Collider", *Proc. 16th IEEE Part. Accel. Conf. and Int'l. Conf. on High Energy Accel's.*, Robt. Siemann ed., Dallas, TX, (1995).

[Spencer 1995b] J. Spencer, J. Irwin, D. Walz and M. Woods, "The SLAC NLC Extraction and Diagnostic Line", 1995 Part. Accel. Conf., Dallas, TX (1995).

[Spencer 1995c] J.E. Spencer, and "Beam-Beam Effects and Generalized Luminosity", SLAC–PUB–7051, in *Proc's: Workshop on Electron-Electron Colliders*, C. Heusch ed., Santa Cruz, CA, (1995);

[Telnov 1987] V.I. Telnov, "Scattering of Electrons on Termal Radiation Photons in Electron-Positron Storage Rings", *Nucl. Instr. Methods A* **260**, 304 (1987).

[Tenenbaum 1995] P. Tenenbaum, D. Burke, R. Helm, J. Irwin, K. Oide, and K. Flöttmann, "Beam-Based Magnetic Alignment of the Final Focus Test Beam", SLAC–PUB–95–6769 (1995).

[Walker 1993] N.J. Walker, J. Irwin, M. Woodley, "Global Tuning Knobs for the SLC Final Focus", *Proc. of the 1993 Part. Acc. Conf.*, Washington, DC (1993).

[Walker 1987] R.P. Walker, "Calculation of the Touschek Lifetime in Electron Storage Rings", Proceedings of IEEE PAC 1987, Washington, DC, 491 (1987).

[Walz, 1967] D.R. Walz and E.J. Seppi, "Radiolysis and hydrogen evolution in the A-beam dump radioactive water system", Report No. SLAC–TN–67–29, Stanford Linear Accelerator Center, (October, 1967).

[Walz 1967a] D.R. Walz *et al.,* "Beam Dumps, energy slits and collimators at SLAC—their final versions and first performance data", *IEEE Trans. Nucl. Sci.* **3** NS-14, 923–927 (1967).

[Walz 1969] D.R. Walz and L.R. Lucas, "The `sphere dump'—a new low-cost high-power beam dump concept and a catalytic hydrogen-oxygen recombiner for radioactive water systems", *IEEE Trans. Nucl. Sci.* **3** NS-16, 613–617 (1969).

[Wilson 1995] P. Wilson supplied the scaling laws of Table 11-38, and the analysis of the consequences of thermal changes of the waveguide.

[Woodley 1994] M.D. Woodley, unpublished (1994).

[Woods 1994] M. Woods, "Polarization at SLAC", SLAC–PUB–6694, (October 1994).

[Yokoya 1986] K. Yokoya, ABEL, "A Computer Code for the Beam-Beam Interaction in Linear Colliders", *Nucl. Instr. and Methods* **B251** 1 (1986); Toshiaki Tauchi *et al., Particle Acclerators* **41**, 29 (1993). We thank Mike Ronan for providing the latest version of ABEL (Analysis of Beam-beam Effects in Linear colliders).

[Yokoya 1988] K. Yokoya and P. Chen, "Depolarization Due to Beam-Beam Interaction in Electron-Positron Linear Colliders", SLAC–PUB–4692 (1988). See also: US-CERN School on Part. Accel's. (1990).

[ZEUS/H1] See numerous papers by ZEUS or H1 collaborations on photoproduction in HERA, *e.g.,* C. Kiesling, "Physics from the First Year of H1 at HERA", DESY–94–137 (1994).

[Zimmermann 1995] F. Zimmermann, R. Helm and J. Irwin, "Optimization of the NLC Final Focus System", SLAC–PUB–95–6791, presented at 1995 Part. Acc. Conf., (1995).

[Zimmermann 1995b] F. Zimmermann *et al.*, "Performance of the 1994/95 SLC Final Focus System", SLAC–PUB–95–6790 (1995). presented at 1995 Part. Acc. Conf., (1995).

Contributors

- Gordon Bowden
- Paul Emma
- Karl Brown
- Dave Burke
- Leif Eriksson
- Dick Helm
- Stan Hertzbach
- John Irwin
- Eugene Kraft
- Robert Messner
- Yuri Nosochkov
- Katsunobu Oide
- Tor Raubenheimer
- Jim Spencer
- Peter Tenenbaum
- Fang Tian
- Dieter Walz
- Perry Wilson
- Mike Woods
- Mark Woodley
- Frank Zimmermann